POLITECHNIKA BYDGOSKA
im. Jana i Jędrzeja Śniadeckich

RADA NAUKOWA DYSCYPLINY INŻYNIERIA MECHANICZNA

ROZPRAWA DOKTORSKA

mgr inż. Jan Seyda

OBSERWACJA MECHANIZMU INICJACJI, PROPAGACJI I KUMULACJI USZKODZEŃ ORAZ PROGNOZOWANIE TRWAŁOŚCI ZMĘCZENIOWEJ W ZAKRESIE CYKLICZNYCH OBCIĄŻEŃ WIELOOSIOWYCH.

Observation of the mechanisms of initiation, propagation and accumulation of fatigue damage and prediction of fatigue life in the range of cyclic multiaxial loadings

DZIEDZINA: NAUKI INŻYNIERYJNO-TECHNICZNE
DYSCYPLINA: INŻYNIERIA MECHANICZNA

PROMOTOR PRACY
DR HAB. INŻ. ŁUKASZ PEJKOWSKI
KATEDRA MECHANIKI I METOD KOMPUTEROWYCH, WYDZIAŁ INŻYNIERII MECHANICZNEJ, POLITECHNIKA BYDGOSKA IM. JANA I JĘDRZEJA ŚNIADECKICH

PROMOTOR POMOCNICZY
DR INŻ. ANDRZEJ SKIBICKI
KATEDRA PODSTAW KONSTRUKCJI MASZYN I INŻYNIERII BIOMEDYCZNEJ, WYDZIAŁ INŻYNIERII MECHANICZNEJ, POLITECHNIKA BYDGOSKA IM. JANA I JĘDRZEJA ŚNIADECKICH

Bydgoszcz, 2024

Źródło finansowania

Wszystkie koszty związane z prowadzeniem badań zostały sfinansowane z funduszy Katedry Mechaniki i Metod Komputerowych, Wydziału Inżynierii Mechanicznej Politechniki Bydgoskiej im. J. i J. Śniadeckich.

Podziękowania

Chciałbym serdecznie podziękować wszystkim osobom i instytucjom, które przyczyniły się do powstania niniejszej rozprawy doktorskiej.

W szczególności pragnę wyrazić moją wdzięczność dla mojego promotora, dr hab. inż. Łukasza Pejkowskiego, za nieustanne wsparcie, cenne wskazówki i inspirację, która była niezbędna do zrealizowania tego projektu. Jego zaangażowanie i profesjonalizm były dla mnie nieocenione.

Nie mogę zapomnieć również o moim promotorze pomocniczym, dr inż. Andrzeju Skibickim, który również okazał mi ogromne wsparcie i udzielił cennych rad i pomocy w trakcie pracy nad rozprawą.

Dziękuję także moim współpracownikom z Politechniki Bydgoskiej im. Jana i Jędrzeja Śniadeckich, którzy byli bardzo pomocni na każdym etapie moich badań. Ich wkład w dyskusje i analizę wyników był niezastąpiony. W szczególności dziękuję panu prof. dr hab. inż. Dariuszowi Skibickiemu, kierownikowi katedry Mechaniki i Metod Komputerowych Wydziału Inżynierii Mechanicznej.

Wyrażam także wdzięczność dla mojej rodziny i przyjaciół za wsparcie emocjonalne i motywację podczas pisania rozprawy. Były one dla mnie nieocenione.

Na zakończenie chciałbym podziękować wszystkim osobom, których nazwisk nie wymieniłem, a które w jakiś sposób przyczyniły się do powstania tej rozprawy.

Spis treści

1 Wstęp

Zmęczenie materiału to proces uszkodzenia strukturalnego wynikający z wielokrotnego obciążania materiału. Jest to zjawisko, które zachodzi bez wyraźnych oznak i stanowi najbardziej powszechną, a jednocześnie najmniej zrozumianą formę pękania, stanowiącą przynajmniej 80% wszystkich awarii w trakcie eksploatacji [1]. Występuje ono w wielu dziedzinach ludzkiego działania, będąc przyczyną poważnych wypadków, takich jak katastrofy mostów, statków, samolotów i pociągów, awarie komponentów samochodowych, problemy strukturalne w przemyśle nuklearnym i energetycznym [2–10].

Badania nad zmęczeniem materiału rozpoczęły się w połowie XIX wieku z powodu występowania pęknięć eksploatacyjnych podczas cyklicznego obciążenia elementów maszyn w rozwijających się nowych gałęziach przemysłu. Pierwsze systematyczne badania zostały przeprowadzone przez Wöhlera (1860) i dotyczyły one identyfikacji zjawiska zmęczenia. Wöhler wprowadził pojęcia „granica zmęczenia" oraz „krzywa zmęczeniowa", zwana również krzywą S-N lub krzywą Wöhlera. Krzywa zmęczeniowa opisuje zależność pomiędzy poziomem obciążenia a trwałością zmęczeniową, umożliwiając przewidzenie chwili wystąpienia awarii. Z kolei „granica zmęczenia" jest to maksymalna wartość naprężenia cyklicznego, przy której umownie nie zachodzi proces zmęczeniowy. Pierwsze badania zależności pomiędzy odkształceniem a naprężeniem podczas cyklicznego obciążania zostały przeprowadzone przez Bauschingera (1886), który zauważył, że granica plastyczności przy rozciąganiu lub ściskaniu obniża się po przyłożeniu obciążenia o przeciwnym znaku wywołującego plastyczne odkształcenie [11]. Zastosowanie ekstensometru w badaniach, umożliwiło zarejestrowanie pętli histerezy zawierającej informacje o plastycznym odkształceniu. Pierwsze badania nad uszkodzeniem zmęczeniowym materiałów zostały przeprowadzone przez Ewinga i Humfreya (1903) [12]. Dotyczyły one obserwacji, za pomocą mikroskopu optycznego, powstającego reliefu oraz pęknięć na powierzchni próbek pod wpływem obciążeń cyklicznych. Badania mikroskopowe dowiodły znaczenia odkształcenia plastycznego w procesie inicjacji pęknięć zmęczeniowych.

Basquin (1910) opisał zależność pomiędzy naprężeniem a trwałością jako funkcję liniową w układzie podwójnie logarytmicznym [13], która do dziś jest przedstawiana w literaturze z różnymi modyfikacjami. Z kolei Masing (1926) stworzył model pętli histerezy wyznaczanej na podstawie krzywej cyklicznej odpowiedzi naprężeniowo-odkształceniowej materiału [14]. Dla większości materiałów, każdą z gałęzi pętli histerezy można uzyskać skalując dwukrotnie

cykliczną krzywę naprężeniowo-odkształceniową. Taka odpowiedź materiału nazywana jest zachowaniem zgodnym z modelem Masinga (*Masing behaviour*). Sformułowanie liniowej reguły kumulacji uszkodzenia Palmegren-Minera (1945) umożliwiło szacowanie trwałości zmęczeniowej dla obciążeń zmienno-amplitudowych [15]. Wraz z rozwojem technologii i wynalezieniem skaningowego mikroskopu elektronowego (SEM), transmisyjnego mikroskopu elektronowego (TEM) i mikroskopu sił atomowych (AFM), badania mikroskopowe dostarczyły coraz dokładniejszych i sięgających do mniejszych skali opisów zjawisk zachodzących w materiałach podczas cyklicznego odkształcania. Obserwacje mikroskopowe umożliwiają odkrycie wpływu przyłożonego obciążenia i mikrostruktury materiału na ruch dyslokacji w sieci krystalicznej, tworzenia się pasm poślizgu, bliźniaków odkształcenia, inicjacji pęknięć oraz propagacji pęknięć. Forsyth (1961) zaproponował podział procesu propagacji pęknięć zmęczeniowych na dwa etapy. Pierwszy etap (*Stage I*) polega na propagacji mikropęknięć wzdłuż płaszczyzny maksymalnego naprężenia tnącego. Z kolei w drugim etapie (*Stage II*) pęknięcia propagują wzdłuż płaszczyzny maksymalnego naprężenia rozciągającego [16].

Sformułowanie równania Mansona-Coffina (1954) podkreśliło znaczenie cyklicznego odkształcenia plastycznego w trwałości zmęczeniowej i zapoczątkowało rozwój modeli szacowania trwałości dla zakresu obciążeń niskocyklowego zmęczenia [17]. Wraz z rozwojem maszyn wytrzymałościowych i ich układów sterowania zaczęto badać nie tylko przebiegi obciążeń zmienno-amplitudowych, ale również przebiegi losowe, lub pseudolosowe. Rzadko w rzeczywistości elementy maszyn obciążone są powtarzającymi się cyklami obciążenia o jednakowej amplitudzie. W odpowiedzi na problematykę zliczania cykli przy losowych przebiegach obciążeń, Matsuishi i Endo (1968) rozwinęli metodę rainflow [18], która do dziś jest jedną z najpopularniejszych metod zliczania cykli obciążenia. Pierwsze badania wpływu przesunięcia fazowego pomiędzy składowymi złożonych obciążeń cyklicznych w zmęczeniu wieloosiowym przeprowadzili Nishihara i Kawamoto (1947) [19,20]. Przy obciążeniach nieproporcjonalnych materiały wykazują wyraźnie krótszą trwałość zmęczeniową w porównaniu do obciążeń proporcjonalnych o takich samych zakresach. Następstwem tych badań było sformułowanie wieloosiowych parametrów uszkodzenia zmęczeniowego (FDPs – *Fatigue Damage Parameters*). Można je pogrupować ze względu na wielkości fizyczne, na których bazują. Wielkości te obejmują zazwyczaj zakresy naprężeń normalnych i stycznych, odkształceń postaciowych i normalnych, a także energię odkształcenia. Bardzo popularne stało się podejście płaszczyzny krytycznej, które zostało zaproponowane przez Stanfielda (1935) [21] i rozwinięta przez Findleya (1959) [22]. Płaszczyzna krytyczna zdefiniowana jest jako płaszczyzna, na której

wartość FDP lub jedna z jego składowych osiąga maksimum. Obecnie nadal powstają nowe FDPs za pomocą których szacuje się trwałość w zakresie zmęczenia wieloosiowego [23–25]. Niemniej jednak nie można jednoznacznie wskazać optymalnego FDP, ponieważ wyniki szacowania różnią się zależnie od badanego materiału i charakterystyki obciążenia [26].

Aby określić trwałość zmęczeniową przy obciążeniach wieloosiowych, nadal rozwijane są metody liczenia cykli i kumulacji uszkodzeń. Najpopularniejszą podstawą modelu kumulacji uszkodzeń jest liniowa reguła Palmgrena-Minera [27]. Reguła ta ma na celu umożliwić dodawanie uszkodzeń generowanych blokami obciążenia o różnej amplitudzie i kombinacji obciążeń oraz obciążeniem w pełni losowym, jak ma to miejsce najczęściej w rzeczywistej eksploatacji maszyn. Uszkodzenie elementu występuje, gdy skumulowane uszkodzenie spowodowane przez każdy cykl obciążenia jest równe jedności. Reguły tej nie stosuje się jednak do wszystkich materiałów i przypadków obciążenia, więc nadal rozwijane są nowe modele kumulacji uszkodzenia zmęczeniowego [28]. Lepsze zrozumienie zjawisk zachodzących w materiałach pod wpływem obciążeń cyklicznych przyczynia się do doskonalenia tych metod.

Kolejnym ważnym zagadnieniem jest metoda zliczania cykli obciążenia zmęczeniowego. Rzeczywiste, eksploatacyjne przebiegi obciążeń maszyn rzadko wykazują stałą amplitudę i częstotliwość obciążenia, gdyż najczęściej mają one charakter losowy. Rozwinięto kilka metod zliczania cykli, czy wyznaczania widma obciążeń, wśród których można wymienić metoda zliczania lokalnych ekstremów (*peak method*), metoda zliczania rozpiętości gałęzi (*range method*), metoda zliczania par rozpiętości (*range-pair method*) oraz metoda obwiedni (*rainflow method*) [29,30]. Największą popularnością cieszy się metoda rainflow [31] opierająca się na zliczaniu i charakteryzowaniu cykli obciążenia w historii czasowej, przy czym łączy w sobie informacje o amplitudach i średnich wartościach obciążenia dla zidentyfikowanych cykli i nawrotów, co czyni ją bardziej kompleksową niż inne metody.

Literatura przedstawia wiele modeli krzywych zmęczeniowych, które opisują związek między amplitudą naprężenia, odkształceniem lub innymi wielkościami a trwałością zmęczeniową [32,33]. Krzywe zmęczeniowe wykorzystywane są do szacowania trwałości zmęczeniowej elementów maszyn na podstawie obliczeniowych przebiegów obciążenia, którym będą poddawane podczas eksploatacji. Modele takie jak Basquin-Manson-Coffin [34], Castillo i in. [35], Pascual i Meeker [36] i inne zostały opracowane dla różnych materiałów i warunków obciążenia.

Odpowiedź metalu lub stopu na obciążenie zależy od budowy jego mikrostruktury [37], gdzie istotny wpływ mają struktura sieci krystalograficznej, wielkość ziaren oraz struktury

wydzieleń i dyslokacji [38,39]. Opis procesu uszkodzenia zmęczeniowego, unikając sprowadzania do zjawisk w skali atomowej, może być realizowany poprzez analizę procesu inicjacji i propagacji małych pęknięć występujących w materiale podczas cyklicznego obciążenia. Taki opis umożliwia tworzenie modeli predykcyjnych [40]. Proces uszkodzenia zmęczeniowego można podzielić na trzy etapy, znane jako zarodkowanie małych pęknięć (*Stage I*), stabilna propagacja pęknięcia (*Stage II*) i niestabilne pękanie (*Stage III*) [16]. Podczas zarodkowania pęknięć, zjawiska w mikroskali zachodzą w obrębie poszczególnych ziaren poprzez tworzenie się pasm poślizgu. Pod wpływem obciążenia mechanicznego aktywują się w ziarnach pasma poślizgu. W wyniku powtarzających się cykli obciążenia, przemieszczające się pasma poślizgu przekształcają się w coraz większe intruzje i ekstruzje aż do utworzenia mikropęknięć. Siłą napędową tego procesu jest odkształcenie postaciowe. Najczęściej pęknięcia zmęczeniowe zarodkują przy powierzchni, ponieważ w tym obszarze ziarna metali są mniej ograniczone sąsiednimi ziarnami, w związku z czym mają większą swobodę ruchu [41]. Na etapie propagacji zainicjowane pęknięcia zwiększają swój rozmiar z każdym cyklem obciążenia. Przy małych rozmiarach pęknięć na propagację wpływa lokalny stan odkształcenia (etap I), a takie pęknięcia nazywane są małymi pęknięciami. Gdy pęknięcia przekroczą pewien rozmiar, zwykle około kilkuset mikrometrów, następuje ich przekształcenie w pęknięcia długie. Dzieje się tak, ponieważ zaczynają one tworzyć własną strefę plastyczną na wierzchołku pęknięcia [42], a mechanizm wzrostu pęknięć przechodzi do etapu II. Etap II obejmuje powstawanie prążków zmęczeniowych, które można zaobserwować na powierzchni przełomu uszkodzonych próbek. Trzeci etap to ostateczne zniszczenie próbki lub niestabilny wzrost pęknięcia (etap III), któremu towarzyszy zauważalny spadek sztywności materiału, a prążki zmęczeniowe na powierzchni pęknięcia przekształcają się w nieregularną powierzchnię przełomu nazywaną strefą resztkową [10]. Analiza mechanizmu inicjacji i propagacji małych pęknięć ma kluczowe znaczenie dla identyfikacji parametrów obciążenia, od których zależy proces akumulacji uszkodzeń zmęczeniowych [43,44].

Wykonanie analiz mikroskopowych znacznie pogłębia zrozumienie zjawisk zachodzących podczas uszkodzenia materiału. Umożliwia ono uzasadnienie założeń modeli oraz poprawne zinterpretowanie zauważonych odchyleń od trendów. Zjawiska zachodzące podczas mechanicznego uszkodzenia materiału często mają tak małą skalę, że mikroskopia elektronowa SEM staje się niezbędnym narzędziem. Z kolei, możliwość prześledzenia zmian w topografii powierzchni próbek, którą oferuje technika replikacji dostarcza bardzo przydatnych informacji na temat zjawisk zachodzących podczas prób zmęczeniowych.

1.1 Problem badawczy

Poznawanie odpowiedzi materiałów na obciążenia mechaniczne w celu tworzenia lub kalibracji modeli przewidujących zachowanie materiałów jest bardzo pracochłonne i wymagające wykonania licznych prób eksperymentalnych. Badania zmęczeniowe pod tym względem są szczególnie pracochłonne i czasochłonne. Co więcej, gdy analizuje się wpływ obciążeń wieloosiowych, ilość możliwych kombinacji parametrów wejściowych przekracza realne możliwości badawcze. Jeszcze większą liczbę możliwych kombinacji wprowadza ciągle rosnąca ilość wykorzystywanych materiałów konstrukcyjnych, stan ich warstwy wierzchniej oraz wpływ warunków środowiskowych takich jak korozja, i temperatura. Przez ponad wiek badań rozwijane są coraz bardziej zaawansowane modele do prognozowania trwałości, lecz pomimo wielkich postępów w tej dziedzinie, w wielu zakresach problem nie został rozwiązany dostatecznie. Pożądaną cechą modeli jest ich uniwersalność, umożliwiająca oszacowanie trwałości zmęczeniowej dla różnych materiałów oraz przypadków obciążenia. W niniejszej pracy doktorskiej uwaga została skupiona na obserwacji mechanizmów inicjacji, propagacji i kumulacji uszkodzeń w materiałach poddawanych obciążeniom mechanicznym, szczególnie wieloosiowym obciążeniom zmęczeniowym, oraz na zrozumieniu wpływu zachodzących zjawisk na dokładność modeli prognozowania trwałości zmęczeniowej.

1.2 Cel i zakres badań

Głównym celem badań przedstawionych w rozprawie doktorskiej było zgłębienie zrozumienia fizycznych mechanizmów uszkodzenia materiałów pod wpływem działania obciążeń mechanicznych. Lepsze ich poznanie ma prowadzić do doskonalenia lub rozwoju nowych narzędzi i metod analizy, które pozwolą na dokładniejsze przewidywanie wytrzymałości doraźnej, a przede wszystkim wytrzymałości i trwałości zmęczeniowej. Badania obejmowały zarówno testy mechaniczne, jak i analizy mikroskopowe rozwoju pęknięć oraz fraktografię SEM przełomów próbek.

Szczegółowe cele wypunktowano poniżej:

- analiza przyczyn rozbieżności w wartościach naprężeń stycznych od skręcania obliczanych różnymi metodami, dla obciążeń cyklicznych w zakresie odkształceń sprężysto-plastycznych (artykuł 3 z cyklu publikacji),
- zbadanie korelacji pomiędzy kierunkiem inicjacji pęknięć a wielkościami mechanicznymi, takimi, jak naprężenia, odkształcenia, czy energia w

zróżnicowanych przypadkach obciążeń dla stopu aluminium PA38-T6, stali E235, E355 oraz X5CrNi18-10 (artykuły 1, 2, 4, 5 i 6 z cyklu publikacji),

- rozpoznanie, za pomocą analizy małych pęknięć na powierzchniach próbek, przyczyny różnic w dokładności szacowania trwałości zmęczeniowej z zastosowaniem najpopularniejszych parametrów uszkodzenia zmęczeniowego w stopie aluminium PA38-T6, stali E235, E355 oraz X5CrNi18-10 (artykuły 1 i 2 z cyklu publikacji),
- zbadanie udziału czasowego formowania się struktur przełomów zmęczeniowych oraz ich znaczenie dla analizy mechanizmu uszkodzenia zmęczeniowego w stopie aluminium PA38-T6 (artykuł 4 z cyklu publikacji),
- zbadanie czasowego udziału w całkowitej trwałości zmęczeniowej etapów inicjacji, stabilnej propagacji i niestabilnego przyrostu pęknięć zmęczeniowych w stopie aluminium PA38-T6 (artykuł 6 z cyklu publikacji),
- zbadanie przyczyn przeszacowania trwałości zmęczeniowej przez stosowanie parametru uszkodzenia zmęczeniowego Fatemi-Socie pomimo zbieżności założeń tego parametru z obserwowanym mechanizmem uszkodzenia zmęczeniowego w stopie aluminium PA38-T6 (artykuł 6 z cyklu publikacji),
- wyznaczenie krzywej zmęczeniowej dla spieku renu oraz zbadanie dokładności uproszczonych metod wyznaczania krzywej zmęczeniowej na podstawie danych z prób monotonicznego rozciągania (artykuł 7 z cyklu publikacji),
- rozpoznanie cech mechanizmu uszkodzenia spieku renu pod wpływem obciążeń monotonicznego rozciągania i jednoosiowego zmęczenia (artykuł 7 z cyklu publikacji),

Rozprawa doktorska obejmuje szereg zagadnień dotyczących zjawisk zachodzących w materiałach pod wpływem obciążeń mechanicznych, ze szczególnym uwzględnieniem wpływu obciążeń zmęczeniowych na proces uszkodzenia materiału. Zakres przeprowadzonych badań obejmował:

- badania zmęczeniowe na próbkach cienkościennych poddawanych obciążeniom wieloosiowym przeprowadzono w zakresie odkształceń ekwiwalentnych od $\varepsilon_{eq} = 0{,}002$ do $\varepsilon_{eq} = 0{,}008$ (artykuły 1, 2, 3, 4, 5 i 6 z cyklu publikacji),

- analizę mikroskopową pęknięć na powierzchni próbek po próbach zmęczeniowych wykonaną dla stopu aluminium PA38-T6, stali E235, E355 oraz X5CrNi18-10; obserwację pęknięć przeprowadzono na mikroskopie metalograficznym. Porównano dokładność szacowania trwałości zmęczeniowej na podstawie odkształcenia ekwiwalentnego Hubera-Misesa oraz parametrów uszkodzenia zmęczeniowego Fatemi-Socie, Smith-Watson-Topper, Ince-Glinka, Ellyin-Gołoś i Itoh-Sakane, wraz z analizą kierunków zaobserwowanych małych pęknięć (artykuł 1 i 2 z cyklu publikacji),
- rejestrowanie rozwoju pęknięć na powierzchni próbek w trakcie trwania prób zmęczeniowych realizowanych na próbkach ze stopu aluminium PA38-T6 za pomocą techniki replikacji folią z octanu celulozy (artykuły 4, 5 i 6 z cyklu publikacji),
- analizę przełomów próbek przeprowadzoną na skaningowym mikroskopie elektronowym (SEM) przy powiększeniu do 5000 razy (artykuły 5, 6 i 13 z cyklu publikacji). Identyfikację rozkładu pierwiastkowego faz mikrostruktury badanych materiałów wykonaną na SEM za pomocą detektora spektrografii energodyspersyjnej (EDS) (artykuły 5 i 6 z cyklu publikacji),
- analizę przyczyn rozbieżności w metodach wyznaczania eksperymentalnych wartości naprężeń stycznych dla próbek cienkościennych poddawanych cyklicznemu skręcaniu. Zamodelowane zostały rozkłady naprężeń po grubości próbek za pomocą modelu plastyczności Chaboche'a, modeli materiału idealnie sprężystego, idealnie plastycznego oraz metody środka przekroju (*midsection*). Dane wejściowe wykorzystane do kalibracji modelu plastyczności oraz do walidacji wyników zostały wygenerowane eksperymentalnie (artykuł 3 z cyklu publikacji),
- monotoniczne rozciąganiu oraz jednoosiowe zmęczenie próbek wykonanych ze spieku renu, w zakresie amplitudy naprężenia $350\ \text{MPa} \leq \sigma_a \leq 410\ \text{MPa}$ oraz w zakresie trwałości zmęczeniowej $4 \cdot 10^4 \leq N_f \leq 4 \cdot 10^6$. Przełomy próbek przeanalizowano za pomocą SEM przy powiększeniu do 10000 razy. Wykonano analizy zgładów metalograficznych przed i po próbach wytrzymałościowych, analizy topografii powierzchni roboczej próbek po próbach zmęczeniowych oraz pomiary twardości spieku w trzech kierunkach względem kierunku spiekania (artykuł 7 z cyklu publikacji),

Wprowadzenie do tematyki pracy, opis problemu badawczego oraz cel i zakres pracy opisano w rozdziale 1. Zbiór oryginalnych publikacji naukowych przedstawiono w rozdziale 2. Opis stosowanych w badaniach materiałów i metod, wyróżniających się wyników badań i analiz oraz spis literatury przedstawiono w rozdziale 3.

2 Zbiór publikacji naukowych stanowiących rozprawę doktorską

Badania zaplanowane w ramach indywidualnego planu badawczego.

1. Pejkowski Ł, Seyda J. Fatigue of four metallic materials under asynchronous loadings: Small cracks observation and fatigue life prediction, International Journal of Fatigue (Elsevier), 2021, 142, 105904, 1-18, DOI: 10.1016/j.ijfatigue.2020.105904, 140 pkt. MNiSW, *IF 5.489*

   Mój udział w pracy polegał na analizie mikroskopowej topografii powierzchni próbek oraz identyfikacji kierunków inicjacji małych pęknięć zmęczeniowych.

2. Pejkowski Ł, Seyda J, Skibicki D. Short cracks observations on surfaces of specimens made of three materials, subjected to synchronous and asynchronous multiaxial loadings, Matec Web of Conferences (EDP Sciences), 2019, 300, 1-8, DOI: 10.1051/matecconf/201930015002, 5 pkt. MNiSW

   Mój udział w pracy polegał na analizie mikroskopowej topografii powierzchni próbek oraz identyfikacji kierunków inicjacji małych pęknięć.

3. Seyda J, Pejkowski Ł, Skibicki D. The shear stress determination in tubular specimens under torsion in the elastic–plastic strain range from the perspective of fatigue analysis. Materials (MDPI), 2020, 13, 23, 1-16, DOI: 10.3390/ma13235583, 140 pkt. MNiSW, *IF 3.623*

   Mój udział w pracy polegał na zamodelowaniu rozkładu naprężeń stycznych na grubości próbek dla kilku poziomów obciążenia w zakresie odkształceń sprężysto-plastycznych, analizie przyczyn niejednorodności rozkładu naprężeń, analizie skutków stosowania aktualnych metod wyznaczania naprężeń stycznych na dokładność obliczeń w badaniach eksperymentalnych.

4. Seyda J, Pejkowski Ł, Skibicki D. Identification of fatigue damage mechanism in PA38-T6 aluminum alloy under multiaxial loadings – Initial research. Procedia Structural Integrity (Elsevier), 2020, 28, - , 1458-1466, DOI: 10.1016/j.prostr.2020.10.119, 5 pkt. MNiSW

   Mój udział w pracy polegał na stworzeniu koncepcji pracy, przygotowaniu próbek, przeprowadzeniu testów zmęczeniowych wraz z wytworzeniem replik powierzchni próbek, analizie danych, wykonaniu obserwacji mikroskopowych replik oraz powierzchni próbek, analizie rozwoju pęknięć na powierzchni próbek dla trzech przypadków obciążenia, analizie zależności cech inicjacji i propagacji pęknięć z parametrami mechanicznymi badanych przypadków obciążenia.

5. Seyda J, Pejkowski Ł. SEM analysis of PA38-T6 aluminum alloy thin-walled tubular specimen fatigue fracture, and comparison to surface replication results, Matec Web of Conferences (EDP Sciences), 2019, 300, 1-8, DOI: 10.1051/matecconf/201930015002, 5 pkt. MNiSW

   Mój udział w pracy polegał na stworzeniu koncepcji pracy, przygotowaniu próbek, przeprowadzeniu testów zmęczeniowych, wykonaniu i analizie fraktograficznej SEM przełomu próbki, redagowaniu wstępnej wersji publikacji.

6. Seyda J, Pejkowski Ł. Study on the behavior of small cracks in PA38-T6 (6060-T6) aluminum alloy under multiaxial fatigue loadings. International Journal of Fatigue (Elsevier), 2024, 184, 108282, DOI: 10.1016/S1003-6326(23)66333-2, 140 pkt. MNiSW, *IF 6.000*

   Mój udział w pracy polegał na stworzeniu koncepcji pracy, przygotowaniu próbek, przeprowadzeniu testów zmęczeniowych wraz z produkcją replik powierzchni próbek, analizie danych, wykonaniu obserwacji mikroskopowych replik, analizie rozwoju pęknięć na powierzchni próbek, wykonaniu i analizie zgładów metalograficznych, analizie faktograficznej SEM przełomów próbek, analizie zależności cech inicjacji i propagacji pęknięć z parametrami mechanicznymi badanych przypadków obciążenia, analizie przyczyn rozbieżności wyników trwałościowych rzeczywistych i szacowanych za pomocą parametru Fatemi-Socie, napisaniu i redakcji artykułu.

Badania powiązane bezpośrednio z tematyką rozprawy doktorskiej.

7. Seyda J, Skibicki D, Pejkowski Ł, Skibicki A, Domanowski P, Maćkowiak P. Mechanical properties and microscopic analysis of sintered rhenium subjected to monotonic tension and uniaxial fatigue, Materials Science and Engineering A (Elsevier), 2021, 817, 141343, 1-13, DOI: 10.1016/j.msea.2021.141343, 140 pkt. MNiSW, *IF 6.044*

   Mój udział w pracy polegał na przygotowaniu próbek, przeprowadzeniu testów zmęczeniowych wraz z wyznaczaniem krzywej zmęczeniowej, wykonaniu badań twardości, przygotowaniu i analizowaniu zgładów metalograficznych, wykonaniu analiz fraktograficznych SEM przełomów próbek wraz z identyfikacją ognisk pęknięć zmęczeniowych, płaszczyzn łupliwości oraz udziału bliźniaków odkształcenia w mechanizmie deformacji materiału pod wpływem obciążeń monotonicznego rozciągania i jednoosiowego zmęczenia.

Pozostały dorobek naukowy

8. Pejkowski Ł, Skibicki D, Seyda J. Stress-strain Response and Fatigue Life of a Material Subjected to Asynchronous Loadings, Matec Web of Conferences (EDP Sciences), 2018, 2028, 020016, 1-8, DOI: 10.1063/1.5066406, 5 pkt. MNiSW

   Mój udział w pracy polegał na przygotowaniu próbek, przeprowadzeniu testów zmęczeniowych oraz wykonaniu obserwacji mikroskopowych powierzchni próbek z identyfikacją pęknięć i analizą korelacji płaszczyzn inicjacji i kierunku propagacji z parametrami przebiegu obciążenia zbadanych przypadków obciążenia.

9. Pejkowski Ł, Skibicki D, Seyda J. Fatigue behaviour of selected materials under multiaxial asynchronous loadings, Matec Web of Conferences (EDP Sciences), 2019, 300, 15006, 1-9, DOI: 10.1051/matecconf/201930015006, 5 pkt. MNiSW

   Mój udział w pracy polegał na przygotowaniu próbek oraz przeprowadzeniu testów zmęczeniowych.

10. Skibicki D, Pejkowski Ł, Karolczuk A, Seyda J. Verification of the Tanaka non-proportional isotropic cyclic hardening model under asynchronous loading. International Journal of Solids and Structures, 2022, 254-255, 111896, DOI: 10.1016/j.ijsolstr.2022.111896, 140 pkt. MNiSW, *IF 3.600*.

    Mój udział w pracy polegał na wykonaniu zgładów metalograficznych oraz na identyfikacji mikrostruktury materiału próbek.

11. Trepczyńska-Łent M, Seyda J. Characteristics of Ledeburite in EDS Analyses of Directionally Solidified Eutectic White Cast Iron. Archives of Foundry Engineering, 2022, 4/2022, 65-71, DOI: 10.24425/afe.2022.143951, 70 pkt. MNiSW, *IF 0.600*.

    Mój udział w pracy polegał na wykonaniu analizy SEM zgładów oraz rozpoznaniu rozkładu pierwiastkowego poszczególnych faz ledeburytu w zależności od prędkości krzepnięcia za pomocą analizy EDS.

12. Karuskevich M, Maslak T, Gavrylov I, Pejkowski Ł, Seyda J. Structural health monitoring for light aircraft. Procedia Structural Integrity, 2022, 36, 92-99, DOI: 10.1016/j.prostr.2022.01.008, 5 pkt. MNiSW.

    Mój udział w pracy polegał na analizie zdjęć mikroskopowych powierzchni próbek za stopu aluminium D16AT oraz ich porównaniu z wynikami symulacji MES.

13. Pejkowski Ł, Seyda J, Nowicki K, Mrozik D. Mechanical performance of non-reinforced, carbon fiber reinforced and glass bubbles reinforced 3D printed PA12 polyamide, Polymer Testing (Elsevier), 2023, 118, 107891, 1-11, DOI: 10.1016/j.polymertesting.2022.107891, 100 pkt. MNiSW, *IF 5.100*

    Mój udział w pracy polegał na wykonaniu analizy fraktograficznej SEM przełomów próbek oraz na identyfikacji przyczyny różnic w wytrzymałości doraźnej, sztywności i relacji odkształcenowo-naprężeniowej kompozytów.

14. Tomaszewski T, Stopel M, Skibicki A, Seyda J, Piątkowski T. Effect of plastic strain under roller bending on fatigue properties of extruded 6063 T66 aluminium alloy profile. Transactions of Nonferrous Metals Society of China, 2023, 33, 3282-3294, DOI: 10.1016/S1003-6326(23)66333-2, 100 pkt. MNiSW, *IF 4.500*.

    Mój udział w pracy polegał na przygotowaniu i analizie zgładów metalograficznych.

15. Karolczuk A, Kurek A, Böhm M, Derda S, Prażmowski M, Kluger K, Żak K, Pejkowski Ł, Seyda J. Heterogeneous effect of aging temperature on the fatigue life of additively manufactured thin-walled 18Ni300 maraging steel tubular specimen. Materials & Design, 2024, 237, 112561, 1-15, DOI: 10.1016/j.matdes.2023.112561, 140 pkt. MNiSW, *IF 8.400*.

    Mój udział w pracy polegał na wykonaniu analizy frakrograficznej przełomów próbek wraz z identyfikacją przyczyn położenia ognisk pęknięć zmęczeniowych.

    Podsumowując przedstawiony cykl publikacji (do 1 do 7) składa się na sumaryczną liczbę 575 punków MNiSW oraz IF 21.156. Cały dorobek naukowy składa się na sumaryczną liczbę 1140 punków MNiSW oraz IF 43.356. Mój udział w pracach dotyczył zbadania mikrostruktury materiału próbek oraz mechanizmów uszkodzenia próbek pod wpływem obciążeń mechanicznych.

3 Uzasadnienie spójności tematycznej cyklu publikacji rozprawy

Opublikowane badania dotyczą analizy mikrostrukturalnej mechanizmów uszkodzenia elementów poddanych zmieniającym się obciążeniom mechanicznym. Przedstawiony cykl artykułów rozpoczyna się od badań stanowiących genezę rozprawy doktorskiej. Na zniszczonych próbkach cienkościennych, wykonanych ze stopu aluminium PA38-T6, ze stali maszynowej E235 i E355, oraz ze stali austenitycznej X5CrNi18-10, została wykonana analiza mikroskopowa powierzchni, na których zaobserwowano liczne pęknięcia. Rozpoznane cechy występujących pęknięć, takie jak: płaszczyzna inicjacji i kierunek propagacji, długość oraz gęstość, umożliwiły zrozumienie przyczyny rozbieżności trwałości zmęczeniowej szacowanej za pomocą popularnych modeli, w zależności od badanego materiału. Wyniki badań zostały opublikowane w artykułach [26,45] (artykuły 1 i 2 z cyklu publikacji). Otrzymane wyniki zrodziły potrzebę zbadania rozwoju pęknięć zmęczeniowych w trakcie trwania prób zmęczeniowych, ponieważ powstało szereg pytań dotyczących kolejności oraz udziału czasowego poszczególnych segmentów pęknięć zmęczeniowych. Po drodze do osiągnięcia tego celu należało rozwiązać kilka problemów badawczych.

Praca [46] (artykuł 3 z cyklu publikacji) przedstawia wyniki badań dotyczących metody wyznaczania naprężeń stycznych w próbkach skręcanych cyklicznie w zakresie odkształceń sprężysto-plastycznych. Poprawne wyznaczanie eksperymentalnych wartości naprężeń stanowi podstawę do wszelkich późniejszych analiz. Wyniki badań wstępnych analiz rozwoju małych pęknięć w trakcie badań zmęczeniowych przedstawiono w pracy [47] (artykuł 4 z cyklu publikacji), w której zbadano rozwój pęknięć na powierzchni próbek cienkościennych ze stopu aluminium PA38-T6 poddanych trzem przypadkom obciążenia. Rozpoznano mechanizm inicjacji pęknięć oraz zidentyfikowano znaczenie zjawiska koalescencji pęknięć dla trwałości prób zmęczeniowych. Praca [48] (artykuł 5 z cyklu publikacji) przedstawia wyniki analiz fraktograficznych SEM przełomu jednej próbki cienkościennej ze stopu aluminium PA38-T6 obciążonej wahadłowym rozciąganiem-ściskaniem. Wyniki obserwacji przełomu wykonano wraz z analizą rozwoju pęknięć na powierzchni. Rozpoznane zostały cechy fragmentów przełomu utworzonego podczas inicjacji małych pęknięć, stabilnej propagacji pęknięć oraz niestabilnej propagacji makropęknięcia. Połączenie wyników otrzymanych za pomocą replik powierzchni próbki i analizy przełomu umożliwiły stwierdzić jaki był czasowy udział poszczególnych etapów rozwoju pęknięć oraz nieoczywisty kierunek propagacji makropęknięcia, które nie propagowało wzdłuż obwodu próbki, lecz w kierunku od wewnętrznej

i zewnętrznej powierzchni próbki do środka przekroju. Praca zwieńczająca całość planowanych badań w ramach indywidualnego planu badawczego [49] (artykuł 6 z cyklu publikacji) zawiera kompleksową analizę mechanizmu uszkodzenia zmęczeniowego wybranego stopu aluminium. Próbki cienkościenne zostały poddane czterem przypadkom obciążenia, wliczając w to przypadki wieloosiowe nieproporcjonalne z przesunięciem fazowym składowych i asynchroniczne. Wykorzystano w sposób synergiczny techniki replikacji powierzchni zewnętrznej próbek podczas trwania badań zmęczeniowych i analizę fraktograficzną SEM. Zarejestrowano również charakterystyki naprężeniowo-odkształceniowe, celem zbadania wpływu obciążeń cyklicznych na inicjację i rozwój pęknięć zmęczeniowych. Badania przeprowadzono na stopie aluminium PA38-T6 przy zastosowaniu obciążeń wieloosiowych zawierających przypadki nieproporcjonalne z przesunięciem fazowym oraz asynchroniczne. Wyniki odnoszą się zarówno do zjawisk zachodzących podczas inicjacji i propagacji pęknięć zmęczeniowych, jak i do zidentyfikowanych wielkości mechanicznych odpowiedzialnych za te zjawiska.

Do cyklu publikacji dołączono również artykuły przedstawiające wyniki badań początkowo nie planowanych w ramach rozprawy doktorskiej, lecz bezpośrednio związanych z jej tematyką. W artykule [50] (artykuł 7 z cyklu publikacji) została opublikowana pierwsza w literaturze krzywa zmęczeniowa spieku czystego renu, oraz zidentyfikowano mechanizm uszkodzenia przy monotonicznym rozciąganiu i przy jednoosiowym zmęczeniu, wraz z identyfikacją orientacji płaszczyzn łupliwości.

Prace [51–58] (artykuły 8 - 15 z cyklu publikacji) są spójne z tematyką rozprawy, ponieważ zostały wykonane analizy mikrostrukturalne i fraktograficzne w celu poznania cech badanych materiałów oraz mechanizmów powstawania uszkodzeń pod wpływem działania obciążeń mechanicznych.

3.1 Materiały i metody badań

W pracach [26] i [45] (artykuły 1 i 2 z cyklu publikacji) zbadano cienkościenne próbki wykonane z czterech materiałów: stopu aluminium PA38-T6 (AW-6060), stali maszynowej E235 (1.0308) i E355 (1.0580), oraz stali austenitycznej X5CrNi18-10 (1.4301, 304/304L). Podstawowe właściwości mechaniczne, takie jak moduł Younga E, umowna granica plastyczności σ_{y02}, wytrzymałość na rozciąganie σ_u i odpowiadające jej odkształcenie ε_{σ_u}, liczba Poissona ν_e, które zostały określone w publikacji [59], przedstawiono w Tab. 1. Geometria próbek cienkościennych została przedstawiona na Rys. 1.

Tab. 1. Podstawowe właściwości mechaniczne zbadanych stopów metali wyznaczane eksperymentalnie [59]

Materiał	E, GPa	σ_y, MPa	σ_u, MPa	ε_{σ_u}, mm/mm	ν_e, –
PA38	68.3	191	229	0.094	0.34
E235	196.4	255	375	0.249	0.32
E355	208.6	380	473	0.237	0.32
1.4301	200.8	265	649	0.687	0.32

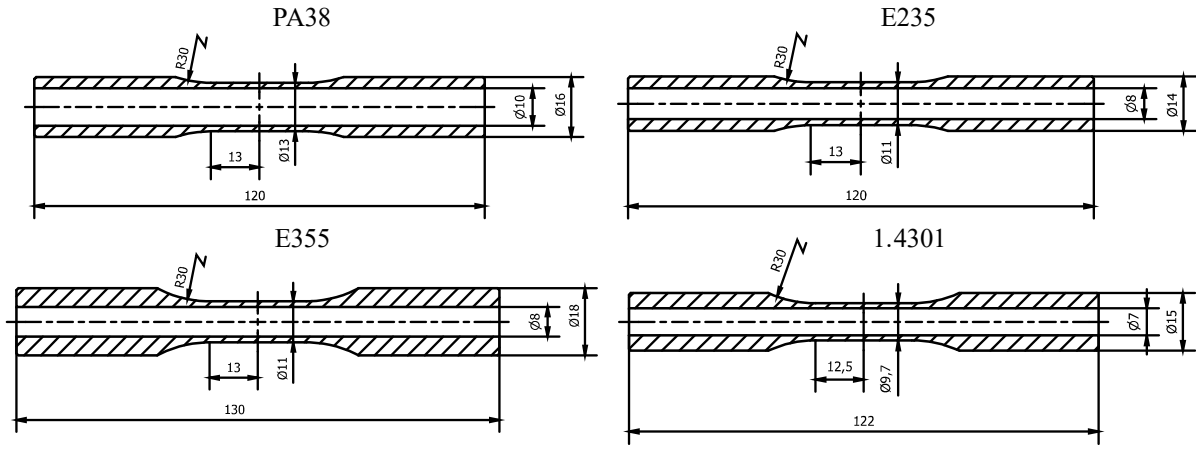

Rys. 1. Geometria cienkościennych próbek ze stopu aluminium PA38-T6 (AW-6060), ze stali maszynowej E235 (1.0308) i E355 (1.0580), oraz ze stali austenitycznej X5CrNi18-10 (1.4301, 304/304L). Wymiary podane w milimetrach

Przeprowadzono próby zmęczeniowe dla czterech podstawowych obciążeń synchronicznych: rozciąganie-ściskanie (TC), skręcanie (TOR), obciążenie proporcjonalne (IP) i nieproporcjonalne obciążenie z przesunięciem fazowym 90° (OP). Następnie przeprowadzono próby zmęczeniowe z wykorzystaniem pięciu różnych obciążeń asynchronicznych. Badania wytrzymałościowe przeprowadzono na dwuosiowej maszynie wytrzymałościowej Instron 8874. Próby sterowano odkształceniem z wykorzystaniem dwuosiowego ekstensometru Epsilon 3550 rejestrując sygnały odkształcenia osiowego i postaciowego, siły i momentu. Programowanie, sterowanie i rejestrowanie sygnałów wykonano za pomocą oprogramowania WaveMatrix. Zarejestrowane sygnały zostały przetworzone i przeanalizowane przy użyciu oprogramowania Matlab R2023a i Microsoft® Excel® for Microsoft 365. Powierzchnie próbek po próbach zmęczeniowych analizowane i sfotografowane na mikroskopie optycznym wyposażonym w cyfrową kamerę. Pojedyncze ujęcia złożono z serii zdjęć składanych po ostrości z wykorzystaniem oprogramowania CombineZ [60].

W badaniach [46–49] (artykuły 3–6 z cyklu publikacji) wykorzystano cienkościenne próbki ze stopu aluminium PA38-T6 (AW-6060). Podstawowe właściwości mechaniczne

przedstawiono w Tab. 1. Geometria próbek została przedstawiona na Rys. 1. Powierzchnia robocza próbek została wypolerowana pastami diamentowymi o gradacji do 8 μm w celu zmniejszenia chropowatości i usunięcia wszystkich zarysowań powstałych przed badaniami zmęczeniowymi.

Badania mechaniczne przeprowadzono na maszynie wytrzymałościowej Instron 8874. Przed rozpoczęciem badan maszyna wytrzymałościowa została wyosiowana zgodnie z wymaganiami normy ASTM E1012 − 14. Badania zmęczeniowe przeprowadzono w dwóch etapach. Początkowo próby sterowano odkształceniem z wykorzystaniem dwuosiowego ekstensometru Epsilon 3550, rejestrując sygnały odkształcenia osiowego i postaciowego, siły i momentu oraz przemieszczeń osiowych i skrętnych głowic maszyny wytrzymałościowej. Następnie powtórzono próby, sterując przemieszczeniem na podstawie zarejestrowanej historii przemieszczeń, w celu wytworzenia replik całkowitej powierzchni roboczej próbek w trakcje trwania badań zmęczeniowych. Programowanie, sterowanie i rejestrowanie sygnałów wykonano za pomocą oprogramowania WaveMatrix. Zarejestrowane sygnały zostały przetworzone i opracowane przy użyciu oprogramowania Matlab R2023a i Microsoft® Excel® for Microsoft 365. Kryterium zniszczenia próbki (N_f) był 5% spadek siły osiowej. Podobną definicję zastosowano dla prób obciążonych czystym skręcaniem na kanale skrętnym. Na podstawie pętli histerezy ze środka trwałości zmęczeniowej określono zakresy odkształceń i naprężeń. Wartości naprężeń tnących obliczono metodą mid-section, zgodnie z zaleceniami normy ASTM E2207-02, dla zakresu odkształceń sprężysto-plastycznych [61]. Wartości naprężeń ekwiwalentnych określono jako maksymalne w czasie jednego okresu.

W wybranych próbkach zastosowano technikę replikacji powierzchni próbek za pomocą folii z octanu celulozy o grubości 125 μm. Próby zmęczeniowe były przerywane co 10% szacowanej trwałości zmęczeniowej. Następnie naklejano na powierzchnię próbek odcinek foli zwilżonej acetonem i pozostawiano do odparowania acetonu przez około 10 minut. Gotowe repliki przechowywano pomiędzy szkiełkami mikroskopowymi. Przy każdym zatrzymywaniu prób wykonane zostały dwie repliki, które wspólnie pokrywały całą roboczą powierzchnię próbek, konieczne stało się przeprowadzenie prób bez użycie ekstensometru. Po zakończeniu prób zmęczeniowych przeanalizowano serie replik w poszukiwaniu pierwotnych pęknięć odpowiedzialnych za ostateczne zniszczenie próbek. Zdjęcia replik zarejestrowano ze światłem przechodzącym, za pomocą mikroskopu metalograficznego Delta Optical MET-1000-TRF, wyposażonego w kamerę cyfrową DLT-Cam PRO 12MP oraz dedykowanego oprogramowania

DLTCamViewer. W większości przypadków pojedyncze ujęcia zostały złożone z serii zdjęć składanych po ostrości z wykorzystaniem oprogramowania CombineZ. Na podstawie zdjęć replik wyznaczono długość i kierunek małych pęknięć, moment zarejestrowania pierwszych pęknięć oraz długość pęknięć w chwili końca trwałości zmęczeniowej N_f.

Analizy fraktograficzne SEM zostały zrealizowane na skaningowym mikroskopie elektronowym JEOL JSM-6480LV, wyposażonym w detektor elektronów wtórnych (SE), detektor elektronów wstecznie rozproszonych (BSE) oraz detektor spektrografii energodyspersyjnej (EDS). Analizy próbek aluminiowych wykonano z napięciem przyspieszania 20 kV w wysokiej próżni. Analizy składu chemicznego wydzieleń za pomocą detektora EDS. Zostały rozpoznane ogniska pęknięć zmęczeniowych, strefy inicjacji, stabilnej propagacji i niestabilnej propagacji pęknięć.

Opisane metody wykorzystano w sposób synergiczny umożliwiający dokładny opis mechanizmu uszkodzenia zmęczeniowego. Metoda replikacji dostarczyła informacji o historii rozwoju pęknięć na powierzchni próbek z identyfikacją czasu, w którym zaszły kolejne etapy rozwoju pęknięć zmęczeniowych, natomiast fraktografia SEM dostarczyła informacji o wielkości i charakterze zjawisk zachodzących w głąb materiału próbek podczas rozwoju uszkodzenia zmęczeniowego.

W pracy [50] (artykuł 7 z cyklu publikacji) próbki ze spieku czystego renu wycięto za pomocą drążarki elektroerozyjnej drutowej, przy ustawieniach napięcia 300V oraz prądu impulsów 5 A. geometria próbek została przedstawiona na Rys. 2, na którym wskazano wymiary próbek do prób zmęczeniowych, a w nawiasie wymiary próbek do prób monotonicznego rozciągania. Powierzchnia robocza próbek została wypolerowana pastami diamentowymi o gradacji od 80 μm do 1 μm w celu usunięcia wpływu obróbki elektroerozyjnej na chropowatość i mikrostrukturę materiału przy powierzchni.

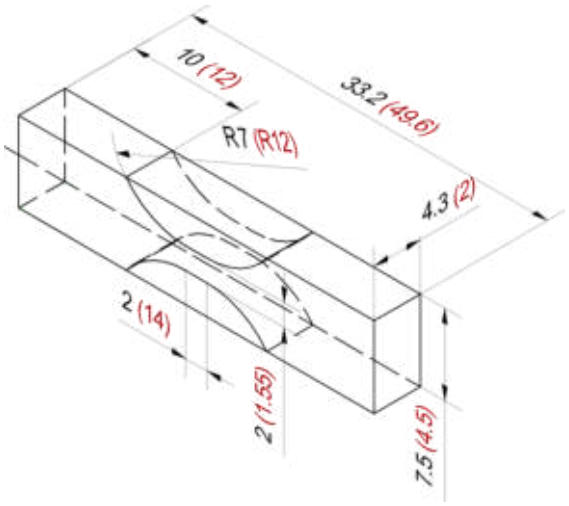

Rys. 2. Geometria próbek ze spieku czystego renu. Wymiary w nawiasach dotyczą próbek do prób monotonicznego rozciągania [50]. Wymiary podane w milimetrach.

Badania mechaniczne przeprowadzono na dwuosiowej maszynie wytrzymałościowej Instron 8874. Badania monotonicznego rozciągania zostały przeprowadzone przy kontrolowanym odkształceniu z wykorzystywaniem ekstensometru jednoosiowego Instron 2620–601. Próby zmęczeniowe, z obciążeniem jednoosiowym w zakresie wysokocyklowym, przeprowadzono sterując siłą. Programowanie, sterowanie i rejestrowanie sygnałów wykonano za pomocą oprogramowania WaveMatrix. Pomiary twardości Vickersa HV1 zrealizowano na mikrotwardościomierzu Shimadzu HMV-G20DT.

Powierzchnie przełomów próbek zarejestrowano na skaningowym mikroskopie elektronowym (SEM), JEOL JSM-5600. Zdjęcia powierzchni próbek zostały uzyskane na mikroskopie metalograficznym Delta Optical MET-1000-TRF. Zdjęcia zgładów metalograficznych wykonano w świetle spolaryzowanym. Powierzchnie zgładów metalograficznych wypolerowano pastami i zawiesinami diamentowymi o gradacji od 80 μm do 1 μm za pomocą szlifierko-polerki metalograficznej FORCIPOL 202. Powierzchnie zgładów zostały wytrawione, zgodnie z zaleceniami normy ASTM E407-07, w temperaturze pokojowej przez 300 sekund, odczynnikiem składającym się z 5 ml HF (40%), 10 ml HNO_3 (80%), oraz 50 ml $C_2H_6O_3$ (80%).

3.2 Wyniki

Na powierzchniach próbek po badaniach zmęczeniowych zaobserwowano liczne pęknięcia posiadające wspólny kierunek propagacji w ramach tego samego przypadku obciążenia [26,45] (artykuły 1 i 2 z cyklu publikacji). Pęknięcia te są niewidoczne gołym okiem, a wiele z nich nie wchodzi w skład pęknięcia głównego, które doprowadziło do zniszczenia próbki. Rozpoznano

różnice w kierunkach inicjacji i propagacji pęknięć, w zależności zarówno od konkretnego przypadku obciążenia, jak i badanego materiału. Na Rys. 3 przedstawiono wybrane ujęcia powierzchni próbek z widocznymi pęknięciami dla dwóch materiałów (stop aluminium PA38-T6 i stal austenityczna X5CrNi18-10) oraz czterech synchronicznych przypadków obciążenia (TC, TOR, IP, OP). Strzałkami wskazano pęknięcia, które w zależności od materiału oraz od przypadku obciążenia rozwinęły się pod innymi kątami względem osi próbki. Na ujęciach umieszczono również biegunowe wykresy maksymalnych w czasie odkształceń postaciowych i normalnych w zależności od położenia płaszczyzny przekroju względem osi próbki. W przypadku stopu aluminium można zaobserwować korelację pomiędzy kierunkiem propagacji pęknięć a płaszczyzną maksymalnych odkształceń postaciowych (γ_{max}). W przypadku stali austenitycznej, kierunki propagacji pęknięć korelują z płaszczyzną maksymalnych odkształceń normalnych (ε_{max}). Korelacja ta wyjaśnia, dlaczego w badanym stopie aluminium bardziej precyzyjnie szacowana jest trwałość zmęczeniowa za pomocą parametrów opartych na płaszczyźnie maksymalnych odkształceń postaciowych, a w przypadku stali austenitycznej za pomocą parametrów opartych na wartościach naprężeń głównych. Zdjęcia powierzchni próbek pozostałych materiałów (w tym stale E235 i E355) i przypadków obciążenia znajdują się w pracy [26].

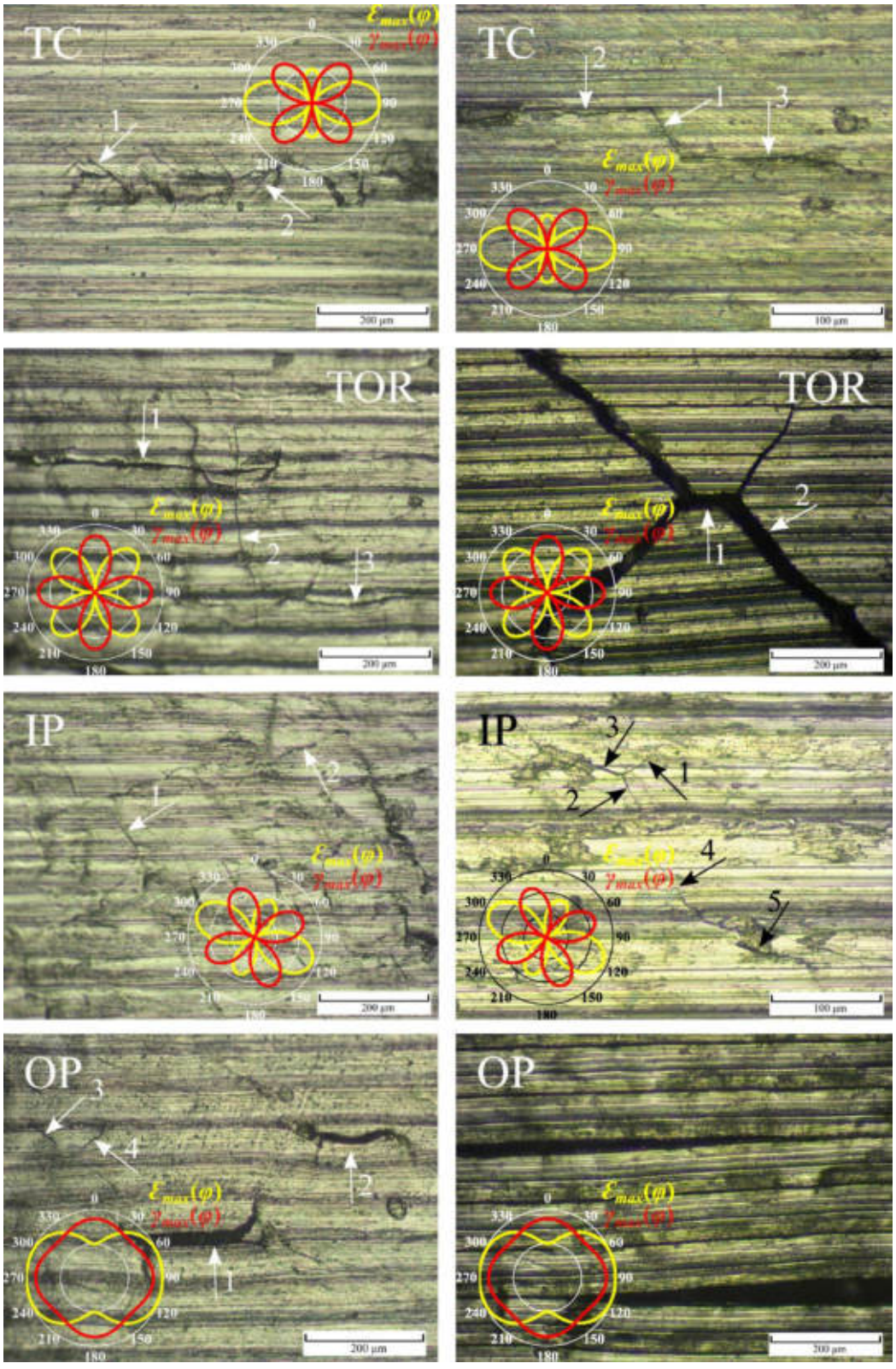

Rys. 3. Wybrane ujęcia próbek po obciążeniach dla czterech podstawowych obciążeń synchronicznych (TC, TOR, IP, OP) dla próbek wytwarzanych ze stopu aluminium PA38-T6 (lewa kolumna) oraz ze stali austenitycznej X5CrNi18-10 (prawa kolumna). [26,45]

W pracy [46] (artykuł 3 z cyklu publikacji) zbadano zjawiska zachodzące w cienkościennych próbkach podczas obciążenia momentem skręcającym z udziałem odkształceń plastycznych. Nieliniowość rozkładu naprężeń w przekroju poprzecznym powoduje niedoszacowanie lub przeszacowanie wyznaczanej wartości naprężeń stycznych w zależności od przyjętej metody obliczeniowej. Rys. 4 przedstawia interpretację rozkładów naprężeń dla metod stosowanych w literaturze, odnoszących się do modelowanego rozkładu naprężeń z wykorzystaniem modelu plastyczności Chaboche'a. Przedstawione modele dotyczą rozwiązania dla materiału idealnie sprężystego (*elastic*), materiału idealnie plastycznego (*plastic*) oraz metody zalecanej przez normę ASTM E2207-02 dla warunków niskocyklowego zmęczenia (*midsection*). Przedstawione ilustracje dotyczą czterech poziomów obciążenia zastosowanych w badaniach zmęczeniowych niskocyklowych. Model plastyczności został skalibrowany dla stopu aluminium PA38-T6 na podstawie danych eksperymentalnych uzyskanych w próbach wahadłowego rozciągania-ściskania. Przy największych obciążeniach dokładniejsze wyniki otrzymano dla założenia materiału czysto plastycznego (*plastic*) oraz midsection (Rys. 4.a i Rys. 4.b), lecz przy najmniejszym obciążeniu dokładniejszy wynik otrzymano dla metody sprężystej (*elastic*) (Rys. 4.d). Pozostałe wyniki wykonanych analiz przedstawiono i opisano w publikacji [46].

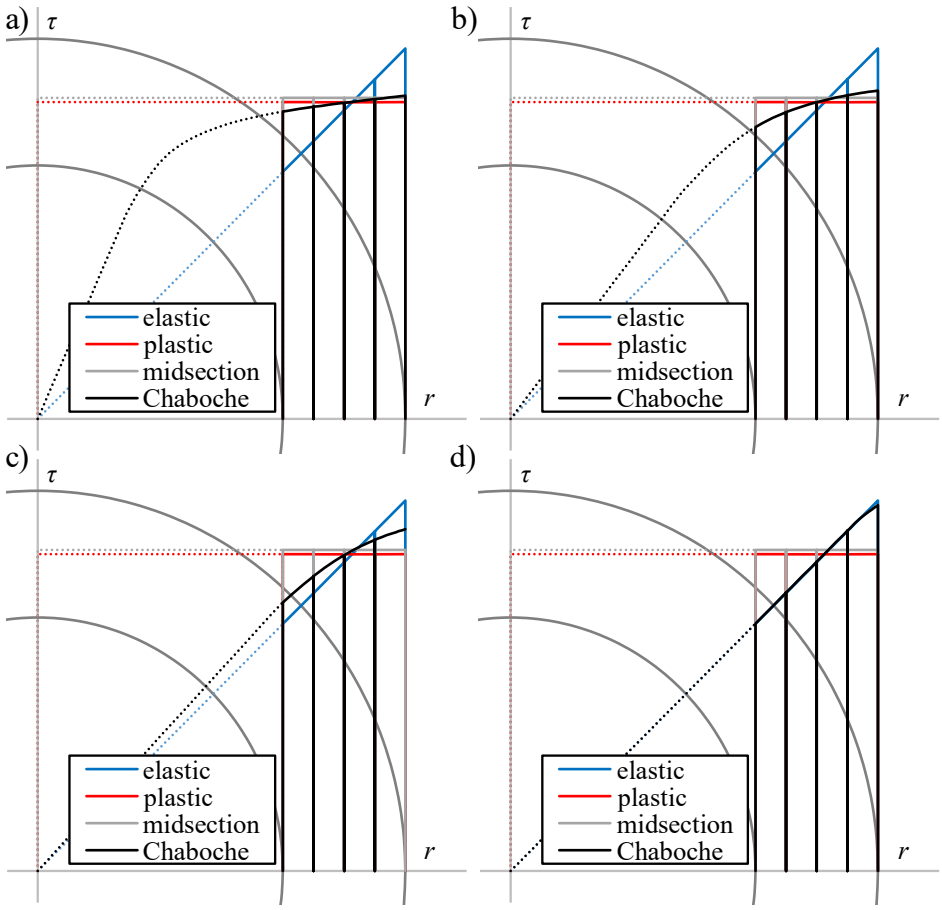

Rys. 4. Porównanie rozkładu naprężeń tnących dla teoretycznej, przewymiarowanej grubości próbki dla różnych wartości amplitud obciążenia (a) $\gamma = 0{,}0139$, (b) $\gamma = 0{,}0069$, (c) $\gamma = 0{,}0052$, (d) $\gamma = 0{,}0035$. [46]

W pracy [47] (artykuł 4 z cyklu publikacji) przedstawiono wyniki wstępnych badań, w których zarejestrowano przebieg rozwoju pęknięć zmęczeniowych na powierzchni próbek z wykorzystaniem techniki replikacji. Rozpoznano zależności pomiędzy poziomami obciążenia a gęstością małych pęknięć oraz pomiędzy przypadkiem obciążenia wieloosiowego a kierunkami małych pęknięć. Zaobserwowano znaczącą rolę mechanizmu koalescencji pęknięć w rozwoju uszkodzenia zmęczeniowego dla badanego materiału. Na Rys. 5 przedstawiono zdjęcia mikroskopowe tego samego pęknięcia dwoma metodami: bezpośrednio na powierzchni próbki oraz na replice z octanu celulozy. Pozostałe wyniki zostały opisane w artykule [47].

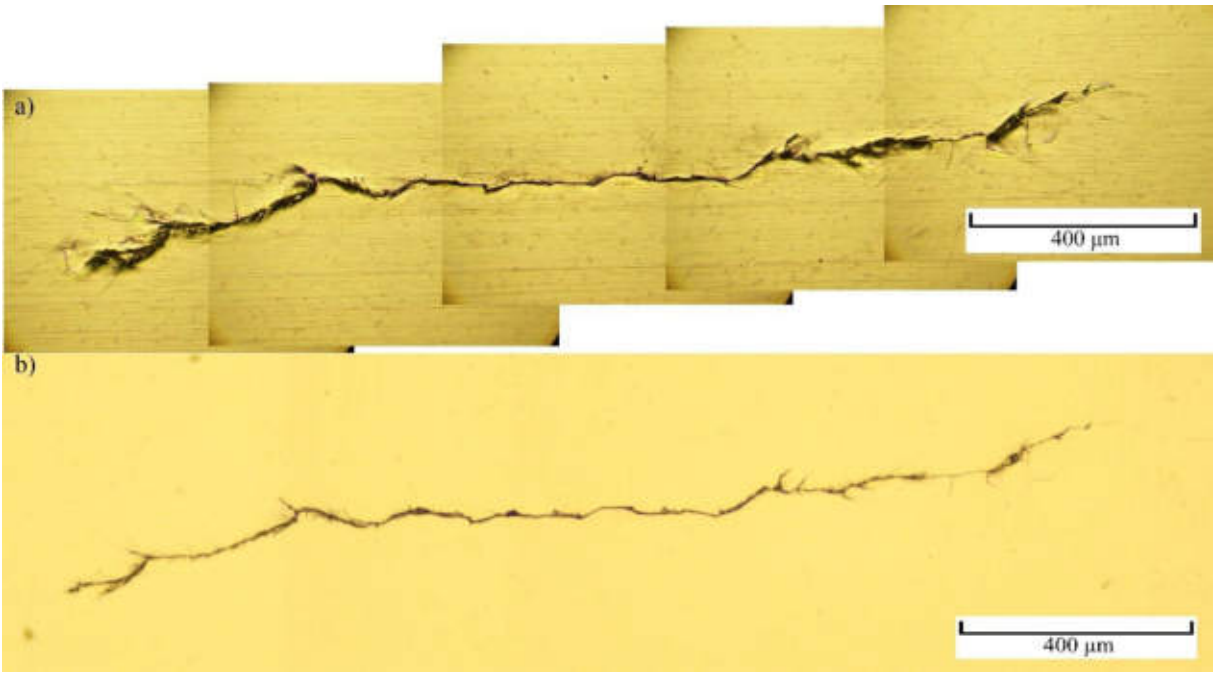

Rys. 5. Porównanie zdjęć pęknięcia zarejestrowanego: (a) bezpośrednio na powierzchni próbki oraz (b) na replice. [47]

W pracy [48] (artykuł 5 z cyklu publikacji) wykorzystano fraktografię SEM do zbadania mechanizmu uszkodzenia zmęczeniowego zachodzącego pod powierzchnią próbki. Obserwacje SEM przełomu połączono z wynikami badań rozwoju pęknięć wykonanymi za pomocą replikacji. Zauważono liczne ogniska pęknięć zarówno na powierzchni zewnętrznej jak i na powierzchni wewnętrznej cienkościennej próbki. Na Rys. 6 przedstawiono przełom próbki obciążonej cyklicznym rozciąganiem-ściskaniem (a) oraz powiększony obszar przełomu, w którym widoczne jest pęknięcie, które połączyło się z głównym pęknięciem. Niebieska strzałka wskazuje miejsce, w którym (na podstawie replik) rozpoznano ognisko (najdłuższe połączone pęknięcia), żółte strzałki wskazują kierunek propagacji w skali makroskopowej. W powiększonym fragmencie widoczny jest kierunek propagacji pęknięć od powierzchni do środka przekroju próbki. Małe pęknięcia łączyły się w coraz większe pęknięcie, lecz kierunek propagacji pozostawał niezmienny. Fragment przełomu, który uformował się przed spełnieniem kryterium zniszczenia próbki zajął mniej niż 5% powierzchni przekroju poprzecznego. Pozostała część przełomu uformowała się po spełnieniu warunku końca trwałości, to znaczy po 5% spadku siły, co w tym przypadku wyniosło 40 cykli. Szczegółowe wyniki badań zostały przedstawione i omówione w publikacji [48].

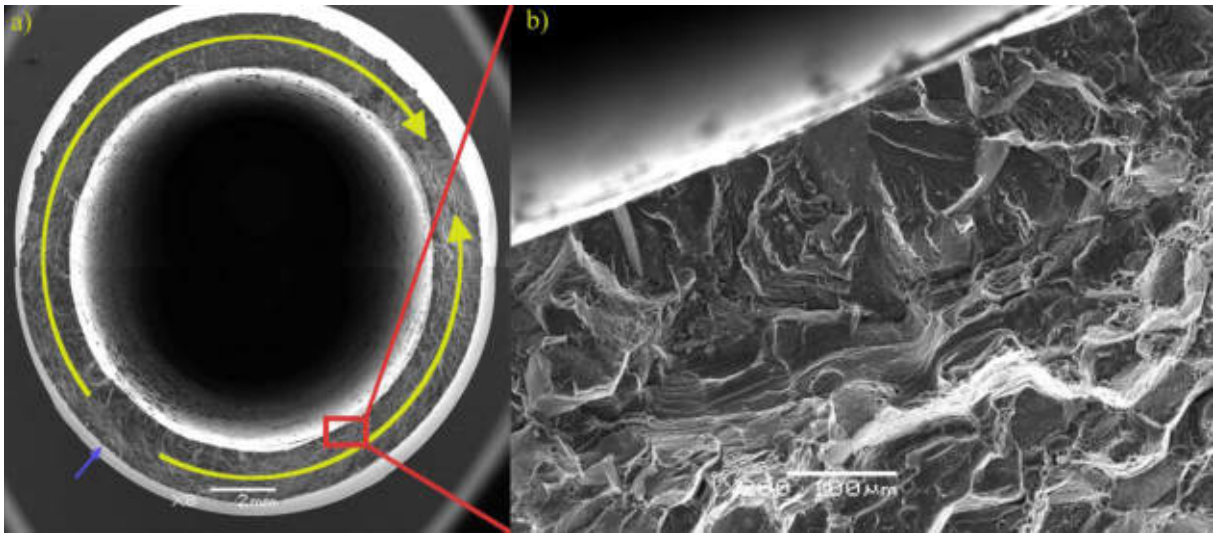

Rys. 6. Koalescencja małych pęknięć podczas rozwoju głównego pęknięcia. (a) schematyczna reprezentacja propagacji głównego pęknięcia podczas otartych 40 cyklach obciążenia, (b) koalescencja małych pęknięć, które dołączyły do głównego pęknięcia. [48]

Publikacja [49] (artykuł 6 z cyklu publikacji) przedstawia wyniki otrzymane z wykorzystaniem techniki replikacji oraz fraktografii SEM dla czterech przypadków obciążenia (TC, TOR, OP i ASN1) i trzech poziomów obciążenia. Próbki cienkościenne ze stopu aluminium PA38-T6 obciążono cyklicznie w zakresie odkształceń ekwiwalentnych od $\varepsilon_{eq} = 0{,}002$ do $\varepsilon_{eq} = 0{,}008$. Zostały zarejestrowane chwile pojawienia się pierwszych pęknięć, kierunki pęknięć, długości najdłuższych pęknięć, przebieg koalescencji, cechy fraktograficzne ognisk, cechy etapów propagacji (zarodkowanie i propagacja małych pęknięć, stabilna propagacja oraz niestabilna propagacja) oraz unikatowe cechy mechanizmu uszkodzenia zmęczeniowego występujące przy zbadanym obciążeniu asynchronicznym (ASN1). Na Rys. 7 przedstawiono ujęcia replik czterech przypadków obciążenia na trzech poziomach obciążenia, wytworzone pod koniec trwałości zmęczeniowej próbek. W górnej części każdego zdjęcia został wskazany przypadek obciążenia, poziom obciążenia, procent liczby cykli w stosunku do N_f oraz wartość bezwzględna liczby cykli w chwili wytworzenia repliki. W niektórych ujęciach widoczne są pęcherzyki powietrza, które nie są częścią topografii próbek, lecz niedoskonałością repliki. Można zauważyć jak wraz ze wzrostem poziomu obciążenia wzrasta gęstość pęknięć, niezależnie od przypadku obciążenia. Bez względu na poziom obciążenia pęknięcia tworzą się i propagują w charakterystyczny sposób dla danego przypadku obciążenia.

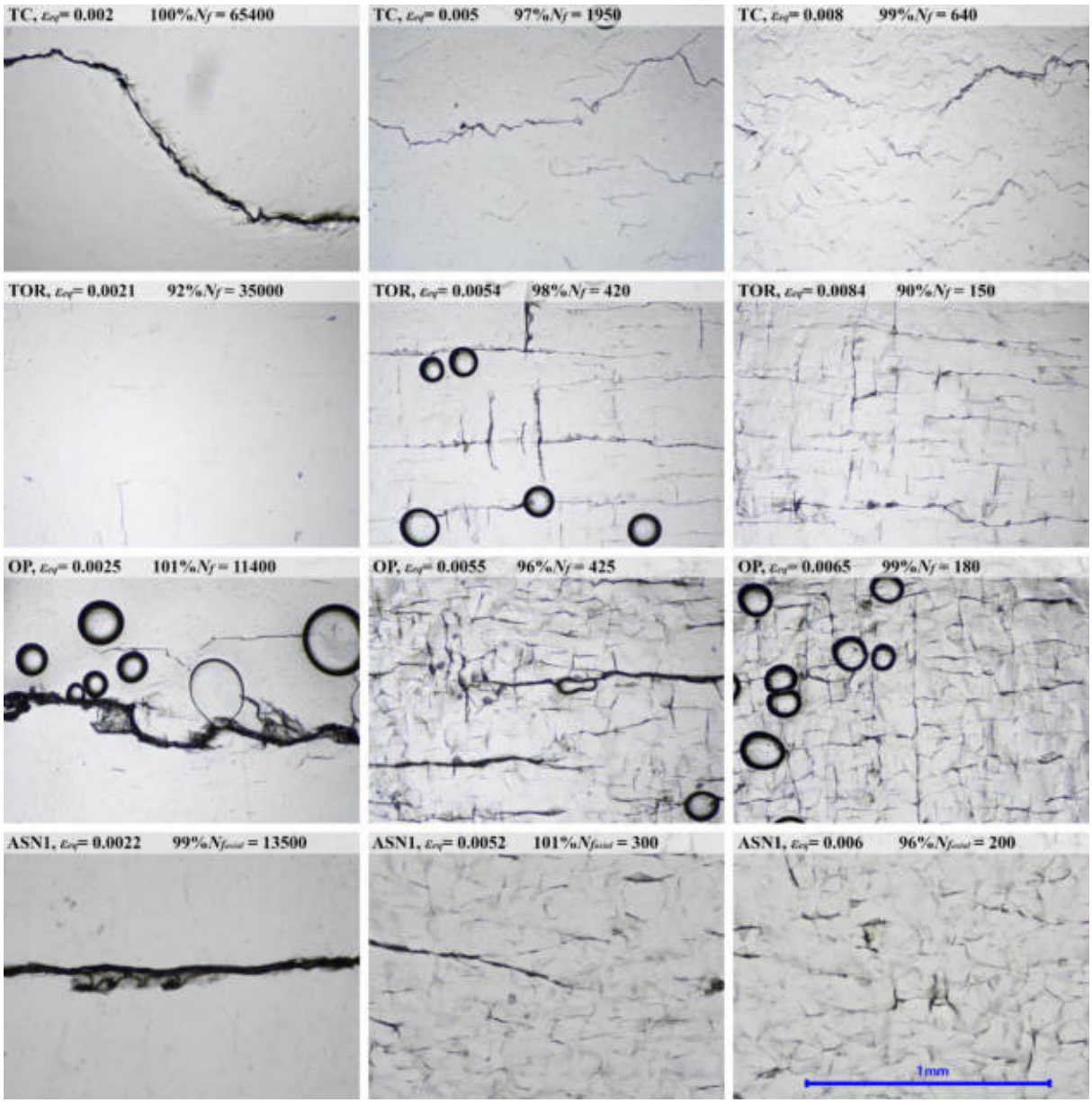

Rys. 7. Topografia powierzchni próbek pod koniec ich trwałości dla trzech poziomów obciążenia i czterech przypadków obciążenia. Dla każdego obrazu podano przypadek obciążenia, poziom obciążenia, procent liczby cykli w stosunku do N_f oraz wartość bezwzględną liczby cykli. [49]

Wśród innych obserwacji, szczegółowo opisanych w publikacji [49] (artykuł 6 z cyklu publikacji), została wyznaczona chwila zarejestrowania pierwszych pęknięć na replikach (N_i). Na Rys. 8 przedstawiono zależność pomiędzy chwilą zarejestrowania pierwszych pęknięć a trwałością zmęczeniową N_f (Rys. 8 (a)) oraz zależność pomiędzy N_i, a stosunkiem N_i/N_f (Rys. 8 (a)). Linią przerywaną wykreślono krzywą potęgową aproksymującą wyniki. Znakiem „X" zaznaczono wyniki, dla których chwila pojawienia się pierwszych pęknięć zaszła znacznie wcześniej od pierwszej wykonanej repliki. Zostało to określone na podstawie gęstości zarejestrowanych pęknięć na replikach. Można zaobserwować jak, niezależnie od przypadku

obciążenia, wszystkie wyniki tworzą jeden trend. Pozostałe wyniki badań przedstawiono i opisano w publikacji [49].

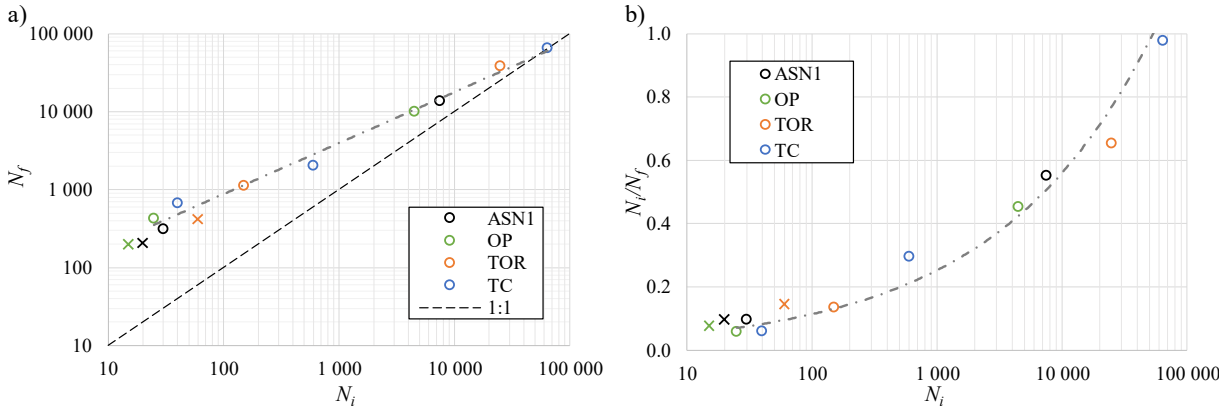

Rys. 8. Porównanie momentu rejestracji pierwszego pęknięcia na powierzchni N_i (a) z całkowitą trwałością zmęczeniową N_f oraz (b) ze stosunkiem N_i/N_f i krzywą potęgową aproksymującą wyniki. [49]

Do cyklu publikacji dodano również artykuł [50] (artykuł 7 z cyklu publikacji), prezentujący wyniki badań monotonicznego rozciągania i jednoosiowego zmęczenia spieku czystego renu, oraz analizujący wpływ odziaływania mechanicznego na mikrostrukturę spieku oraz kształtowanie się przełomów. Została wykreślona pierwsza dostępna w literaturze krzywa zmęczeniowa tego rzadkiego materiału oraz opisano mechanizm uszkodzenia pod wpływem obciążenia monotonicznego oraz cyklicznego. Na Rys. 9 przedstawiono wyniki trwałościowe prób jednoosiowego zmęczenia wraz z krzywą Basquina oraz krzywe zmęczeniowe oszacowane dwoma uproszczonymi metodami na podstawie wyników badań monotonicznego rozciągania.

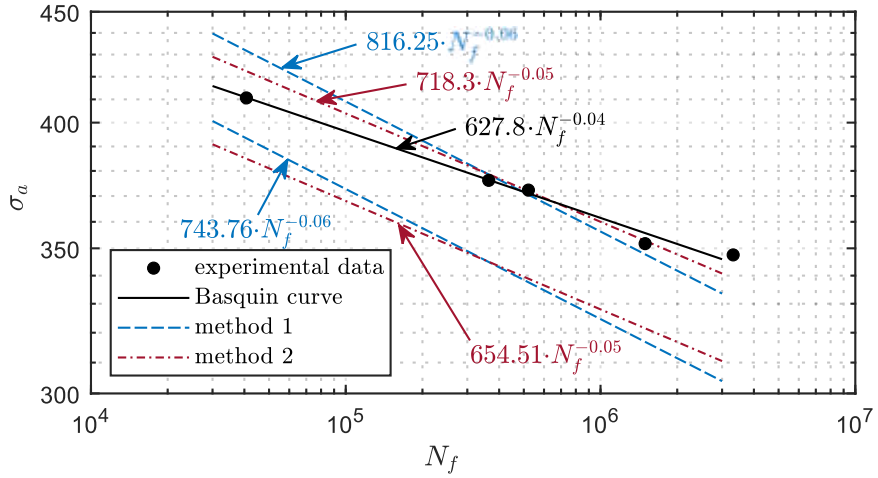

Rys. 9. Krzywa S-N wyznaczona eksperymentalnie: czarna linia – krzywa Basquina; niebieskie i czerwone przerywane linie – krzywe S-N oszacowane przy użyciu dwóch uproszczonych metod na podstawie danych z monotonicznego rozciągania [50].

Badania fraktograficzne wykazały, że w początkowej fazie pęknięcia zainicjowały się i propagowały transkrystalicznie w płaszczyznach łupliwości, przez nie więcej niż trzy ziarna, po czym propagowały międzykrystalicznie. Rys. 10 przedstawia wybrane fragmenty pęknięcia łupliwego. Widoczne są na nim pory, będące efektem ubocznym procesu spiekania renu, które podczas wyżarzania ukształtowały się w „negatyw" kryształu. Na podstawie orientacji ścianek pęcherzyków powietrza rozpoznano kierunki krystalograficznych płaszczyzn przełomu. Na zdjęciach pęknięcia łupliwego można znaleźć następujące kierunki łupliwości: płaszczyzna podstawowa {0001} i płaszczyzna piramidalna {1011} oraz płaszczyzna pryzmatyczna {1120}. Najczęściej pojawiającymi się płaszczyznami łupliwości były płaszczyzny podstawowe {0001} i pryzmatyczne {1120}. Powierzchnie pęknięć płaszczyzn podstawowych były gładkie (Rys. 10(d), niebieska strzałka). Są to płaszczyzny o największej podatności na rozszczepianie (łupliwość). Szczegółowe wyniki badań zostały przedstawione i opisane w artykule [50].

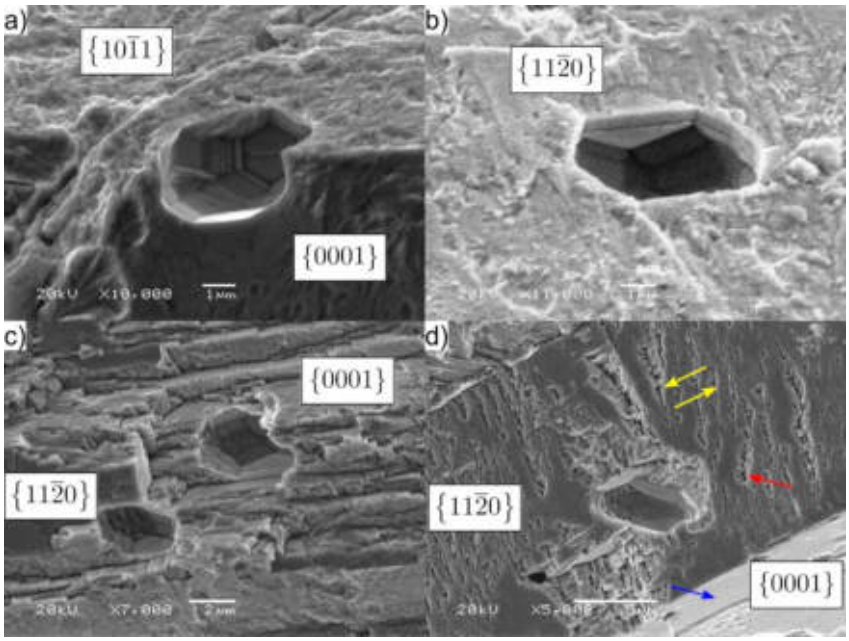

Rys. 10. Zdjęcia SEM fragmentów przełomu łupliwego z widocznymi porami, wskazujące kierunek krystalograficzny, na podstawie których wyznaczono płaszczyzny pęknięcia. [50]

3.3 Dyskusja

W przedstawionym cyklu publikacji główny nacisk położono na badanie zjawisk występujących w cienkościennych próbkach ze stopu aluminium PA38-T6 pod wpływem złożonych obciążeń cyklicznych, zarówno proporcjonalnych, jak i nieproporcjonalnych, uwzględniając także obciążenia asynchroniczne. Na Rys. 11 przedstawiono rozkłady kątowe maksymalnych odkształceń normalnych $\varepsilon(\varphi)$ i postaciowych $\gamma(\varphi)$ w zależności od położenia płaszczyzny przekroju względem osi próbki, dla czterech wybranych przypadków obciążenia.

Linią przerywaną zaznaczono płaszczyzny γ_{max} oraz ε_{max}, gdzie osiągane były maksymalne wartości odkształceń postaciowych i normalnych. Rozpoznane kierunki małych pęknięć wykazały korelację z płaszczyznami γ_{max}. Większość trwałości zmęczeniowej zajmował etap I (*stage I*) procesu uszkodzenia zmęczeniowego, obejmującego zarodkowanie mikropęknięć i propagację małych pęknięć. Stwierdzono to porównując długości pęknięć na replikach powierzchni próbek ze strukturą przełomów zniszczonych próbek.

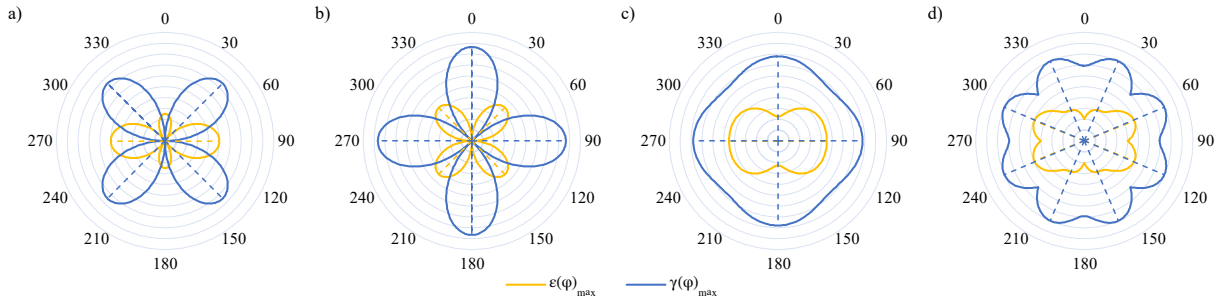

Rys. 11. Rozkład maksymalnych odkształceń normalnych $\varepsilon(\varphi)$ i odkształceń postaciowych $\gamma(\varphi)$ w zależności od położenia płaszczyzny przekroju względem osi próbki dla: (a) TC, (b) TOR, (c) OP i (d) ASN1 [49].

Analiza przebiegów odkształceń normalnych i postaciowych na płaszczyznach, gdzie częściej inicjowały się pęknięcia, rzuciła nowe światło na powiązania pomiędzy stanem odkształcenia a rozwojem pęknięć. Na Rys. 12 przedstawiono przebiegi odkształceń na płaszczyźnie γ_{max} dla zbadanych przypadków obciążenia przy jednakowym poziomie odkształcenia ekwiwalentnego sygnałów sterujących ($\varepsilon_{eq} = 0{,}005$). Z takiej perspektywy porównanie przypadków obciążenia umożliwiło wyjaśnienie, dlaczego, pomimo umownie tego samego poziomu obciążenia, pęknięcia inicjowały się i propagowały z różną intensywnością w zależności od przebiegu odkształceń postaciowych i normalnych na tej płaszczyźnie. Amplituda odkształceń postaciowych odpowiadała za zarodkowanie małych pęknięć, natomiast propagacja pęknięć przebiegała szybciej przy większej amplitudzie odkształceń normalnych na płaszczyźnie małych pęknięć.

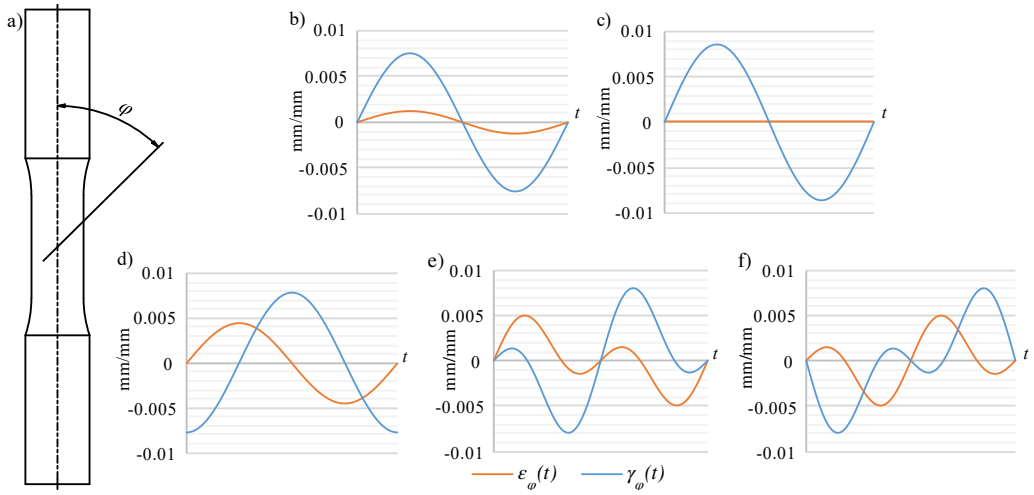

Rys. 12. Przebieg odkształceń postaciowych i normalnych na płaszczyźnie maksymalnego odkształcenia postaciowego przy poziomie obciążenia $\varepsilon_{eq} = 0{,}005$: a) definicja kąta φ, b) TC dla $\varphi = 45°$, c) TOR dla $\varphi = 0°$, d) OP dla $\varphi = 90°$, e) ASN1 dla $\varphi = 68°$, f) ASN1 dla $\varphi = 112°$ [49].

Opis rozpoznanego mechanizmu inicjacji i propagacji pęknięć zmęczeniowych w zbadanym stopie aluminium wykazuje silną korelację z założeniami i strukturą parametru uszkodzenia zmęczeniowego Fatemi-Socie [62]. Należałoby spodziewać się, że przy zastosowaniu tego parametru najdokładniej szacowana jest trwałość zmęczeniowa tego stopu. Jednak, jak wykazano w pracy [26], przy trwałościach mniejszych od ok. $N_{f,exp} < 10^3$ trwałość modelowana staje się przeszacowana. Na Rys. 13 przedstawiono porównanie eksperymentalnej trwałości zmęczeniowej i trwałości zmęczeniowej obliczonej przy użyciu parametru uszkodzenia Fatemi-Socie. Przedstawione zostały wyniki badań próbek pod wpływem obciążeń proporcjonalnych i nieproporcjonalnych, wliczając w to obciążenia asynchroniczne, w zakresie niskocyklowego zmęczenia. Szarym pasmem zostało symbolicznie zaznaczone odchylenie trendu wyników. Przeszacowanie trwałości zmęczeniowej wynika z faktu, że parametr Fatemi-Socie zakłada rozwój jednego pęknięcia, jednak, gdy ze względu na gęstość zainicjowanych pęknięć zaczynają się one łączyć ze sobą, rozwój uszkodzenia znacznie przyspiesza. Na Rys. 13 wskazano zakres trwałości, przy której zjawisko koalescencji pęknięć stało się główną przyczyną szybkiego zniszczenia próbek, gdzie obserwuje się również największe odchylenie wyników.

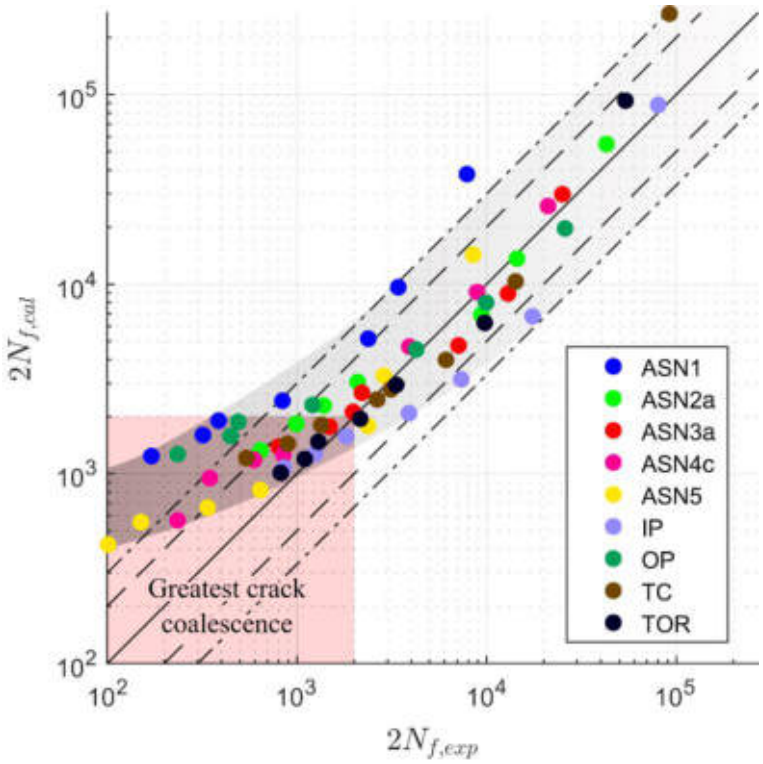

Rys. 13. Porównanie eksperymentalnej trwałości zmęczeniowej $2N_{f,exp}$ i obliczonej trwałości zmęczeniowej $2N_{f,cal}$ dla stopu aluminium PA38-T6, przy użyciu parametru uszkodzenia Fatemi-Socie. [26]

W artykule [49] przedstawiono podejście czysto fenomenologiczne do analizy trwałości zmęczeniowej różnych przypadków obciążenia. Analiza ta, oparta na obserwacji pojawiających się pęknięć na powierzchni próbek oraz końcowej trwałości zmęczeniowej, pozbawiona jest uwarunkowań wynikających ze wstępnych założeń, takich jak porównanie przypadków obciążenia ze względu na ich poziom odkształcenia lub naprężenia ekwiwalentnego. Analiza ta również pozwala unikać niedokładności związanej z wyznaczaniem naprężeń stycznych podczas skręcania w zakresie odkształceń sprężysto-plastycznych (Rys. 4) [46]. Po zestawieniu ze sobą chwil zarejestrowania pierwszych pęknięć na powierzchni próbek z trwałością zmęczeniową prób ujawnił się wspólny trend dla zbadanych przypadków obciążenia (Rys. 8). Widoczny jest wspólny mianownik dla wszystkich przypadków obciążenia, co wskazuje na to, że do lepszego zrozumienia różnic oraz części wspólnej badanych przypadków obciążenia należałoby porównać próby o podobnej trwałości. Wykres na Rys. 8(b) ilustruje potencjał predykcyjny analizy stanu powierzchni w zakresie obciążeń sprężysto-plastycznych, niezależnie od przypadku obciążenia. Monitorując stan powierzchni poprzez regularne pobieranie i analizowanie replik fragmentu powierzchni uprzednio wypolerowanej oraz liczbę cykli obciążenia, można oszacować końcową trwałość zmęczeniową. Idąc dalej, analizując ilościowo gęstość, długość i kierunek pęknięć

wychwyconych przez repliki, można podjąć próbę stworzenia miary skumulowanego uszkodzenia zmęczeniowego. Podobne podejście zostało przedstawione w pracach [63,64], w których analiza obrazów mikroskopowych powierzchni próbek została wykorzystana do stworzenia parametru uszkodzenia zmęczeniowego. Rozwój metody szacowania skumulowanych uszkodzeń zmęczeniowych w oparciu o analizę replik powierzchni próbek ma potencjał dla praktyki inżynierskiej w celu oceny rzeczywistych elementów maszyn bez konieczności przenoszenia struktur do laboratorium.

Wykonanie analiz mikroskopowych umożliwiło rozpoznanie i opisanie zjawiska niewykrywalnego na podstawie analizy sygnałów zarejestrowanych na maszynie wytrzymałościowej. W przypadku badań spieku czystego renu [50] pozwoliły one na scharakteryzowanie mechanizmu uszkodzenia pod wpływem obciążeń monotonicznych i jednoosiowego zmęczenia wraz z rozpoznaniem kierunków krystalograficznych płaszczyzn łupliwości.

3.4 Podsumowanie i wnioski

Celem naukowym rozprawy doktorskiej było pogłębienie zrozumienia fizycznych mechanizmów uszkodzenia materiałów pod wpływem działania obciążeń mechanicznych. Mechanizmy te zostały zbadane na próbkach poddawanych obciążeniom monotonicznym oraz, przede wszystkim, zmęczeniu wieloosiowemu. W tym celu przeprowadzono eksperymenty wytrzymałościowe w postaci: prób monotonicznego rozciągania, badania wysokocyklowego, jednoosiowego zmęczenia sterowanego siłą (naprężeniem), badania wieloosiowego zmęczenia niskocyklowego sterowane odkształceniem oraz przemieszczeniem. Sterowanie przemieszczeniem zastosowano aby umożliwić wytwarzanie replik powierzchni próbek w trakcje trwania prób zmęczeniowych. Do analizy mikroskopowej wykorzystane zostały technika replikacji powierzchni pomiarowej próbek, umożliwiająca śledzenie rozwoju pęknięć w trakcje trwania prób zmęczeniowych oraz analiza fraktograficzna SEM, pozwalająca na zbadanie z dużą rozdzielczością cech przełomów próbek na poszczególnych etapach rozwoju uszkodzenia. Dodatkowo zostały wykonane analizy zgładów metalograficznych i analizy rozkładu pierwiastkowego EDS, które dostarczyły informacji o mikrostrukturze zbadanych materiałów.

Wszystkie wyniki badań zostały opublikowane w przedstawionym i załączonym cyklu artykułów naukowych. Wśród najważniejszych osiągnięć naukowych można wyróżnić:

- analiza zakresu stosowalności różnych metod wyznaczania wartości naprężeń stycznych w kołowo-symetrycznych próbkach skręcanych,

- opisanie wpływu kombinacji składowych obciążenia cyklicznego na kierunek inicjacji i propagacji pęknięć dla różnych stopów metali,
- rozpoznanie związku pomiędzy cechami mechanizmu uszkodzenia różnych stopów metali, a dokładnością szacowania trwałości zmęczeniowej przy zastosowaniu najczęściej stosowanych parametrów uszkodzenia zmęczeniowego,
- określenie udziału czasowego poszczególnych etapów rozwoju uszkodzenia zmęczeniowego dla próbek cienkościennych ze stopu aluminium PA38-T6, w zależności od przypadku i poziomu obciążenia wieloosiowego,
- rozpoznanie znaczenia występowania zjawiska koalescencji pęknięć dla dokładności szacowanej trwałości zmęczeniowej przy stosowaniu modeli opartych na założeniu rozwoju pojedynczego pęknięcia zmęczeniowego,
- wyznaczenie pierwszej dostępnej w literaturze krzywej zmęczeniowej dla spieku czystego renu oraz opisanie cech mechanizmu uszkodzenia spieku poddawanego monotonicznemu rozciąganiu oraz jednoosiowemu zmęczeniu,

Przeprowadzone badania z wykorzystywaniem analiz mikroskopowych umożliwiły rozpoznanie i opisanie szeregu zjawisk zachodzących w materiałach pod wpływem obciążeń mechanicznych. Badania wniosły oryginalne wyniki rozszerzając stan wiedzy w dyscyplinie Inżynieria Mechaniczna, w dziedzinie Nauk Inżynieryjno-Technicznych. Analiza metod wyznaczania wartości naprężeń stycznych przy skręcaniu w zakresie odkształceń sprężysto-plastycznych umożliwiła opisanie zjawisk, które negatywnie wpływają na poprawność i dokładność wyznaczania odpowiedzi naprężeniowo-odkształceniowej materiałów. Z kolei różnice w wyznaczanych wartościach naprężeń tnących przekładają się bezpośrednio na wartość parametrów uszkodzenia zmęczeniowego (FDPs). Zastosowanie odpowiednej dla danego zakresu odkształceń metody wyznaczania naprężeń tnących w próbach zmęczeniowych skręcanych jest istotne dla jakości wykonanych analiz opartych o wyniki eksperymentalne. Kolejnym krokiem rozwojowym będzie opracowanie metody wyznaczania naprężeń tnących w próbkach skręcanych, w oparciu o przedstawione wyniki badań [46] oraz wcześniejszych prac [65–74], umożliwiającą dokładniejsze obliczenia zarówno dla zakresu odkształceń sprężystych jak i sprężysto-plastycznych. Metoda ta, aby znalazła zastosowanie w praktyce naukowej i inżynierskiej, powinna być opisana modelem matematycznym nie wymagającym tworzenia algorytmów iteracyjnych do znalezienia rozwiązania. Przyczyni się to do wzrostu jakości

wyników eksperymentalnych, co w konsekwencji do wzrostu jakości analiz wykonanych w poszukiwaniu rozwiązania problemu dokładnego szacowania trwałości zmęczeniowej.

Identyfikacja kierunku inicjacji i propagacji pęknięć, udziału czasowego etapów rozwoju procesu uszkodzenia zmęczeniowego oraz cech analizy zmiany gęstości i długości pęknięć, stanowią opis zjawisk fizycznych, które zachodzą w materiale poddanym obciążeniom cyklicznym. Opis procesu uszkodzenia zmęczeniowego w warunkach obciążeń wieloosiowych, w tym asynchronicznych, umożliwiło identyfikację fizycznych przyczyn niedokładności w wynikach zamodelowanej trwałości zmęczeniowej za pomocą popularnych FDPs względem wyników otrzymanych drogą eksperymentu. Koalescencja pęknięć jest konsekwencją dużej gęstości zainicjowanych małych pęknięć, która zależy od przypadku i poziomu obciążenia. Rozpoznanie znaczenia występowania tego zjawiska pozwoliło zrozumieć przyczyny, przez które, pomimo zbieżnego opisu mechanizmu uszkodzenia materiału z założeniami modelu matematycznego, parametr Fatemi-Socie skutkował znacznym przeszacowaniem trwałości zmęczeniowej w zakresie $N_f < 10^3$ dla stopu aluminium PA38-T6. Analizy wykonane w pracy dotyczą, w tym przypadku, jednego materiału, lecz zjawisko koalescencji pęknięć zostało zaobserwowany w wielu innych materiałach [75–83]. W przyszłych pracach należałoby analizować dokładniej warunki obciążenia wpływające na gęstość zainicjowania się pęknięć oraz rozwijać FDPs uwzględniających fakt, że przy większej gęstości małych pęknięć, katastrofalne uszkodzenie próbek lub elementów maszyn, następuje przy krótszej długości najdłuższego pęknięcia. Wyniki przeprowadzonych badań wytrzymałościowych i mikroskopowych spieku renu stanowią nie tylko opis nieznanych wcześniej właściwości tego materiału, lecz mogą być również wykorzystane w procesie projektowo-konstrukcyjnym elementów maszyn narażonych na cykliczne obciążenia mechaniczne. Otrzymane wyniki stanowią również podstawę do zaplanowania przyszłych badania poszerzających wiedzę na temat właściwości zmęczeniowych spieku renu w zakresie niskocyklowego zmęczenia czy zmęczenia wieloosiowego. Nowe wyniki badań umożliwiają zwiększenie zakresu zastosowania tego metalu zarówno w postaci czystej, kompozytowej oraz jako składnika stopów metali.

Bibliografia

[1] Milne I, Ritchie RO, Karihaloo B. Comprehensive Structural Integrity, Volumes 1-10. Elsevier 2003.

[2] Esslinger V, Kieselbach R, Koller R, Weisse B. The railway accident of Eschede - technical background. Eng Fail Anal 2004;11:515–35. https://doi.org/10.1016/j.engfailanal.2003.11.001.

[3] Frendo F. Analysis of the catastrophic failure of a dockside crane jib. Eng Fail Anal 2013;31:394–411. https://doi.org/10.1016/j.engfailanal.2013.02.026.

[4] Vargas JA, Wilches JE, Gómez HA, Pacheco JA, Hernandez RJ. Analysis of catastrophic failure of axial fan blades exposed to high relative humidity and saline environment. Eng Fail Anal 2015;54:74–89. https://doi.org/10.1016/J.ENGFAILANAL.2015.04.007.

[5] Nath Patel S, Kumar Singh D, Prasad Akula D, Adhikary M, Kumar A. Investigation of catastrophic failure of API grade pipes used for hydraulic oil in an integrated steel plant. Eng Fail Anal 2022;138:106336. https://doi.org/10.1016/J.ENGFAILANAL.2022.106336.

[6] Zhao X, Jin N, Liu X, Shi Z. Fatigue failure analysis of steel crane beams with variable-section supports. Eng Fail Anal 2022;136:106217. https://doi.org/10.1016/J.ENGFAILANAL.2022.106217.

[7] Godefroid LB, Faria GL, Cândido LC, Viana TG. Failure analysis of recurrent cases of fatigue fracture in flash butt welded rails. Eng Fail Anal 2015;58:407–16. https://doi.org/10.1016/J.ENGFAILANAL.2015.05.022.

[8] Hegde SR, Rakshan Kumar JK, Sondar P, Dsilva PC. Catastrophic failure of urea prill-tower fan. Eng Fail Anal 2021;121:105207. https://doi.org/10.1016/J.ENGFAILANAL.2020.105207.

[9] Iordachescu M, Valiente A, De Abreu M. Effect of environmentally assisted damage on fatigue resistance of tie-down cables after 30 years of service in a cable-stayed bridge. Eng Fail Anal 2021;126:105455. https://doi.org/10.1016/J.ENGFAILANAL.2021.105455.

[10] Milella PP. Fatigue and corrosion in metals. Milano: Springer Milan; 2013. https://doi.org/10.1007/978-88-470-2336-9.

[11] Bauschinger J. On the change of the position of the elastic limit of iron and steel under cyclic variations of stress. Mitt Mech-Tech Lab, Munich 1886;13.

[12] Ewing JA, Humfrey JCW. The Fracture of Metals under Repeated Alternations of Stress. Philos Trans R Soc London Ser A 1903;200:241–50.

[13] Basquin OH. The Exponential Law of Endurance Tests. Am Soc Test Mater Proc 1910;10:625–30.

[14] Massing G. Eigenspannungen and verfestigung Beim Messing. Proc Second Int Congr Appl Mech Zurich, Orell Fiissliverlag 1926:332–5.

[15] Miner MA. Cumulative Damage in Fatigue. J Appl Mech 1945;12:A159–64. https://doi.org/10.1115/1.4009458.

[16] Forsyth PJE. A Two Stage Process of Fatigue Crack Growth. Proceeding Crack Propag Symp 1961;1:76–94.

[17] Tavernelli JF, Coffin LF. Experimental support for generalized equation predicting low cycle fatigue. J Basic Eng 1962;84:533–7. https://doi.org/10.1115/1.3658701.

[18] ENDO T, MITSUNAGA K, NAKAGAWA H. Fatigue of metals subjected to varying stress-prediction of fatigue lives. Prelim Proc Chugoku-Shikoku Dist Meet 1967.

[19] NISHIHARA T, KAWAMOTO M. The Strength of Metals under Combined Alternating Bending and Torsion. Trans Japan Soc Mech Eng 1941;7:85–95. https://doi.org/10.1299/kikai1938.7.29-1_85.

[20] NISHIHARA T, KAWAMOTO M. The Strength of Metals under Combined Alternating Bending and Torsion with Phace Difference. Trans Japan Soc Mech Eng 1947;12:44–53. https://doi.org/10.1299/kikai1938.12.44.

[21] Stanfield G. Discusson on “The strength of metals under combined alternating stresses.” Proc Inst Mech Eng 131 1935;131:93.

[22] Karolczuk A, Macha E. A review of critical plane orientations in multiaxial fatigue failure criteria of metallic materials. Int J Fract 2005;134:267–304. https://doi.org/10.1007/s10704-005-1088-2.

[23] Karolczuk A, Liu Y, Kluger K, Derda S, Skibicki D, Pejkowski Ł. Physics-constrained Gaussian process for life prediction under in-phase multiaxial cyclic loading with superposed static components. Int J Fatigue 2023;175:107776. https://doi.org/10.1016/j.ijfatigue.2023.107776.

[24] Papuga J, Margetin M, Chmelko V. Various parameters of the multiaxial variable amplitude loading and their effect on fatigue life and fatigue life computation. Fatigue Fract Eng Mater Struct 2021;44:2890–912. https://doi.org/10.1111/ffe.13560.

[25] Wei Z, Dong P, Mei J, Pei X, Ravi SK. A moment of load path-based parameter for modeling multiaxial fatigue damage of welded structures. Int J Fatigue 2023;171:107575. https://doi.org/10.1016/J.IJFATIGUE.2023.107575.

[26] Pejkowski Ł, Seyda J. Fatigue of four metallic materials under asynchronous loadings: Small cracks observation and fatigue life prediction. Int J Fatigue 2021;142:105904. https://doi.org/10.1016/j.ijfatigue.2020.105904.

[27] Miner MA. Cumulative Damage in Fatigue. J Appl Mech 1945;12:A159–64. https://doi.org/10.1115/1.4009458.

[28] Fatemi A, Yang L. Cumulative fatigue damage and life prediction theories: a survey of the state of the art for homogeneous materials. Int J Fatigue 1998;20:9–34. https://doi.org/10.1016/S0142-1123(97)00081-9.

[29] Kocańda S, Szala J. Podstawy obliczeń zmęczeniowych. 3rd ed. Warszawa: Wydawnictwo Naukowe PWN; 1997.

[30] ASTM. E1049-85: Standard Practices for Cycle Counting in Fatigue Analysis. E1049 - 85 2011;85:1–10. https://doi.org/10.1520/E1049-85R11E01.2.

[31] Endo T, Masanori M, Koichi M, Kakuichi K, Kiyohumi T. Rain flow method, the proposal and the applications. Kyushu Inst Technol Acad Repos 1974;28:33–62.

[32] Wang Y, Susmel L. The Modified Manson-Coffin Curve Method to estimate fatigue lifetime under complex constant and variable amplitude multiaxial fatigue loading. Int J Fatigue 2016;83:135–49. https://doi.org/10.1016/j.ijfatigue.2015.10.005.

[33] Strzelecki P. Accuracy of determined S-N curve by selected models. J Theor Appl Mech 2019;57:859–68. https://doi.org/10.15632/jtam-pl/112065.

[34] Morrow J. Cyclic Plastic Strain Energy and Fatigue of Metals. Intern Frict Damping, Cycl Plast 2009:45-45–43. https://doi.org/10.1520/stp43764s.

[35] Castillo E, Fernández-Canteli A. A unified statistical methodology for modeling fatigue damage. A Unified Stat Methodol Model Fatigue Damage 2009:1–232. https://doi.org/10.1007/978-1-4020-9182-7.

[36] Pascual FG, Meeker WQ. Estimating Fatigue Curves with the Random Fatigue-Limit Model. Technometrics 1999;41:277. https://doi.org/10.2307/1271342.

[37] Zheng Z, Zhan M, Fu MW. Microstructural and geometrical size effects on the fatigue of metallic materials. Int J Mech Sci 2022;218. https://doi.org/10.1016/j.ijmecsci.2021.107058.

[38] Lu D, Lin B, Liu T, Deng S, Guo Y, Li J, et al. Effect of grain structure on fatigue crack propagation behavior of Al-Cu-Li alloys. J Mater Sci Technol 2023. https://doi.org/10.1016/J.JMST.2022.10.085.

[39] Tang K, Chen K, Ferro P, Berto F. Quantifying lamellar microstructural effect on the

fatigue performance of bimodal Ti-6Al-4V with microdefect. Int J Fatigue 2022;163. https://doi.org/10.1016/J.IJFATIGUE.2022.107045.

[40] Kurath P, Socie DF. The Relationship Between Observed Fatigue Damage and Life Estimation Models. vol. 182191. 1988.

[41] Tu S-T, Zhang X-C. Fatigue Crack Initiation Mechanisms. Ref Modul Mater Sci Mater Eng 2016. https://doi.org/10.1016/B978-0-12-803581-8.02852-6.

[42] Shamsaei N, Fatemi A. Small fatigue crack growth under multiaxial stresses. Int J Fatigue 2014;58:126–35. https://doi.org/10.1016/J.IJFATIGUE.2013.02.002.

[43] Gates N, Fatemi A. Notched fatigue behavior and stress analysis under multiaxial states of stress. Int J Fatigue 2014;67:2–14. https://doi.org/10.1016/j.ijfatigue.2014.01.014.

[44] Fatemi A, Gates N, Socie DF, Phan N. Fatigue crack growth behaviour of tubular aluminium specimens with a circular hole under axial and torsion loadings. Eng Fract Mech 2014;123:137–47. https://doi.org/10.1016/j.engfracmech.2014.04.010.

[45] Pejkowski Ł, Seyda J, Skibicki D. Short cracks observations on surfaces of specimens made of three materials, subjected to synchronous and asynchronous multiaxial loadings. MATEC Web Conf 2019;300:15002. https://doi.org/10.1051/matecconf/201930015002.

[46] Seyda J, Pejkowski Ł, Skibicki D. The shear stress determination in tubular specimens under torsion in the elastic–plastic strain range from the perspective of fatigue analysis. Materials (Basel) 2020;13:1–16. https://doi.org/10.3390/ma13235583.

[47] Seyda J, Pejkowski Ł, Skibicki D. Identification of fatigue damage mechanism in PA38-T6 aluminum alloy under multiaxial loadings - Initial research. Procedia Struct Integr 2020;28:1458–66. https://doi.org/10.1016/j.prostr.2020.10.119.

[48] Seyda J, Pejkowski Ł. SEM analysis of PA38-T6 aluminum alloy thin-walled tubular specimen fatigue fracture, and comparison to surface replication results. MATEC Web Conf 2021;338:01023. https://doi.org/10.1051/matecconf/202133801023.

[49] Seyda J, Pejkowski Ł, Mateusz C. Study on the behavior of small cracks in PA38-T6 (6060-T6) aluminum alloy under multiaxial fatigue loadings. Int J Fatigue 2024;184. https://doi.org/https://doi.org/10.1016/j.ijfatigue.2024.108282.

[50] Seyda J, Skibicki D, Pejkowski Ł, Skibicki A, Domanowski P, Maćkowiak P. Mechanical properties and microscopic analysis of sintered rhenium subjected to monotonic tension and uniaxial fatigue. Mater Sci Eng A 2021;817. https://doi.org/10.1016/j.msea.2021.141343.

[51] Pejkowski Ł, Skibicki D, Seyda J. Stress-strain response and fatigue life of a material

subjected to asynchronous loadings. AIP Conf Proc 2018;2028. https://doi.org/10.1063/1.5066406.

[52] Pejkowski Ł, Skibicki D, Seyda J. Fatigue behaviour of selected materials under multiaxial asynchronous loadings. MATEC Web Conf 2019;300:15006. https://doi.org/10.1051/matecconf/201930015006.

[53] Skibicki D, Pejkowski Ł, Karolczuk A, Seyda J. Verification of the Tanaka non-proportional isotropic cyclic hardening model under asynchronous loading. Int J Solids Struct 2022;254–255. https://doi.org/10.1016/j.ijsolstr.2022.111896.

[54] Trepczyńska-Łent M, Seyda J. Characteristics of Ledeburite in EDS Analyses of Directionally Solidified Eutectic White Cast Iron. Arch Foundry Eng 2022;22:65–71. https://doi.org/10.24425/afe.2022.143951.

[55] Karuskevicha M, Maslaka T, Gavrylova I, Pejkowski Ł, Seyda J. Structural health monitoring for light aircraft. Procedia Struct Integr 2022;36:92–9. https://doi.org/10.1016/j.prostr.2022.01.008.

[56] Pejkowski Ł, Seyda J, Nowicki K, Mrozik D. Mechanical performance of non-reinforced, carbon fiber reinforced and glass bubbles reinforced 3D printed PA12 polyamide. Polym Test 2023;118:1–11. https://doi.org/10.1016/j.polymertesting.2022.107891.

[57] Tomaszewski T, Stopel M, Skibicki A, Seyda J, Piątkowski T. Effect of plastic strain under roller bending on fatigue properties of extruded 6063 T66 aluminium alloy profile. Trans Nonferrous Met Soc China 2023;33. https://doi.org/10.1016/S1003-6326(23)66333-2.

[58] Karolczuk A, Kurek A, Böhm M, Derda S, Prężmowwski M, Kluger K, et al. Heterogeneous effect of aging temperature on the fatigue life of additively manufactured thin-walled 18Ni300 maraging steel tubular specimen. Mater Des 2024;237. https://doi.org/10.1016/j.matdes.2023.112561.

[59] Pejkowski Ł, Skibicki D. Stress-strain response and fatigue life of four metallic materials under asynchronous loadings : Experimental observations. Int J Fatigue 2019;128. https://doi.org/10.1016/j.ijfatigue.2019.105202.

[60] CombineZP designed to process Stacks of digital images n.d. https://combinezp.software.informer.com/ (accessed March 17, 2024).

[61] E2207-02 (ASTM International). Standard Practice for Strain-Controlled Axial-Torsional Fatigue Testing with Thin-Walled Tubular Specimens n.d.;03.

[62] Fatemi A, Socie DF. a Critical Plane Approach To Multiaxial Fatigue Damage Including

Out-of-Phase Loading. Fatigue Fract Eng Mater Struct 1988;11:149–65. https://doi.org/10.1111/j.1460-2695.1988.tb01169.x.

[63] Karuskevich M, Karuskevich O, Maslak T, Schepak S. Extrusion/intrusion structures as quantitative indicators of accumulated fatigue damage. Int J Fatigue 2012;39:116–21. https://doi.org/10.1016/j.ijfatigue.2011.02.007.

[64] Pejkowski Ł, Karuskevich M, Maslak T. Extrusion/intrusion structure as a fatigue indicator for uniaxial and multiaxial loading. Fatigue Fract Eng Mater Struct 2019;42:2315–24. https://doi.org/10.1111/ffe.13066.

[65] Shamsaei N, Fatemi A. Effect of hardness on multiaxial fatigue behaviour and some simple approximations for steels. Fatigue Fract Eng Mater Struct 2009;32:631–46. https://doi.org/10.1111/J.1460-2695.2009.01369.X.

[66] Brown MW. Torsional stresses in tubular specimens. Http://DxDoiOrg/101243/03093247V131023 1978;13:23–8. https://doi.org/10.1243/03093247V131023.

[67] MILLER KJ, CHANDLER DC. High Strain Torsion Fatigue of Solid and Tubular Specimens. Http://DxDoiOrg/101243/PIME_PROC_1969_184_035_02 1969:433–48. https://doi.org/10.1243/PIME_PROC_1969_184_035_02.

[68] Shoemaker EM. Second order effects in the elastic-plastic torsion problem. Meccanica 1973;8:125–8. https://doi.org/10.1007/BF02155854/METRICS.

[69] Wu PD, Van der Giessen E. Analysis of elastic-plastic torsion of circular bars at large strains. Arch Appl Mech 1991;61:89–103. https://doi.org/10.1007/BF00787401/METRICS.

[70] Rubinstein R. On the elastic-plastic torsion problem. J Eng Math 1977;11:319–23. https://doi.org/10.1007/BF01537091/METRICS.

[71] Caffarelli LA, Friedman A. Unloading in the elastic-plastic torsion problem. J Differ Equ 1981;41:186–217. https://doi.org/10.1016/0022-0396(81)90057-7.

[72] Annin BD. Existence and uniqueness of the solution of the elastic-plastic torsion problem for a cylindrical bar of oval cross-section. J Appl Math Mech 1965;29:1038–47. https://doi.org/10.1016/0021-8928(65)90124-3.

[73] Idone G, Maugeri A, Vitanza C. Variational inequalities and the elastic-plastic torsion problem. J Optim Theory Appl 2003;117:489–501. https://doi.org/10.1023/A:1023941520452/METRICS.

[74] Bildhauer M, Fuchs M, Repin S. The Elastic–Plastic Torsion Problem: A Posteriori Error

Estimates for Approximate Solutions. Numer Funct Anal Optim 2009;30:653–64. https://doi.org/10.1080/01630560903123452.

[75] Ogawa F, Itoh T, Yamamoto T. Evaluation of multiaxial low cycle fatigue cracks in Sn-8Zn-3Bi solder under non-proportional loading. Int J Fatigue 2018;110:215–24. https://doi.org/10.1016/J.IJFATIGUE.2018.01.021.

[76] Gao N, Brown MW, Miller KJ, Reed PAS. An effective method to investigate short crack growth behaviour by reverse bending testing. Int J Fatigue 2007;29:565–74. https://doi.org/10.1016/j.ijfatigue.2006.04.005.

[77] Makabe C, Socie DF, Sueyoshi T. Shear mode fatigue crack growth in 1050 aluminium. Fatigue Fract Eng Mater Struct 2004;27:669–78. https://doi.org/10.1111/j.1460-2695.2004.00788.x.

[78] Mazánová V, Polák J. Initiation and growth of short fatigue cracks in austenitic Sanicro 25 steel. Fatigue Fract Eng Mater Struct 2018;41:1529–45. https://doi.org/10.1111/ffe.12794.

[79] Ochi Y, Ishii A, Sasaki SK. An Experimental and Statistical Investigation of Surface Fatigue Crack Initiation and Growth. Fatigue Fract Eng Mater Struct 1985;8:327–39. https://doi.org/10.1111/j.1460-2695.1985.tb00431.x.

[80] Turnbull A, De Los Rios ER. the Effect of Grain Size on the Fatigue of Commercially Pure Aluminium. Fatigue Fract Eng Mater Struct 1995;18:1455–67. https://doi.org/10.1111/j.1460-2695.1995.tb00868.x.

[81] Suzuki K, Koyama M, Hamada S, Tsuzaki K, Noguchi H. Planar slip-driven fatigue crack initiation and propagation in an equiatomic CrMnFeCoNi high-entropy alloy. Int J Fatigue 2020;133:105418. https://doi.org/10.1016/j.ijfatigue.2019.105418.

[82] Wang YZ, Atkinson JD, Akid R, Parkins RN. Crack interaction, coalescence and mixed mode fracture mechanics. Fatigue Fract Eng Mater Struct 1996;19:51–63. https://doi.org/10.1111/j.1460-2695.1996.tb00931.x.

[83] Dudrova E, Kabátova M. A review of failure of sintered steels: fractography of static and dynamic crack nucleation, coalescence, growth and propagation. Powder Metall 2016;59:148–67. https://doi.org/10.1080/00325899.2016.1145786.

4 Streszczenie

Obserwacja mechanizmu inicjacji, propagacji i kumulacji uszkodzeń oraz prognozowanie trwałości zmęczeniowej w zakresie cyklicznych obciążeń wieloosiowych

mgr inż. Jan Seyda

Słowa kluczowe: wieloosiowe zmęczenie materiału; rozwój pęknięć zmęczeniowych; mechanizm uszkodzenia; charakterystyka naprężeniowo-odkształceniowa; analiza mikroskopowa**.**

W ciągu ostatniego stulecia prowadzone są coraz bardziej zaawansowane badania w celu rozwinięcia modeli przewidywania trwałości materiałów podczas procesu zmęczenia. Pomimo znaczących postępów, wiele problemów nadal pozostaje nierozwiązanych. Kluczową cechą pożądaną w tych modelach jest ich uniwersalność, pozwalająca na oszacowanie trwałości zmęczeniowej dla różnych materiałów i przypadków obciążenia. W niniejszej pracy doktorskiej skupiono się na obserwacji mechanizmów inicjacji, propagacji i kumulacji uszkodzeń w materiałach poddawanych obciążeniom mechanicznym, szczególnie wieloosiowym obciążeniom zmęczeniowym, oraz na zrozumieniu wpływu tych zjawisk na dokładność modeli przewidywania trwałości zmęczeniowej.

Głównym celem badań przedstawionych w cyklu publikacji zawartych w rozprawie doktorskiej było lepsze zrozumienie fizycznych mechanizmów uszkodzenia materiałów pod wpływem obciążeń mechanicznych. Ich lepsze poznanie ma prowadzić do doskonalenia lub rozwoju nowych narzędzi i metod analizy, które umożliwią dokładniejsze przewidywanie wytrzymałości doraźnej, a przede wszystkim wytrzymałości i trwałości zmęczeniowej. W tym celu przeprowadzono eksperymenty wytrzymałościowe, w tym próby monotonicznego rozciągania, badania wysokocyklowego jednoosiowego zmęczenia sterowanego siłą, badania wieloosiowego zmęczenia niskocyklowego sterowanego odkształceniem oraz przemieszczeniem. Sterowanie przemieszczeniem zastosowano w celu wytwarzania replik powierzchni próbek w trakcie trwania prób zmęczeniowych. Do analizy mikroskopowej wykorzystano technikę replikacji powierzchni pomiarowej próbek, umożliwiającą śledzenie rozwoju pęknięć w trakcie trwania prób zmęczeniowych oraz analizę fraktograficzną SEM. Te eksperymenty pozwoliły na bardziej szczegółowe zrozumienie procesów zachodzących podczas zmęczenia materiałów i analizę mikrostruktury próbek poddanych obciążeniom mechanicznym.

Badania opisane w rozprawie doktorskiej skoncentrowały się na identyfikacji i zrozumieniu zjawisk zachodzących w materiałach poddanych obciążeniom cyklicznym. Przeprowadzone analizy mikroskopowe przyniosły oryginalne wnioski, rozszerzając wiedzę w dziedzinie Inżynierii Mechanicznej. Analizie poddano metodologię wyznaczania naprężeń tnących od skręcania, co pozwoliło lepiej zrozumieć procesy uszkodzeń materiałów poddanych obciążeniom. Rozwój nowych metod analizy naprężeń tnących jest istotny dla jakości analiz opartych na danych eksperymentalnych. Badania dotyczyły również identyfikacji inicjacji i propagacji pęknięć zmęczeniowych w warunkach obciążeń wieloosiowych, w tym asynchronicznych. Zjawisko koalescencji pęknięć okazało się istotne dla zrozumienia trwałości zmęczeniowej. Pomijanie tego zjawiska może skutkować przeszacowaniem trwałości przez niektóre popularne modele zmęczeniowe. Wyniki badań wytrzymałościowych i mikroskopowych spieku renu poszerzyły wiedzę na temat jego właściwości zmęczeniowych i stanowią podstawę dla projektowania elementów maszyn poddawanych cyklicznym obciążeniom. Nowe odkrycia umożliwiają zwiększenie zakresu zastosowania spieku renu w różnych formach, zarówno w postaci czystej, kompozytowej, jak i jako składnika stopu metali.

5 Abstract

Observation of the mechanisms of initiation, propagation and accumulation of fatigue damage and prediction of fatigue life in the range of cyclic multiaxial loadings

mgr inż. Jan Seyda

Key words: multiaxial fatigue; fatigue crack growth; damage mechanism; stress-strain response; microscopic analysis.

Over the past century, increasingly sophisticated research has been conducted to develop models for predicting the fatigue life of materials. Despite significant progress, many problems still remain unsolved. A key feature desired in these models is their versatility, allowing fatigue life to be estimated for different materials and loading cases. This dissertation focuses on observing the mechanisms of damage initiation, propagation and cumulation of damage in materials subjected to mechanical loading, especially multiaxial fatigue loading, and on understanding the impact of these phenomena on the accuracy of fatigue life prediction models.

The main objective of the research presented in the series of publications included in the dissertation was to better understand the physical mechanisms of damage to materials under mechanical loads. A better understanding of these is expected to lead to the improvement or development of new tools and methods of analysis that will enable more accurate prediction of adhesion strength and, most importantly, strength and fatigue life. For this goal, strength tests, including monotonic tensile tests, high-cycle uniaxial force-controlled fatigue tests, strain-controlled low-cycle multiaxial fatigue tests, and displacement-controlled fatigue tests were conducted. Displacement control was used to produce replicas of specimen surfaces during fatigue tests. For microscopic analysis, the technique of replicating the gauge surface of the specimens was used to track the development of cracks throughout the fatigue tests, as well as SEM fractographic analysis. These experiments allowed a more detailed understanding of the processes occurring during fatigue and analysis of the microstructure of specimens subjected to mechanical loading.

The research described in the dissertation focused on identifying and understanding the phenomena occurring in materials subjected to cyclic loading. The microscopic analyses conducted yielded original conclusions, expanding knowledge in the area of Mechanical Engineering. Methodologies for the determination of shear stresses were investigated, providing

a better understanding of the damage processes of materials subjected to loading. The development of new methods for shear stress analysis is important for the quality of analyses based on experimental data. The research also concerned the identification of fatigue crack initiation and propagation under multiaxial and asynchronous loading conditions. The phenomenon of crack coalescence turned out to be important for understanding fatigue life; ignoring this phenomenon can result in an overestimation of life by some popular fatigue models. The results of strength and microscopic studies of rhenium sinter have expanded the knowledge of its fatigue properties and provide a basis for the design of machine components subjected to cyclic loading. The new findings make it possible to increase the range of applications of rhenium sinter in various forms, whether in pure form, composite form or as a component of a metal alloy.

6 Załączniki

6.1 Kopie artykułów naukowych stanowiących cykl publikacji rozprawy doktorskiej

International Journal of Fatigue 142 (2021) 105904

Contents lists available at ScienceDirect

International Journal of Fatigue

journal homepage: www.elsevier.com/locate/ijfatigue

Fatigue of four metallic materials under asynchronous loadings: Small cracks observation and fatigue life prediction

Łukasz Pejkowski*, Jan Seyda

UTP University of Science and Technology in Bydgoszcz, Poland

ARTICLE INFO

Keywords:
Multiaxial fatigue
Non-proportional loading
Asynchronous loading
Fatigue life prediction
Small cracks

ABSTRACT

This paper is a continuation of previously published work. It presents the results of small cracks observation on the surfaces of fatigued specimens subjected to multiaxial loadings. Specimens were manufactured from four materials: PA38-T6 aluminum alloy, E235 and E355 non-alloy steels, and X5CrNi18-10 austenitic steel. Based on the cracking analysis, it was found that the aluminum alloy and low-alloy steels exhibited shear damage mechanism, while the austenitic steel showed the tensile damage mechanism. Fatigue life prediction was performed based on six popular damage parameters. A correlation between the observed damage mechanism and the fatigue life prediction quality was noted.

1. Introduction

There are many multiaxial fatigue damage parameters and life prediction approaches in the literature. Some of them are dedicated to including selected features of loading or material behavior [1,2], while others are of a more general-purpose [3,4]. There are published papers that evaluate the new or classical multiaxial fatigue life prediction models and draw conclusions without correlating the results with the cracking behavior of the material [5,6]. Other authors compare the quality of fatigue life prediction using different models with the material damage mechanism [7–9]. It is also worth noting, that despite the significant progress in the understanding of multiaxial fatigue as well as in materials and components behavior modeling, researchers still work on the development of multiaxial fatigue models [10–12]. New proposals are focused for example on improvement in taking into account material parameters [13] or not considering them at all [14]. Many of the new models tend to be more universal [15,16]. An interesting trend showing that the new proposals are often based on the energy parameters can be observed [17–20]. Though there are several new models, researchers still use classic damage parameters for fatigue life prediction or to compare with the performance of new methods [21–24].

In the previous paper [25], research was conducted using multiaxial loadings, including asynchronous cases. Fatigue tests were performed on tubular specimens loaded by tension–torsion, with strain control in the elastic–plastic strain range. Specimens were manufactured from four materials: PA38-T6 (AW 6060-T6) aluminum alloy, E235 (1.0308) and E355 (1.0580) non-alloy steels, and X5CrNi18-10 (1.4301, 304/304L) austenitic stainless steel. The details are given in the previous paper [25]. The focus of that work was on experimental observations regarding the fatigue life and cyclic stress–strain response. Phenomena like non-proportional, loading-related life shortening, additional hardening, equivalent stress histories, and features of strain hysteresis loops were studied. It was shown that both fatigue life and stress–strain response are material- and path-dependent. In one of the conclusions, it was stated that due to complexity and non-proportionality, the asynchronous loadings are interesting and challenging for the fatigue damage and life prediction models.

Based on that observation, six popular multiaxial fatigue damage parameters were employed for fatigue life prediction in the present work. Fatigue life calculations were preceded by the observation and analysis of the small cracks visible on the specimens' surfaces. Small cracks observation reported in the literature is usually conducted using mirror-polished specimens [26,27]. Sometimes, the details of preparation of specimens used for multiaxial testing are not mentioned [8,28]. In present research, the specimens were left in the CNC machining condition, with visible machining marks. Such specimens preparation is closer to many of the real applications, where engineering components are not necessarily mirror-polished. Our investigation showed that in case of austenitic steel the machining marks had a significant influence on the cracking behavior under non-proportional loadings. Next, the features of cracks were used to determine the damage mechanism of the materials. The results of fatigue life prediction were then correlated with the cracks observation, a method which is not always practiced in the literature. It was shown that the quality of fatigue life prediction

* Corresponding author.
E-mail address: lukasz.pejkowski@utp.edu.pl (Ł. Pejkowski).

https://doi.org/10.1016/j.ijfatigue.2020.105904
Received 2 July 2020; Received in revised form 17 August 2020; Accepted 19 August 2020
Available online 26 August 2020
0142-1123/

Nomenclature

A	cross section's area
b	fatigue strength exponent
b_0	shear fatigue strength exponent
c	fatigue ductility exponent
c_0	shear fatigue ductility exponent
CCM	Cycle Counting Method
D	damage
DAH	Damage Accumulation Hypothesis
F	axial force
FDP	Fatigue Damage Parameter
f_c, f_γ	frequency of normal and shear strain, respectively
m	coefficient of the power fatigue life curve
n	exponent of the power fatigue life curve
$2N_{f,exp}$, $2N_{f,cal}$	experimental and calculated fatigue life, respectively
N_f, $2N_f$	cycles and reversals to failure
r_m	mean radius
subscripts: a, max, n	amplitude, maximum and normal component, respectively
superscripts: e, p	elastic and plastic component, respectively
t	time
T	torque
T_N	mean dispersion of fatigue life
T_{RMS}	fatigue life prediction mean-squared error
W	strain energy
γ'_f	shear fatigue ductility coefficient
Δ	range of a given quantity
ε'_f	fatigue ductility coefficient
ε_x, γ_{xy}	normal (axial) strain, shear strain
ε_y, ε_z	transverse strains
ε_{yz}, ε_{zy}	shear components of the strain tensor
λ	shear to normal strain ratio
ν, E, G	Poisson ratio, Young modulus, shear modulus
σ_1, ε_1	maximum principal stress and strain, respectively
σ_{eq}, ε_{eq}	Huber-Mises equivalent stress and strain, respectively
σ'_f	fatigue ductility coefficient
$\sigma_{i,j}$, $\varepsilon_{i,j}$	stress and strain tensor, respectively
σ_x, τ_{xy}	normal (axial) stress, shear stress
σ_y	yield stress
τ'_f	shear fatigue strength coefficient

does not only depend on the model itself. The best estimations were achieved by the models which reflect the observed damage mechanism. Although the present work is fundamental research mostly, the presented results may be useful for other researchers and engineers, when choosing the multiaxial fatigue life prediction method, for instance.

2. Experiment description

Axial-torsional, strain-controlled fatigue tests were conducted on tubular specimens manufactured from PA38-T6 (AW 6060-T6) aluminum alloy, E235 (1.0308) and E355 (1.0580) non-alloy steels, and X5CrNi18-10 (1.4301, 304/304L) austenitic stainless steel. The source material for specimens consisted of seamless, precise pipes. PA38-T6 aluminum alloy was delivered as solution heat-treated and artificially aged, E235 steel as soft annealed, E355 as cold drawn, and X5CrNi18-10 as soft annealed. E355 steel was annealed prior to testing. All specimens were machined o the CNC lathe. The materials selected for testing showed ductile behavior in the monotonic tension test [25].

Four basic synchronous loadings were applied first: tension–compression (TC), torsion (TOR), in-phase loading (IP), and 90° out-of-phase non-proportional loading (OP). IP and OP multiaxial tests were performed with the λ ratio equal to $\sqrt{3}$. Next, the fatigue tests using asynchronous loadings were carried out. The parameters of applied asynchronous loadings, i.e. λ and f_γ/f_ε, are given in Table 1. The scheme of applied loadings in the case of a particular material is presented in Table 2. For further details of the experiment, please refer to the previous paper [25]. It contains also the tabulated experimental data, like basic material parameters, fatigue life (given as the number of reversals to failure for both axial and torsional channel), applied amplitudes of normal and shear strain, resultant amplitudes of normal and shear stress, and numerous figures presenting that data.

3. Small cracks observation

The surfaces of fatigued specimens were investigated under an optical microscope equipped with a digital camera. The evolution of cracks was not followed during the tests, thus only the information on the location of cracks with respect to the specimens' axes was available. Usually, the observation was made at some distance from the macrocrack due to the strong deformation of the macrocrack's surroundings. Moreover, the formation of the macrocrack took a very small fraction of the specimens' fatigue life, typically only the last few cycles. Thus, the macrocrack's formation period and its orientation were considered irrelevant. Specimens' surfaces were in CNC-machined condition, hence machining marks are visible in the pictures.

Images of specimens' surfaces were taken for PA38-T6 aluminum alloy, E235 steel, and X5CrNi18-10 steel. E355 steel showed a very similar overall fatigue behavior to E235 steel, thus the surfaces of specimens were not investigated in the case of this material. Charts presenting the maximum normal and shear strain distributions in polar coordinates were imposed on images to ease the cracks' direction analysis. The direction of 0° is parallel to the specimens' axes.

3.1. PA38-T6 aluminum alloy

Typical images of the surfaces of PA38-T6 aluminum alloy specimens are presented in Fig. 1. The image taken for TC loading presents the tip of the macrocrack. The macrocrack is formed from the small cracks, oriented under the ± 45° angle to the specimen axis. For TOR loading, short cracks can be observed under the 0° and 90° angles. In the case of IP loading, two directions of small cracks are visible, 70° and 160°. The directions of the small cracks observed for the aforementioned loadings correlate with the locations of maximum shear strain planes, which are constant. In the case of OP loading, small cracks can be observed in many different directions. This is the result of the rotation of principal axes and planes of maximum shear strain.

Table 1
Parameters of asynchronous loadings.

loading	ASN1	ASN2a	ASN2b	ASN3a	ASN3b	ASN4a	ASN4b	ASN4c	ASN5
λ	$\sqrt{3}$	$\sqrt{3}/2$	$\sqrt{3}$	$2\sqrt{3}$	$2\sqrt{3}$	$\sqrt{3}/2$	$3\sqrt{3}/5$	$\sqrt{3}$	$\sqrt{3}$
f_γ/f_ε	0.5	4	4	0.2	0.25	2/3	6	8	0.7

Table 2
Asynchronous loadings applied for individual materials.

Material	Applied asynchronous loadings				
PA38	ASN1	ASN2a	ASN3a	ASN4c	ASN5
E235	ASN1	ASN2a	ASN3b	ASN4a	
E355	ASN1	ASN2b	ASN3b	ASN4b	ASN5
1.4301	ASN1	ASN2a	ASN3a	ASN4b	ASN5

Furthermore, the shear strain on different directions has a range close to the maximum range. However, the cracks located at 0° are more developed. This is due to the maximum shear strain range and the maximum normal strain acting in that direction, which reduces the friction between the crack surfaces.

In cases of synchronous loadings (TC, TOR, IP, OP), there are only two planes of maximum shear strain, while in cases of asynchronous loadings, the maximum shearing is experienced by four planes. Thus, it

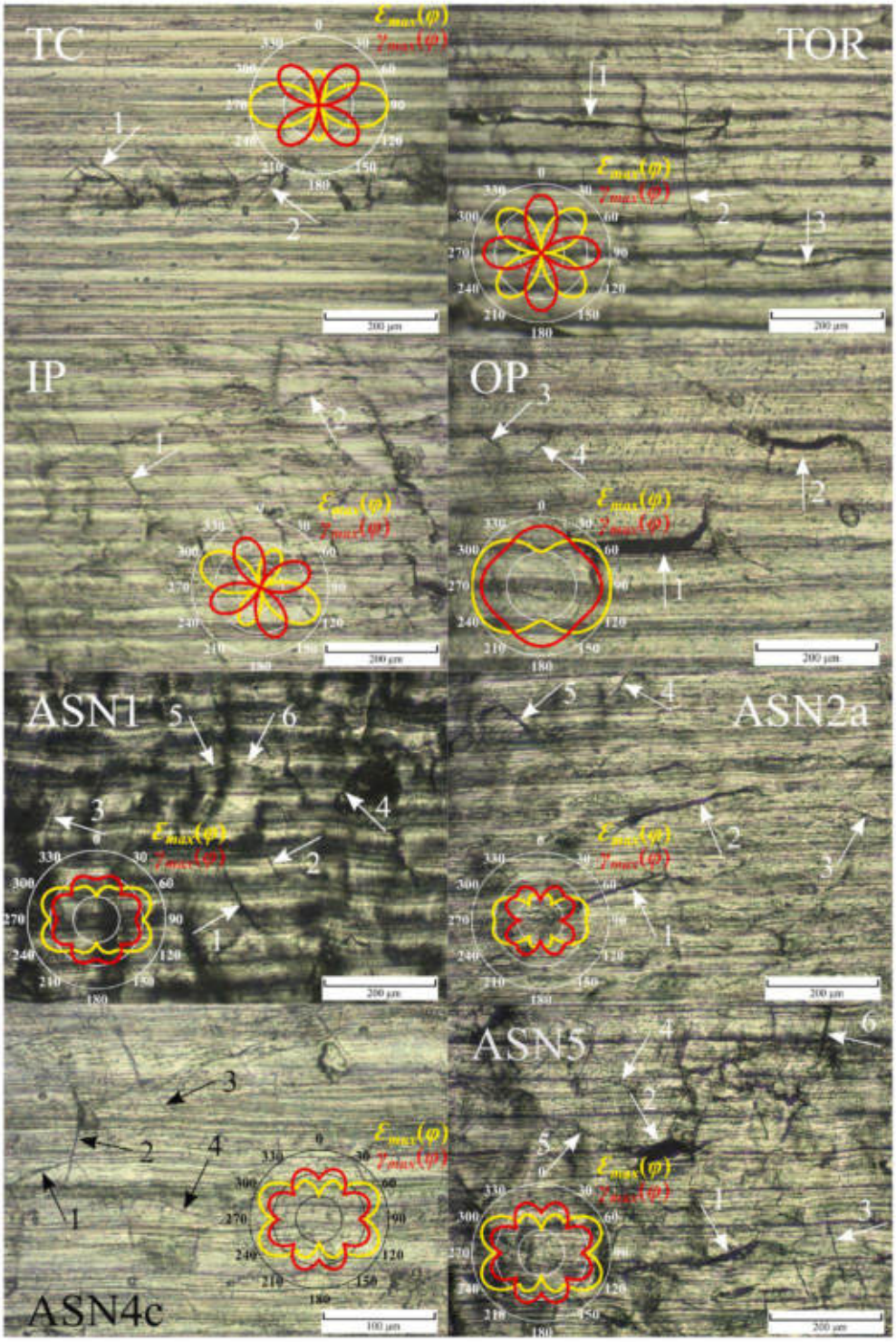

Fig. 1. Small cracks on the surfaces of PA38-T6 aluminum alloy specimens.

was interesting to investigate the effect of the increased number of maximum shear strain planes on cracking behavior.

The characteristic feature of the fatigued specimens subjected to ASN1 loading is a strong deformation of the surface. ASN1 loading resulted in images of worse quality than images of other loadings. However, the observation of small cracks was still possible. The maximum shear strain range occurs on planes located at 22°, 68°, 112°, and 158°. The observed cracks were approximately placed in all these directions. Cracks at 68° and 112° were often more developed, which can be explained by the maximum normal strain also occurring on these planes. For ASN2a loading, small cracks were also located on all the planes of maximum shear strain range, namely 30°, 60°, 120°, and 150°. Cracks in directions with higher normal strain (60° and 120°) were more developed. For ASN4c and ASN5 loadings, the maximum shear and normal strain loci are the same. Cracks were again present on all the maximum shear strain range planes (20°, 70°, 110°, and 160°), and those located on planes of maximum normal strain were more developed.

Considering the above observations, it was concluded that PA38-T6 aluminum alloy exhibits a shear damage mechanism for the applied

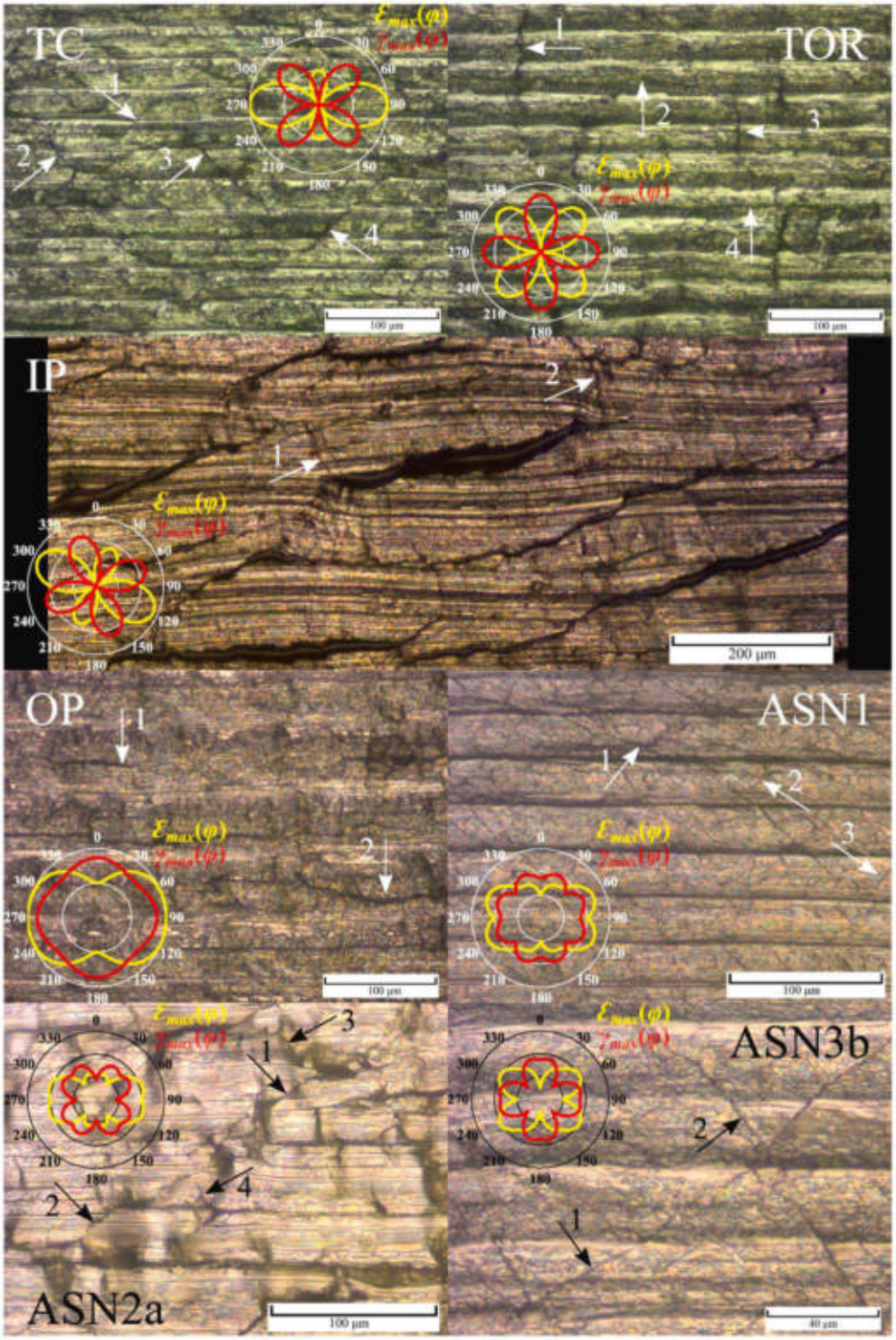

Fig. 2. Small cracks on the surfaces of E235 steel specimens.

loading cases and loading level ranges. Regardless of the loading case, small cracks were always observed in directions coinciding with the maximum shear strain planes. In cases of non-proportional loadings, namely OP and asynchronous loadings, small cracks formed in many directions. If one or two of the pairs of maximum shearing planes were also the planes of higher normal strain value, the cracks were more developed.

3.2. E235 steel

Fig. 2 presents the typical small cracks observed on the surfaces of the E235 steel specimens. For axial loading (TC), cracks formed at ± 45° angles. For TOR loading, cracks were observed both at 0° and 90°. In the case of IP loading, cracks were placed at 70° and 160° angles. Some of the cracks could also be noticed in the direction of machining marks. For OP loading, small cracks were usually observed solely on the plane perpendicular to the specimen axis (90°), even though near-maximum values of shear strain act in all directions. Yet, the 90°

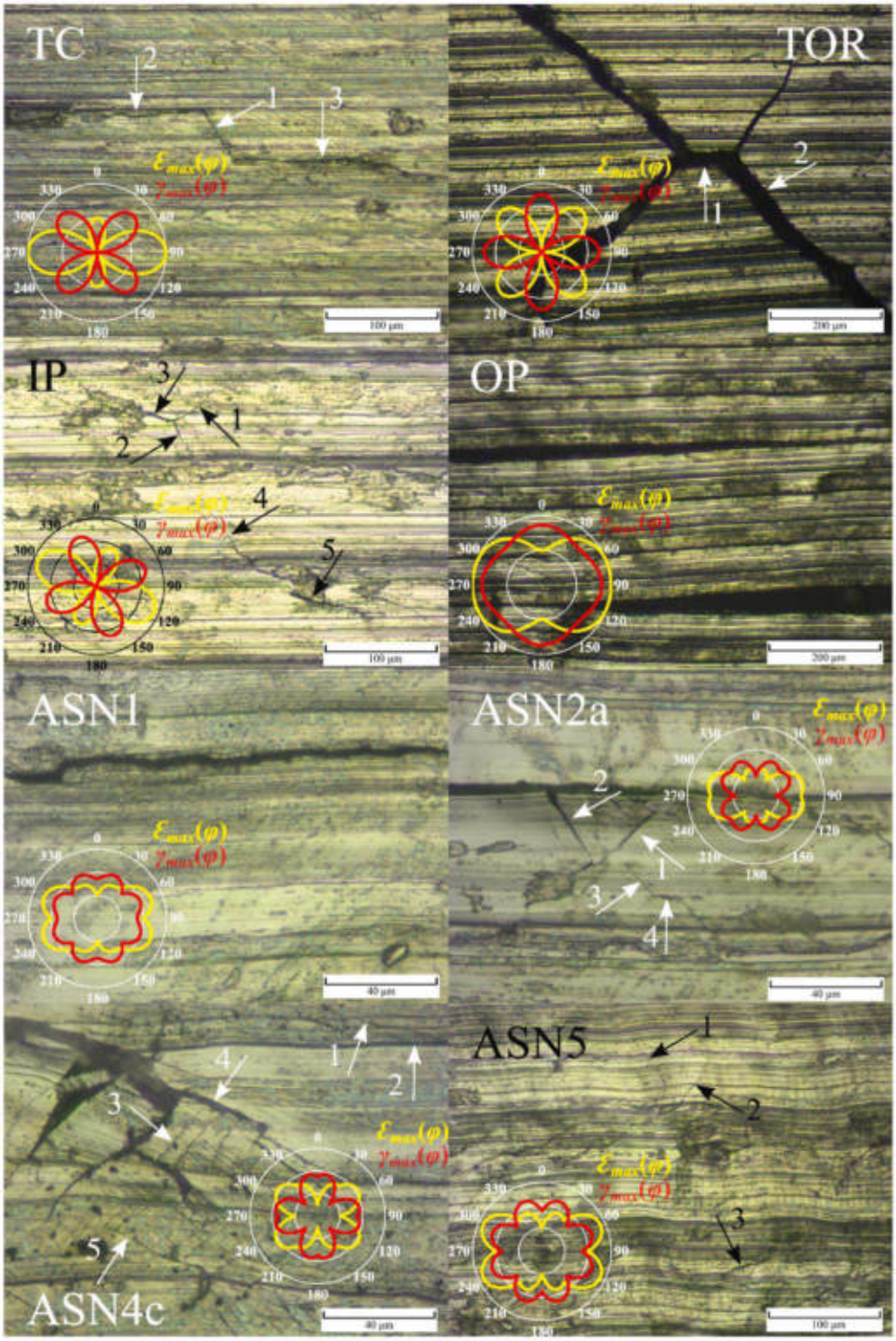

Fig. 3. Small cracks on the surfaces of X5CrNi18-10 steel specimens.

direction experiences the maximum normal strain. For ASN1 loading, small cracks were observed in all the maximum shear strain directions (22°, 68°, 112°, and 158°). In the case of ASN2a loading, the cracks were again present in the directions of maximum shear strain (30°, 60°, 120°, and 150°). Some of the cracks formed in the directions of the machining marks as well. Similarly, for ASN3b loading, cracks were visible in the directions of maximum shearing (11°, 79°, 110°, and 168°).

For all loading cases, some cracks corresponded to one pair of maximum shear strain directions centralized on certain areas of the specimens' surfaces, while in other areas the cracks corresponded to the other pair. Usually, the density of cracks was higher compared to PA38-T6 aluminum alloy.

3.3. X5CrNi18-10 steel

Selected images of small cracks on the surfaces of specimens manufactured from X5CrNi18-10 steel are presented in Fig. 3. For TC loading, the exemplary crack consists of three parts. The first part is located approximately at an angle of 135°, which is the direction of maximum shear strain. The two other parts are roughly perpendicular to the specimen's axis. This direction coincides with the plane of maximum normal strain. In the case of TOR loading, the direction of the first part of the crack agrees with the plane of maximum shear strain range. Then, the crack branches in four directions of maximum normal strain – 45°/225° and 135°/315°. For IP loading, there are cracks which are in the directions of both maximum shear and normal strain. In the case of OP loading, the plane at an angle of 90° is of maximum shear and normal strain. Moreover, it coincides with the direction of machining marks. Thus, this direction was the most preferable for the development of fatigue cracks. In the majority of cases, no cracks in other directions were observed for this type of loading.

For all studied cases of asynchronous loadings, it was found that cracks were most prone to develop in the directions of machining marks. The machining marks are local stress concentrators. In the case of austenitic steel, a martensitic transformation could also take place due to machining [29]. A martensite phase is a structural notch, which can also be the crack initiator. Nevertheless, it is known that fatigue cracks always initiate on the planes of maximum shear stress. Therefore, small cracks in the directions of maximum shearing were also found in cases of asynchronous loading. Their length was a few times shorter than the length of cracks observed in the direction of machining marks. Furthermore, for non-proportional loadings (OP and asynchronous), the cracks were quite often found to initiate from inclusions, which were potentially identified as built-up edge depositions on the machined surface [30,31].

3.4. Summary

Based on the observation of small cracks, it was concluded that PA38-T6 aluminum alloy exhibits the shear damage mechanism for all investigated loadings. Cracks were always found in the direction of the maximum shear strain range, no matter what the loadings' parameters were. If there were few planes of the same shear strain range, cracks were more developed, and these planes which experienced higher values of normal strain. The same mechanism was noticed for E235 steel. Without a quantitative evaluation, it was presumed that the density of small cracks on the surface was higher compared to PA38-T6 aluminum alloy. In the case of X5CrNi18-10 steel, short cracks fragments were observed in the direction of maximum shear strain, and longer fragments were present in the direction of maximum normal strain. The fragments of cracks that coincided with the direction of maximum shearing were ascribed to Stage I propagation, and those which coincided with the direction of maximum normal strain were ascribed to Stage II propagation [32,33]. However, only observing the surfaces of fatigued specimens does not explain what fractions of fatigue life were spent on Stage I and II propagation. A further, thorough examination by following the crack propagation history would be needed to fully explain the patterns of observed cracks. Notwithstanding, the tensile damage mechanism can be assumed for this steel, which may be surprising in case of a ductile material. The tensile damage mechanism for 304 stainless steel (equivalent to X5CrNi18-10) was also reported by Kurath and Socie [34]. Kalnaus and Jiang described both shear and tensile cracking in AL6XN stainless steel, depending on the loading type and level [35].

4. Selected fatigue life prediction models and methodology

First, it should be expounded what exactly is understood as a fatigue life prediction model in this work. A variety of nomenclature regarding this field can be found in the literature. Terms like "fatigue criterion" [8,10,15] "fatigue damage parameter", "fatigue parameter" [14,36,37], or "model" [38] are often used. Depending on the author, these quoted phrases can either be used as synonyms or have slightly different meanings, so it can be difficult to understand what is meant when the phrases are used.

According to the terminology adopted in the present work, a fatigue prediction model for a constant amplitude loading can be expressed by the following relationship:

$$FDP(\sigma_{ij}, \varepsilon_{ij}, t, k) = f(N_f) \tag{1}$$

where $f(N_f)$ is a function describing a reference fatigue life curve. *FDP* value depends on stress and strain tensors. These tensors describe the stress and strain states in a point of the material being analyzed, and their components' values vary in time due to cyclic loading. Material parameters are represented symbolically by variable k. This terminology has been recently used directly by Karolczuk et al. [13,39] and such an approach can be found in work by other authors [11,40]. The selected *FDPs* represent critical plane, energy and equivalent strain approach.

For random loadings, the mathematical form and physical basis of some *FDP's* require utilization of the cycle counting method (*CCM*) or the damage accumulation hypothesis (*DAH*) [41], often both. Failure is expected when the accumulated fatigue damage is greater than one, which may be expressed by the following inequality:

$$D(FDP, f, CCM, DAH) \leq 1 \tag{2}$$

The calculated damage value can also be used to predict the expected fatigue life given in the number of random loading block repetitions [42]. In the present work, the Palmgren-Miner linear damage accumulation rule [43,44] was used in all cases. According to this rule, the number of loading block repetitions N_B is given by:

$$N_B = \frac{1}{D} \tag{3}$$

In the case of selected *FDPs* that require cycle counting (i.e. Fatemi-Socie and Smith-Watson-Topper), for random loading cases, the rainflow cycle counting algorithm was used. For that purpose, a MATLAB rainflow function included in the Signal Processing Toolbox, compliant with the ASTM E1049 standard, was utilized. No cycle counting was performed in the case of other FDPs. The equivalent strain calculated from the strain ranges is the simplest and often used method. Wherefore, this generally accepted approach was followed. The Ince-Glinka and Ellyin-Gołoś damage parameters are energy-based quantities. The values of these parameters were calculated for the whole loading blocks since the energy is an additive quantity. In the case of the Itoh-Sakane damage parameter, the mathematical formulation is quite complicated and it is not clear how the loading cycles should be counted to correctly keep the sense of the non-proportionality factor.

Every time the term "fatigue prediction model" is referred to in this work, the framework expressed by Eqs. (1)–(3) is considered.

Various approaches to the determination of the stress and strain components are also present in the literature. In this study, all the

quantities used to calculate the *FDP*s and material parameters are based on the signals directly measured in the previous experiment [25]. Normal and shear strain were measured by the biaxial extensometer attached to the specimen. Normal stress was calculated based on the axial force and the cross-section area:

$$\sigma_x = F/A \tag{4}$$

In the case of the elastic–plastic deformation regime, the shear stress is not distributed uniformly through the thickness of the specimen's wall. The midsection value (acting at the mean diameter) was used as a representative quantity, according to the recommendations of the ASTM E2207 standard:

$$\tau_{xy} = \frac{T}{A \cdot r_m} \tag{5}$$

F and T were measured by the testing system's loading cell. For axial–torsional loading, stress and strain tensors are given by:

$$\sigma_{ij} = \begin{bmatrix} \sigma_x & \tau_{xy} & 0 \\ \tau_{yx} & 0 & 0 \\ 0 & 0 & 0 \end{bmatrix}, \quad \varepsilon_{ij} = \begin{bmatrix} \varepsilon_x & \varepsilon_{xy} & 0 \\ \varepsilon_{yx} & \varepsilon_y & 0 \\ 0 & 0 & \varepsilon_z \end{bmatrix} \tag{6}$$

Note that ε_{xy} component equals half of the shear strain, $\varepsilon_{xy} = \gamma_{xy}/2$. Transverse components were calculated as:

$$\varepsilon_y = \varepsilon_z = -(\nu^e \varepsilon_x^e + \nu^p \varepsilon_x^p) \tag{7}$$

Plastic Poisson's ratio equal to 0.5 was assumed since in the elastic–plastic strain regime, the distortional deformation of the material is usually observed with no change in volume. The values of elastic Poisson's ratio are given in Table 2 of [25]. The elastic and plastic part of the axial strain and were calculated using equations:

$$\varepsilon_x^e = \frac{\sigma_x}{E}, \quad \varepsilon_x^p = \varepsilon_x - \varepsilon_x^e \tag{8}$$

4.1. Huber-Mises equivalent strain (HM)

The Huber-Mises equivalent stress and strain, based on the yield hypothesis [45,46], are some of the most popular and basic damage parameters. For the analyzed axial–torsional loading, the equivalent stress amplitude was calculated as half of the range:

$$\sigma_{eq,a} = \frac{\Delta\sigma_{eq}}{2} = \sqrt{\left(\frac{\Delta\sigma_x}{2}\right)^2 + 3\left(\frac{\Delta\tau_{xy}}{2}\right)^2} \tag{9}$$

In turn, the equivalent strain amplitude was calculated using the following set of equations:

$$\varepsilon_{eq,a} = \frac{\Delta\varepsilon_{eq}^e}{2} + \frac{\Delta\varepsilon_{eq}^p}{2}$$
$$\Delta\varepsilon_{eq}^e = \frac{\Delta\sigma_{eq}}{E}, \quad \Delta\varepsilon_{eq}^p = \sqrt{(\Delta\varepsilon_x^p)^2 + \frac{1}{3}(\Delta\gamma_{xy}^p)^2}, \quad \Delta\gamma_{xy}^e = \frac{\Delta\tau_{xy}}{G},$$
$$\Delta\gamma_{xy}^p = \Delta\gamma_{xy} - \Delta\gamma_{xy}^e, \tag{10}$$

In the case of the Huber-Mises equivalent strain, no cycle counting or damage accumulation were performed, a method which is often practiced as the simplest approach [47,48]. The ranges of stresses and strains were determined for one loading block, recorded at midlife. This means that the number of components' cycles in asynchronous loading blocks was neglected, and the whole loading block was considered as one cycle. Based on the equivalent strain amplitude, fatigue life was estimated by the transformation of Eq. (1). For this damage parameter, the reference fatigue life curve was described by the Basquin-Manson-Coffin (BMC) equation [49–51] in notation proposed by Morrow [52] (after [53]):

$$\varepsilon_{eq,a} = \frac{\sigma_f'}{E}(2N_f)^b + \varepsilon_f'(2N_f)^c \tag{11}$$

4.2. Parameters of the above equation were obtained by fitting the curve to the experimental data for uniaxial tension–compression.

4.2.1. Fatemi-Socie parameter (FS)

The Fatemi-Socie (FS) multiaxial damage parameter was first proposed in [54]. It represents the critical plane approach and is given by:

$$FS = \frac{\Delta\gamma_{max}}{2}\left(1 + k\frac{\sigma_{n,max}}{\sigma_y}\right) \tag{12}$$

where $\Delta\gamma_{max}$ is the maximum shear strain range, $\sigma_{n,max}$ is the maximum normal stress acting on the maximum shear strain range plane, and k is a constant material parameter. This damage parameter reflects the experimental observation that crack nucleation and small crack growth are driven by shear strain, and positive normal stress causes crack opening and reduction of friction between crack surfaces.

Over the years, the Fatemi-Socie parameter became one of the most discussed and used multiaxial fatigue damage parameters. Many modifications have been proposed by various authors. Two such modifications were considered in this work. The first regards the variation of k depending on the fatigue life [39,55]. The second modification was proposed by Gates and Fatemi [55]. This modification consists of replacing σ_y with $G\Delta\gamma$:

$$FS_m = \frac{\Delta\gamma_{max}}{2}\left(1 + k\frac{\sigma_{n,max}}{G\Delta\gamma}\right) \tag{13}$$

It was found in this study that the modified parameter gave better results than the original, and the constant value of k was sufficient for the applied loading levels. Thus, only these results are presented. The shear version of the BMC equation was used for the referential fatigue curve:

$$\gamma_a = \frac{\Delta\gamma}{2} = \frac{\tau_f'}{G}(2N_f)^{b_0} + \gamma_f'(2N_f)^{c_0} \tag{14}$$

Parameters of the above equation were determined based on the experimental data for fully reversed torsion.

For all applied loadings, the Bannantine-Socie (BS) cycle counting method was utilized [56]. Shear strain and normal stress histories were projected on different planes with a one-degree step. Then, rainflow cycle counting was performed on the shear strain, which is the primary channel in the case of the Fatemi-Socie parameter. For the time intervals corresponding to counted cycles and reversal, the maximum normal stress was determined. In the next step, the values of the Fatemi-Socie parameter were calculated for every cycle on each plane, and subsequent linear damage accumulation was performed. The plane with the maximum accumulated damage was considered as the critical plane. A more detailed description of this procedure can be found in [57]. Cycles that resulted in a predicted fatigue life longer than $5{\cdot}10^8$ reversal were considered as non-damaging [58].

4.2.2. Smith-Watson-Topper parameter (SWT)

The Smith-Watson-Topper damage parameter was another considered quantity. In its original form, it was dedicated to axial loading cases [59]. Socie proposed a critical-plane based, generalized form of the SWT parameter [60]:

$$SWT = \sigma_{1,max}\frac{\Delta\varepsilon_1}{2} \tag{15}$$

where $\sigma_{1,max}$ is the maximum normal stress on the maximum principal strain plane.

Either a simple power function (Eq. (16)) or a BMC equation-based function (Eq. (17)) were used to describe the referential fatigue curve, whichever gave better results (compare Eq. (11)):

$$SWT = m(2N_f)^n \tag{16}$$

$$SWT = \sigma_f'\varepsilon_f'(2N_f)^{b+c} + \frac{\sigma_f'^2}{2}(2N_f)^{2b} \tag{17}$$

where coefficient m and exponent n were determined using experimental data for fully reversed axial loading by the least-squares fitting. Rainflow cycle counting of normal strain was performed successively on different planes with a one-degree step. For counted cycles and reversals, corresponding maximum normal stress values were determined and SWT parameter values were calculated. The plane that experienced the maximum damage was selected as the critical plane.

4.2.3. Ince-Glinka parameter (IG)

The Ince-Glinka (IG) multiaxial fatigue damage parameter is an energy-based, critical plane parameter, called "a generalized strain energy parameter" by the authors [61]. In their early work, Glinka and co-authors noticed that some of the damage parameters are confusing from the continuum mechanics point of view [62]. This is due to their mathematical form, where the parameter value is an algebraic sum of normal and shear stress and strain components. This observation was one of the basics for the formulation of a new parameter. The IG parameter is interesting and unique because it does not require any material-related parameters. It is given by:

$$IG = \left(\tau_{max}\frac{\Delta\gamma^e}{2} + \frac{\Delta\tau}{2}\frac{\Delta\gamma^p}{2} + \sigma_{n,max}\frac{\Delta\varepsilon_n^e}{2} + \frac{\Delta\sigma_n}{2}\frac{\Delta\varepsilon_n^p}{2}\right)_{max} \tag{18}$$

The above quantities are determined on all planes passing the considered material point, and the plane experiencing maximum damage, (has the maximum value of the IG parameter) is a critical plane.

A power equation identical to Eq. (16) was used for the referential fatigue curve. However, its parameters m and n take different values. No information on the approach to random loadings was provided by Ince and Glinka [61]. Thus, the energy components in Eq. (18) were calculated for the whole loading block (loading path).

4.2.4. Ellyin-Gołoś parameter (EG)

Another energy-based parameter considered in this paper was the multiaxial fatigue damage parameter formulated by Ellyin and Gołoś [63]:

$$EG = \frac{\Delta W^p}{\rho} + \Delta W^{e+} \tag{19}$$

where ρ is the multiaxiality factor [64]:

$$\Delta W^p = \int_0^t \sigma_{ij}\,d\varepsilon_{ij}^p \tag{20}$$

$$\Delta W^{e+} = \frac{1+\nu^e}{3E}(\sigma_{eq,max})^2 + \frac{1-2\nu^e}{6E}(I_1^{max})^2 \tag{21}$$

$$\rho = (1+\nu_{eq})\frac{\hat{\varepsilon}_{max}}{\hat{\gamma}_{max}} \tag{22}$$

In the case of axial–torsional loading, the total plastic strain energy is equal to the sum:

$$\Delta W^p = \int_0^t \sigma_x\,d\varepsilon_x^p + 2\int_0^t \tau_{xy}\,d\varepsilon_{xy}^p = \int_0^t \sigma_x\,d\varepsilon_x^p + \int_0^t \tau_{xy}\,d\gamma_{xy}^p \tag{23}$$

In Eq. (21), $I_1 = \mathrm{tr}(\sigma_{ij})$ is a first invariant of the stress tensor. The equivalent Poisson's ratio ν_{eq}, as well as quantities $\hat{\varepsilon}_{max}$ and $\hat{\gamma}_{max}$ in Eq. (22), are calculated as:

$$\nu_{eq} = \frac{\nu^p(1-\nu^e)(\varepsilon_a+\varepsilon_t) + (\nu_e-\nu_p)(\varepsilon_a^e+\varepsilon_t^e)}{(1-\nu^e)(\varepsilon_a+\varepsilon_t) + (\nu_e-\nu_p)(\varepsilon_a^e+\varepsilon_t^e)} \tag{24}$$

$$\hat{\varepsilon}_{max} = \max(\varepsilon_a, \varepsilon_t) \tag{25}$$

$$\hat{\gamma}_{max} = max(|\varepsilon_a-\varepsilon_r|, |\varepsilon_t-\varepsilon_r|) \tag{26}$$

where ε_a and ε_t are axial and transverse in-plane principal strains, and the radial strain ε_r is represented by:

$$\varepsilon_r = -\frac{\nu_{eq}}{(1-\nu_{eq})}(\varepsilon_a+\varepsilon_t) \tag{27}$$

A detailed discussion of these quantities is provided in [65].

Again, the power function (Eq. (16)) was used for the referential fatigue curve, with m and n values unique to the EG parameter. It was assumed that the total strain energy was simply an additive quantity, and the EG parameter values were determined for the complete loading blocks (loading paths).

4.2.5. Itoh-Sakane parameter (IS)

Of the many multiaxial fatigue damage parameters, the Itoh-Sakane (IS) parameter stands out as a strain parameter. The parameter and fatigue life prediction methodology were developed by the authors over the years, and many versions and variants were proposed [66–68]. In the present work, an initail form of the IS parameter was applied based on the assumption that the damage under non-proportional loading is a result of an additional hardening [69]. The IS parameter is an equivalent non-proportional strain range:

$$\Delta\varepsilon_{NP} = (1+\alpha f_{NP})\Delta\varepsilon_l \tag{28}$$

The maximum principal strain range$\Delta\varepsilon_l$ is defined as:

$$\Delta\varepsilon_l = \max_t[\varepsilon_l(t)\cdot\cos\xi(t) + \varepsilon_{l,max}] \tag{29}$$

The history of ε_l is determined using the formula:

$$\varepsilon_l(t) = \begin{cases} |\varepsilon_1(t)| & \text{for } |\varepsilon_1(t)| \geq |\varepsilon_3(t)| \\ |\varepsilon_3(t)| & \text{for } |\varepsilon_1(t)| < |\varepsilon_3(t)| \end{cases} \tag{30}$$

where ε_1 and ε_3 are the maximum and minimum principal strains. The $\varepsilon_{l,max}$ quantity is the maximum value of ε_l in time, while $\xi(t)$ represents the values of an angle between $\varepsilon_{l,max}$ and the sequential positions of $\varepsilon_l(t)$. The α coefficient is a material parameter that expresses the sensitivity of a material to non-proportional loading in terms of an additional hardening:

$$\alpha = \frac{\sigma_{1,NP}}{\sigma_{1,P}} - 1 \tag{31}$$

where $\sigma_{1,NP}$ and $\sigma_{1,P}$ are maximum principal stress values for 90° out-of-phase loading and in-phase loadings, respectively. The non-proportionality factor f_{NP} reflects the severity of the non-proportional loading path:

$$f_{NP} = \frac{k}{T\varepsilon_{l,max}}\int_0^{T_c}[|\sin(\xi(t))|\cdot\varepsilon_l(t)]\,dt \tag{32}$$

where T_c is a period of loading cycle and k is a coefficient equal to $\pi/2$. The role of k is to bring the value of f_{NP} to unity for 90° out-of-phase loading and zero for proportional loading.

No cycle counting was performed for the IS damage parameter, since the authors did not provide the adequate cycle counting procedure for the parameter. Also, the cycle definition used by the authors is not clear in some cases, as already noticed by Mei and Dong [70]. On the other hand, for short loading blocks like those analyzed in this paper, the f_{NP} factor should to some extent be able to reflect the influence of the loading path on the fatigue damage. The referential fatigue curve was described by the BMC equation (Eq. (11)), with parameters determined for reversed axial loading.

5. Fatigue life prediction results

5.1. Qualitative analysis

The results of fatigue life prediction using the previously described

models are first presented qualitatively. For this purpose, the typical charts comparing the calculated and experimental fatigue life were used. The solid line represents perfect matching of experimental and calculated fatigue life, the dashed lines denote a scatter band of factor 2, and the dash-dot lines denote a scatter band of factor 3.

5.1.1. PA38-T6 aluminum alloy

Fig. 4 shows the fatigue life prediction results for PA38-T6

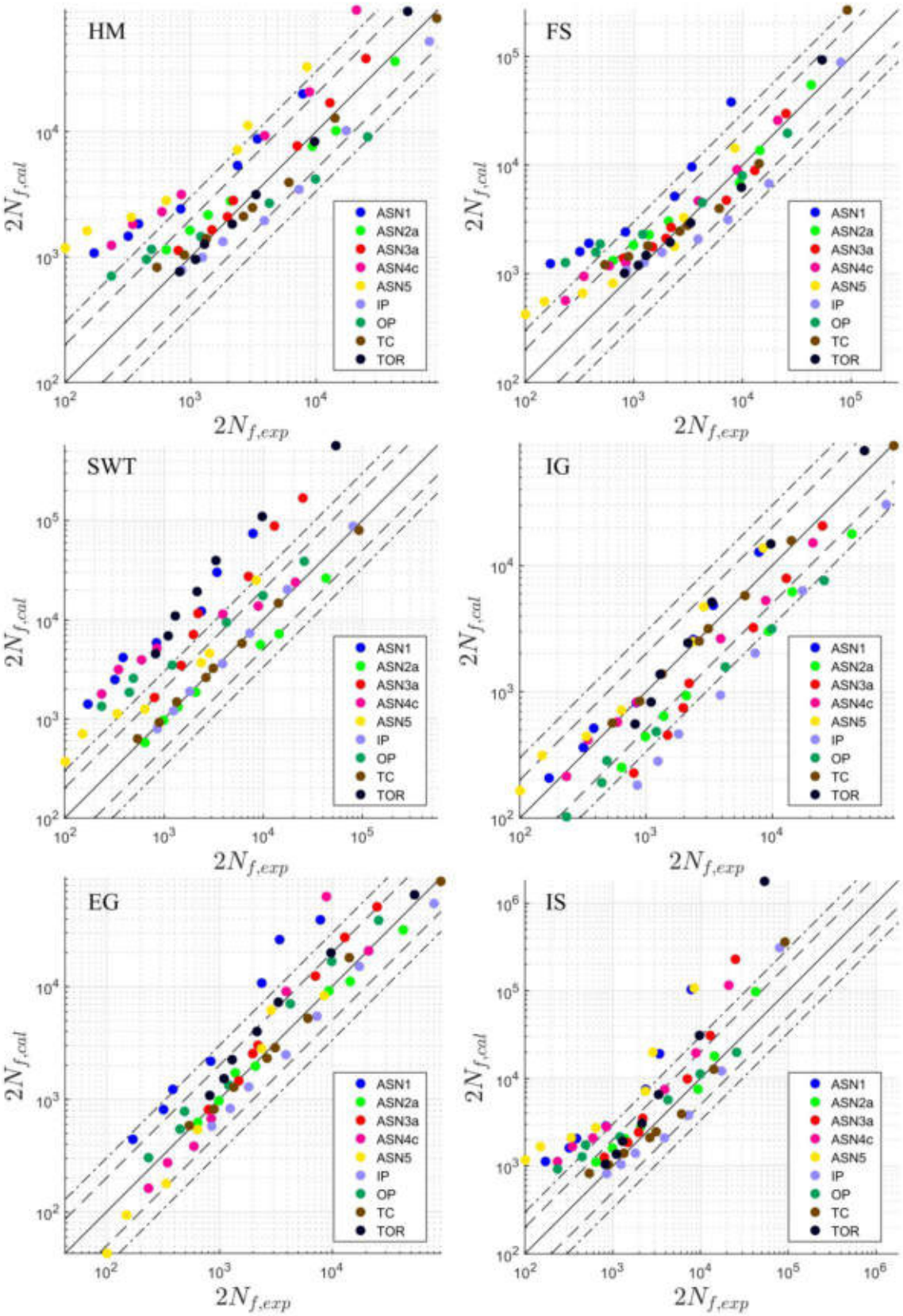

Fig. 4. Comparison of experimental $2N_{f,exp}$ and calculated $2N_{f,cal}$ fatigue life for PA38-T6 aluminum alloy.

aluminum alloy. For this material, the HM equivalent strain correlates with fatigue life relatively well. In the case of asynchronous loadings, the results are worse compared to those for synchronous loadings. The reason is that the loading path (block) consists of several cycles of normal or shear strain. Worse results show that asynchronous loadings require cycle counting, despite the fact that the number of cycles of strain components in the loading block is very small. The scatter of results is also affected by the different slopes of the data points for different loadings (compare [25]). It is also worth noting that using half of the equivalent strain range as a damage parameter gave better results

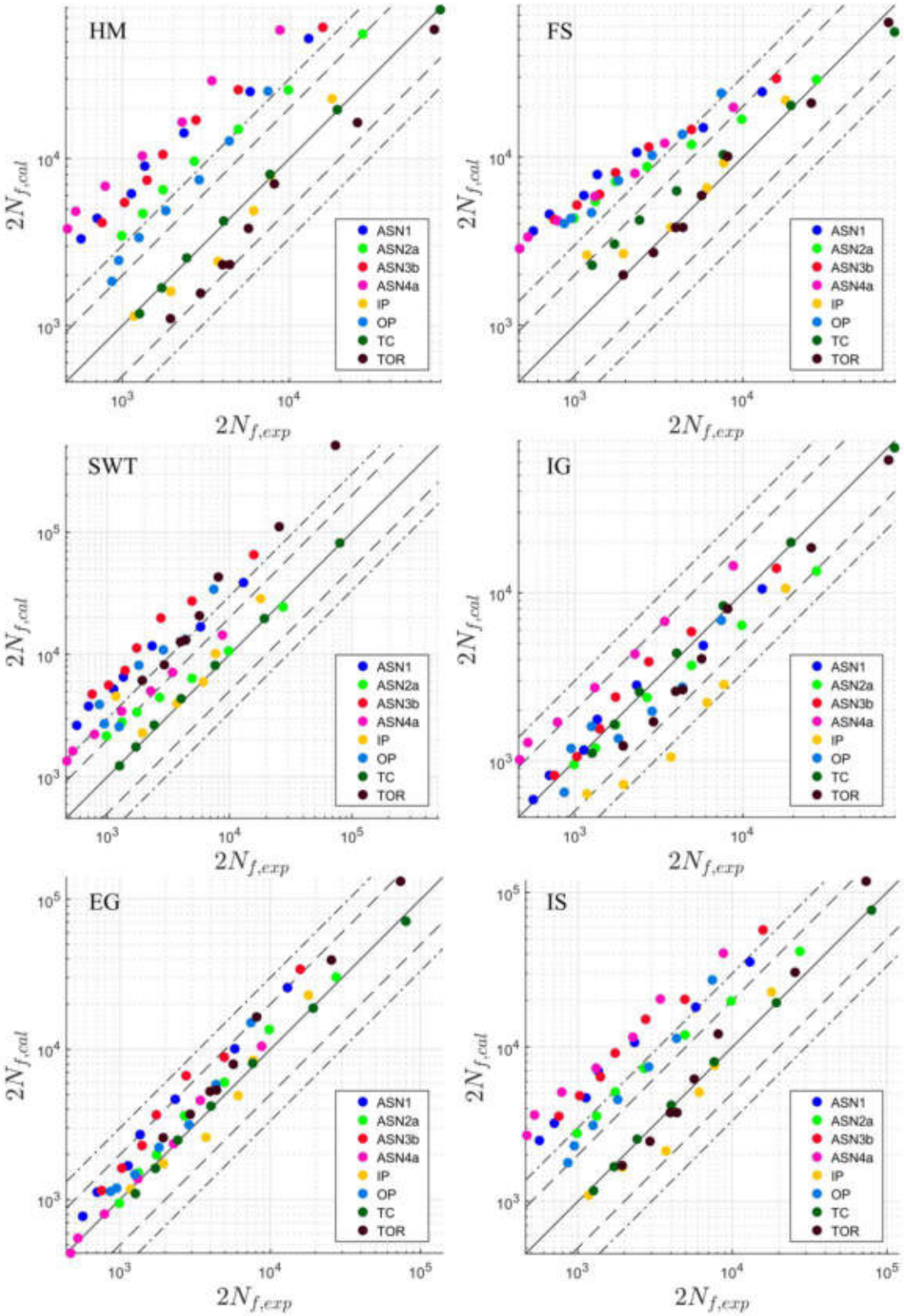

Fig. 5. Comparison of experimental $2N_{f,exp}$ and calculated $2N_{f,cal}$ fatigue life for E235 steel.

than using the maximum value (compare [25]).

The modified FS damage parameter gave better results. Most of the data points are placed in a scatter band of 2 or 3. Fatigue life is underestimated for higher loading levels. Again, the influence of the data points' trends can be observed. The overestimation of fatigue life is the highest for ASN1 loading. However, no significant discrepancy between the results for synchronous and asynchronous loadings can be seen. This means that rainflow cycle counting was successful for the asynchronous loadings.

The first thing to note for/about/regarding the SWT damage

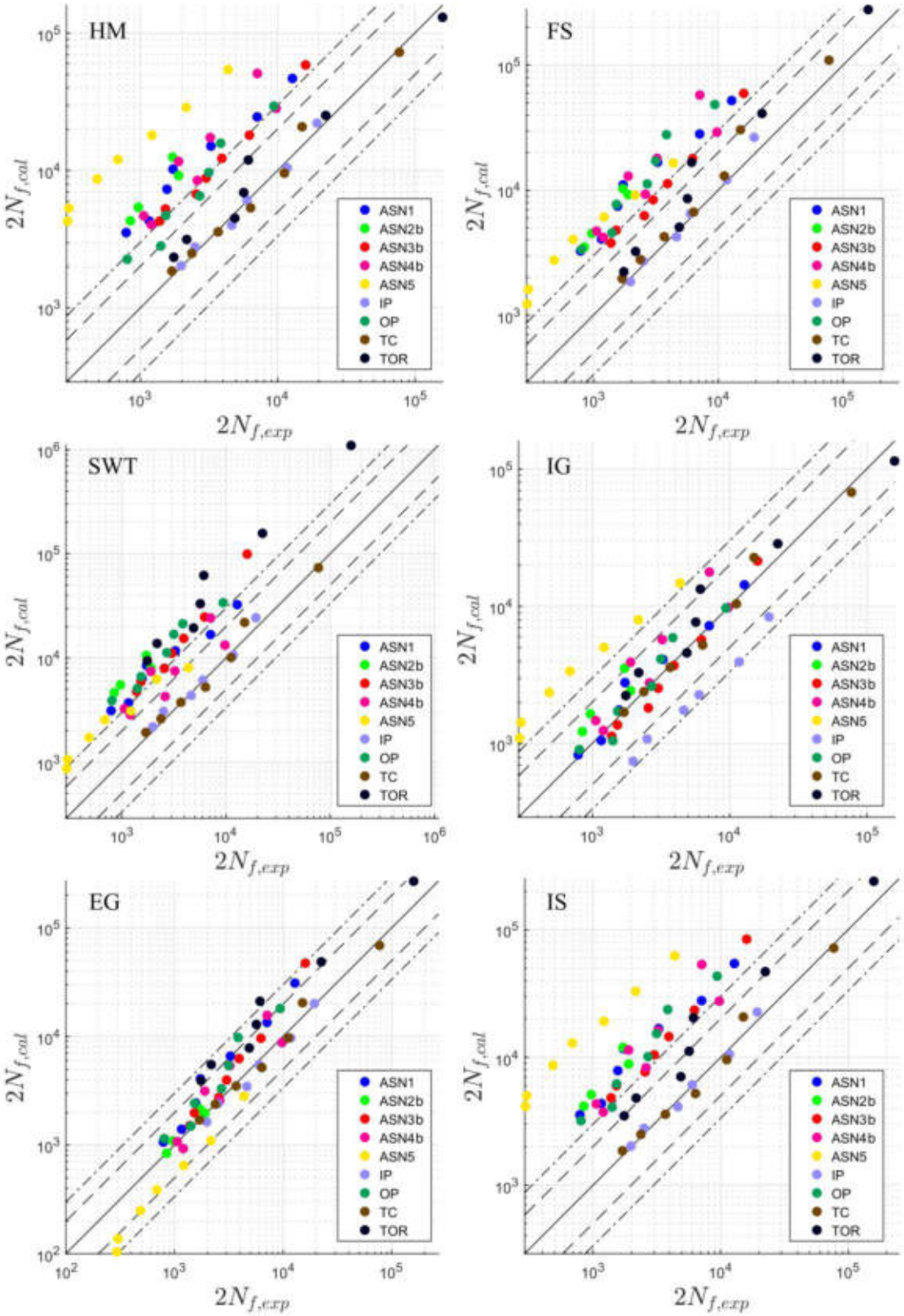

Fig. 6. Comparison of experimental $2N_{f,exp}$ and calculated $2N_{f,cal}$ fatigue life for E355 steel.

parameter is the divergence between the data points corresponding to TC and TOR loadings. Although the SWT parameter is based on maximum principal stress and strain, it was observed that PA38-T6 aluminum alloy exhibits the shear damage mechanism. This clearly explains poor fatigue life prediction for torsional loading. Consequently, all other results are affected by this problem.

In the case of the IG damage parameter, most of the results are placed on the conservative side of the chart, which is desirable. There is no evident difference between asynchronous and synchronous loadings. This means that the IG parameter successfully captured the specificity

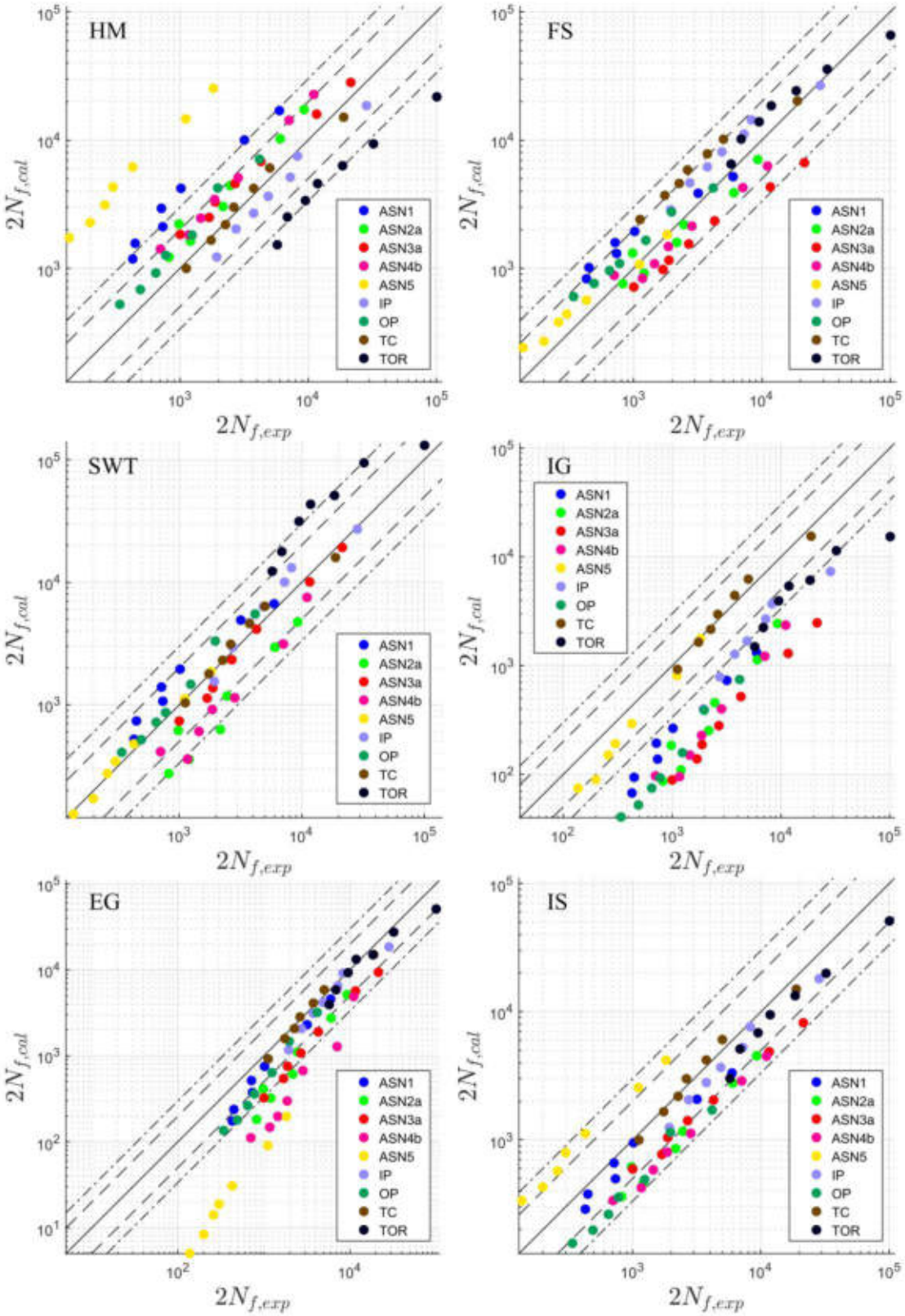

Fig. 7. Comparison of experimental $2N_{f,exp}$ and calculated $2N_{f,cal}$ fatigue life for X5CrNi18-10 steel.

of asynchronous loadings, although the model didn't include cycle counting.

For the EG damage parameter, most of the results were placed in the scatter band of factor 2, both on the safe and unsafe side. The worst results were found for ASN1 loading, for which some of the data points exceeded the scatter band of factor 2 or even 3. In general, the effect of nonproportionality and asynchronous loadings was well covered.

For the IS damage parameter, the results of fatigue life prediction seem to be worse for asynchronous loadings than for synchronous loadings. The worst results were found for ASN1 and ASN5 loadings. It can also be noticed that for a longer fatigue life, the difference between the results for TOR and TC loadings increases.

5.1.2. E235 steel

Results of the fatigue life prediction for E235 steel are presented in Fig. 5. The model based on the HM equivalent strain only gave good results for proportional loadings. The data points corresponding to OP loading barely fit the scatter band of factor 3. For asynchronous loadings, fatigue life was even more overestimated due to several components' cycles forming the strain path.

In the case of the modified FS parameter, the data points for proportional loadings were located in the scatter band of 3. The data points corresponding to OP and asynchronous loadings form approximately one band. The more the fatigue life for these loadings was overestimated, the shorter it was. The possible explanation lies in the physical basis of the FS parameter. The effect of non-proportionality is mostly captured by additional non-proportional hardening, which is reflected by higher normal stress on the critical plane. The E235 steel showed low non-proportional hardening [25].

The effect of a physical basis that does not match the observed damage mechanism can be seen for the SWT parameter. The points for TOR loading lie outside of the scatter band of 3. The results for all other loadings strongly depend on the same cause.

The results obtained using the model based on the IG parameter were located mostly in the scatter band of 2. The effect of non-proportionality was almost perfectly captured – see the results for OP loading. Fatigue life for asynchronous loadings was also well estimated.

Almost all the data points resulting from fatigue life prediction using the EG parameter-based model were located in the upper scatter band of factor 2, which means they were slightly overestimated. All the effects of applied loadings were covered quite well.

For the IS model, the features of the results are similar to those observed for the FS parameter. Fatigue life for proportional loadings is well predicted and is worse for non-proportional loading. The explanation seems to be the same as in the case of the FS parameter. The IS damage parameter captures the effect of non-proportionality by non-proportional hardening, and for E235 it was very low. Additionally, the non-proportionality factor failed to take into account the effect of the asynchronous loading path.

5.1.3. E355 steel

As was previously mentioned, the fatigue behavior of E355 and E235 steels was quite similar. This was due to the materials having similar chemical composition, microstructure (ferrite and pearlite according to Fe-C phase equilibrium diagram), and the same heat treatment. Hence, the results of fatigue life prediction for both materials had many common features.

Fatigue life prediction based on the HM equivalent strain was almost perfect for proportional loadings (see Fig. 6). Points for OP loading were placed on the borderline of scatter band 3. Prediction of fatigue life was worse for asynchronous loadings due to non-proportionality and a loading block built of few cycles of strain components.

For the modified FS parameter, fatigue life was overestimated for non-proportional loadings. A possible explanation is the same as that for E235 steel – low non-proportional hardening. The results for asynchronous loadings were not worse than for OP loading, which suggests that rainflow cycle counting was successful.

In the case of the SWT parameter, all the fatigue life predictions were again affected by the tensile damage mechanism assumption, which is inconsistent with the experimentally identified mechanism. The consequence is the general overestimation of fatigue life.

For the IG damage parameter, the results were located in the scatter band of factor 2, excluding IP and ASN5 loadings. The fatigue life was slightly underestimated for IP loading, just like in the case of E235 steel. For ASN5 loading, fatigue life was overestimated.

Fatigue life prediction results obtained using the EG parameter were mostly located in the scatter band of 2 with some landing in the scatter band of 3. The effect of non-proportionality and asynchronous loadings was quite well-reflected. The overall fatigue life estimation was considered successful.

In the case of the IS model, the calculated fatigue lives were generally longer than the experimental fatigue lives. This is due to the low non-proportional hardening of the material, which is the basis for the damage parameter. The worst results were obtained for ASN5 loading. This loading path consisted of the highest number of strain components, which is the most probable explanation for inaccurate life prediction.

5.1.4. X5CrNi18-10 steel

The fatigue life prediction based on HM equivalent strain was better than the predictions for E235 and E355 steels (Fig. 7). This is surprising since X5CrNi18-10 steel showed a high amount of non-proportional hardening, which suggests high sensitivity to non-proportionality of loading. However, this conclusion is incorrect. It can be seen that there was a significant difference between the position of data points for TC and TOR loadings. For the latter, the fatigue life was underestimated. This effect brought down all other data points in the direction of a safe region. The equivalent strain was based on distortion energy and assigns a major role to the shear component of strain. The material exhibited a tensile damage mechanism, which explains the results of the fatigue life prediction.

Very good prediction results were obtained when using the modified FS parameter. This can be confusing, since this parameter is shear strain-based, and the material showed a tensile damage mechanism. However, the fatigue crack always initiates and initially propagates on maximum shearing planes. The period of crack initiation and Stage I propagation could have been long enough that the shear strain component played an important role. However, the data points for TC loading barely fit the scatter band of 2. This was a worse result than the results for the other investigated materials and the worst among all applied loadings. The high amount of non-proportional hardening resulted in high values of normal stress on the critical plane. Thus, the fatigue life prediction for non-proportional loadings was accurate. Rainflow cycle counting and linear damage accumulation were successful in the case of asynchronous loadings.

Good fatigue life predictions were also obtained using the SWT parameter. This parameter is based on the principal stress and strain components. X5CrNi18-10 steel showed the tensile damage mechanism, which explains the good results. The effect of non-proportionality and asynchronous loadings were well-reflected. This means that rainflow cycle counting and the linear damage accumulation rule worked well. It can be noted that the results were the worst for TOR loading. If they are compared to the results obtained using the modified FS parameter, it can be assumed that the crack propagation on both maximum shear and normal strain directions was important.

The predicted fatigue life using the IG parameter was mostly underestimated. The exception was ASN5 loading, which can potentially be explained through observation of the results for TC and TOR loading. It can be seen that the fatigue life for TOR loading was underestimated. For the IG parameter, shear and normal strain energy components are equally responsible for damage. However, the experimental observation of short cracks suggests that the normal parameter is more important.

In the case of the EG parameter, the data points were located in the scatter band of factor 3 for synchronous and ASN1 loading. For the other asynchronous loadings, the fatigue life was underestimated. The shorter the fatigue life, the more pronounced the underestimation. An explanation could be that the total accumulation of strain energy-based damage is not suitable for materials which exhibit a tensile damage mechanism.

In the case of the IS damage parameter, the results of fatigue life prediction were very good. Again, this can be explained by taking into account the effect of nonproportionality and the damage mechanism. The IS parameter is based on the maximum principal strain, and the effect of nonproportionality is incorporated by the non-proportionality factor and the non-proportional hardening coefficient, which are very high for X5CrNi18-10 steel [25].

Recently, Arora et al. [71] used the experimental data for PA38-T6 aluminum alloy, E235 and E355 steel, taken from [25], to verify the newly developed model [38]. Achieved fatigue life prediction results were also compared to other models. Thus, the reference [71] can be considered as complementary to the present work.

5.1.5. Quantitative analysis

Two parameters, also used by other authors [72,73], were applied to compare the results quantitively. The first parameter was a mean dispersion of fatigue life, given by:

$$T_N = 10^{\bar{E}} \tag{33}$$

where

$$\bar{E} = \frac{1}{n}\sum_{i=1}^{n} \log\left(\frac{N_{exp,i}}{N_{cal,i}}\right) \tag{34}$$

and the second parameter was a fatigue life prediction mean-squared error, given by:

$$T_{RMS} = 10^{E_{RMS}} \tag{35}$$

where

$$E_{RMS} = \sqrt{\frac{\sum_{i=1}^{n} log^2\left(\frac{N_{exp,i}}{N_{cal,i}}\right)}{n}} \tag{36}$$

The quantitative analysis shows that the most conservative fatigue life predictions for PA38-T6 aluminum alloy were achieved using the IG parameter (Fig. 8). In the case of the FS parameter, results were only slightly non-conservative. For all other models, non-conservative results were obtained. Additionally, the scatter of results was low for the FS and IG damage parameters. A low scatter of results was also achieved for the EG parameter. However, the results were a bit more non-conservative than in the case of the IG and FS parameters. The highest scatter and the most non-conservative fatigue lives were obtained in the case of the SWT and IS damage parameters. This confirms previous observations that these parameters are based on a different damage mechanism than observed experimentally for PA38-T6 aluminum alloy.

For E235 steel, the results of fatigue life prediction were mostly conservative in the case of the IG parameter only. Also, the scatter of results was the smallest for this parameter. Calculated fatigue life was mostly non-conservative for the rest of the applied damage parameters. The least non-conservative results, with quite low scatter, were achieved using the EG parameter. The worst performance was shown by HM, SWT, and IS parameters.

In the case of E355 steel, all the calculated fatigue life predictions were mostly non-conservative. The safest results were given by models based on IG and EG parameters with similar values of T_N and T_{RMS}. Again, the worst results were obtained using HM, SWT, and IS parameters.

The most conservative results of fatigue life prediction were achieved using IG and EG parameters. However, for the IG parameter, the fatigue life was strongly underestimated, and for the EG parameter, significant differences between loading cases occurred (compare Fig. 7). For both parameters, the scatter of results expressed by T_{RMS} is also high. The most accurate results with the lowest scatter were obtained using the SWT and FS parameters. The results for the IG parameter had similar scatter and were more conservative.

5.2. A comparison of predicted and observed experimentally small crack directions

For the models based on the critical plane approach, i.e. FS, SWT, and IG parameters, calculated positions of the critical plane were compared to small crack directions observed on surfaces of fatigued specimens. They are presented using polar charts, where 90° and 270° angles mean a direction parallel to the specimen axis. The blue areas represent the measured directions of small cracks. Their thickness corresponds to ± standard deviation and their middle corresponds to the arithmetic mean. The red lines represent the position of small cracks. Additionally, the maximum shear (solid line) and normal (dashed line) strain loci were imposed.

In the case of PA38-T6 aluminum alloy, the position of critical planes according to the FS parameter perfectly matches the position of small cracks for synchronous loadings (Fig. 9). The matching is also good for ASN2a, ASN3a, and ASN5 loadings. In the case of ASN4c loading, the directions of small cracks and critical planes do not seem to conform. However, they lie in the same directions as the values of maximum shear and normal strain. Thus, there is no difference. For ASN1 loading, the positions of critical planes disagree with the directions of small cracks. Cracks formed in the same directions as the maximum shear strain (as indicated by critical planes), but at lower values of normal strain. This is a possible explanation for the worse fatigue life prediction for this loading (compare Fig. 4). For the SWT parameter, the positions of critical planes do not reflect the directions of small cracks. In a few cases, their positions are similar, but this is due

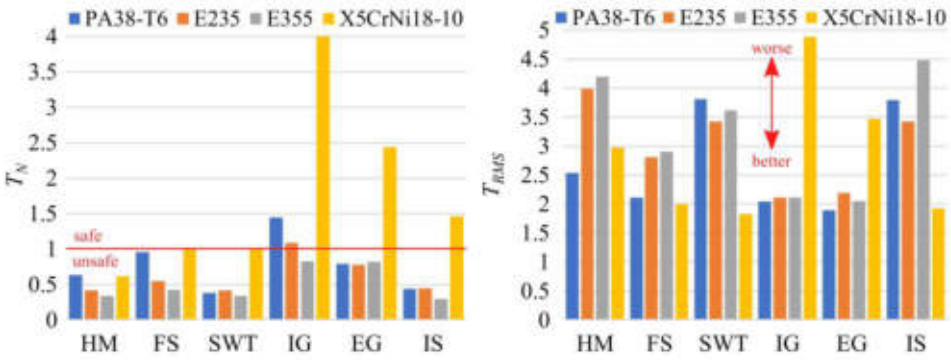

Fig. 8. A comparison of T_N and T_{RMS} values for analyzed materials and models.

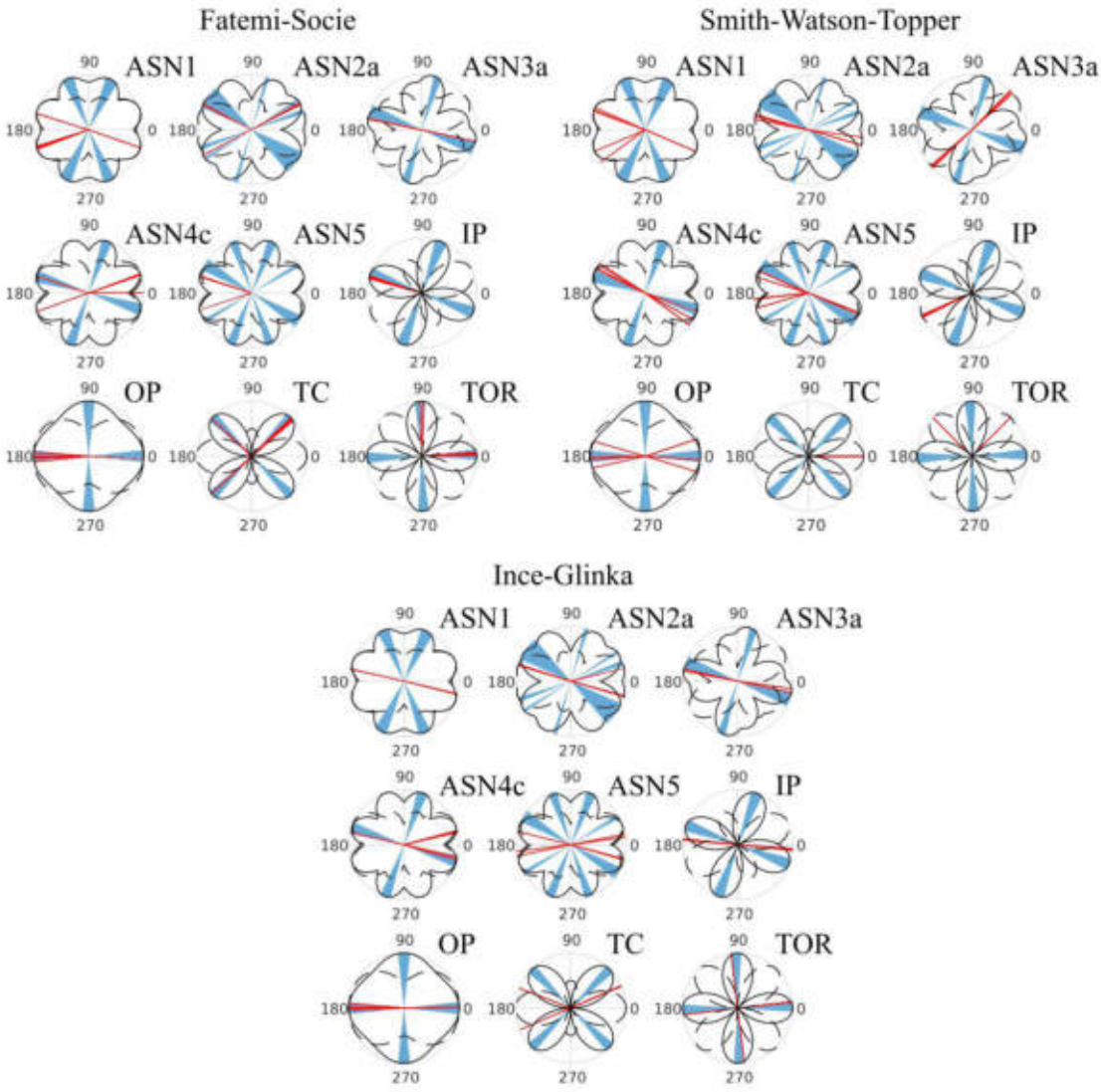

Fig. 9. A comparison of crack orientations observed experimentally and orientations of the critical plane according to models based on the critical plane approach for PA38-T6 aluminum alloy.

to the close position of maximum shear and normal strain planes, and it does not improve the fatigue life prediction. In the case of the IG parameter, the matching of positions of critical planes and small crack directions is good or is only slightly deviated for some types of loading (OP, TOR, ASN3a, ASN4c), while for others there is a mismatch (ASN1, TC, ASN5). No clear correlation between the position of critical planes and the quality of fatigue life prediction can be found.

For E235 steel, a good overall agreement between the positions of critical planes and small crack directions can be observed in the case of the FS parameter (Fig. 10). Positions of critical planes according to the SWT parameter are different than the directions of cracks. This is particularly evident for TC and TOR loadings. For some loadings, the positions of critical planes are close to the directions of cracks. This is a result of similar or equal positions of shear and normal strain extrema. In the case of the IG parameter, the directions of critical planes and small cracks coincide for some loading cases. Others do not, just as was observed for PA38-T6 aluminum alloy.

For X5CrNi18-10 steel, a high agreement between the directions of critical planes and the directions of small cracks was achieved for both the FS and SWT parameters (see Fig. 11). The reason is that the cracks were observed on planes of maximum shear strain, as well as on planes of maximum normal strain. Also, the fatigue life was predicted well for these damage parameters. Again, the most problematic loading case for predicting the critical plane position using the applied methods was ASN1. Similar to other materials, the IG parameter resulted in agreement between the positions of critical planes and the directions of small cracks for some cases of loadings, but resulted in a disagreement for others.

6. Conclusions

Based on the observation of small cracks on the surfaces of fatigued specimens, it was found that PA35-T6 aluminum alloy and E235 steel exhibit a shear fatigue damage mechanism. The same was assumed for E355, as other aspects of fatigue behavior were similar to those of E235. For these materials, small cracks initiated and developed in directions close to the positions of the maximum shear strain planes. X5CrNi18-10 steel showed a tensile damage mechanism. Small cracks were observed both in the directions of maximum shear and normal strain. Based on these observations, it can be stated that cracks initiated and initially propagated on the planes of maximum shear strain, and then changed direction to correspond with the directions of maximum normal strain. The influence of machining marks and surface inclusions was pronounced for this material.

Six fatigue life prediction models, based on popular multiaxial fatigue damage parameters, were evaluated. The model based on the

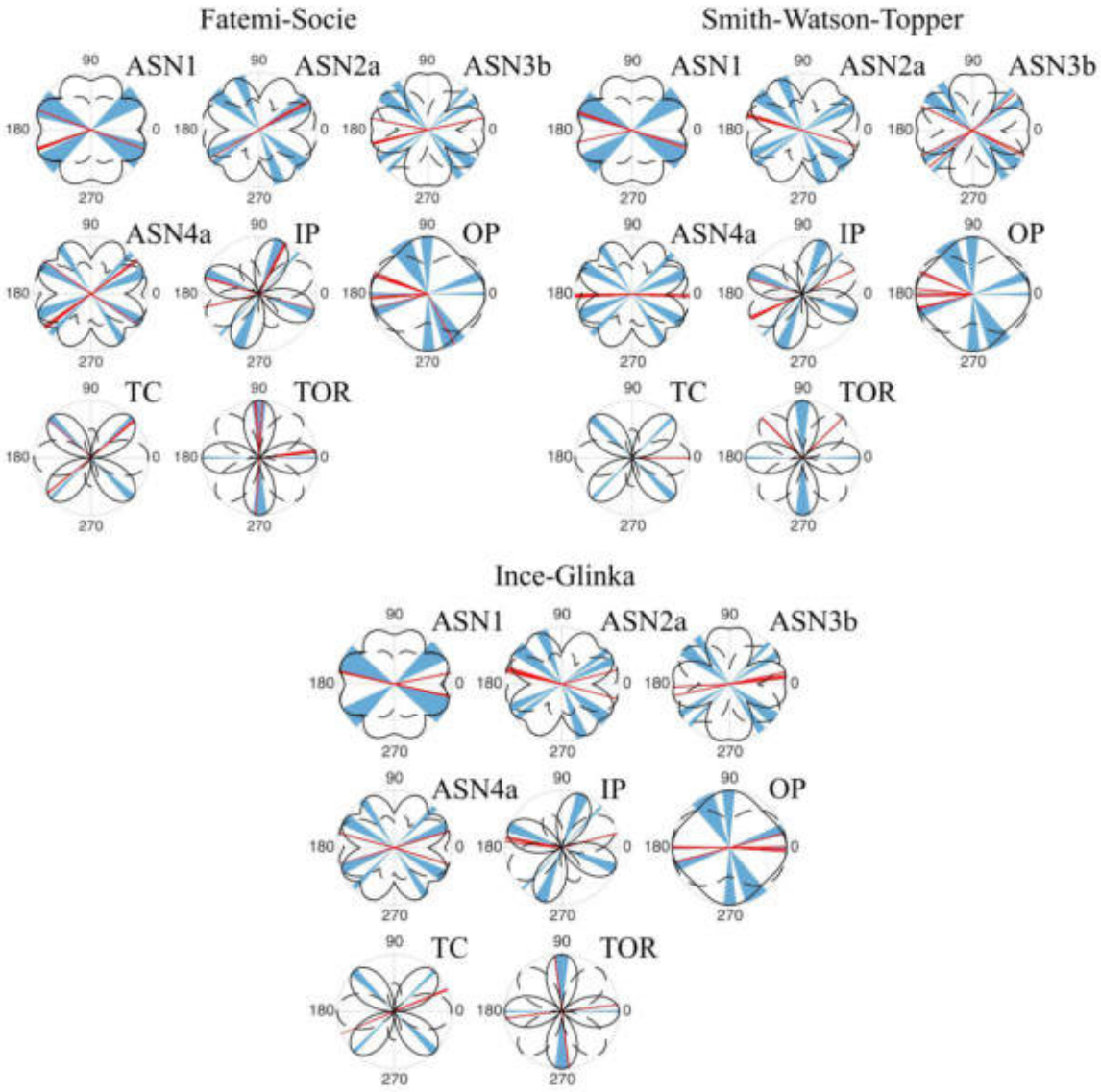

Fig. 10. A comparison of crack orientations observed experimentally and orientations of the critical plane according to models based on the critical plane approach for E235 steel.

Huber-Mises equivalent strain range gave unsatisfactory results in a majority of cases.

Although the same conclusion was already made by many authors, the present work is novel due to the utilization of asynchronous loadings. Even though the asynchronous loading paths consist of very short loading blocks, the lack of cycle counting caused worse prediction results than in cases of synchronous loadings. The model using a modified Fatemi-Socie parameter resulted in a good fatigue life prediction for PA38-T6 aluminum alloy and X5CrNi18-10 steel. For the first of these materials, there is a clear correlation between the physical basis of the FS parameter and the damage mechanism. The second material showed a tensile damage mechanism. However, the good fatigue life prediction results using the FS parameter can be interpreted to mean that the stage of initiation and initial propagation of cracks was long enough to play an important role. Fatigue life prediction was worse for E235 and E355 steel, although the assumption of a damage mechanism is correct for these materials. The overestimation of fatigue life was noticed for non-proportional loadings. A possible explanation could be a low amount of non-proportional hardening, which could result in lower values of the damage parameter. The need for cycle counting also works to the disadvantage of this model. Since the loading blocks were very short and the counting was performed with the real signals rather than the idealized ones, some of the cycles were identified as reversals, which often results in lower accumulated damage. The Smith-Watson-Topper parameter is based on principal stress and strain, thus the fatigue life prediction model using it did not give good results for PA38-T6 aluminum alloy, E235 steel, and E355 steel. However, for X5CrNi18-10 steel, the prediction was satisfactory. This result can be correlated with the observed tensile damage mechanism. The model based on the Ince-Glinka parameter resulted in a very good overall fatigue life prediction, as well as better results compared to other models for materials that showed a shear damage mechanism. It is to be noted that this parameter does not require any material parameters or cycle counting. For X5CrNi18-10 steel, fatigue lives were underestimated. However, the results were safe. The model using the Ellyin-Gołoś damage parameter worked well when materials exhibited a shear damage mechanism. The estimated fatigue life was not longer than three times the experimental life in most cases.

In the case of austenitic steel, the calculated fatigue life was underestimated for asynchronous loadings. As a parameter based on principal strain and non-proportional hardening, the Itoh-Sakane damage parameter resulted in a good fatigue life prediction only for

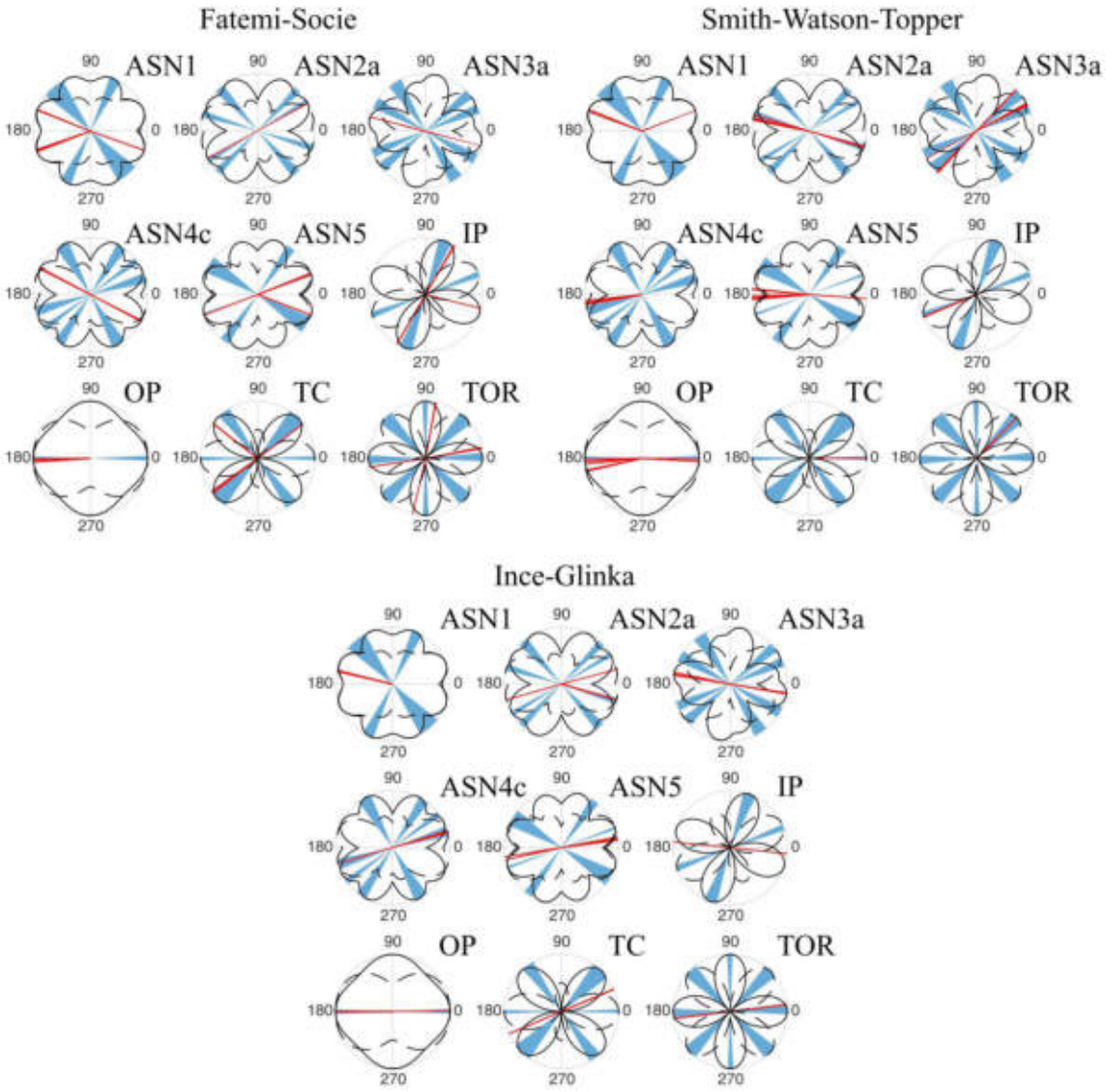

Fig. 11. A comparison of crack orientations observed experimentally and orientations of the critical plane according to models based on the critical plane approach for X5CrNi18-10 steel.

X5CrNi18-10 steel, which showed a tensile damage mechanism and high non-proportional hardening. Most of the predicted fatigue lives were two to three times shorter than the experimental fatigue lives.

Declaration of Competing Interest

The authors declare that they have no known competing financial interests or personal relationships that could have appeared to influence the work reported in this paper.

Acknowledgment

The work was realized within the framework of the research project No. 2017/01/X/ST5/00143 funded by the National Science Centre in Poland.

References

[1] Skibicki D. Multiaxial fatigue life and strength criteria for non-proportional loading. Mater Test 2006;48:99–102.
[2] Pejkowski Ł. On the material's sensitivity to non-proportionality of fatigue loading. Arch Civ Mech Eng 2017;7:711–27. https://doi.org/10.1016/j.acme.2016.09.010.
[3] Kluger K, Karolczuk A, Derda S. Application of life-dependent material parameters to fatigue life prediction under multiaxial. Materials (Basel) 2020;13.
[4] Lu C, Melendez J, Martínez-Esnaola JM. Modelling multiaxial fatigue with a new combination of critical plane definition and energy-based criterion. Int J Fatigue 2018;108:109–15. https://doi.org/10.1016/j.ijfatigue.2017.12.004.
[5] Zhong B, Wang Y, Wei D, Wang J. A new life prediction model for multiaxial fatigue under proportional and non-proportional loading paths based on the pi-plane projection. Int J Fatigue 2017;102:241–51. https://doi.org/10.1016/j.ijfatigue.2017.04.013.
[6] Lu Y, Wu H, Zhong Z. A simple energy-based model for nonproportional low-cycle multiaxial fatigue life prediction under constant-amplitude loading. Fatigue Fract Eng Mater Struct 2018:1–10. https://doi.org/10.1111/ffe.12785.
[7] Wu ZR, Hu XT, Song YD. Multiaxial fatigue life prediction for titanium alloy TC4 under proportional and nonproportional loading. Int J Fatigue 2014;59:170–5. https://doi.org/10.1016/j.ijfatigue.2013.08.028.
[8] Chmelko V, Margetin M. The performance of selected multiaxial criteria under tension/torsion loading conditions. Int J Fatigue 2020;135:105532. https://doi.org/10.1016/j.ijfatigue.2020.105532.
[9] Branco R, Prates PA, Costa JD, Borrego LP, Berto F, Kotousov A, et al. Rapid assessment of multiaxial fatigue lifetime in notched components using an averaged strain energy density approach. Int J Fatigue 2019;124:89–98. https://doi.org/10.1016/j.ijfatigue.2019.02.005.
[10] Łagoda T, Kurek M, Głowacka K. A formulation of the criterion for multiaxial fatigue in terms of complex number as proposed by Macha. Int J Fatigue 2020;133. https://doi.org/10.1016/j.ijfatigue.2019.105430.
[11] Xue L, Shang DG, Li DH, Li LJ, Xia Y, Hui J. Online multiaxial fatigue damage evaluation method by real-time cycle counting and energy-based critical plane criterion. Fatigue Fract Eng Mater Struct 2020;43:1184–98. https://doi.org/10.1111/ffe.13192.
[12] Luo P, Yao W, Susmel L. An improved critical plane and cycle counting method to

assess damage under variable amplitude multiaxial fatigue loading. Fatigue Fract Eng Mater Struct 2020:1–16. https://doi.org/10.1111/ffe.13281.
[13] Karolczuk A, Papuga J, Palin-Luc T. Progress in fatigue life calculation by implementing life-dependent material parameters in multiaxial fatigue criteria. Int J Fatigue 2020;134:105509. https://doi.org/10.1016/j.ijfatigue.2020.105509.
[14] Xue L, Shang DG, Li DH, Li LJ, Liu XD, Chen H. Equivalent energy-based critical plane fatigue damage parameter for multiaxial LCF under variable amplitude loading. Int J Fatigue 2020;131:105350. https://doi.org/10.1016/j.ijfatigue.2019.105350.
[15] Benedetti M, Berto F, Le Bone L, Santus C. A novel Strain-Energy-Density based fatigue criterion accounting for mean stress and plasticity effects on the medium-to-high-cycle uniaxial fatigue strength of plain and notched components. Int J Fatigue 2020;133. https://doi.org/10.1016/j.ijfatigue.2019.105397.
[16] Faruq NZ, Susmel L. Proportional/nonproportional constant/variable amplitude multiaxial notch fatigue: cyclic plasticity, non-zero mean stresses, and critical distance/plane. Fatigue Fract Eng Mater Struct 2019. https://doi.org/10.1111/ffe.13036.
[17] Lu Y, Wu H, Zhong Z. A modified energy-based model for low-cycle fatigue life prediction under multiaxial irregular loading. Int J Fatigue 2019;128:105187. https://doi.org/10.1016/j.ijfatigue.2019.105187.
[18] Gan L, Wu H, Zhong Z. Use of an energy-based/critical plane model to assess fatigue life under low-cycle multiaxial cycles. Fatigue Fract Eng Mater Struct 2019:ffe.3090. https://doi.org/10.1111/ffe.13090.
[19] Zhu H, Wu H, Lu Y, Zhong Z. A novel energy-based equivalent damage parameter for multiaxial fatigue life prediction. Int J Fatigue 2019;121:1–8. https://doi.org/10.1016/J.IJFATIGUE.2018.11.025.
[20] Feng ES, Wang XG, Jiang C. A new multiaxial fatigue model for life prediction based on energy dissipation evaluation. Int J Fatigue 2019;122:1–8. https://doi.org/10.1016/j.ijfatigue.2019.01.003.
[21] Saito S, Ogawa F, Itoh T. Investigation of fatigue strength under wide-ranged biaxial stress for two types of stainless steel using a thin-walled hollow cylinder specimen. Int J Fatigue 2020;136:105611. https://doi.org/10.1016/j.ijfatigue.2020.105611.
[22] Han Q, Wang P, Lu Y. Low-cycle multiaxial fatigue behavior and life prediction of Q235B steel welded material. Int J Fatigue 2019;127:417–30. https://doi.org/10.1016/J.IJFATIGUE.2019.06.027.
[23] Sun J, Yuan H. Life assessment of multiaxial thermomechanical fatigue of a nickel-based superalloy Inconel 718. Int J Fatigue 2019;120:228–40. https://doi.org/10.1016/J.IJFATIGUE.2018.11.018.
[24] Castro FC, Mamiya EN, Malcher L, Canut FA, Ferreira GV, Neves RS. Multiaxial fatigue of quenched and tempered U2 steel: Testing and fatigue life prediction. Fatigue Fract Eng Mater Struct 2019. https://doi.org/10.1111/ffe.13047.
[25] Pejkowski Ł, Skibicki D. Stress-strain response and fatigue life of four metallic materials under asynchronous loadings: Experimental observations. Int J Fatigue 2019;128:105202. https://doi.org/10.1016/j.ijfatigue.2019.105202.
[26] Sharifimehr S, Fatemi A. On the interaction of normal and shear stresses in multiaxial fatigue damage. Fatigue Fract Eng Mater Struct 2019. https://doi.org/10.1111/ffe.13070.
[27] Sharifimehr S, Fatemi A. Fatigue analysis of ductile and brittle behaving steels under variable amplitude multiaxial loading. Fatigue Fract Eng Mater Struct 2019;42:1722–42. https://doi.org/10.1111/ffe.13014.
[28] Bonniot T, Doquet V, Hai MS. Fatigue crack growth under non-proportional mixed-mode I + II. Role of compression while shearing. Int J Fatigue 2020;134:105513. https://doi.org/10.1016/j.ijfatigue.2020.105513.
[29] Li Y, Yu D, Li B, Chen X. Martensitic transformation of an austenitic stainless steel under non-proportional cyclic loading. Int J Fatigue 2019;124:338–47. https://doi.org/10.1016/j.ijfatigue.2019.03.020.
[30] Ahmed YS, Fox-Rabinovich G, Paiva JM, Wagg T, Veldhuis SC. Effect of built-up edge formation during stable state of wear in AISI 304 stainless steel on machining performance and surface integrity of the machined part. Materials (Basel) 2017;10:1–15. https://doi.org/10.3390/ma10111230.
[31] Seid Ahmed Y, Arif AFM, Veldhuis SC. Application of the wavelet transform to acoustic emission signals for built-up edge monitoring in stainless steel machining. Meas J Int Meas Confed 2020;154:107478. https://doi.org/10.1016/j.measurement.2020.107478.
[32] Socie D, Marquis G. Multiaxial fatigue. Society of Automotive Engineers; 2000.
[33] Krupp U. Crack propagation: microstructural aspects. Fatigue crack propag. met. alloy. John Wiley & Sons, Ltd; 2007. p. 135–206. https://doi.org/10.1002/9783527610686.ch6.
[34] Kurath P, Socie DF. The relationship between observed fatigue damage and life estimation models. Urbana 1988.
[35] Kalnaus S, Jiang Y. Fatigue of AL6XN stainless steel. J Eng Mater Technol Trans ASME 2008;130:0310131–03101312. https://doi.org/10.1115/1.2931154.
[36] Basan R, Marohnić T. Multiaxial fatigue life calculation model for components in rolling-sliding line contact with application to gears. Fatigue Fract Eng Mater Struct 2019;42:1478–93. https://doi.org/10.1111/ffe.12997.
[37] Fatemi A, Molaei R, Phan N. Multiaxial fatigue of additive manufactured metals: Performance, analysis, and applications. Int J Fatigue 2020;134:105479. https://doi.org/10.1016/j.ijfatigue.2020.105479.
[38] Arora P, Gupta SK, Samal MK, Chattopadhyay J. Development of new critical plane model for assessment of fatigue life under multi-axial loading conditions. Int J Fatigue 2019;129:105209. https://doi.org/10.1016/j.ijfatigue.2019.105209.
[39] Karolczuk A, Skibicki D, Pejkowski Ł. Evaluation of the Fatemi-Socie damage parameter for the fatigue life calculation with application of the Chaboche plasticity model. Fatigue Fract Eng Mater Struct 2019;42:197–208. https://doi.org/10.1111/ffe.12895.
[40] Amjadi M, Fatemi A. Multiaxial fatigue behavior of thermoplastics including mean stress and notch effects: experiments and modeling. Int J Fatigue 2020;136:105571. https://doi.org/10.1016/j.ijfatigue.2020.105571.
[41] Fatemi A, Yang L. Cumulative fatigue damage and life prediction theories: a survey of the state of the art for homogeneous materials. Int J Fatigue 1998;20:9–34. https://doi.org/10.1016/S0142-1123(97)00081-9.
[42] Stephens RI, Fatemi A, Stephens RR, Fuchs HO. Metal fatigue in engineering. Wiley; 2000.
[43] Palmgren A. Die lebensdauer von kugellagern. Zeitschrift Des Vereins Dtsch Ingenieure 1924;68:339–41.
[44] Miner MA. Cumulative damage in fatigue. J Appl Mech 1945;12:A159–64. https://doi.org/10.1007/978-3-642-99854-6_35.
[45] Huber MT. Właściwa praca odkształcenia jako miara wytężenia materiału (in Polish). Czas Tech 1904;22:38–50.
[46] von Mises R. Mechanik der festen Körper im plastisch-deformablen Zustand [in German]. Math Klasse: Nachrichten von Der Gesellschaft Der Wissenschaften Zu Göttingen; 1913. p. 582–92.
[47] Zhong B, Wang Y, Wei D, Zhang K, Wang J. Multiaxial fatigue life prediction for powder metallurgy superalloy FGH96 based on stress gradient effect. Int J Fatigue 2018;109:26–36. https://doi.org/10.1016/J.IJFATIGUE.2017.12.006.
[48] Ogawa F, Itoh T, Yamamoto T. Evaluation of multiaxial low cycle fatigue cracks in Sn-8Zn-3Bi solder under non-proportional loading. Int J Fatigue 2018;110:215–24. https://doi.org/10.1016/j.ijfatigue.2018.01.021.
[49] Basquin OH. The exponential law of endurance tests. Proc Am Soc Test Mater 1910;10:625–30.
[50] Manson SS. Behavior of materials under conditions of thermal stress; 1954. doi: 10.1016/s0016-0032(38)90451-x.
[51] Coffin LFJ. A study of the effects of cyclic thermal stresses on a ductile metal. Schenectady (New York): Knolls Atomic Power Laboratory; 1953.
[52] Morrow JD. Fatigue properties of metals. Presented at a meeting of division 4 of the SAE iron and steel technical committee. 1964.
[53] Manson SS, Halford GR. Fatigue and durability of structural materials. ASM International; 2006.
[54] Fatemi A, Socie DF. A critical plane approach to multiaxial fatigue damage including out-of-phase loading. Fatigue Fract Eng Mater Struct 1988;11:149–65. https://doi.org/10.1111/j.1460-2695.1988.tb01169.x.
[55] McClaflin D, Fatemi A. Torsional deformation and fatigue of hardened steel including mean stress and stress gradient effects. Int J Fatigue 2004;26:773–84. https://doi.org/10.1016/j.ijfatigue.2003.10.019.
[56] Bannantine JA, Socie DF. A variable amplitude multiaxial fatigue life prediction method. Third int conf biaxial/multiaxial fatigue, Stuttgart. 1989. p. 12.1–20.
[57] Shamsaei N, Fatemi A, Socie DF. Multiaxial fatigue evaluation using discriminating strain paths. Int J Fatigue 2011;33:597–609. https://doi.org/10.1016/j.ijfatigue.2010.11.002.
[58] Gates NR, Fatemi A. Multiaxial variable amplitude fatigue life analysis using the critical plane approach, Part I: Un-notched specimen experiments and life estimations. Int J Fatigue 2017;105:283–95. https://doi.org/10.1016/J.IJFATIGUE.2017.09.008.
[59] Smith K, Topper TH, Watson P. A stress-strain function for the fatigue of metals. J Mater 1970;5:767–78.
[60] Socie DF. Multiaxial fatigue damage models. J Eng Mater Technol ASME 1987;109:293–8. https://doi.org/10.4028/www.scientific.net/KEM.324-325.747.
[61] Ince A, Glinka G. A generalized fatigue damage parameter for multiaxial fatigue life prediction under proportional and non-proportional loadings. Int J Fatigue 2014;62:34–41. https://doi.org/10.1016/j.ijfatigue.2013.10.007.
[62] Glinka G, Shen G, Plumtree A. A multiaxial fatigue strain energy density parameter related to the critical fracture plane. Fatigue Fract Eng Mater Struct 1995;18:37–46. https://doi.org/10.1111/j.1460-2695.1995.tb00140.x.
[63] Ellyin F, Gołoś K. Multiaxial fatigue damage criterion. J Eng Mater Technol 1988;110:63–8. https://doi.org/10.1016/B978-0-08-034912-1.50086-2.
[64] Ellyin F, Golos K, Xia Z. In-phase and out-of-phase multiaxial fatigue. J Eng Mater Technol 1991;113:112. https://doi.org/10.1177/089124168601500202.
[65] Ellyin F. Fatigue damage, crack growth and life prediction. Chapman & Hall; 1997. 10.1007/978-94-009-1509-1.
[66] Itoh T, Yang T. Material dependence of multiaxial low cycle fatigue lives under non-proportional loading. Int J Fatigue 2011;33:1025–31. https://doi.org/10.1016/j.ijfatigue.2010.12.001.
[67] Wu M, Itoh T, Shimizu Y, Nakamura H, Takanashi M. Low cycle fatigue life of Ti–6Al–4V alloy under non-proportional loading. Int J Fatigue 2012;44:14–20. https://doi.org/10.1016/j.ijfatigue.2012.06.006.
[68] Morishita T, Itoh T. Evaluation of multiaxial low cycle fatigue life for type 316L stainless steel notched specimen under non-proportional loading. Theor Appl Fract Mech 2016;84:98–105. https://doi.org/10.1016/j.tafmec.2016.02.007.
[69] Itoh T, Sakane M, Ohnami M, Socie DF. Nonproportional low-cycle fatigue criterion for type 304 stainless steel. J Eng Mater Technol ASME 1995;117:285–92. https://doi.org/10.1115/1.2804541.
[70] Mei J, Dong P. A new path-dependent fatigue damage model for non-proportional multi-axial loading. Int J Fatigue 2016;90:210–21. https://doi.org/10.1016/j.ijfatigue.2016.05.010.
[71] Arora P, Gupta SK, Samal MK, Chattopadhyay J. Validating generality of recently developed critical plane model for fatigue life assessments using multiaxial test database on seventeen different materials. Fatigue Fract Eng Mater Struct 2020. https://doi.org/10.1111/ffe.13169.
[72] Robak G, Tadeusz Ł. Variability of fatigue parameters under uniaxial loading in the function of the number of cycles to failure. Int J Fatigue 2018;113:246–52. https://doi.org/10.1016/j.ijfatigue.2018.04.003.
[73] Sun J, Yuan H, Vormwald M. Thermal gradient mechanical fatigue assessment of a nickel-based superalloy. Int J Fatigue 2020;135:105486. https://doi.org/10.1016/j.ijfatigue.2020.105486.

Short cracks observations on surfaces of specimens made of three materials, subjected to synchronous and asynchronous multiaxial loadings

Łukasz Pejkowski[1], *Jan* Seyda[1], and *Dariusz* Skibicki[1,1]

[1]UTP University of Science and Technology in Bydgoszcz, Kaliskiego 7, 85-796 Bydgoszcz, Poland

Abstract. In this paper analysis of short cracks observed on surfaces of specimens subjected to axial, torsional, synchronous in-phase and out-of-phase as well as a number of asynchronous loadings was performed. The tests were conducted on PA38-T6 aluminum alloy, E235 non-alloy steel and 1.4301 austenitic stainless steel thin-walled specimens, in strain-control mode. It was concluded that for PA38-T6 aluminum alloy and E235 steel, fatigue cracks initiated and propagated on the plane of maximum shear strain, regardless of the loading case. Fatigue cracks observed on the surface of 1.4301 steel specimens developed predominantly on the levels of maximum normal strain. For this material, the surface condition resulting from the machining had a significant impact on the cracks growth. In the case of non-proportional loadings, at high levels of strain, cracks often propagated along the machining marks.

1 Introduction

Short cracks are defined as measuring less than 1 mm in length [1, 2]. Their analysis is important because the process of initiation and growth of short cracks constitutes the majority of fatigue life of the specimens. The observations made during the research show that the occurrence of macro-cracks takes place in just the last few loading cycles. Moreover, Socie stated that based on the observation of the damage mechanism of a given material, the choice of the fatigue model should be made [3].

In this paper an analysis of short cracks observed on the surface of specimens made of PA38 aluminum alloy, E235 steel and 1.4301 steel has been performed. The subjects of the analysis were: a) determination of damage mechanism based on crack direction observation, and b) correlation of damage mechanism with multiaxial fatigue models, especially for the asynchronous loadings.

2 Materials and methods

1 Corresponding author: dariusz.skibicki@utp.edu.pl

69:10912673

Materials and experimental procedure were already described in detail in [4, 5]. Fatigue tests were performed on thin-walled cylindrical specimens in strain-controlled mode on an Instron 8874 axial-torsional closed-loop servo-hydraulic testing system. Specimens were made of PA38-T6 (AW 6060-T6) aluminum alloy, solution heat-treated and artificially aged, E235 (1.0308) non-alloy quality steel, normalized, and 1.4301 (X5CrNi18-10, 304) austenitic stainless steel, soft annealed.

In case of fully reversed sine-shaped loadings, which were applied in this study, the waveforms of controlled normal ε and shear γ strains can be written as:

$$\varepsilon(t) = \varepsilon_a \sin(2\pi f_\varepsilon t) \tag{1}$$

$$\gamma(t) = \gamma_a \sin\left(2\pi f_\gamma t + \delta\right) \tag{2}$$

where ε_a and γ_a are amplitudes, f_ε and f_γ are frequencies of normal and shear strain, respectively, and δ is a phase shift angle. The parameters of loadings applied in case of individual materials are listed in **Table 1**. First, four basic synchronous loadings were utilized: tension-compression (TC), torsion (TOR), in-phase loading (IP) and 90° out-of-phase loading. Then, a number of asynchronous loadings (ASN) with different parameters were applied.

Table 1. Parameters of loadings applied with regard to individual materials.

Loading case	λ	δ, degress	f_γ/f_ε	Material
TC	0	0	1	PA38-T6, E235, 1.4301
TOR	∞	0	1	PA38-T6, E235, 1.4301
IP	$\sqrt{3}$	0	1	PA38-T6, E235, 1.4301
OP	$\sqrt{3}$	90	1	PA38-T6, E235, 1.4301
ASN1	$\sqrt{3}$	0	0.5	PA38-T6, E235, 1.4301
ASN2a	$\sqrt{3}/2$	0	4	PA38-T6, E235, 1.4301
ASN3a	$2\sqrt{3}$	0	0.2	PA38-T6, 1.4301
ASN3b	$2\sqrt{3}$	0	0.25	E235
ASN4a	$\sqrt{3}/2$	0	2/3	E235
ASN4b	$3\sqrt{3}/5$	0	6	1.4301
ASN4c	$\sqrt{3}$	0	8	PA38-T6
ASN5	$\sqrt{3}$	0	0.7	PA38-T6, E235, 1.4301

In the present study short cracks observed on the surfaces of the specimens were analyzed. Observations were performed on failed specimens. Crack photos were taken on a metallographic optical microscope equipped with a digital camera. A scale and graphs showing the distribution of the maximum normal $\varepsilon_{max}(\varphi)$ and shear $\gamma_{max}(\varphi)$ strain on the plane, whose position in the polar coordinate system is given by the angle φ, were plotted on the photos [6]. The angle $\varphi = 0°$ corresponds to the position of the specimen axis. The images of fatigue cracks representative for a given type of load were presented.

3 Cracks observations

3.1 PA38-T6 aluminum alloy

Typical short cracks observed on the surfaces of specimens made of PA38-T6 aluminum alloy were presented in **Fig. 1** for all the applied loading cases.

For TC loading it can be observed that macrocrack occurs due to the coalescence of short cracks, oriented at approximately 45° and 135° angles. These directions coincide with the directions of maximum shear strain planes.

In the case of TOR loading, the observed cracks are located at an angle of 0° and 90°, which in this case corresponds to the location of maximum shear strain planes. Macrocracks were oriented along the specimen's axis, which is characteristic for torsional loading with a high level of strain, in the case of materials exhibiting a shear damage mechanism [1, 7].

In the case of IP loading, short fatigue cracks can be observed located at an angle of approximately 70° and 160°. These directions are consistent with the location of the maximum shear strain planes too.

Regarding the OP loading, short cracks occur in many directions, because high-value shear strains occur on all planes. However, cracks located at a 90° angle are much more developed. This plane is also subjected to the maximum normal strain causing the crack opening, which in turn results in a reduction of friction between the fracture surfaces. This phenomenon accelerates the development of fatigue cracks. Macrocracks are also formed from these cracks.

For asynchronous loadings only selected pictures of crack were presented in this study. In case of all ASN loading cases extreme values of shear strain occurs on four directions, located at 22º, 68º, 112º and 158º for ASN1, 30°, 60°, 120° and 150° for ASN2a, 78°, 168°, 11° and 101° for ASN3a, 20°, 70°, 110° and 160° for ASN4c and 20°, 70°, 110° and 160° for ASN5 loading. Short cracks usually occur in all of these directions, but in general, cracks are most developed at planes on which normal strains with a higher value also act.

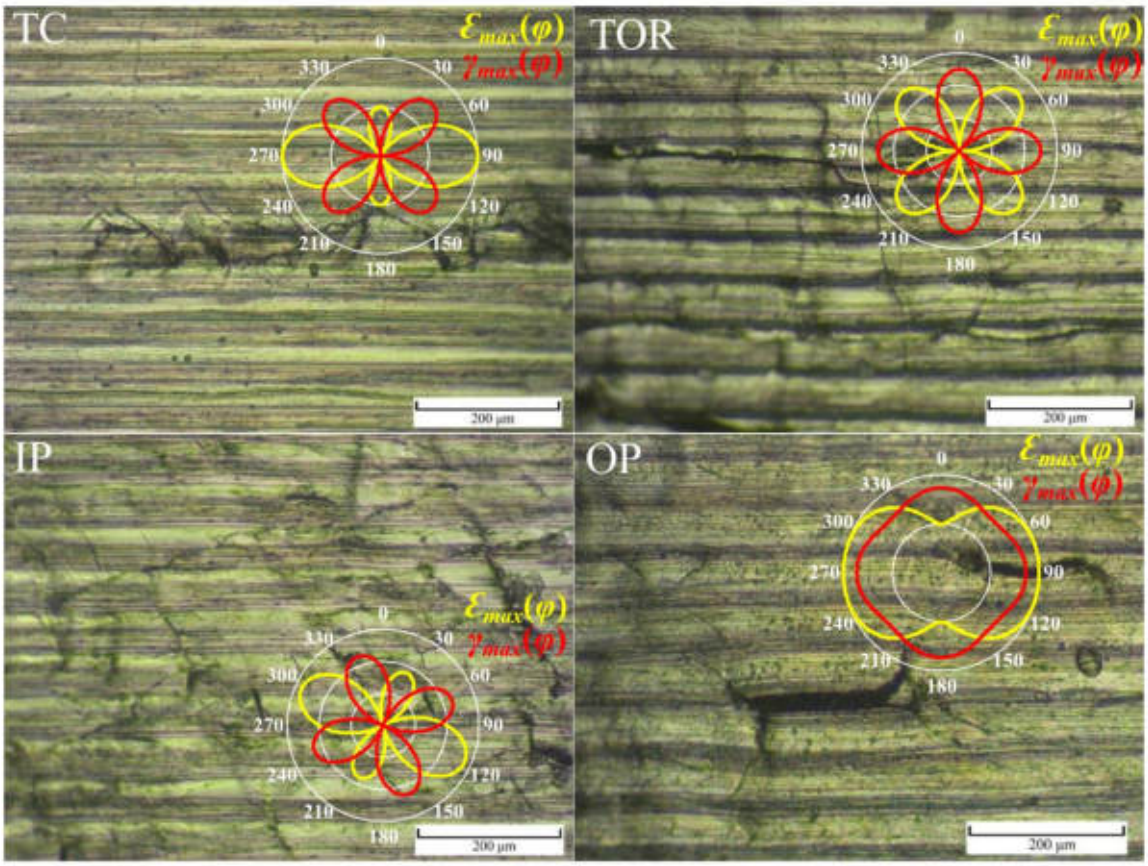

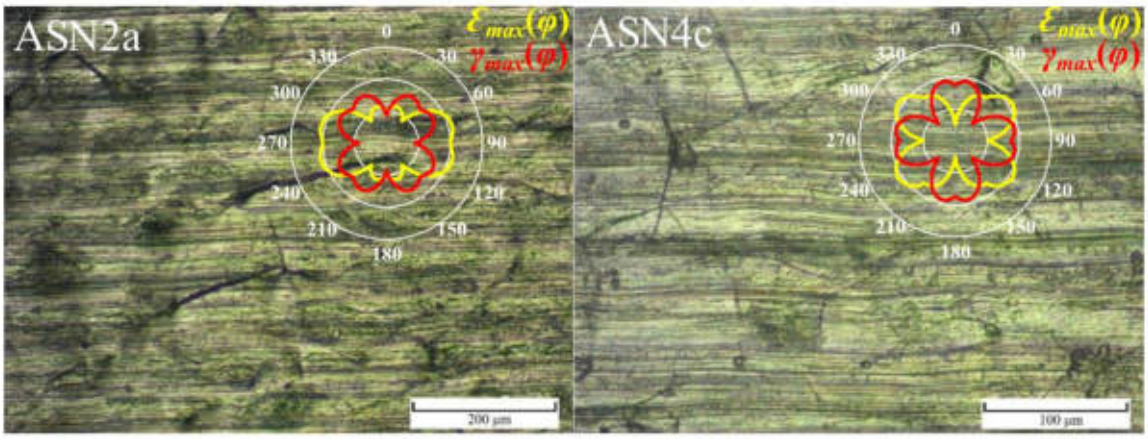

Fig. 1. Typical short cracks observed on the surfaces of PA38-T6 aluminum alloy specimens.

3.2 E235 steel

Pictures of fatigue cracks present on the surfaces taken in case of E235 steel specimens are presented in **Fig. 2**.

In the case of TC loading on the surfaces of the specimens, numerous fatigue cracks were observed at an angle of 45° and 135°. These are the directions of maximum shear strains.

Specimens subjected to TOR loading were characterized by cracks in the direction of 0° and 90°. For this loading case, these are directions of maximum shear strains.

In the case of IP loading, most cracks are located at an angle of 70°. In this direction, cracks of greater length also occur. In the direction of 160°, cracks can also be observed, but they are much shorter. Both of these directions coincide with the directions on which the maximum shear strains acts.

In the case of OP loading, fatigue cracks were oriented in the 90° direction. This is the plane on which both the maximum shear and maximum normal strains occur.

For asynchronous loadings, pictures for selected loading cases are presented. Maximum shear strain directions are: 22°, 68°, 112° and 158° for ASN1, 30°, 60°, 120° and 150° for ASN2a, 11°, 79°, 110° and 168° for ASN3b and 30°, 60°, 120° and 150° for ASN4a loading. Just like in the case of PA38-T6 aluminium alloy, cracks developed in directions of maximum shear strains. Those of them, for which normal strain was also high are more developed. It was noticed that depending on the location on the surface of the specimen, cracks in one direction were more developed than in others, but the distribution was random.

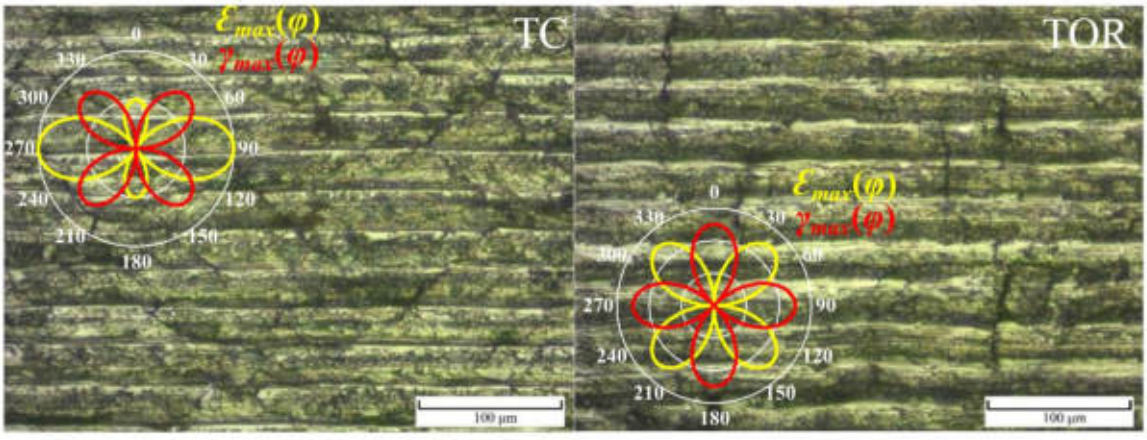

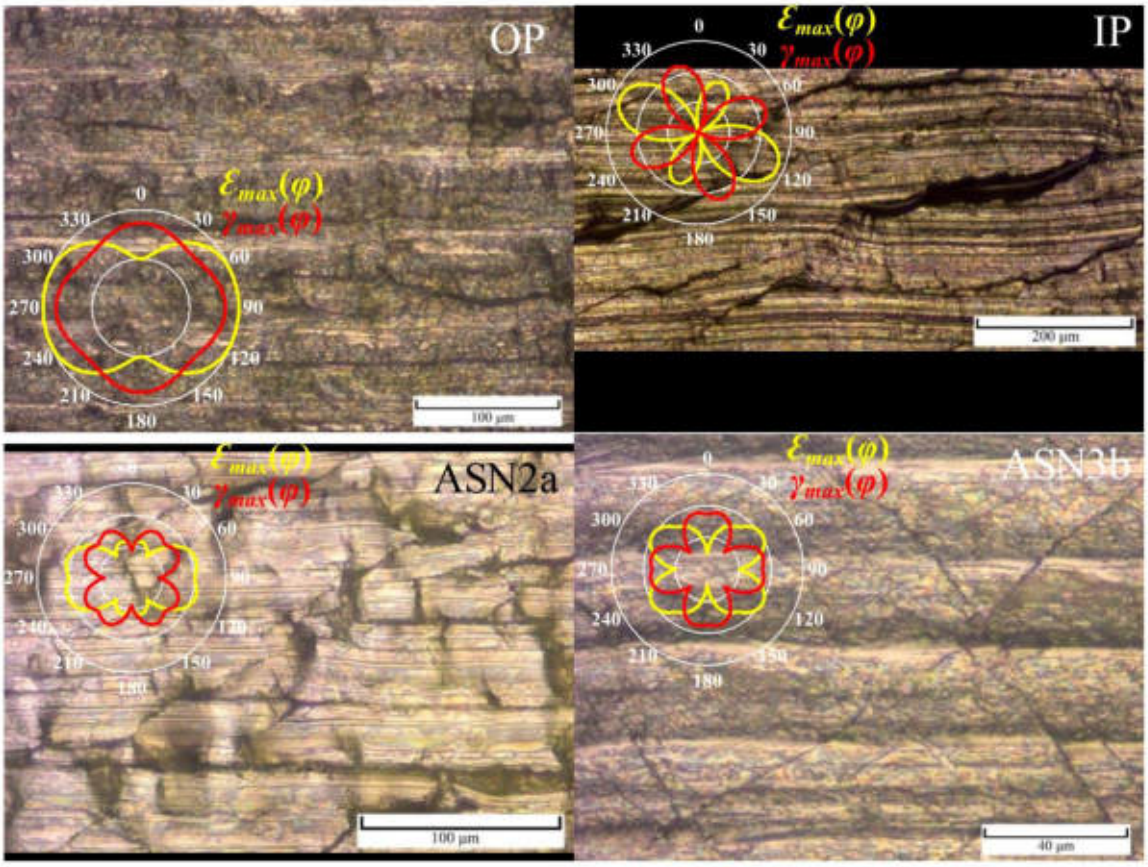

Fig. 2. Typical short cracks observed on the surfaces of E235 steel specimens.

3.3 1.4301 steel

Under TC loading two stages of cracks propagation can be noticed (**Fig. 3**). In the first stage, the crack developed at an angle of 45°, i.e. towards the maximum shear strain. Further development occurred towards the maximum normal strain. The fragment of the crack developed in this direction is longer.

In the case of loading the TOR, the crack also initiated and initially propagated in the direction of the maximum shear strain, followed by its branching and further propagation towards the maximum normal strain. Many cracks of this type have been observed on the entire surface. There are many such cracks at a low level of load, while at a higher load level, fewer cracks have been observed that have developed to larger sizes.

In the case of IP loading, fatigue cracks located at an angle of 70° and 160°, as well as 115°, can be seen. The first two angles correspond to the position of the plane of maximum shear strains, while the angle of 115° corresponds to the plane of the maximum normal strain.

Under the OP loading, the positions of the plane of the maximum shear and normal strain are the same. This is a plane at 90º. Fatigue cracks observed for this loading case always developed at the bottom of the machining marks, which is also located at an angle of 90 °. Macro crack occurred in this direction due to the merging of short cracks formed in the bottom of the same machining mark.

For ASN1 loading, the longest fragments of fatigue cracks are located in the bottom of the machining marks, as in the case of OP loading, although there are no strain extremes in this direction. In some cases, under a low loading level, very short fragments of cracks were also observed, the direction of which coincides with the direction of maximum shear strains. Presumably, the fatigue crack was initiated and initially propagated towards the maximum

shear strain direction, similar to the previously discussed loadings, after which further propagation took place in the bottom of the trace machining marks.

Very similar behaviour of fatigue cracks was noted for all other cases of asynchronous loadings. For ASN2a loading cracks also propagated mainly along the machining marks, although at a low level of strain, fragments were also observed whose direction is consistent with the location of the maximum shear strain planes. Very short cracks can also be found on the surface of the samples, the direction of which is consistent with the direction of the maximum shear strain.

In the case of ASN3a and ASN4b loadings, for a high loading level, cracks were observed, which propagated in the direction perpendicular to the axis of the specimen, along with the machining marks. These cracks then merged to form macrocracks. For low loading levels, very short cracks can be noticed, the direction of which is generally consistent with the location of the maximum normal strain planes.

Similarly, on the surface of specimens subjected to ASN5 loading, cracks propagated along the machining marks for high loading levels. In the case of lower levels of loading, short cracks developed towards the extremes of normal and shear strains are noticeable, which in this case are the same. Most often, slightly more developed cracks were observed for the direction on which normal strains a higher value.

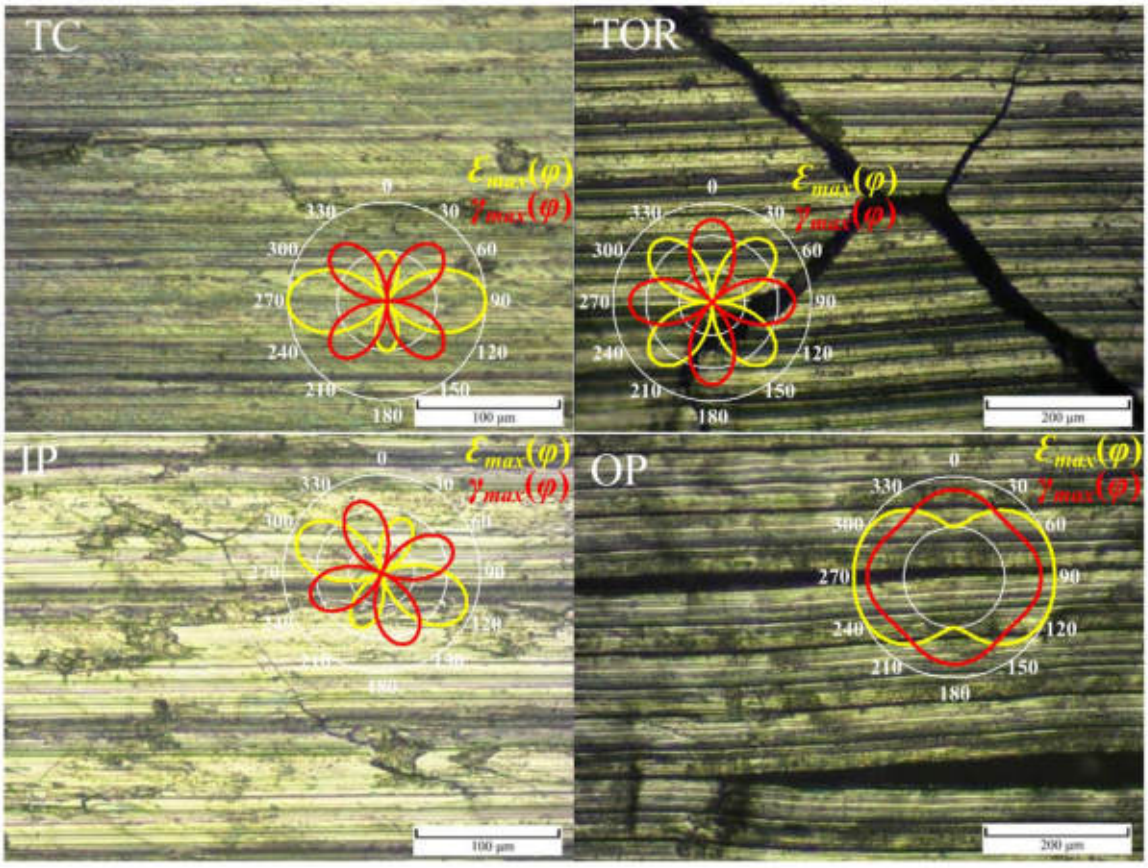

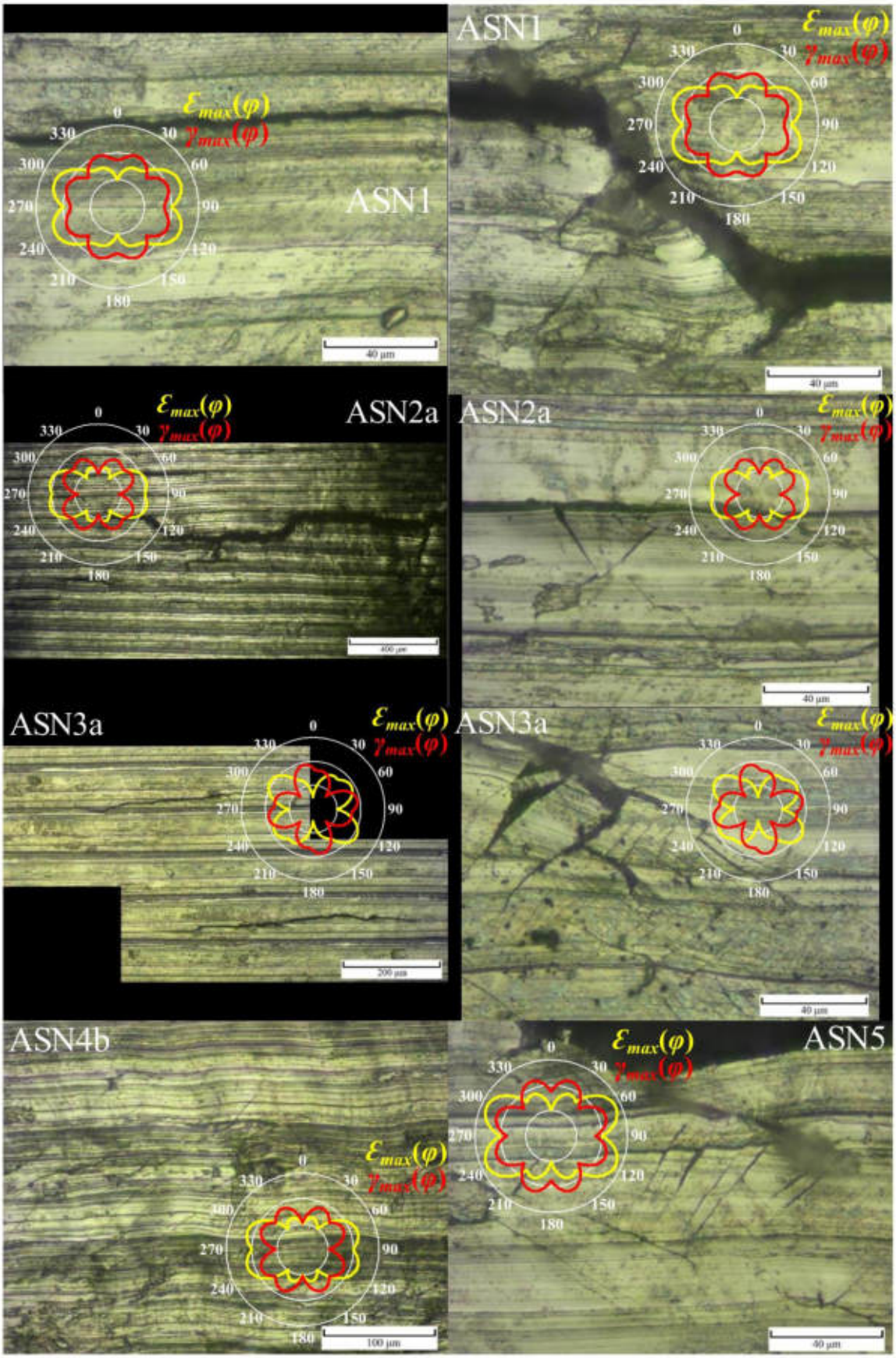

Fig. 3. Typical short cracks observed on the surfaces of 1.4301 steel specimens.

4 Discussion and conclusions

In the case of PA38-T6 aluminum alloy and E235 steel, fatigue cracks initiated and propagated on the plane of maximum shear strain, regardless of the loading case. If the maximum or near-maximum values of the shear occurred on many planes, short cracks can be observed in all of these directions. However, cracks are more developed on planes for which also large positive values of normal strain occurred, causing crack opening.

Fatigue cracks observed on the surface of 1.4301 steel specimens developed predominantly on the levels of maximum normal strain (planes of principal strains). For some cases and loading levels, very short parts of cracks can be observed, the direction of which is consistent with the direction of the plane of maximum shear strain. However, these cracks branched towards the maximum normal strain after reaching a certain length. For this material, the surface condition resulting from the machining had a significant impact on the cracks growth. In the case of non-proportional loadings, at high levels of strain, cracks often propagated along the machining marks. Potential reasons for this behavior include the stresses concentration in the machining marks roots and the martensitic transformation taking place at these points. It was also observed that in case of asynchronous loadings, fatigue cracks were often initiated in the vicinity of inclusions visible on the surface of the material. These inclusions probably occurred due to the formation of a built-up edge on the cutting tool.

Taking into account the above observations, it could be assumed that for the first two materials the more accurate should be the models based on the maximum shear strain plane, like Brown-Miller, Fatemi-Socie or Glinka-Wang-Plumtree, whereas in case of 1.4301 steel, the maximum normal strain-based models, e.g. SWT, is expected to give better results.

References

1. Socie, D., Marquis, G.: Multiaxial Fatigue. SAE International, United States (2000).
2. Shamsaei, N., Fatemi, A.: Small fatigue crack growth under multiaxial stresses. Int. J. Fatigue. 58, 126–135 (2014).
3. Socie, D.: Critical plane approaches for multiaxial fatigue damage assessment. ASTM Spec. Tech. Publ. 1191, 7–36 (1993).
4. Skibicki, D., Pejkowski, Ł.: The relationship between additional non-proportional hardening coefficient and fatigue life. Int. J. Fatigue. 123, 66–78 (2019).
5. Pejkowski, Ł., Skibicki, D.: Fatigue behavior of selected materials under multiaxial asynchronous loadings. In: The 12th International Conference on Multiaxial Fatigue and Fracture. , Bordeaux (2019).
6. Albinmousa, J.: Investigation on multiaxial fatigue crack path using polar stress–strain representation. Int. J. Fatigue. 92, 406–414 (2016).
7. Kurath, P., Socie, D.F.: The Relationship Between Observed Fatigue Damage and Life Estimation Models. , Urbana (1988).

materials

MDPI

Article

The Shear Stress Determination in Tubular Specimens under Torsion in the Elastic–Plastic Strain Range from the Perspective of Fatigue Analysis

Jan Seyda, Łukasz Pejkowski * and Dariusz Skibicki

Faculty of Mechanical Engineering, University of Science and Technology in Bydgoszcz, Kaliskiego 7, 85-796 Bydgoszcz, Poland; jan.seyda@utp.edu.pl (J.S.); dariusz.skibicki@utp.edu.pl (D.S.)

* Correspondence: lukasz.pejkowski@utp.edu.pl

Received: 5 November 2020; Accepted: 3 December 2020; Published: 7 December 2020

Abstract: The comparison of shear stress determination methods in tubular specimens under torsion is presented in this paper. Four methods were analyzed: purely elastic solutions, purely plastic solutions, the midsection approach, and the Chaboche nonlinear kinematic hardening model. Using experimental data from self-designed and conducted fatigue experiments, an interesting insight on this problem was obtained that is not often tackled in the literature. It was shown that there are differences in determined shear stress values, and their level depends on a few factors. The midsection approach and purely plastic solution gave values of surface shear stress very close to the values obtained using the Chaboche nonlinear kinematic hardening model for high strain levels. The purely elastic solution gave proper results for the low strain ranges, close to the cyclic yield limit. Since none of the methods can be trusted in the full range of loading, an important conclusion from these analyses regards the formulated ranges of their applicability. It was also shown that the calculated values of shear stress and plastic and elastic strain energy density determined on this basis have a strong impact on fatigue life predictions. Finally, the influence of predicted values of shear stresses on the interpretation of cyclic hardening phenomena was also presented.

Keywords: cyclic torsion; shear stress; tubular specimens; elastic–plastic torsion

1. Introduction

Usually, fatigue cracks originate on a free surface due to the stress concentration on a micro and macro scale. Given polycrystalline materials, plastic deformation is also higher on a surface as a result of lower constraints from neighboring grains [1]. In the case of elements that are loaded with bending moment or torque, stresses are additionally higher on a surface due to their gradient [2,3]. These types of loading are often studied [4,5], also in an elastic–plastic strain range [6,7]. Considering this, it is clear that the proper analysis of stress and strain on the surface of elements undergoing fatigue loading is an important issue. On the other hand, a compromise between the accuracy and simplicity of the solution is usually desired.

In the present study, the focus is placed on the analysis of shear stress in thin-walled tubular specimens, which are most often used in strain-controlled multiaxial fatigue tests [8,9]. The problem of elastic–plastic torsion has already been studied by other authors. Usually, some advanced mathematical models are made regarding this issue, together with proposals of numerical solutions devoted to the determination of the twist angle or accumulated energy [10–16]. Other papers concern an application of the Finite Elements Method or the Finite Differences Method to model the torsion of different profiles [17–19]. Sometimes, the topic of the study is very narrow, e.g., it concerns only a selected issue related to the yield point, which the authors term the "small corrugations of the elastic–plastic

boundary" [20]. Unfortunately, quite often such works do not provide practical solutions and explanations on how to correctly determine the surface shear stress for tubular specimens subjected to cyclic torsion, based on experimental data like torque and shear strain on the surface of the specimen. If any cyclic plasticity models are involved, they assume perfectly elastic or perfectly plastic material behavior. More practical considerations regarding the cyclic torsion of cylindrical specimens have previously been performed by Miller and Chandler [21] and Brown [22].

In fatigue analysis, authors use various approaches to solve the problem of shear stress determination in tubular specimens under torsion. Shamsaei and Fatemi [23] used midsection shear stress values, which were further fitted with a Ramberg–Osgood-type function and extrapolated on the surface. However, this method can be used only for materials that exhibit Masing behavior (the upper branches of hysteresis loops form one common curve) and do not show significant differences in stress history depending on the loading level. Furthermore, the fit and extrapolation procedure must be separately repeated for each loading case. The midsection approach was also used by Socie [24], Zhong et al. [25], Wu et al. [26], Zhang and Jiang [27,28], and in other works by Fatemi and coauthors [29,30]. Dey et al. used an elastic solution, even though they applied relatively high strain values [31]. There are also several papers where the shear stress determination method was not mentioned [32–35].

In the present paper, three different approaches based on the measured value of torque were applied to determine shear stress in tubular specimens made of PA38-T6 (AW-6060) aluminum alloy subjected to torsion. They were further compared to values calculated using the Chaboche kinematic hardening model. This thorough approach to the problem makes it possible to become aware of differences in shear stress values obtained using various methods and to find their dependence on factors such as specimen size and loading level. The results of this work also give an idea of the order of magnitude of these differences, the impact on the interpretation of cyclic hardening, and on the prediction of fatigue life. Considering these factors, the guidance was provided according to the applicability of these methods. Furthermore, it is worth noting that all analyses were conducted based on a self-designed and conducted experiment. The adopted research methodology of the experiment assumed continuous recording of all signals from the testing system with a high sampling frequency. This enabled accurate calculations and detailed analyses.

2. Theoretical Background

2.1. Shear Stress Distribution under Elastic–Plastic Torsion

Nonuniform shear stress distribution occurs in every specimen subjected to torsion if the stress is higher than the yield limit [19]. Such distributions make it dubious to apply simple elastic solutions for accurate determination of shear stress since they assume a linear relationship between stress and strain. Furthermore, several other phenomena influence the shear stress value on the surface of the specimen. For example, the torque can be high enough to induce yielding of the outer layers of the material, but at the same time small enough to remain elastic at internal layers [12]. The boundary between elastic and elastic–plastic deformation also moves along the radius during the cyclic loading and unloading processes [21]. The torque, which is a measured quantity, depends on the stresses acting in the whole cross-section of the specimen; thus, the stress–strain and torque–twist angle relationship differ (Figure 1). These relationships become even more complicated when considering cyclic loadings [36]. When twisting right (conventionally) and subsequent unloading, the stress in the outer layer is not yet zero, while the stress in the internal layer exceeds zero, so it is already compressed (stressed left) [18] (Figure 2). Therefore, when the torque being measured equals zero, the value of shear stress in the external layer differs from zero (points 3 and 7). This influences the shape of the hysteresis loop and the calculated plastic strain energy density. If the material hardens or softens cyclically, the amount of hardening/softening depending on strain level varies for different layers (in the radial direction) of the specimen. This hardening or softening is difficult to consider during the

analysis of data that is only recorded from the testing system. All the abovementioned phenomena depend further on the level of loading, on internal and external diameters of the specimen, and on the specimen's thickness.

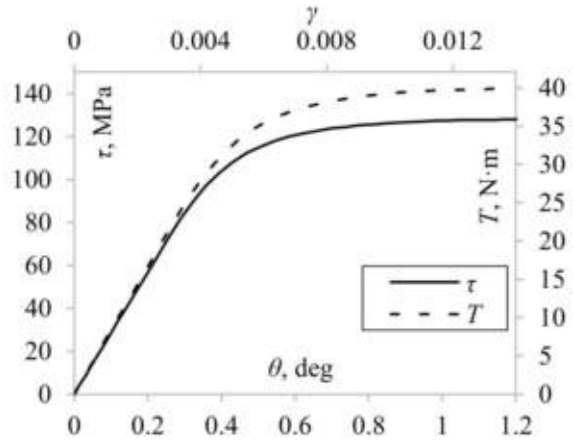

Figure 1. An example of shear-stress–shear-strain (τ-γ) and torque–twist angle (T-θ) curves.

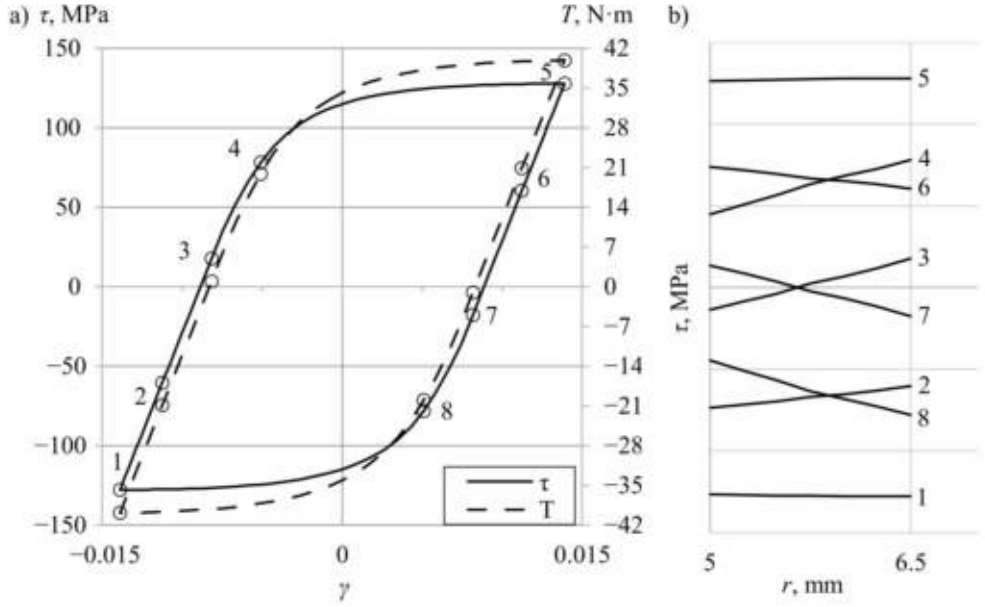

Figure 2. An example of (**a**) shear-stress–shear-strain (τ-γ) and torque–shear-strain (T-τ) hysteresis loops and (**b**) shear stress distribution through the wall thickness for 8 selected points.

2.2. Selected Methods of the Shear Stress Determination in Case of Tubular Specimens

The first of the considered approaches for determining shear stress in tubular specimens is based on a purely elastic solution. The relationship between torque T and shear stress τ is given by [37]

$$T = \int_A \tau(r) r dA = 2\pi \int_r \tau(r) r dr = 2\pi \int_{r_i}^{r_o} \tau(r) \cdot r^2 dr, \quad (1)$$

where r_i and r_o are internal and outer radii of the specimen, respectively. By the assumption that the shear stress is a linear function of radius, $\tau(r) = ar$, where a is the slope of function, after integration and substitution of a by τ_o, we get

$$T = \frac{\pi \tau_o (r_o^4 - r_i^4)}{2}. \quad (2)$$

The shear stress on the surface is then given by

$$\tau_o = \frac{T}{J_0} r_o = \frac{2 r_o T}{\pi (r_o^4 - r_i^4)}, \tag{3}$$

where J_0 is the polar moment of inertia. The resulting distribution of shear stress along the radial direction is presented in Figure 3a.

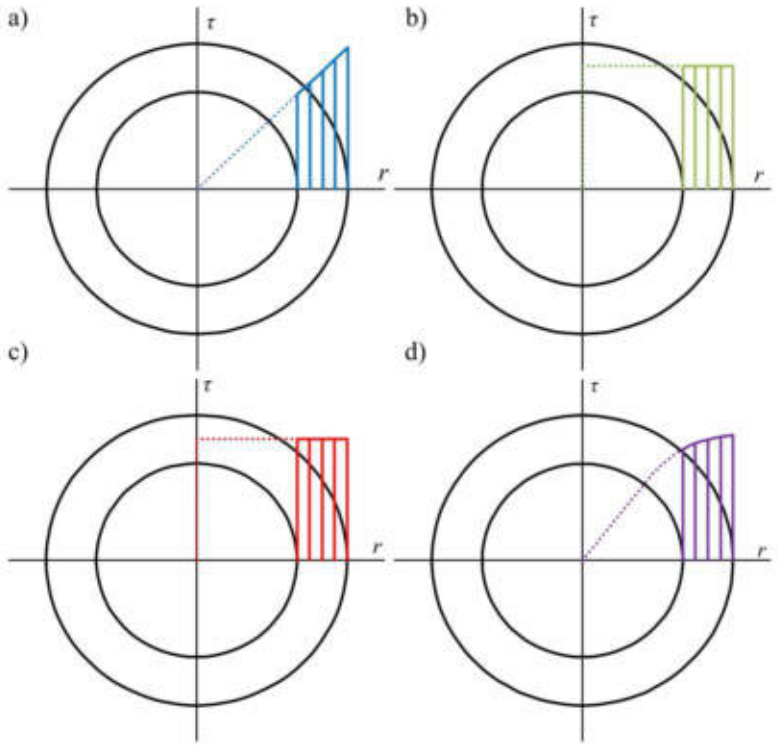

Figure 3. Shear stress distribution along the radius of a tubular specimen for (**a**) elastic solution, (**b**) midsection approach, (**c**) plastic solution, and (**d**) Chaboche model.

The second method is recommended by the ASTM standard [57] for the low-cycle fatigue regime. It is assumed that the shear stress distribution is uniform through the wall thickness (Figure 3b) and is equal to the midsection value τ_m. The torque is given by the following simplified Equation (1):

$$T = \tau_m r_m A, \tag{4}$$

and τ_m by

$$\tau_m = \frac{T}{A r_m} = \frac{16T}{\pi (d_o^2 - d_i^2)(d_o + d_i)}, \tag{5}$$

where r_m is the mean radius. The standard also specifies the criterion for a thin wall, for which the shear stress variation in the radial direction is negligible. Specimens that do not meet the criterion of a thin wall are examined in the work of Brown [22].

The next approach is based on a purely plastic solution. The assumption is the same as in the case of the midsection method (Figure 3c), and the relationship between shear stress and the radius of the specimen is given by

$$\tau(r) = \text{const.} \tag{6}$$

After substituting (6) into (1) and integration, the following formula is obtained:

$$T = \frac{2}{3} \pi \tau (r_o^3 - r_i^3), \tag{7}$$

and after conversion, the shear stress on the surface is then given by

$$\tau_o = \frac{3T}{2\pi(r_o^3 - r_i^3)}. \tag{8}$$

The shear stress distributions and values obtained by the previously presented approaches were compared to the values calculated using the Chaboche nonlinear kinematic hardening model [38,39]. The set of applied equations is listed below. The yield surface according to Huber–Mises yield criterion describes the formula:

$$f = \sqrt{\frac{3}{2}(s-\alpha) : (s-\alpha)} - R, \tag{9}$$

where s is a deviatoric stress tensor, R is cyclic yield stress, and α is a backstress tensor given by

$$d\alpha = \sum_{i=1}^{m} \frac{2}{3} C^{(i)} d\varepsilon^p - \gamma^{(i)} \alpha^{(i)} dp, \tag{10}$$

where $C^{(i)}$ and $\gamma^{(i)}$ (not to be confused with the shear strain) are material parameters and $d\varepsilon^p$ is a plastic strain tensor rate, given by the associated plastic flow rule:

$$d\varepsilon^p = \frac{3}{2} \frac{ds : n}{H} n, \tag{11}$$

where n is an outward unit tensor determining the direction normal to the yield surface:

$$n = \frac{\frac{\partial f}{\partial s}}{\sqrt{\frac{\partial f}{\partial s} : \frac{\partial f}{\partial s}}}. \tag{12}$$

H is a plastic hardening modulus and dp is the accumulated equivalent plastic strain rate:

$$dp = \sqrt{\frac{2}{3} d\varepsilon^p : d\varepsilon^p}. \tag{13}$$

The value of H can be determined from the yield surface consistency condition:

$$\frac{\partial f}{\partial s} : ds + \frac{\partial f}{\partial \alpha} : d\alpha = 0. \tag{14}$$

Using the Chaboche model, a nonlinear distribution of the shear stress along the specimen's radius is achieved (Figure 3d).

2.3. Influence of Shear Stress on Fatigue Life Prediction

For fatigue of materials, the ability to determine the correct shear stress value is crucial. The most popular multiaxial fatigue damage parameters, like Fatemi–Socie [40], generalized Smith–Watson–Topper [24,41], Łagoda–Macha [42], Ince–Glinka [43], or Garud [44], depend directly or indirectly on the determined value of this stress. Such a fatigue damage parameter is proposed by Gołoś and Ellyin [45,46]:

$$\frac{\Delta W^p}{\rho} + \Delta W^{e+}, \tag{15}$$

where ΔW^p and ΔW^{e+} are total plastic and positive elastic strain energy densities and ρ is a multiaxiality coefficient given by

$$\rho = (1 + \nu_{eq}) \frac{\varepsilon_1}{\gamma_{max}}, \tag{16}$$

where ν_{eq} is an equivalent Poisson ratio, ε_1 is maximum principal strain, and γ_{max} is the maximum shear strain. The Gołoś–Ellyin parameter was further employed in the present work to analyze the influence of the shear stress value on fatigue life prediction in an energy-based approach.

3. Materials and Methods

The experimental data used in this work comes from a broader research program [47,48]. The present work considers previous research regarding the cyclic torsion and axial loading of tubular specimens made of PA38-T6 (AW-6060) aluminum alloy. The chemical composition of this material is given in Table 1. Basic mechanical properties, Young's modulus E, 0.2% offset yield stress σ_{y02}, ultimate tensile strength σ_u and corresponding strain ε_{σ_u}, elastic Poisson ratio ν_e, cyclic strength coefficient K', and cyclic strain hardening exponent n' are given in Table 2. The dimensions of the specimens are presented in Figure 4. All fatigue tests were performed on an Instron 8874 servohydraulic axial/torsional testing system. Axial and shear strains were measured and controlled using an Epsilon 3550 biaxial extensometer, and the axial force and torque were measured by the system's load cell. For further details of the experiment, the reader is referred to [47,48].

Table 1. Chemical composition of PA38-T6 aluminum alloy according to EN 573-3 standard.

Element	Si	Fe	Cu	Mn	Mg	Cr	Zn	Ti	Other	Al
Share (%)	0.3–0.6	0.1–0.3	0.1	0.1	0.35–0.6	0.05	0.15	0.1	0.15	Balance

Table 2. Basic mechanical properties of PA38-T6 aluminum alloy determined experimentally.

E, GPa	σ_{y02}, MPa	σ_u, MPa	ε_{σ_u}, mm/mm	ν_e, -	K', MPa	n', -
68.3	191.5	229.1	0.094	0.35	288.1	0.051

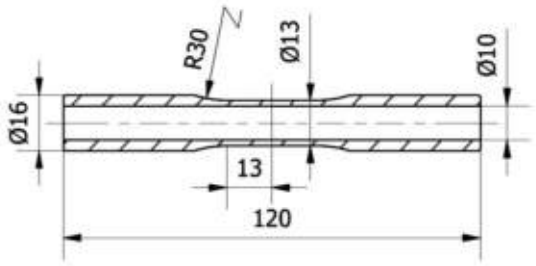

Figure 4. Dimensions of PA38-T6 specimens, given in millimeters.

The values of the Chaboche model material parameters were determined by using the Interior-Point optimization algorithm to find the best fit of the plastic strain–stress curve for the experimental data recorded for axial loading at midlife [49]. The value of $m = 3$ decomposition parts of the backstress tensor was found to be optimal. Determined material parameters are given in Table 3. All the calculations were further performed analytically, using own-developed Matlab code, employing the tensor algebra. The strain tensor was used as a controlled quantity and the stress tensor increments were determined for the corresponding strain tensor increments.

The results of the cyclic stress–strain response calculations for fully reversed axial straining are shown in Figure 5. The Chaboche model with correctly determined parameters resulted in accurate modeling of the stress response for several strain amplitudes.

Table 3. Chaboche model material parameters determined for PA38-T6 aluminum alloy.

C^1, MPa	C^2, MPa	C^3, MPa	γ^1, -	γ^2, -	γ^3, -	R, MPa
1.3723×10^5	5.3704×10^4	1.6667×10^4	7.8078×10^3	1.9759×10^3	459.3	141.1

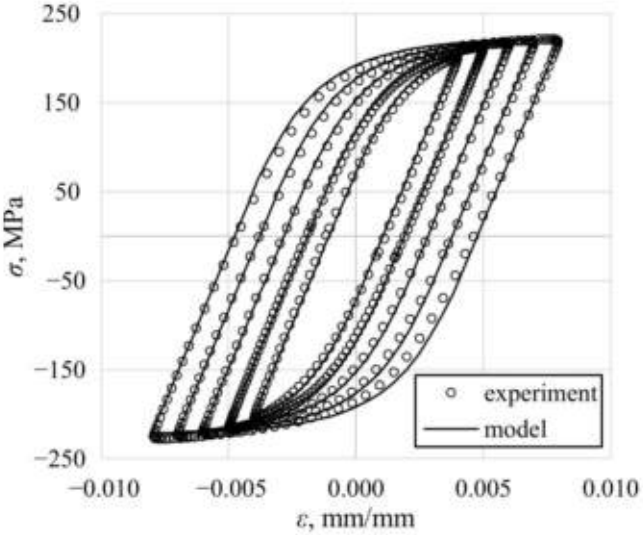

Figure 5. A comparison of experimental and calculated cyclic midlife axial stress–strain response of PA38-T6 aluminum alloy.

4. Results

4.1. Shear Stress Distribution Comparison

The shear stress distributions along the radial direction, according to the different shear strain levels determined by the aforementioned approaches, are shown in Figure 6. For this purpose, twice the theoretical thickness of the real specimen (Figure 4) was assumed to best show the differences in shear stress distribution. In the first step, the shear stress distribution for a given shear strain level on the surface was calculated using the Chaboche model. Based on this distribution, the torque was calculated using Equation (1), and then the shear stress distribution was determined using other approaches for the same torque value. This procedure was applied since, in the case of the Chaboche model, the shear stress value is calculated based on the shear strain. With other methods, the shear stress value is determined based on torque. It should be noted that the most important quantity is the shear stress on the specimen's surface. In reality, it falls between the values resulting from purely elastic and purely plastic solutions.

Based on the similarity between experimental values of stress under axial loading and values calculated using the Chaboche model (Figure 5), it was assumed that when torsion occurs, the shear stress determined using the Chaboche model is closer to the actual values than when it is obtained using other selected approaches. It was then concluded that for high levels of plastic strain, the midsection approach and the purely plastic solution reflect the real values of the shear stress quite well (Figure 6a,b). However, as the strain level decreases and approaches the purely elastic state of deformation, the elastic solution gives better results (Figure 6c,d). Generally, the elastic solution overestimates shear stress with higher strain levels. On the contrary, the midsection approach and the purely plastic solution underestimate shear stress. The underestimation is very small for high levels of strain (Figure 6a,b), while it is higher for small strain levels (Figure 6c,d).

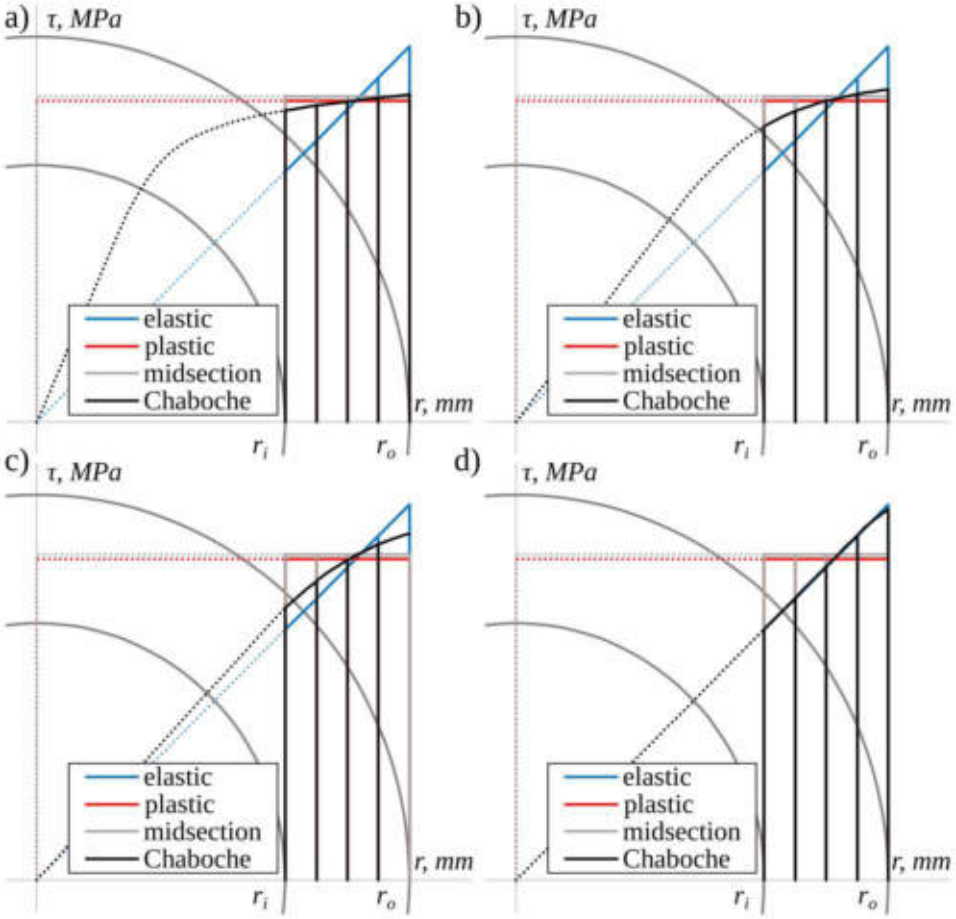

Figure 6. A comparison of the shear stress distribution for the specimen's theoretical, oversized thickness for (**a**) $\gamma = 0.0139$, (**b**) $\gamma = 0.0069$, (**c**) $\gamma = 0.0052$, (**d**) $\gamma = 0.0035$.

4.2. Application of the Selected Methods to Experimental Data Analysis

In Figure 7, experimental fatigue life was presented against applied shear strain amplitudes. Results were fitted with a power curve. Shear stress was calculated using the midsection method for the purpose of the presentation only. For four selected levels of strain, midlife hysteresis loops were presented to show the plastic-to-total strain ratio with respect to loading level. The applied loading ranges resulted in various stress–strain responses, from almost perfectly elastic to having a high share of plastic strain.

Figure 8 presents the shear stress distribution along the specimen radius obtained using the selected methods for different shear strain levels. The difference compared to the data shown in Figure 6 is that in the case of elastic, plastic, and midsection solutions, the shear stress was calculated directly from the torque measured during the fatigue tests using a load cell. The actual specimens' diameters were considered as well. Using the Chaboche model, the shear stress was calculated based on the measured shear strain, regardless of the real torque value. It can be seen that for the highest level of loading, i.e., $\gamma = 0.0139$ (Figure 8a), the surface shear stress determined from torque using the midsection and a perfectly plastic solution was very close to the surface shear stress calculated using the plasticity model. The elastic solution gave higher values. The same observation was made for other relatively high levels of loading, namely, $\gamma = 0.0121, 0.0104$, and 0.0087 (black dots in Figure 7). A noticeable discrepancy between the results obtained from the plasticity model, midsection and the plastic solution began from $\gamma = 0.0069$ (Figure 8b). For that level of shear strain amplitude, the surface shear stresses determined using the Chaboche model were higher than those calculated using the midsection and plastic methods. Similarly, so was the stress obtained from using the elastic solution. In the case of $\gamma = 0.0052$, the surface shear stress calculated from the plasticity model, midsection,

and plastic solution was nearly the same (Figure 8c). However, the whole shear stress distribution curve based on the Chaboche model is below the midsection and plastic solution. Again, the elastic approach gave higher values. For the lowest examined level of loading ($\gamma = 0.0035$), the surface shear stress from the midsection and purely plastic solution is considerably higher than the stress calculated by the Chaboche model (Figure 8d).

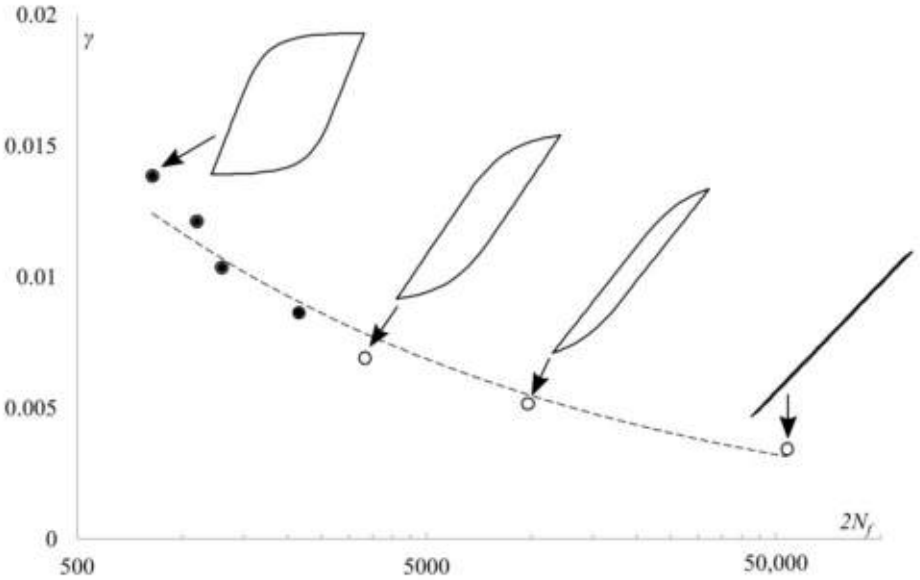

Figure 7. Shear strain amplitudes vs. fatigue life given in reversals for fully reversed torsion of PA38-T6 tubular specimens with midlife hysteresis loops presenting plastic strain level for selected levels of total strain.

In general, it is worth noting that if the shear stress distribution curve resulting from the application of the Chaboche model lies above the midsection and plastic values (Figure 8a,b), the experimental torque value was lower than expected from the plasticity model and vice versa. The purely elastic approach always resulted in surface shear stress higher than stress obtained using other applied methods, which seems to be obvious. Although the PA38-T6 aluminum alloy was found to be isotropic, quite cyclically stable, and to follow the Masing behavior, the application of the plasticity model did not offer a significantly better solution than other, much simpler methods. Stress evolution during the experiments can be given here as an explanation.

In Figure 9, the Huber–Mises midsection equivalent stress histories are presented. Stresses from the beginning of the test to midlife were more stable for high strain amplitudes. The least stability can be seen in the loading levels that result in stress values close to the cyclic yield stress (the curves with black dots). The consequence of this instability is differences in midlife stress values for low levels of loading, as shown in Figure 10 (black hysteresis loops). Similar behavior was also found by other authors [50,51]. A much more sophisticated and complicated cyclic plasticity model would have to be used to describe this phenomenon, which would make its application less practical.

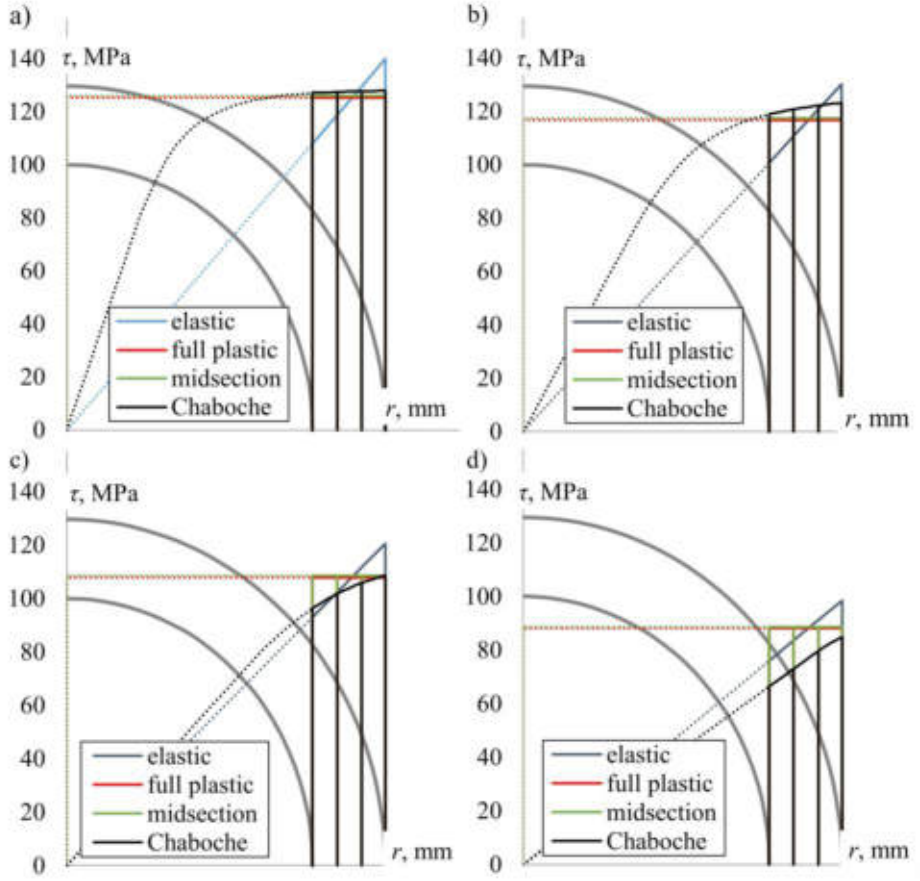

Figure 8. A comparison of the shear stress distribution obtained using selected methods for (**a**) $\gamma = 0.0139$, (**b**) $\gamma = 0.0069$, (**c**) $\gamma = 0.0052$, (**d**) $\gamma = 0.0035$.

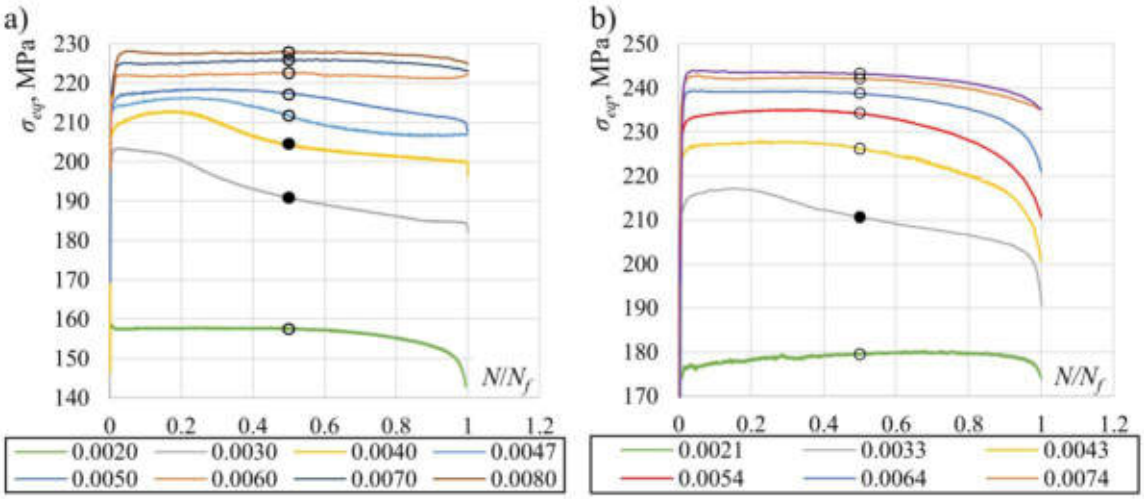

Figure 9. Huber–Mises-equivalent stress histories for (**a**) axial and (**b**) torsional loading, calculated for midsection values; circles indicate midlife values.

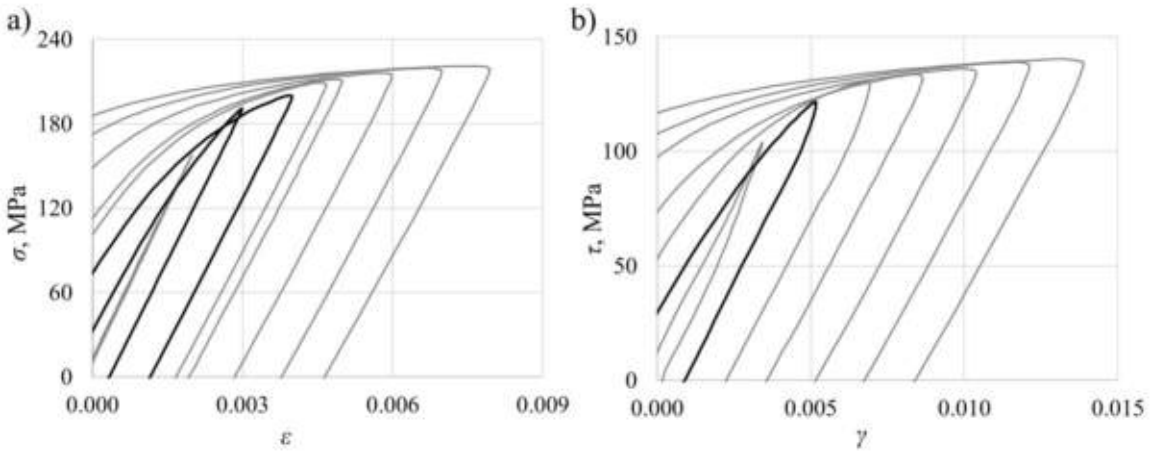

Figure 10. Right-upper quarters of hysteresis loops for (**a**) axial and (**b**) torsional loading; for torsion, the midsection stresses are presented.

Two quantities often used in fatigue analysis were further evaluated and compared, based on selected approaches to shear stress determination. The first was the maximum surface shear stress. The best-fit power-law shear-stress–fatigue life curves are presented in Figure 11. The curves for the midsection approach and perfectly plastic solution are almost identical. The data points for the Chaboche model are also very close, except for the lowest level of loading. In the case of an elastic solution, the curve is located significantly above the others. If only stress values are considered, about a 10% difference exists between plastic or midsection and elastic solutions. However, due to quite small slopes of the curves, that difference results in fatigue lives eight times higher. In the same figure, a "hybrid" curve was also presented. It was fitted for midsection value points corresponding to the six highest levels of strain and one elastic value point corresponding to the lowest level of strain, for which an almost perfectly elastic response was observed. Such a curve seems to be the most adequate.

The second selected quantity was a sum of plastic and positive elastic strain energy density, similar to the case of the Gołoś–Ellyin energy parameter (compare (15)). Calculated values of energy are presented in Figure 12. This quantity turned out to be less sensitive for the shear stress determination approach, even for the elastic solution. Differences between the best-fit curves for the midsection approach or the plastic and elastic solutions in terms of fatigue life were approximately 15%. The explanation can be seen in Figure 13, where shear strain hysteresis loops according to different stress determination methods were plotted for $\gamma = 0.0139$. Compared to the hysteresis loop obtained using the plasticity model, the hysteresis loop based on the elastic solution has stress underestimated for the lower strain range and overestimated for the higher range. However, these differences even each other out and the resulting energies are quite similar.

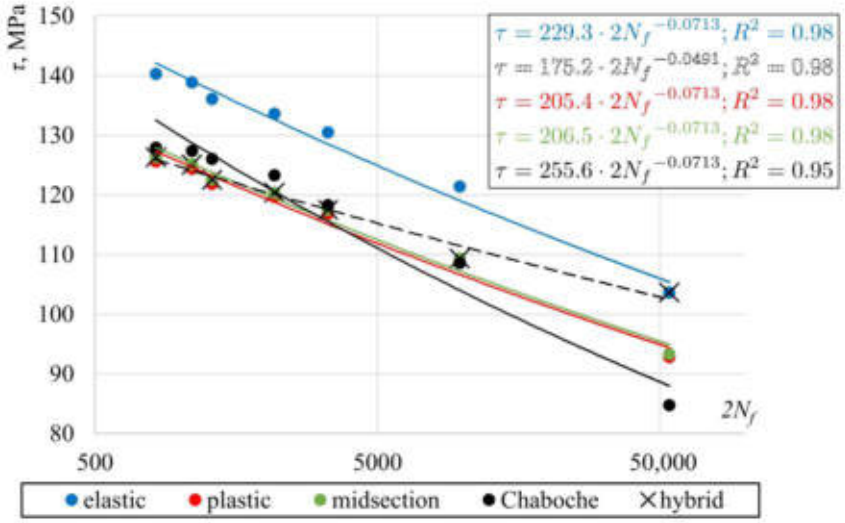

Figure 11. Shear stress vs. fatigue life curves for different shear stress determination methods.

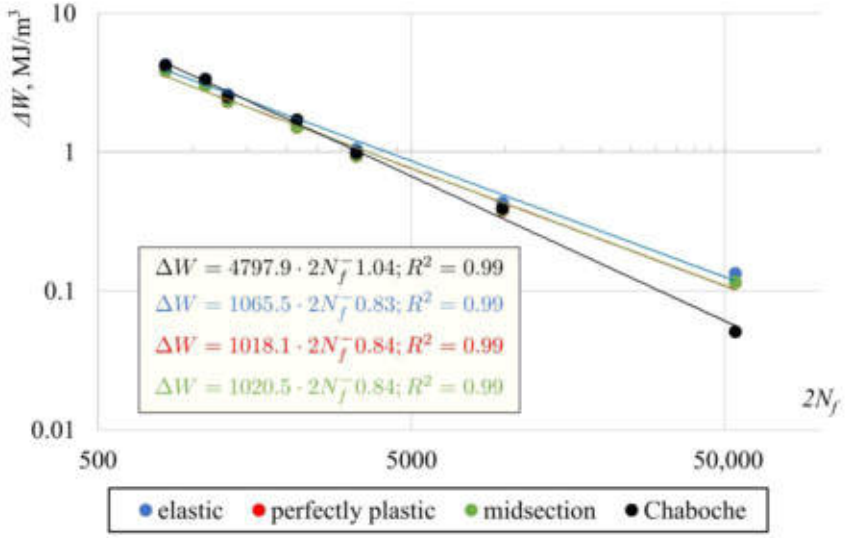

Figure 12. Gołoś–Ellyin energy parameter vs. fatigue lives for different shear stress determination methods.

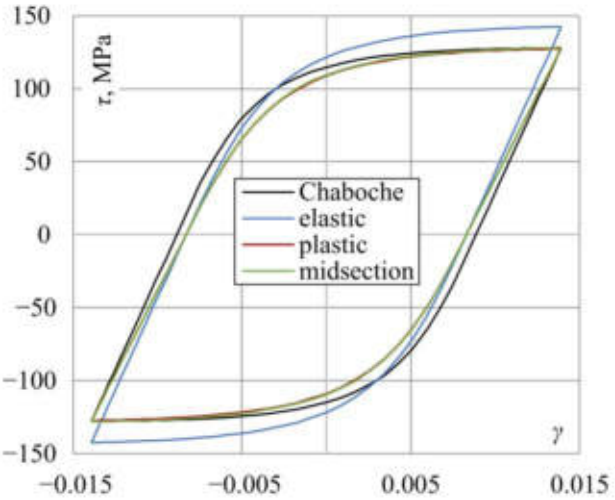

Figure 13. A comparison of shear strain hysteresis loops with stresses determined using different methods for $\gamma = 0.0139$.

Cyclic hardening is another phenomenon often investigated by researchers [52–54]. The interpretation of the experimental results is strongly related to the applied method of shear stress determination. To support this conclusion, the midlife Huber–Mises equivalent peak stresses from axial and torsional fatigue tests are presented in Figure 14 with a superimposed fragment of the monotonic tension stress–strain curve. For torsion, the equivalent stress was calculated based on the surface shear stress determined using the selected methods. A moderate cyclic axial hardening can be observed. If the elastic solution was applied for the shear stress determination, a higher amount of cyclic hardening under torsion could be found. This observation may be further interpreted as anisotropy in yield stress and hardening [55,56]. However, if the midsection or plastic solution were applied, the equivalent stresses under axial and torsional loading would be quite similar.

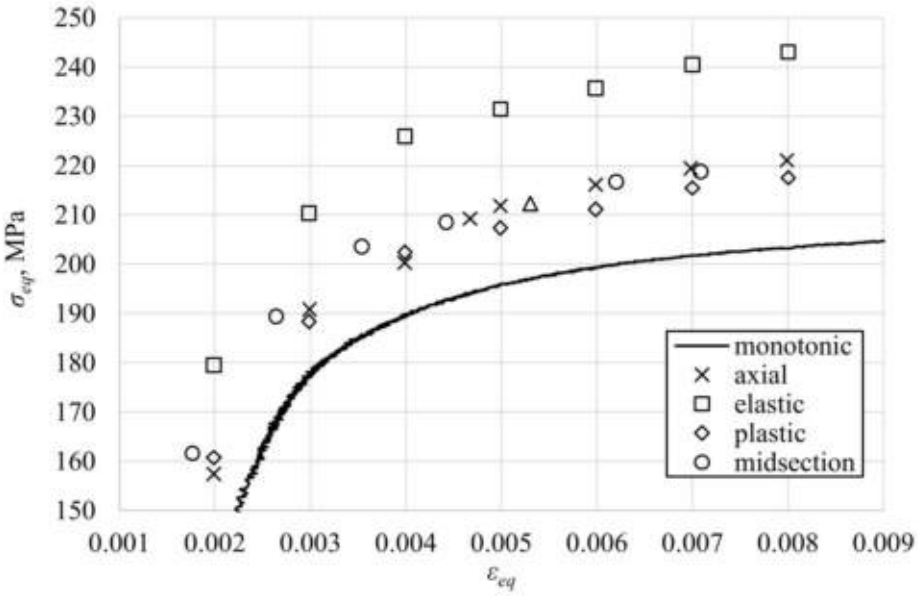

Figure 14. Cyclic midlife hardening analysis by application of different methods of shear stress determination.

5. Summary

Based on the performed analyses of the experimental results of fatigue tests on thin-walled tubular specimens of PA38-T6 aluminum alloy, the following conclusions can be drawn:

1. None of the considered approximate solutions can determine the exact value of surface shear stress for tubular specimens under elastic–plastic cyclic torsional loading.
2. Using the midsection approach and purely plastic solution for high strain levels, it was found that values of surface shear stress were very close to the values obtained using the Chaboche nonlinear kinematic model, calibrated using the experimental data for the axial loading.
3. The largest differences between shear stress values calculated using the plasticity model and other methods were found for the low strain ranges, close to the cyclic yield limit.
4. When the ratio of inner and outer diameters of tubular specimens is close to 1, the effect of the nonuniform shear stress distribution through wall thickness is less pronounced.
5. It was confirmed that the recommendations of the ASTM standard can be successfully implemented to approximately determine the surface shear stress under torsion; however, if the applied loading levels cover the boundary between elastic and elastic–plastic deformation, it should be carefully considered which loading levels justify choosing a purely elastic or midsection approach.
6. The methods discussed are not valid for the full range of loadings. The selection of the approach should be based on the applied loading level and observed material response.

7. The calculated values of shear stress can have a strong impact on the fatigue life prediction, depending on the selected fatigue damage parameter. Thus, it is recommended to clearly indicate how the shear stress values are determined in a study when presenting the results of an experiment.

Author Contributions: Conceptualization, Ł.P.; methodology, J.S. and Ł.P.; software, J.S. and Ł.P.; validation, J.S. and Ł.P.; formal analysis, D.S.; investigation, J.S. and Ł.P.; resources, J.S., Ł.P., and D.S.; data curation, Ł.P.; writing–original draft preparation, J.S. and Ł.P.; writing–review and editing, Ł.P. and D.S.; visualization, J.S. and Ł.P.; supervision, D.S.; project administration, Ł.P.; funding acquisition, Ł.P. All authors have read and agreed to the published version of the manuscript.

Funding: Experimental part of this research was supported by a grant no. 2017/01/X/ST5/00143 funded by the National Science Centre in Poland.

Conflicts of Interest: The authors declare no conflict of interest.

References

1. Tu, S.T.; Zhang, X.C. Fatigue Crack Initiation Mechanisms. *Ref. Modul. Mater. Sci. Mater. Eng.* **2016**, 1–23. [CrossRef]
2. Rozumek, D.; Marciniak, Z. The investigation of crack growth in specimens with rectangular cross-sections under out-of-phase bending and torsional loading. *Int. J. Fatigue* **2012**, *39*, 81–87. [CrossRef]
3. Macek, W. Fractal analysis of the bending-torsion fatigue fracture of aluminium alloy. *Eng. Fail. Anal.* **2019**, *99*, 97–107. [CrossRef]
4. Karolczuk, A.; Kluger, K.; Łagoda, T. A correction in the algorithm of fatigue life calculation based on the critical plane approach. *Int. J. Fatigue* **2016**, *83*, 174–183. [CrossRef]
5. Wei, Z.; Dong, P. A generalized cycle counting criterion for arbitrary multi-axial fatigue loading conditions. *J. Strain Anal. Eng. Des.* **2014**, *49*, 325–341. [CrossRef]
6. Macek, W.; Łagoda, T.; Mucha, N. Energy-based fatigue failure characteristics of materials under random bending loading in elastic-plastic range. *Fatigue Fract. Eng. Mater. Struct.* **2018**, *41*, 249–259. [CrossRef]
7. Krzyżak, D.; Kurek, M.; Łagoda, T.; Sówka, D. Influence of changes of the bending plane position on the fatigue life. *Mater. Werkst.* **2014**, *45*, 1018–1029. [CrossRef]
8. Arora, P.; Gupta, S.K.; Bhasin, V.; Singh, R.; Sivaprasad, S.; Tarafder, S. Testing and assessment of fatigue life prediction models for Indian PHWRs piping material under multi-axial load cycling. *Int. J. Fatigue* **2016**, *85*, 98–113. [CrossRef]
9. Skibicki, D.; Pejkowski, Ł.; Stopel, M. Finite element analysis of ventilation system fire damper dynamic time-history. *Pol. Marit. Res.* **2017**, *24*, 116–123. [CrossRef]
10. Bildhauer, M.; Fuchs, M.; Repin, S. The elastic-plastic torsion problem: A posteriori error estimates for approximate solutions. *Numer. Funct. Anal. Optim.* **2009**, *30*, 653–664. [CrossRef]
11. Idone, G.; Maugeri, A.; Vitanza, C. Variational inequalities and the elastic-plastic torsion problem. *J. Optim. Theory Appl.* **2003**, *117*, 489–501. [CrossRef]
12. Hout, J.W.; Benedict, R.L. The Elastic-Plastic Torsion Problem: A Direct Boundary Approach. *J. Struct. Mech.* **1984**, *12*, 447–463. [CrossRef]
13. Annin, B.D. Existence and uniqueness of the solution of the elastic-plastic torsion problem for a cylindrical bar of oval cross-section. *J. Appl. Math. Mech.* **1965**, *29*, 1038–1047. [CrossRef]
14. Caffarelli, L.A.; Friedman, A. Unloading in the elastic-plastic torsion problem. *J. Differ. Equations* **1981**, *41*, 186–217. [CrossRef]
15. Rubinstein, R. On the elastic-plastic torsion problem. *J. Eng. Math.* **1977**, *11*, 319–323. [CrossRef]
16. Wu, P.D.; Van der Giessen, E. Analysis of elastic-plastic torsion of circular bars at large strains. *Arch. Appl. Mech.* **1991**, *61*, 89–103. [CrossRef]
17. May, I.M.; Al-Shaarbaf, I.A. Elasto-plastic analysis of torsion using a three-dimensional finite element model. *Comput. Struct.* **1989**, *33*, 667–678. [CrossRef]
18. Stout, R.B.; Hodge, P.G. Elastic/plastic torsion of hollow cylinders. *Int. J. Mech. Sci.* **1970**, *12*, 91–108. [CrossRef]
19. Wagner, W.; Gruttmann, F. Finite element analysis of Saint-Venant torsion problem with exact integration of the elastic-plastic constitutive equations. *Comput. Methods Appl. Mech. Eng.* **2001**, *190*, 3831–3848. [CrossRef]

20. Shoemaker, E.M. Second order effects in the elastic-plastic torsion problem. *Meccanica* **1973**, *8*, 125–128. [CrossRef]
21. Miller, K.; Chandler, D.C. High Strain Torsion Fatigue of Solid and Tubular Specimens. *Proc. Inst. Mech. Eng.* **1969**, *184*, 433–448. [CrossRef]
22. Brown, M.W. Torsional stresses in tubular specimens. *J. Strain Anal. Eng. Des.* **1978**, *13*, 23–28. [CrossRef]
23. Shamsaei, N.; Fatemi, A. Effect of hardness on multiaxial fatigue behaviour and some simple approximations for steels. *Fatigue Fract. Eng. Mater. Struct.* **2009**, *32*, 631–646. [CrossRef]
24. Socie, D.F. Multiaxial Fatigue Damage Models. *J. Eng. Mater. Technol. Trans. ASME* **1987**, *109*, 293–298. [CrossRef]
25. Zhong, B.; Wang, Y.; Wei, D.; Zhang, K.; Wang, J. Multiaxial fatigue life prediction for powder metallurgy superalloy FGH96 based on stress gradient effect. *Int. J. Fatigue* **2018**, *109*, 26–36. [CrossRef]
26. Wu, Z.R.; Li, X.; Fang, L.; Song, Y.D. Evaluation of multiaxial fatigue life prediction criteria for Ni-based superalloy GH4169. *Proc. Inst. Mech. Eng. Part J Mech. Eng. Sci.* **2018**, *232*, 1823–1837. [CrossRef]
27. Zhang, J.; Jiang, Y. Constitutive modeling of cyclic plasticity deformation of a pure polycrystalline copper. *Int. J. Plast.* **2008**, *24*, 1890–1915. [CrossRef]
28. Zhang, J.; Jiang, Y. An experimental investigation on cyclic plastic deformation and substructures of polycrystalline copper. *Int. J. Plast.* **2005**, *21*, 2191–2211. [CrossRef]
29. Sharifimehr, S.; Fatemi, A. Fatigue analysis of ductile and brittle behaving steels under variable amplitude multiaxial loading. *Fatigue Fract. Eng. Mater. Struct.* **2019**, *42*, 1722–1742. [CrossRef]
30. McClaflin, D.; Fatemi, A. Torsional deformation and fatigue of hardened steel including mean stress and stress gradient effects. *Int. J. Fatigue* **2004**, *26*, 773–784. [CrossRef]
31. Dey, R.; Tarafder, S.; Sivaprasad, S. Influence of proportional and non-proportional loading on deformation behaviour of austenitic stainless steel-macro and micro analysis. *Theor. Appl. Fract. Mech.* **2019**, *100*, 342–353. [CrossRef]
32. Gryguć, A.; Behravesh, S.; Shaha, S.; Jahed, H.; Wells, M.; Williams, B.; Su, X. Multiaxial cyclic behaviour of extruded and forged AZ80 Mg alloy. *Int. J. Fatigue* **2019**, *127*, 324–337. [CrossRef]
33. Han, Q.; Wang, P.; Lu, Y. Low-cycle multiaxial fatigue behavior and life prediction of Q235B steel welded material. *Int. J. Fatigue* **2019**, *127*, 417–430. [CrossRef]
34. Albinmousa, J.; Adinoyi, M.J.; Merah, N. Multiaxial fatigue of extruded ZK60 magnesium alloy. *Fatigue Fract. Eng. Mater. Struct.* **2019**, *42*, 2276–2289. [CrossRef]
35. Ogawa, F.; Itoh, T.; Yamamoto, T. Evaluation of multiaxial low cycle fatigue cracks in Sn-8Zn-3Bi solder under non-proportional loading. *Int. J. Fatigue* **2018**, *110*, 215–224. [CrossRef]
36. Ting, T.W. The repeated loading-unloading processes of elastic-plastic torsion of solid bars. *Ann. Mat. Pura Appl.* **1979**, *119*, 333–378. [CrossRef]
37. Bruhns, O.T. *Advanced Mechanics of Solids*; Springer: Berlin/Heidelberg, Germany, 2003. [CrossRef]
38. Chaboche, J.L. Time-independent constitutive theories for cyclic plasticity. *Int. J. Plast.* **1986**, *2*, 149–188. [CrossRef]
39. Chaboche, J. Constitutive equations for cyclic plasticty and cyclic viscoplasticity. *Int. J. Plast.* **1989**, *5*, 247–302. [CrossRef]
40. Fatemi, A.; Socie, D.F. A Critical Plane Approach To Multiaxial Fatigue Damage Including Out-of-Phase Loading. *Fatigue Fract. Eng. Mater. Struct.* **1988**, *11*, 149–165. [CrossRef]
41. Smith, K.; Watson, P.; Topper, T. Stress-Strain Function for the Fatigue of Metals. *J. Mater.* **1970**, *5*, 767–778.
42. Walat, K.; Kurek, M.; Ogonowski, P.; Łagoda, T. The multiaxial random fatigue criteria based on strain and energy damage parameters on the critical plane for the low-cycle range. *Int. J. Fatigue* **2012**, *37*, 100–111. [CrossRef]
43. Ince, A.; Glinka, G. A generalized fatigue damage parameter for multiaxial fatigue life prediction under proportional and non-proportional loadings. *Int. J. Fatigue* **2014**, *62*, 34–41. [CrossRef]
44. Garud, Y.S. A New Approach to the Evaluation of Fatigue Under Multiaxial Loadings. *J. Eng. Mater. Technol.* **1981**, *103*, 118. [CrossRef]
45. Ellyin, F.; Golos, K.; Xia, Z. In-Phase and Out-of-Phase Multiaxial Fatigue. *J. Eng. Mater. Technol.* **1991**, *113*, 112. [CrossRef]
46. Ellyin, F. *Fatigue Damage, Crack Growth and Life Prediction*; Chapman & Hall: London, UK, 1997. [CrossRef]

47. Skibicki, D.; Pejkowski, Ł. The relationship between additional non-proportional hardening coefficient and fatigue life. *Int. J. Fatigue* **2019**, *123*, 66–78. [CrossRef]
48. Pejkowski, Ł.; Skibicki, D. Stress-strain response and fatigue life of four metallic materials under asynchronous loadings: Experimental observations. *Int. J. Fatigue* **2019**, *128*, 105202. [CrossRef]
49. Karolczuk, A.; Skibicki, D.; Pejkowski, Ł. Evaluation of the Fatemi-Socie damage parameter for the fatigue life calculation with application of the Chaboche plasticity model. *Fatigue Fract. Eng. Mater. Struct.* **2019**, *42*, 197–208. [CrossRef]
50. Li, H.; Lv, F.; Xiao, Z.; Liang, X.; Sang, F.; Li, P. Low-cycle fatigue behavior of a cast Mg–Y–Nd–Zr alloy by T6 heat treatment. *Mater. Sci. Eng. A* **2016**, *676*, 377–384. [CrossRef]
51. Wu, D.L.; Xuan, F.Z.; Guo, S.J.; Zhao, P. Uniaxial mean stress relaxation of 9–12% Cr steel at high temperature: Experiments and viscoplastic constitutive modeling. *Int. J. Plast.* **2016**, *77*, 156–173. [CrossRef]
52. Li, Y.; Yu, D.; Li, B.; Chen, X. Martensitic transformation of an austenitic stainless steel under non-proportional cyclic loading. *Int. J. Fatigue* **2019**, *124*, 338–347. [CrossRef]
53. Molaei, R.; Fatemi, A.; Phan, N. Significance of hot isostatic pressing (HIP) on multiaxial deformation and fatigue behaviors of additive manufactured Ti-6Al-4V including build orientation and surface roughness effects. *Int. J. Fatigue* **2018**, *117*, 352–370. [CrossRef]
54. Fu, Y.S.S.; Chen, S.S.X. Torsional fatigue with axial constant stress of oligo-crystalline 316L stainless steel thin wire. *Fatigue Fract. Eng. Mater. Struct.* **2018**, *41*, 1929–1937. [CrossRef]
55. Lin, H.; Nayeb-Hashemi, H.; Pelloux, R.M. Constitutive relations and fatigue life prediction for anisotropic Al-6061-T6 rods under biaxial proportional loadings. *Int. J. Fatigue* **1992**, *14*, 249–259. [CrossRef]
56. Zhang, J.; Yu, Q.; Jiang, Y.; Li, Q. An experimental study of cyclic deformation of extruded AZ61A magnesium alloy. *Int. J. Plast.* **2011**, *27*, 768–787. [CrossRef]
57. *Standard Practice for Strain-Controlled Axial-Torsional Fatigue Testing with Thin-Walled Tubular Specimens*; ASTM E2207-02; STM International: West Conshohocken, PA, USA, 2002.

Available online at www.sciencedirect.com

ScienceDirect

Procedia Structural Integrity 28 (2020) 1458–1466

Structural Integrity Procedia

www.elsevier.com/locate/procedia

1st Virtual European Conference on Fracture

Identification of fatigue damage mechanism in PA38-T6 aluminum alloy under multiaxial loadings – initial research

Jan Seyda[a]*, Łukasz Pejkowski[a], Dariusz Skibicki[a]

[a]*Faculty of Mechanical Engineering, University of Science and Technology, Kaliskiego 7, 85-796 Bydgoszcz, Poland*

Abstract

This paper presents results of the initial research which originated from previous work, which was aimed to study the effect of asynchronous loadings in elastic-plastic strain range. Among the others, a study of fatigue cracks on the fatigued specimens' surfaces, was performed.

The aim of the present work is to identify the mechanisms of initiation and propagation of small fatigue cracks in selected materials under multiaxial loadings, including asynchronous cases. To study the evolution of small cracks and main crack formation, the cellulose acetate thin foil replication technique was utilized. Fatigue tests were performed on thin-walled tubular specimens, which were mirror-polished after CNC machining, to avoid the influence of unwanted factors.

This paper presents the first part of fatigue tests, performed on specimens manufactured from PA38-T6 (AW 6060-T6) aluminum alloy. Fully reversed axial, torsional and 90º out-of-phase loadings were applied in elastic-plastic strain regime, with strain control. For these loading cases a shear damage mechanism was identified, based on the observation of small cracks. The small cracks initiated ate grew on maximum shear strain planes. The main crack formed at the very end of fatigue life by coalescence of small cracks of high density, regardless the applied loading case and level. An interesting difference in cracking behavior was observed in case of out-of-phase loading, on the low loading level. Small cracks propagated, and the main crack formed by linking of a few propagating cracks.

The research is in progress and will be extended to the lower levels of strain as well as other cases of loadings, including asynchronous loadings. It is planned to conduct the research using other materials, for example non-alloy steel and austenitic stainless steel.

* *E-mail address:* jansey002@utp.edu.pl

2452-3216
10.1016/j.prostr.2020.10.119

Keywords: multiaxial fatigue, small cracks, replication, elastic-plastic strain;

1. Introduction

The initiation and growth of small cracks is usually an important portion of fatigue life as described by Shamsaei and Fatemi (2014). Often, the overall direction of macrocrack can be different than the direction of small crack, from which it originated. McClaflin and Fatemi (2004) showed that in SAE 9254 AL FG quenched and tempered steel subjected to torsion some of the main cracks formed on the maximum principal stress plane. However, initially cracks grew in the maximum shear stress direction. Consequently, the fatigue life prediction based on principal stress or strain values gave poor results. Foletti et al. (2018) showed that the application of the fatigue damage parameter, which reflect the cracking behavior, resulted in an accurate fatigue life prediction for high strength quenched and tempered 30NiCrMoV12 steel. Hence, the observation of small cracks behavior is very useful to understand the fatigue damage mechanism and to associate the damage mechanism with multiaxial fatigue models, as presented by Kurath and Socie (1988).

The present research is a continuation of previous work aimed to study the fatigue behavior of materials subjected to multiaxial loadings, especially asynchronous cases conducted by Pejkowski and Skibicki (2019) and observation of small cracks on surfaces of fatigued specimens conducted by Pejkowski et al. (2019). The first stage of research concerns identification of fatigue damage mechanism in PA38-T6 (AW 6060-T6) aluminum alloy. The development of small cracks was registered by replication using cellulose acetate think foils, which is a convenient and known technique used by Foletti et al. (2018), Main et al. (2019) and Molari et al. (2020). Three cases of basic loadings were applied in elastic-plastic strain range – fully reversed axial, torsional and 90° out-of-phase loading.

2. Materials and methods

Thin-walled tubular specimens, manufactured from PA38-T6 aluminum alloy, were used. The chemical composition of this material is given in Table 1. Basic mechanical properties, Young modulus E, 0.2% offset yield stress σ_{y02}, ultimate tensile strength σ_u and corresponding strain ε_{σ_u}, elastic Poisson ratio ν_e, cyclic strength coefficient K' and cyclic strain hardening exponent n' are given in Table 2. The dimensions of the specimens are presented in Fig. 1. The specimens' surfaces were carefully mirror-polished using different grades of diamond paste in order to remove all machining marks and scratches.

Specimens were subjected to fully reversed axial, torsional and 90° out-of-phase loading with sine waveforms. All tests were performed on Instron 8874 servohydraulic axial/torsional testing system. Axial and shear strains were measured and controlled using an Epsilon 3550 biaxial extensometer. The loading parameters, programs and signals recording were conducted using Instron WaveMatrix software.

Table 1. Chemical composition of PA38-T6 aluminum alloy according to EN 573-3 standard

Element	Si	Fe	Cu	Mn	Mg	Cr	Zn	Ti	Other	Al
Share in %	0.3-0.6	0.1-0.3	0.1	0.1	0.35-0.6	0.05	0.15	0.1	0.15	Balance

Table 2. Basic mechanical properties of PA38-T6 aluminum alloy determined experimentally

E, GPa	σ_{y02}, MPa	σ_u, MPa	ε_{σ_u}, mm/mm	ν_e, –	K', MPa	n', –
68.3	191.5	229.1	0.094	0.35	288.1	0.051

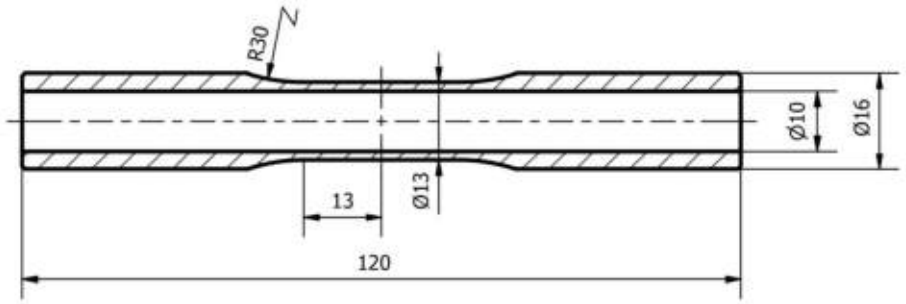

Fig. 1. Dimensions of PA38-T6 specimens, given in millimeters.

The materials used for specimen surface replication are 125 μm thick cellulose acetate foil and a set of auxiliary tools. The micro photographs were taken on a metallographic microscope Delta Optical MET-1000-TRF equipped with DLT-Cam PRO 12MP digital camera with dedicated image processing software DLTCamViewer. In order to capture features of the whole surface of specimen's working part, the first test was conducted in strain-control mode. Next, based on the recorded displacement history, the second test was performed in displacement-control mode. The tests were paused every 10% of expected fatigue life to make the replica on both sides of the specimen. The cellulose acetate sheet was attached by spraying a drop of acetone between tape and specimen. The acetone melts the tape, which sticks to the specimen. Next it evaporates for 7 to 10 minutes. When the cellulose acetate was dry again, it was gently taken off with a plastic pincer and put between microscope slide glass. Very small details of specimen surface topography imprint on the replica. Moreover, the replica can be observed using transmitted light. Thanks to that, there is no interference caused by light reflection or curved surface effect. The greatest advantage of this technique is an ability to track the crack development history. To show the capabilities of this technique, the image of replica and direct image of specimen surface are compared in Fig. 2. Shots were captured in such a way that the vertical direction is in line with the specimen axis.

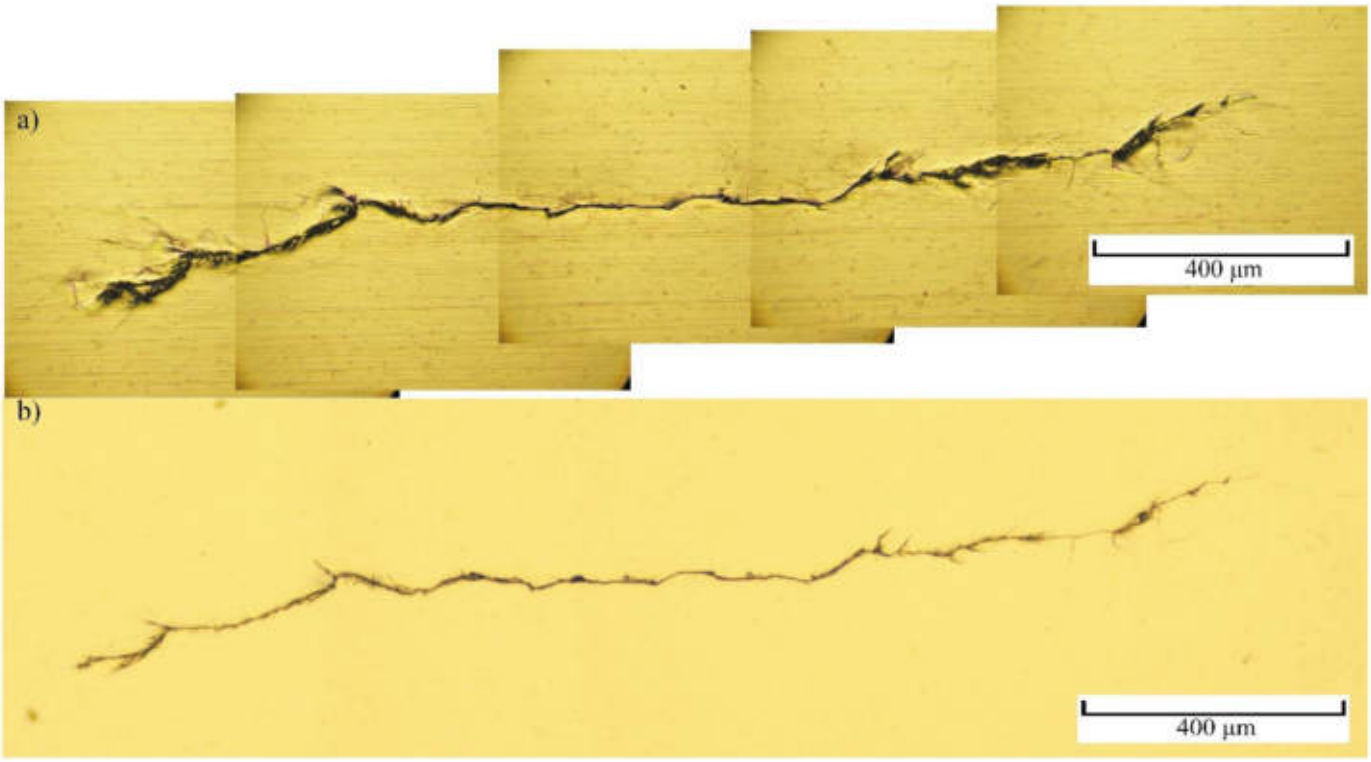

Fig. 2. Comparison of crack images: (a) taken directly on specimen surface and (b) from replica.

3. Cracks evolution observation

Fig. 3 presents the fatigue life of specimens for the analyzed cases of loadings (including the data from Pejkowski and Skibicki (2019) research) and the Basquin-Manson-Coffin curve fitted for tension-compression data points. Fig. 4 shows the maximum normal and shear strain distribution in polar diagrams, for the tested loading cases. The directions of global maxima of shear and normal strain with respect to the specimen axis were also marked.

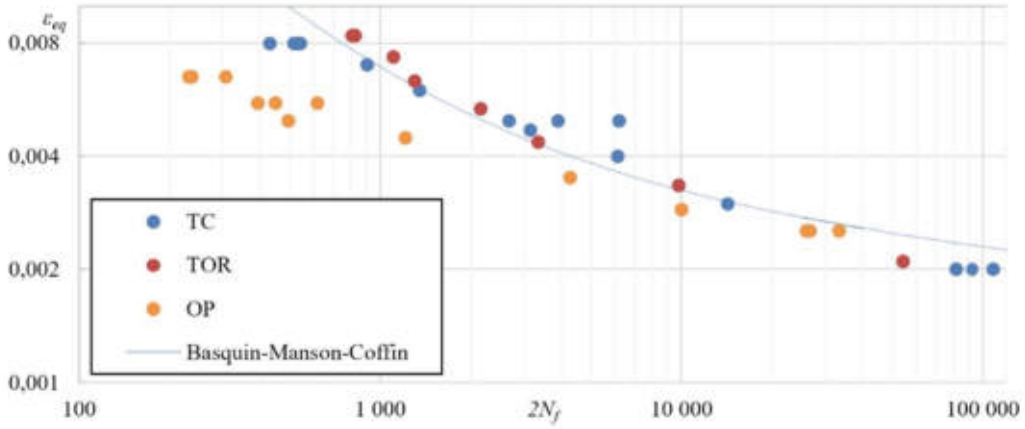

Fig. 3. Fatigue lives of PA38-T6 aluminum alloy for axial, torsional and out of-phase loadings.

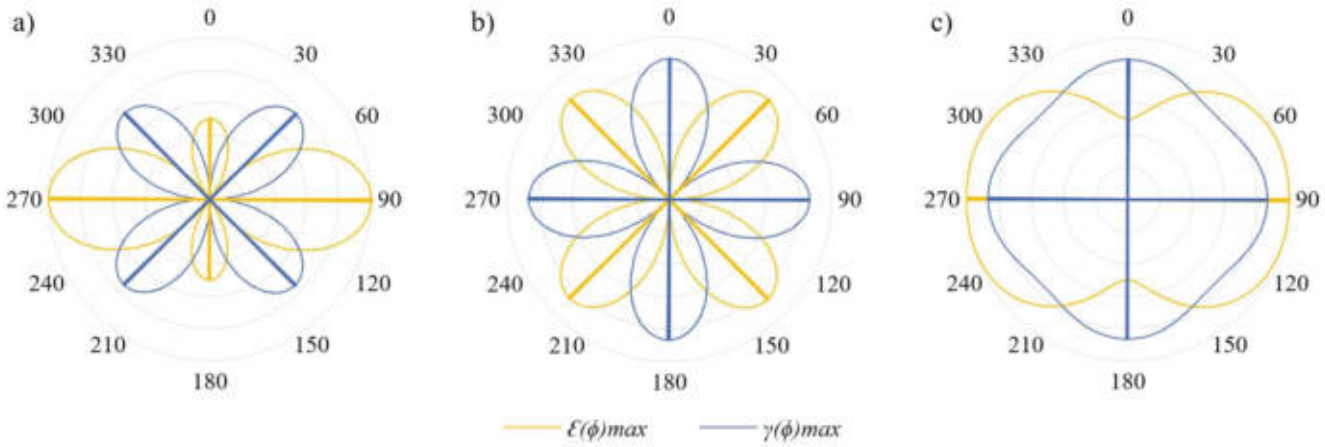

Fig. 4 The values of the maximum normal $\varepsilon(\varphi)$ end shear $\gamma(\varphi)$ strain, as a function of angular position with respect to the specimen axis for different loading cases: (a) axial loading, (b) torsional loading and (c) out-of-phase loading.

Fig. 5 presents small cracks for high level of applied strain under axial loading, for which small cracks could be observed from 60% of specimen's fatigue life, approximately. The density of small cracks was much higher than for the low strain level for which cracks could be barely seen after 90% of fatigue life (Fig. 6).

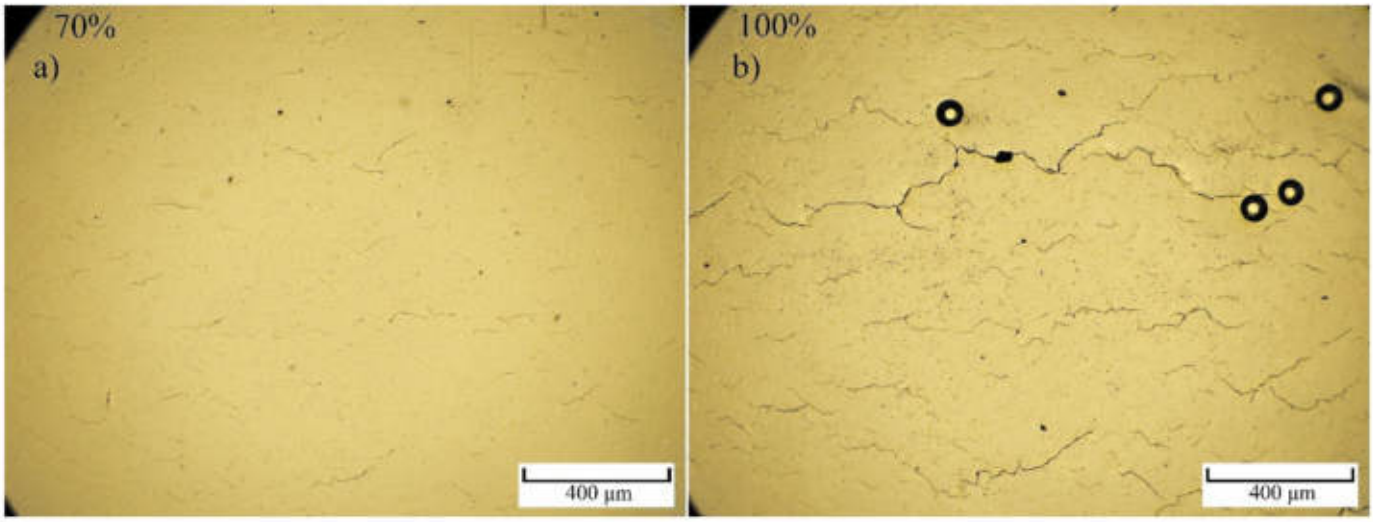

Fig. 5. Evolution of small cracks under axial loading at $\varepsilon_{eq} = 0.005$: (a) at 70% of fatigue life, (b) few cycles before failure.

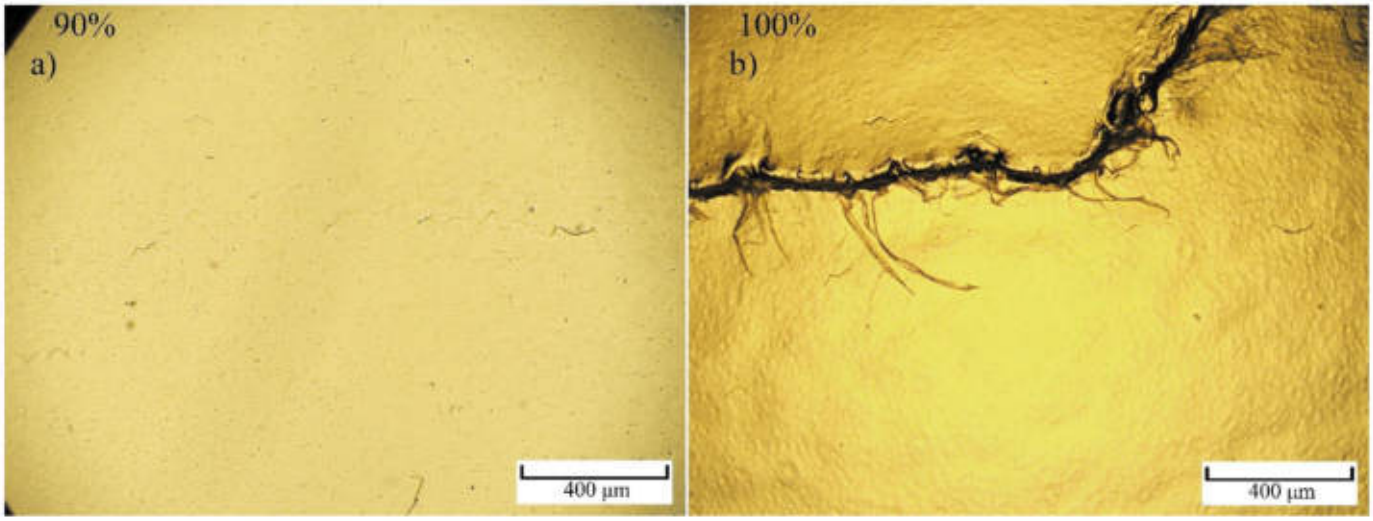

Fig. 6. Evolution of small cracks under axial loading at $\varepsilon_{eq} = 0.002$: a) at 90% of fatigue life, b) failure.

In both cases, the main crack formed in the very last cycles, that is less than 5% of fatigue life. The identified damage mechanism for axial loading in the applied loading levels range was a coalescence of small cracks. The initiation and growth of small cracks followed a shear damage mechanism. Cracks initiated and grew in directions of maximum shear strain, which are ± 45° for tension-compression. Next, the cracks linked with each other without a change in direction. Cracks initiated and propagated on the whole surface, in directions of maximum shear strain, that is from 0° to 45° to the horizontal axis, up to 15 to 100 µm of length. After that, they coalesced to form the main crack.

The same damage mechanism was observed under torsional loading (Fig. 7). Small cracks initiated and grew in the directions of maximum shear strain, that is parallelly and perpendicularly to the specimen axis. Next, the coalescence was observed. For this case of loading, small cracks grew longer, up to 400 µm, and, by contrast, they crossing most often. This was very rarely observed under axial loading. This is the only loading case where the value of normal deformations is zero on the plane of maximum shear strain. Perhaps, this explains the above-described phenomenon because cracks do not interact with each other.

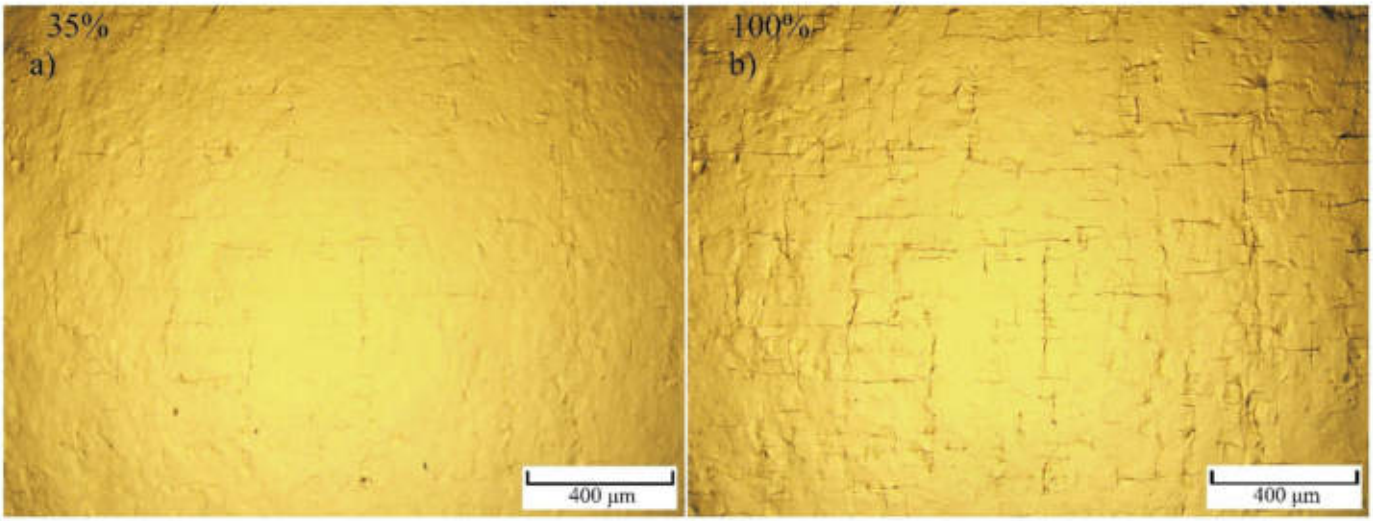

Fig. 7. Evolution of small cracks under torsional loading at ε_{eq} = 0.008: (a) at 35% of real life, (b) failure.

In case of the out-of-phase loading, small cracks could be observed in many directions, since principal axes, so also the shear strain vector, rotate (Fig. 8). The most developed cracks were visible in the direction normal to specimen axis. It corresponds to the plane of maximum shear and normal strain. On the loading level corresponding to similar fatigue life as the highest level of axial loading, a very high density of small cracks was observed. At the end of specimen's fatigue life, the coalescence of small cracks occurred.

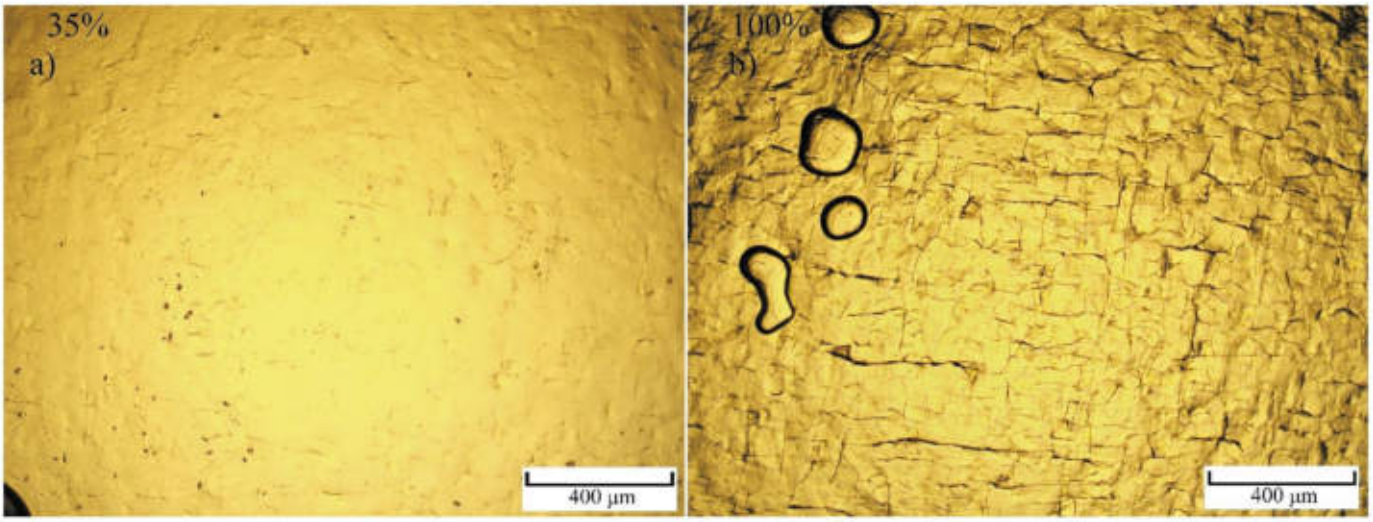

Fig. 8. Evolution of small cracks under out-of-phase loading at ε_{eqv} = 0.008: (a) at 35% of real life, (b) failure.

The small cracks initiated in many directions, forming a dense net. It can be clearly seen on Fig. 8 (b) that the preferred direction of cracking is a horizontal plane, on which maximum shear and normal strain act. Differences in cracking behavior occurred at the lowest level of out-of-phase loading (Fig. 9). In which much less density of small cracks was observed. All cracks propagated in the horizontal direction, but only after 50% of fatigue life they could be observed on the replica. The main crack formed in the last few cycles of loading, from four cracks only, with an average length of 2 mm (Fig. 10). In Fig. 9 (d) and Fig. 10 (b) branching of cracks can be seen, forming due to the local change of the stress at the crack tip of suitable length. The shades at the bottom right on Fig. 10 (b) are the edge of replica tape.

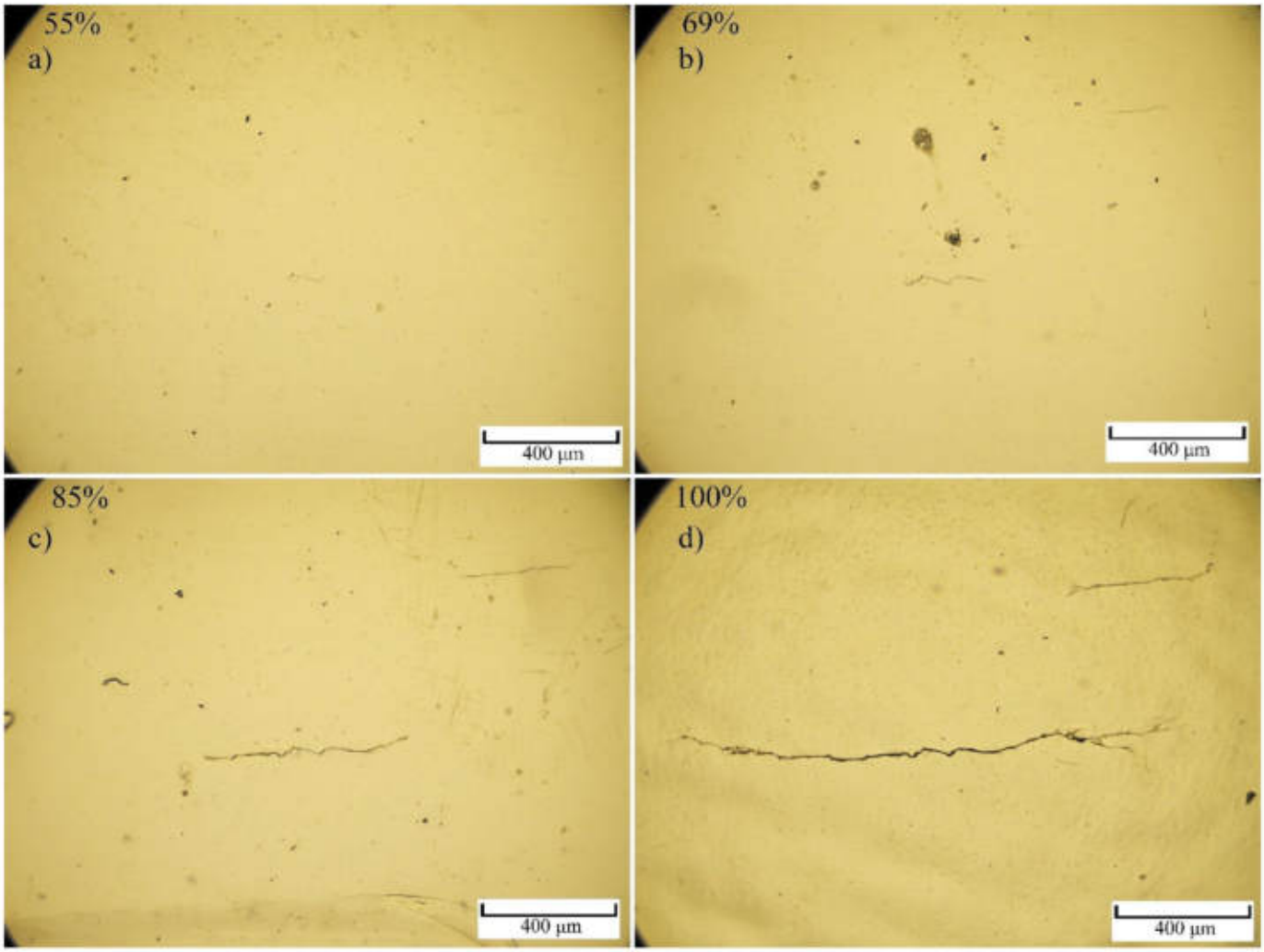

Fig. 9. Evolution of small cracks at OP loading at ε_{eq} = 0.002 at: (a) 55%, (b) 69%, (c) 85% of fatigue life, (d) failure.

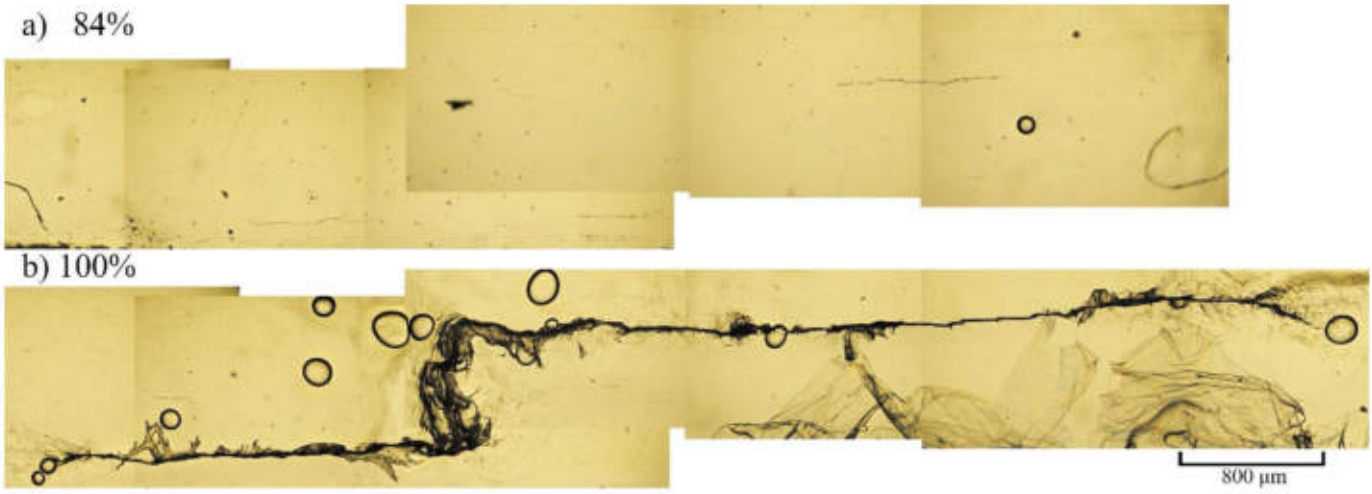

Fig. 10. Main crack formation for OP at ε_{eq} = 0.002 at: a) 84% of fatigue life b) failure.

4. Discussion

The first trend that can be seen is that the density of the resulting small cracks increased with the level of loading, regardless of the loading case. The main crack is formed by the coalescence of small cracks. This phenomenon depends on the density of small cracks and the their growth rate. They both depend primarily on the loading level and material microstructure as reported by Ochi et al. (1985). The case of torsional loading is characterized by the longest fatigue life, compared to other cases. In this case, the cracks formed and grew only in two directions, 0° and 90° with respect to the specimen's axis, on planes where only shear strain acted (Fig. 4 (b)). In turn, under axial loading, at which the fatigue life is a little shorter than for torsion, cracks formed and propagated in many directions from 0 ° to ± 45 ° (Fig. 4 (a)), more often coinciding with the planes of easy glide of the crystal lattice in individual metal grains, which has been described by Zhang and Miller (1996). On the other hand, normal strain accelerating the development of cracks also occur in the planes of maximum shear strain. The out-of-phase loading is characterized by the shortest fatigue life. The vector of maximum shear strain rotates in time in all directions (Fig. 4 (c)) activating many slip systems in the material. Small cracks initiated and propagated in all directions. However the longest and most opened cracks were those at which the maximum normal strain occurred.

5. Conclusions

Replication technique and displacement-control, based on previously recorded history, were useful for tracking the small cracks on surfaces of specimens manufactured from PA38-T6 aluminum alloy. The small cracks were imprinted in replicas only after linking of at least 3 cracks. Only then, the crack is wide enough to be penetrated by the melted cellulose acetate sheet. Single cracks were visible only as shadows at higher magnifications. A different behavior was noticed under OP loading. Single small cracks of comparable length were more opened. This is most likely because in the plane of crack, the maximum shear strain act together with the highest normal strain opening the cracks. For the tested specimens, creating replicas of the specimens' surfaces at the highest loading levels has become a difficult task, due to the extremely large surface irregularities resulting from high deformation which increase the number of defects on the replicas, such as air bubbles, wrinkles, and non-stick fragments.

Shear damage mechanism was identified at the applied loading levels, regardless the loading case. Main crack formed by coalescence of small cracks. The exception was noted for out-of-phase loading at 0.002 equivalent strain, where propagation of cracks occurred. The main crack formed from 4 propagating cracks, and the total time of the main crack formation took less than 2% of fatigue life.

In these preliminary tests, it was possible to observe differences in the fatigue process, not only depending on the loading level, but also on the loading case. The number of directions of small cracks as well as the level of shear and normal strain in these directions seem to be of particular importance.

The research is still in progress. It will be extended, to some point, to the lower loading levels (high cycle regime), to see if there is a change in damage mechanism. Other cases of loadings than currently applied will be used, including asynchronous loadings. It is planned to perform the same research on austenitic stainless steel.

References

Shamsaei N., Fatemi A., 2014 .Small fatigue crack growth under multiaxial stresses. Int. J. Fatigue. 58, 126–135.

McClaflin D., Fatemi A., 2004. Torsional deformation and fatigue of hardened steel including mean stress and stress gradient effects. Int. J. Fatigue. 26, 773–784.

Foletti S., Corea F., Rabbolini S., Beretta S., 2018. Short cracks growth in low cycle fatigue under multiaxial in-phase loading. Int. J. Fatigue. 107, 49–59.

Kurath P., Socie D.F., 1988. The Relationship Between Observed Fatigue Damage and Life Estimation Models. NASA Contractor Report 182191.

Pejkowski Ł., Skibicki D., 2019. Stress-strain response and fatigue life of four metallic materials under asynchronous loadings: Experimental observations. Int. J. Fatigue. 128, 105202.

Pejkowski Ł., Seyda J., Skibicki D., 2019. Short cracks observations on surfaces of specimens made of three materials, subjected to synchronous and asynchronous multiaxial loadings, MATEC Web Conf. 300, 15002.

Main B., Molent L., Singh R., Barter S., 2020. Fatigue crack growth lessons from thirty-five years of the Royal Australian Air Force F/A-18 A/B Hornet Aircraft Structural Integrity Program. Int. J. Fatigue. 133, 105426.

Molaei R., Fatemi A., Phan N., 2020. Multiaxial fatigue of LB-PBF additive manufactured 17–4 PH stainless steel including the effects of surface roughness and HIP treatment and comparisons with the wrought alloy. Int. J. Fatigue. 13, 105646.

Skibicki D., Pejkowski Ł., 2019. The relationship between additional non-proportional hardening coefficient and fatigue life. Int. J. Fatigue. 123, 66–78.

Zhang W., Miller K.J., A study of cumulative fatigue damage under variable loading-mode conditions. Fatigue & Fracture of Engineering Materials & Structures. 19, 229–239.

Ochi Y., Ishii A., Sasaki S.K., 1985. An Experimental and Statistical Investigation of Surface Fatigue Crack Initiation and Growth, Fatigue Fract. Eng. Mater. Struct. 8, 327–339.

SEM analysis of PA38-T6 aluminum alloy thin-walled tubular specimen fatigue fracture, and comparison to surface replication results

Jan Seyda[1,2*], and *Łukasz* Pejkowski[1]

[1] UTP University of Science and Technology, Faculty of Mechanical Engineering, Kaliskiego 7, 85-796 Bydgoszcz, Poland
[2] UTP University of Science and Technology, Doctoral School UTP, Kaliskiego 7, 85-796 Bydgoszcz, Poland

Abstract. The paper presents results of SEM analysis of fatigue fracture surface of thin-walled tubular specimen manufactured from PA38-T6 aluminum alloy. In the previous research specimens were subjected to multiaxial loadings. They were axial, torsional, in-phase, 90° out-of-phase and asynchronous loadings. During the fatigue experiments, the process of initiation and development of cracks was tracked using the surface replication technique, using cellulose acetate thin foils. In the present work, SEM observations of fatigue fracture surface were conducted and compared to previously obtained data. It was confirmed, that the dominating mechanism of fatigue crack formation was the coalescence of small crack, regardless of loading type and level.

1 Introduction

Microscopic analysis of phenomena occurring in the material under fatigue loadings is an important issue, because the stages of initiation and propagation of small cracks take, in most cases, a significant part of the fatigue life [1]. Sometimes, the direction of the cracks on the macroscopic scale does not coincide with the direction of the small cracks [2]. The development of fatigue cracks may be different depending on the material and the loading case, and on the scale of observation: the crack can grow on the planes of maximum shear strain [1], the planes of maximum principal stress [3], or on the planes of maximum shear strain to some length, and then change the propagation direction [4]. It may be also observed that the small cracks can propagate independently [5], or can connect by the coalescence mechanism [6,7].

The study of the fatigue crack development mechanism, depending on the loading case and on the material, is important for the analysis of experimental results and the improvement of fatigue failure accumulation and fatigue life prediction models. These models are based on the critical plane [8], principal strains [9] or energy parameters [10].

* Corresponding author: jansey002@utp.edu.pl

10.22725408

The present work presents the initial results of research, in which two techniques were used to analyze the development of fatigue cracks. The surface replication technique using the cellulose acetate tape was applied to observe the damage mechanism with regard to the subsequent stages of fatigue life. These stages are initiation and growth of small cracks, and development of the main crack. The replication technique can be used to track the changes on the outer specimens' surfaces only. The SEM fractography may be applied to observe the fatigue fracture of the specimen with much higher magnifications than those used to observe the replicas under the optical microscope. The research where these two techniques are applied together are sometimes conducted for other metallic alloys [11].

2 Materials and Methods

The research was conducted on thin-walled tubular specimens, manufactured from PA38-T6 (AW 6060-T6) aluminum alloy (**Table 1**). **Table 2** presents basic mechanical properties, Young modulus E, 0.2% offset yield stress σ_{y02}, ultimate tensile strength σ_u and corresponding strain $\varepsilon_{\sigma u}$, elastic Poisson ratio ν_e, cyclic strength coefficient K' and cyclic strain hardening exponent n' The dimensions of the specimens are shown in **Fig. 1**. The specimens' surfaces were mirror-polished using different grades of diamond paste in order to remove all machining marks and scratches.

Specimens were subjected to fully reversed axial, torsional and 90° out-of-phase sine-shaped loadings. All tests were performed on Instron 8874 servohydraulic axial/torsional testing frame. Strains were measured and controlled using an Epsilon 3550 biaxial extensometer.

This work is a continuation of the research aimed to study the multiaxial fatigue of metallic alloys in the elastic-plastic strain range. In the previous papers, the influence of additional non-proportional hardening on the fatigue life was studied [12,13], the directions of initiation and growth of small cracks on the specimens' surfaces were observed [14], and, initially, the development of fatigue cracks during the fatigue tests using the replication technique was studied [15].

Table 1. Chemical composition of PA38-T6 aluminum alloy according to EN 573-3 standard

Element	Si	Fe	Cu	Mn	Mg	Cr	Zn	Ti	Other	Al
Share in %	0.3-0.6	0.1-0.3	0.1	0.1	0.35-0.6	0.05	0.15	0.1	0.15	Balance

Table 2. Basic mechanical properties of PA38-T6 aluminum alloy determined experimentally

E, GPa	σ_{y02}, MPa	σ_u, MPa	ε_{σ_u},	ν_e, –	K', MPa	n', –
68.3	191.5	229.1	0.094	0.35	288.1	0.051

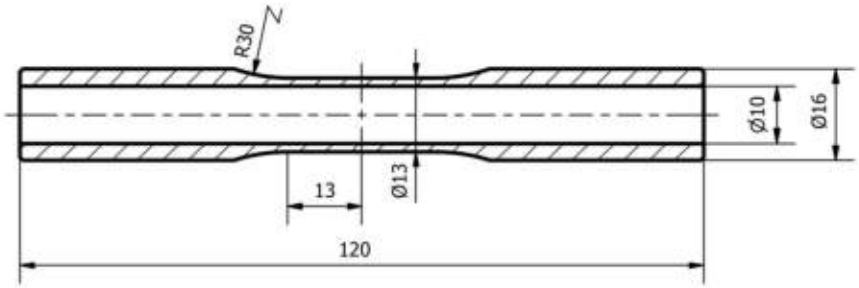

Fig. 1 Dimensions of PA38-T6 specimens, given in millimetres

The material used for specimen surface replication was 125 μm thick cellulose acetate foil. The micro photographs were taken on a metallographic microscope Delta Optical MET-

1000-TRF equipped with DLT-Cam PRO 12MP digital camera with dedicated image processing software DLTCamViewer.

The first test using a given loading case and level was always conducted in strain-control mode. Next, based on the recorded displacement history, the second test was performed in displacement-control mode. The fatigue tests were paused every 10% of expected fatigue life to take the replica on both sides of the specimen's gauge section. This technique was described more in-detail in [15]. In **Fig. 2** the capabilities of replication are presented by comparison of a crack picture taken directly on the specimen's surface (a) and on the replica (b). The greatest advantage of this technique is the ability to track the history of cracks development.

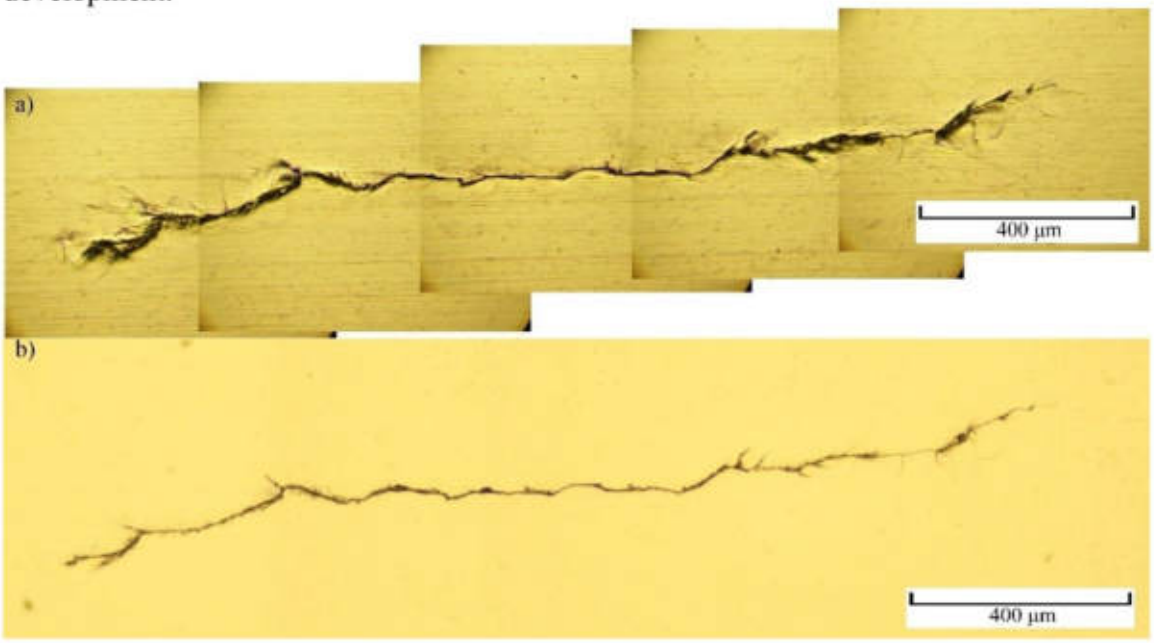

Fig. 2 Comparison of crack image taken from specimen (a) and from replica (b)

The SEM images were taken on JEOL 6480LV device, in which a dedicated working table was attached to grip the cylindric specimens vertically, with ability to tilt the specimen.

3 Results and discission

This work regards the results of tests performed using a single specimen, subjected to fully reversed axial loading, on the level of strain $\varepsilon = 0.005$. This is the point marked with an arrow in **Fig. 3**.

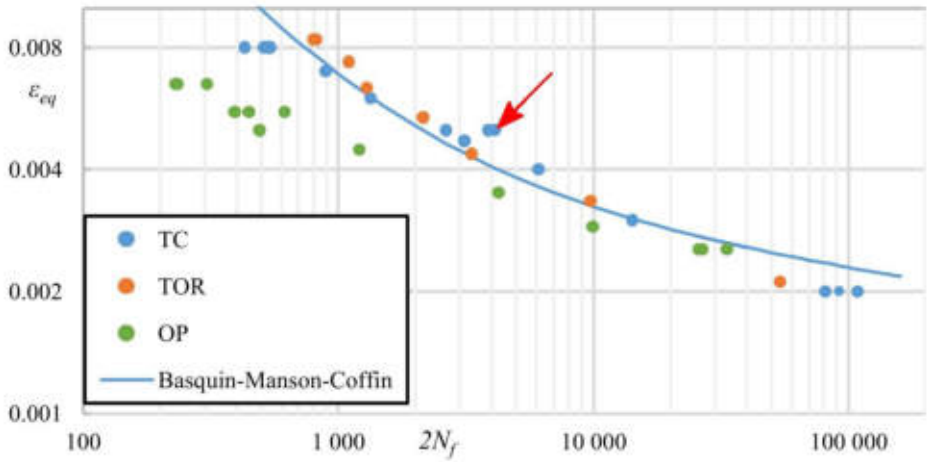

Fig. 3 Basquin-Manson-Coffin chart for PA38-T6 aluminum alloy for basic loading cases: TC – tension-compression, TOR – torsion, OP – 90° out-of-phase

The coalescence of small cracks was identified as a main crack development mechanism by the analysis of replicas, showing the cracking history. At the initial stage, the small cracks initiated and grew independently to small sizes. Next, they linked with nearby cracks forming a greater crack. The main crack development rate increased with the size of linked cracks.

The first small cracks were visible at, approximately, 50% of fatigue life. In **Fig. 4.a**, many cracks, formed by the linkage of about 5 small cracks, can be seen. After the cracks reached the surface length of about 2 mm, a rapid increase in the rate of damage process occurred, during which, drop of the axial force was recorded. **Fig. 4.b** presents the replica at the moment when the first notable decrease in the axial force value occurred. It took only 2% of fatigue life to the total fracture of the specimen.

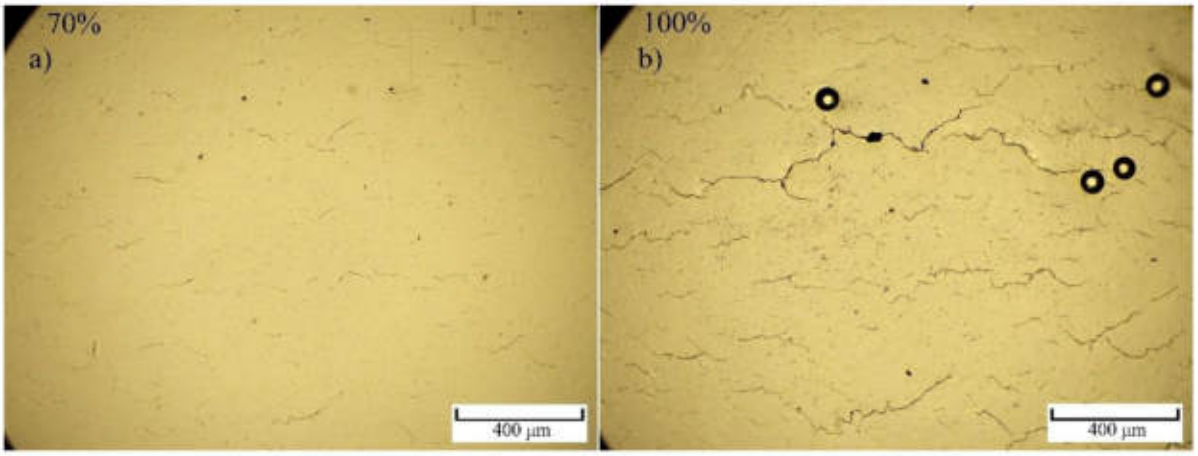

Fig. 4 The replicas' fragment presenting the origin of the main crack

Replication provides the information on the changes occurring on the outer surfaces of the specimens. The SEM fracture analysis, despite it is used after the experiment, provides the information on the phenomena taking please inside the material. **Fig. 5** presents the fatigue fracture of specimen subjected to axial loading at $\varepsilon = 0.005$, with marked fragments, which are discussed below.

The blue arrow in **Fig. 5** points the area, in which, using the replication technique, the initiation of the main crack was identified. Multiple small cracks can be seen on a magnification of this fragment (**Fig. 6**). All origins were on the surface of the specimen. Next, they linked into one larger crack. Fatigue striations are also visible. The distance between striations increased with each loading cycle. The main fracture is not elliptic-shaped, but

rather is a single front of interconnected cracks propagating deep into the specimen's material.

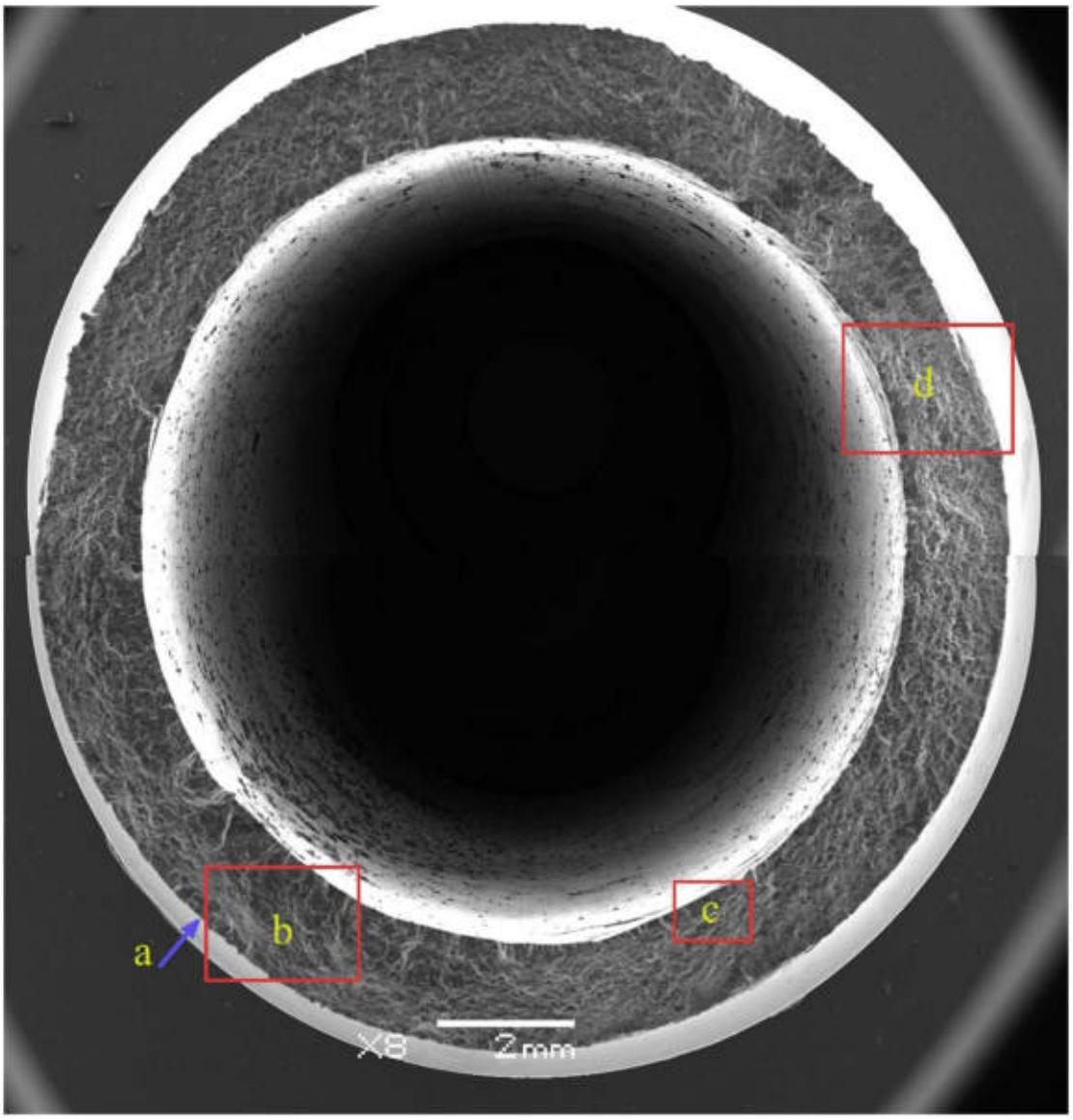

Fig. 5 SEM image of specimen's fatigue fracture: a) fragment where the onset of coalescence of small crack was identified by replication, b) the fragment on which the longest propagating crack developed, c) another small cracks initiation site that linked with the main crack, d) overload zone

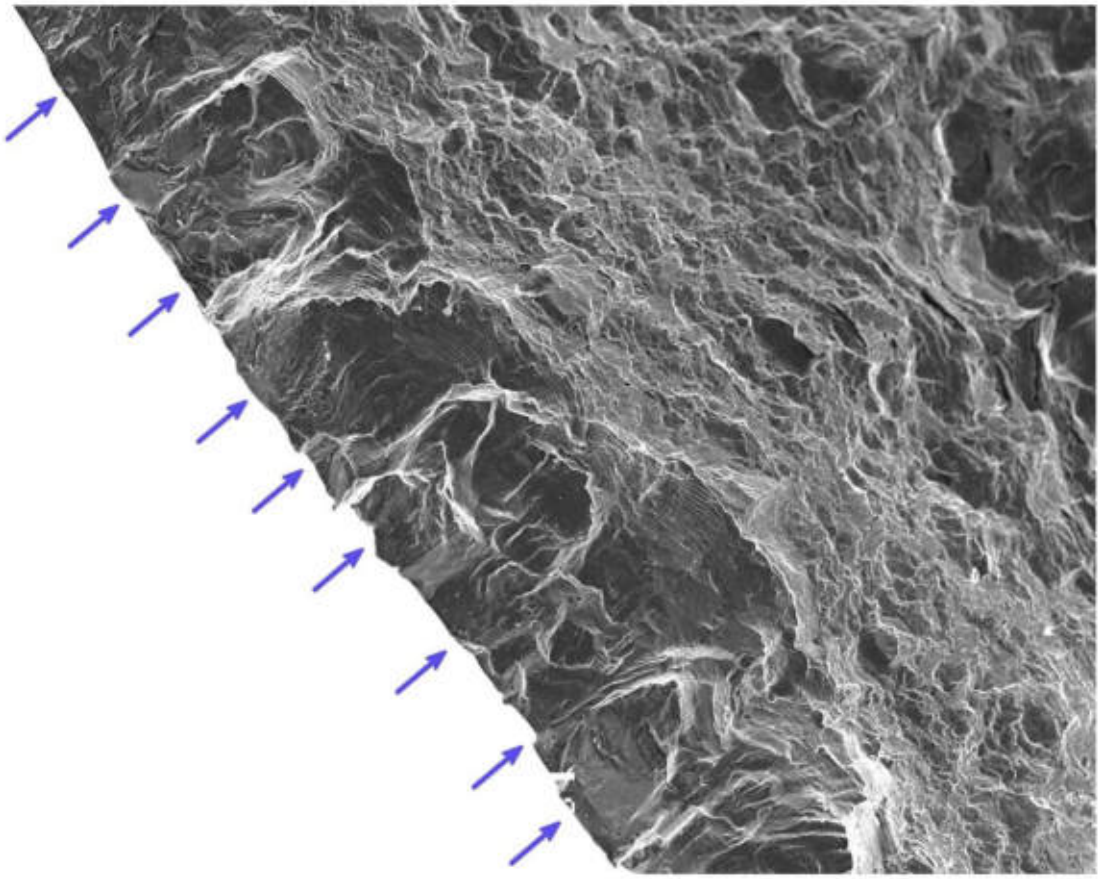

Fig. 6 Fatigue fracture's fragment (**Fig. 5.a**), in which the beginning of coalescence of small cracks, which further formed the main crack, was identified using replicas

When the specimen is tilted in the microscope's grip, the side surface of the specimen can also be observed (**Fig. 7**), and the other cracks, that did not link with the main crack. The size of these cracks is the same as observed on the replicas. The origin of this particular small crack is in the grain, which (due to machining) was almost completely removed. Therefore, it had more degrees of freedom which resulted in the initiation of crack [16]. On the fracture surface some inclusion can be seen. Using the EDS analysis it was detected that they contain Al, Fe and Si. Most likely, they are AlFeSi precipitations identified in other research regarding this alloy [17,18]. In **Fig. 7.b,** the magnified initiation site is presented (blue arrow). AlFeSi precipitations (red arrows) did not have any visible effect in the first stage. However, when the first striations appeared (green arrow), indicating the change in crack development mechanism, some perturbations around the precipitations can be seen.

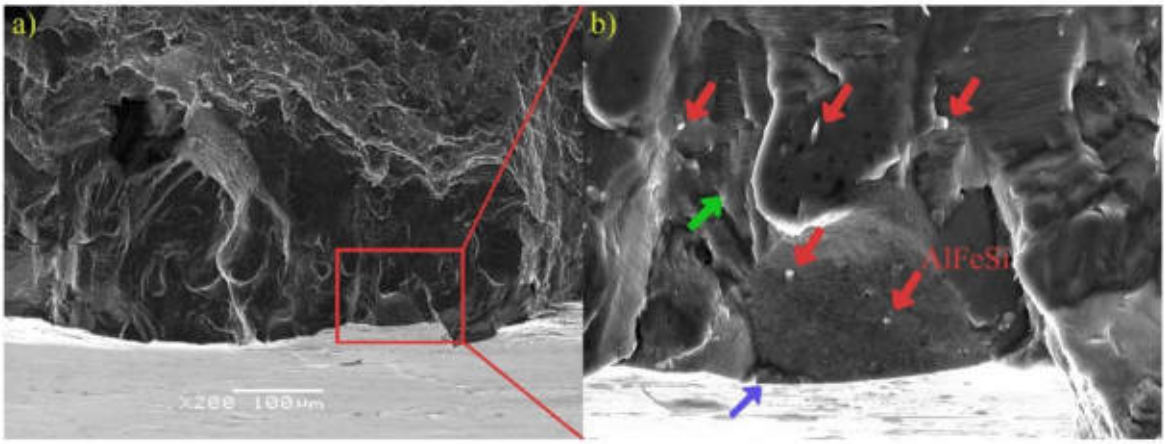

Fig. 7 Fatigue fracture's fragment presented previously in **Fig. 6**, after the specimen was tilted; side specimen's surface can be seen

The biggest, and probably the longest propagating crack, formed due to coalescence of small cracks present on the inner specimen's surface (**Fig. 8**). The blue arrows point the small cracks' origins, which are both on the inner and outer specimen's surface. It is not surprising for the axial loading, since the stress is the same in the whole cross section.

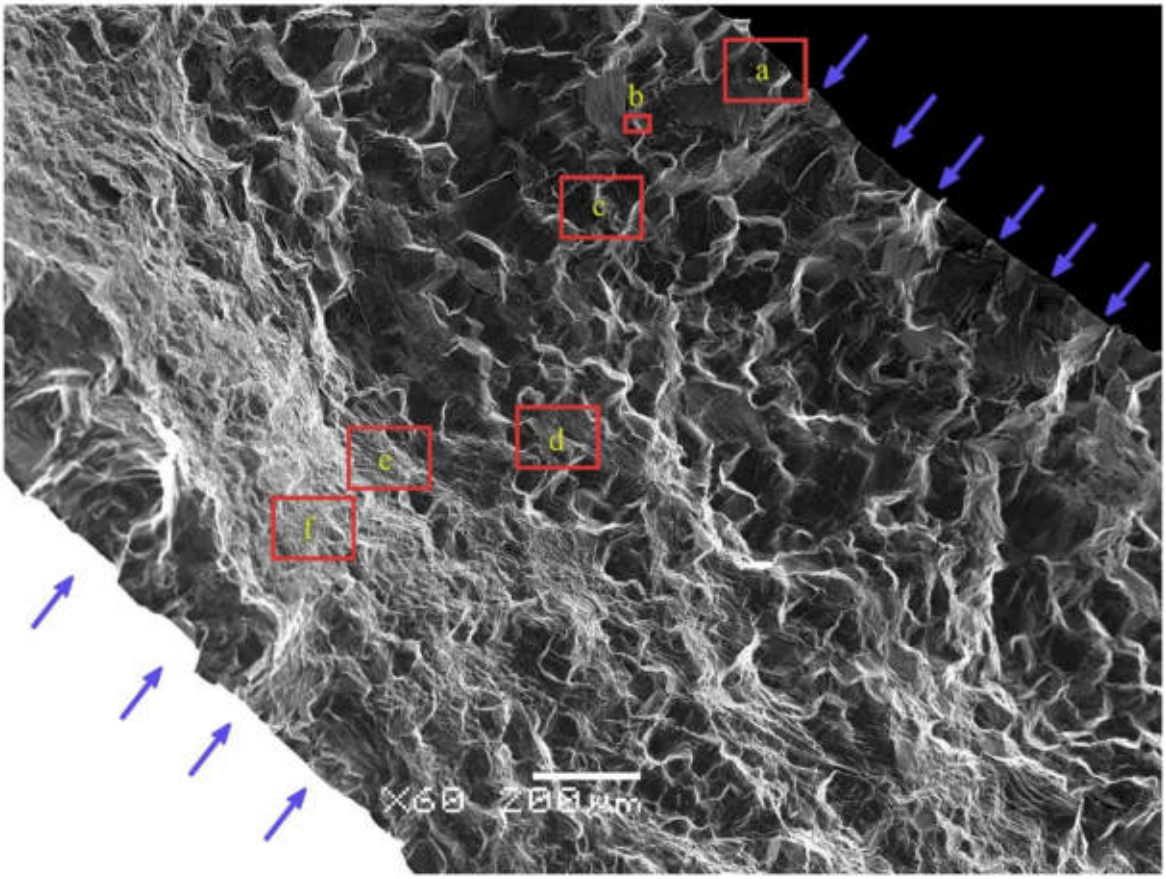

Fig. 8 Fatigue fracture's fragment (**Fig. 5.b**), in which the crack formed by the coalescence of small cracks on the inner surface of specimen, is visible. The marks regard the magnifications presented in **Fig. 9**

The first stage of fatigue crack development was the initiation and development of small cracks (**Fig. 9.a**). In the small cracks' initiation area, the fracture is brittle and forms the flat surfaces, on which the mutual influence of neighboring cracks was not observed. The small crack grew this way through approximately three grains, and then linked to form the common

front, which propagated into the specimen's material. The first striations can be observed at a distance of approximately 0.2 mm from the specimen's surface (**Fig. 9.b**). They can be noted using higher magnifications. The rate of the crack growth increased with the increment of the crack's size, as evidenced by the increasing distances between the striations (**Fig. 9.c**). In **Fig. 9.d**, apart from the increasing size of the striations, there are also visible numerous secondary cracks, indicated by yellow arrows. **Fig. 9.e** shows a fragment of the fracture where it is still possible to recognize the direction of the crack growth, but it became impossible to distinguish the striations. In **Fig. 9.f**, the local instantaneous zone is observed, i.e. the fracture fragment where the cracks initiated on the inner and outer surfaces linked. There are many voids with the features of ductile fracture. Based on the replication it is known, that this fragment formed in the last 40 cycles of fatigue life. On a macroscopic scale, the major crack propagated from the location indicated by the blue arrow in **Fig. 10.a**, along the circumference to the instantaneous zone. But when magnifying such a fracture fragment (**Fig. 10.b**), it is observed that nothing indicates such a direction of crack propagation. Small cracks, linked by a coalescence mechanism, propagated in the direction from the inner and outer surfaces to the center of the specimen's cross section.

Fig. 11.a shows a fragment of the instantaneous fracture zone which has the features of a ductile fracture. There is a visible narrowing of the specimen's wall thickness and numerous voids, which indicate a very high deformation. Under magnification (**Fig. 11.b, Fig. 11.c**), larger transgranular fracture voids that nucleated around the AlFeSi precipitations, and smaller intergranular fracture voids can be distinguished.

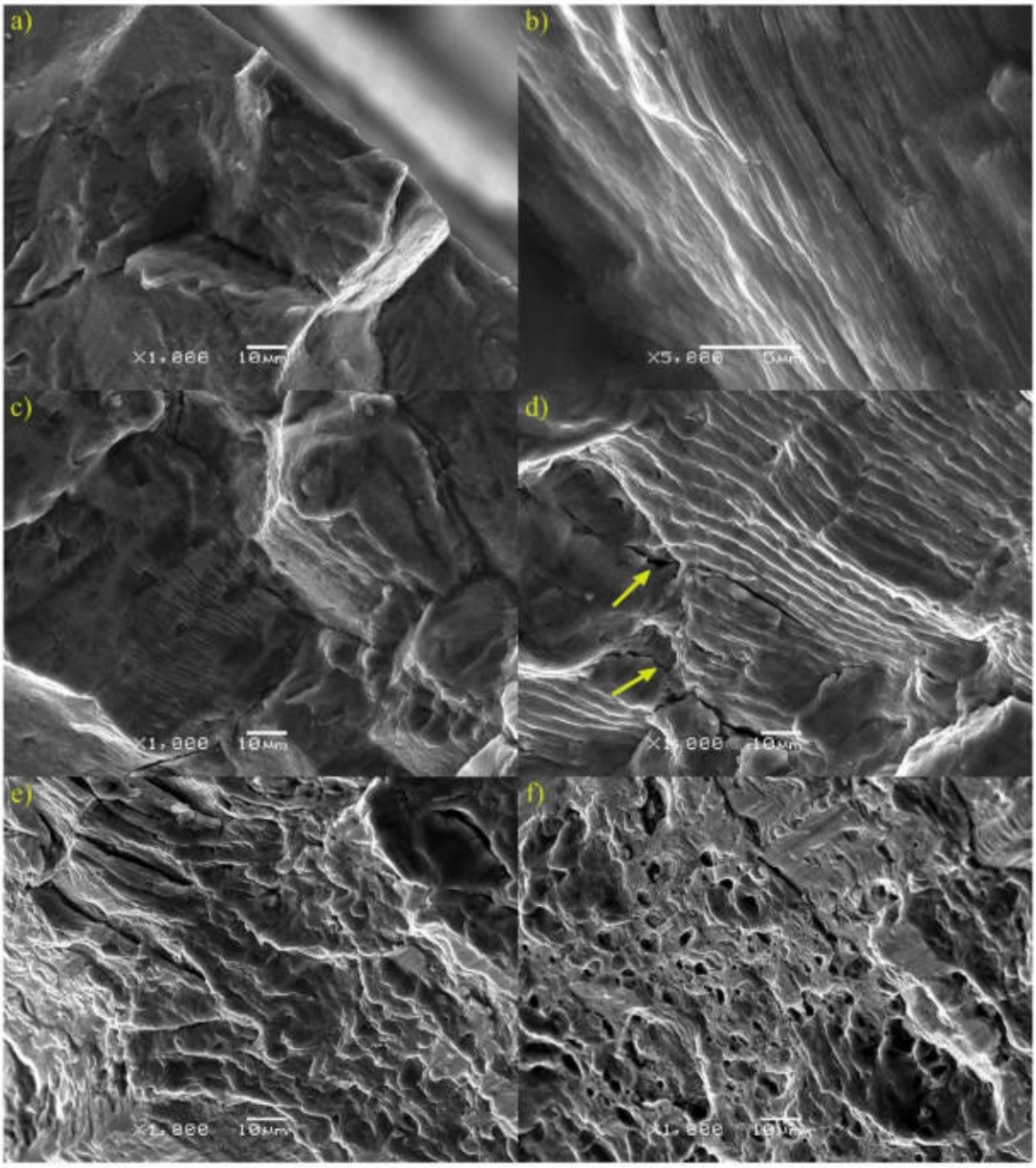

Fig. 9 Magnification of successive fracture fragments shown in Fig. 8. a) initiation of small cracks, b), c), d) propagation with the striations, e, f) rapid growth of the main crack

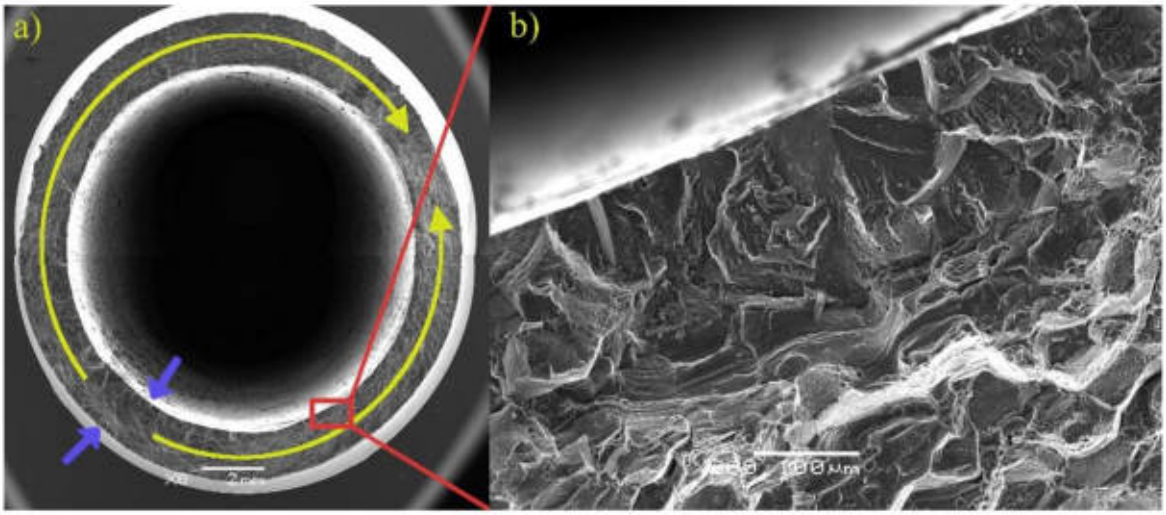

Fig. 10 The coalescence of small cracks during the main crack propagation. a) a schematic representation of the main crack propagation in the last 40 fatigue life cycles, b) coalescence of small cracks included in the main crack

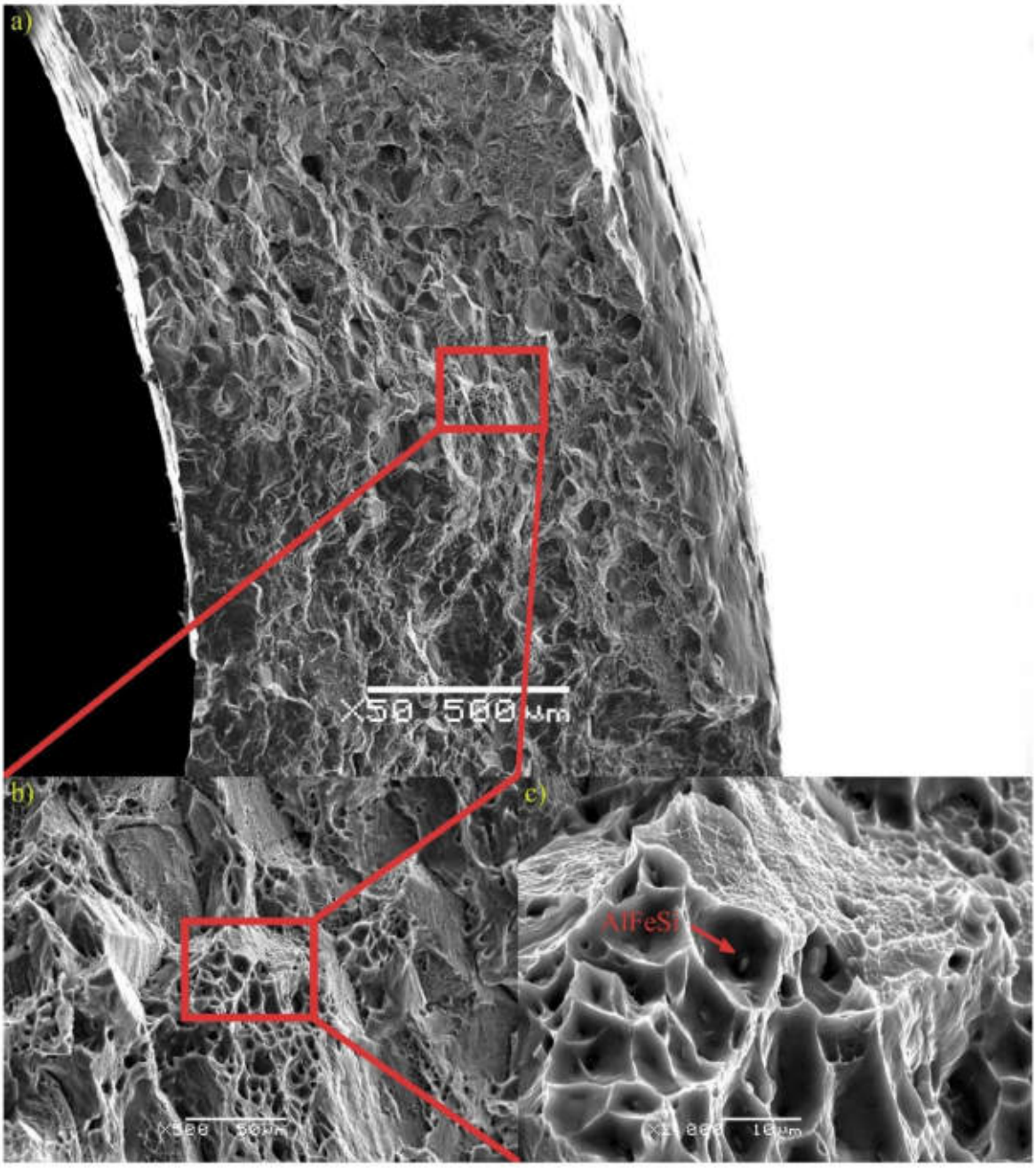

Fig. 11 Fragment of the instantaneous fracture zone shown in **Fig. 5**.d. Figures b) and c) are the further magnifications of this shot

4 Conclusions

The research confirmed the coalescence of small cracks, and at the same time showed that the cracks propagated towards the center of the specimen's cross-section. Using surface replication technique, it was observed that the crack propagation stage was a relatively small part of the fatigue life of the specimen. The main crack propagation proceeds from the inner and outer surfaces of the sample towards the center of the cross-section, and not from one origin to the instantaneous fracture zone. Ductile fracture with voids and narrowing is observed in the instantaneous fracture zone.

The presence of AlFeSi precipitates has a distinctly different impact on the various stages of fatigue crack development. There was no noticeable effect on the initiation and

propagation of small cracks. At the propagation stage, in which striations are visible, these precipitations had little effect on the development of the crack. A very clear effect can be noticed in the instantaneous fracture zone of the specimen, in which they became the nucleus of voids, but from the point of view of the entire fatigue process, this stage is of little importance.

The conducted research shows that the vast majority of the specimen's fatigue life is spent to the formation of small cracks, which initiate as a result of the shear mechanism. This explains the results of the previous analyzes of fatigue life prediction methods. They showed that the application of the fatigue damage parameter, based on the maximum shear strain, resulted in the most accurate estimation of the fatigue life [14].

References

1. N. Shamsaei and A. Fatemi, Int. J. Fatigue **58**, 126 (2014)
2. K. S. Chan and J. Lankford, Acta Metall. **36**, 193 (1988)
3. R. Molaei, A. Fatemi, and N. Phan, Int. J. Fatigue **117**, 352 (2018)
4. W. Zhang and R. Akid, Fatigue Fract. Eng. Mater. Struct. **20**, 547 (1997)
5. N. Gao, M. W. Brown, K. J. Miller, and P. A. S. Reed, Int. J. Fatigue **29**, 565 (2007)
6. C. T. Hua and D. F. Socie, Fatigue Fract. Eng. Mater. Struct. **8**, 101 (1985)
7. Y. Z. Wang, J. D. Atkinson, R. Akid, and R. N. Parkins, Fatigue Fract. Eng. Mater. Struct. **19**, 51 (1996)
8. J. Szusta and A. Seweryn, Int. J. Fatigue **33**, 255 (2011)
9. T. Itoh and T. Yang, Int. J. Fatigue **33**, 1025 (2011)
10. K. Walat, M. Kurek, P. Ogonowski, and T. Łagoda, Int. J. Fatigue **37**, 100 (2012)
11. C. Cauthen, K. V. Anderson, D. Z. Avery, A. Baker, C. J. Williamson, S. R. Daniewicz, and J. B. Jordon, Int. J. Fatigue **140**, 105790 (2020)
12. Ł. Pejkowski and D. Skibicki, Int. J. Fatigue **128**, (2019)
13. D. Skibicki and Ł. Pejkowski, Int. J. Fatigue **123**, 66 (2019)
14. Ł. Pejkowski and J. Seyda, Int. J. Fatigue **142**, 105904 (2021)
15. J. Seyda, L. Pejkowski, and D. Skibicki, Procedia Struct. Integr. **28**, 1458 (2020)
16. S.-T. Tu and X.-C. Zhang, Ref. Modul. Mater. Sci. Mater. Eng. (2016)
17. L. Aydi, M. Khlif, C. Bradai, S. Spigarelli, M. Cabibbo, and M. El Mehtedi, Mater. Today Proc. **2**, 4890 (2015)
18. S. K. Panigrahi, R. Jayaganthan, and V. Pancholi, Mater. Des. **30**, 1894 (2009)

International Journal of Fatigue 184 (2024) 108282

Contents lists available at ScienceDirect

International Journal of Fatigue

journal homepage: www.elsevier.com/locate/ijfatigue

Study on the behavior of small cracks in PA38-T6 (6060-T6) aluminum alloy under multiaxial fatigue loadings

Jan Seyda [a,b], Łukasz Pejkowski [a,b,*], Mateusz Chorobiński [a,b]

[a] Faculty of Mechanical Engineering, Bydgoszcz University of Science and Technology, al. prof. S. Kaliskiego 7, 85-796 Bydgoszcz, Poland
[b] Faculty of Chemical Technology and Engineering, Bydgoszcz University of Science and Technology, al. prof. S. Kaliskiego 7, 85-796 Bydgoszcz, Poland

ARTICLE INFO

Keywords:
Multiaxial loading
Asynchronous loading
Small cracks
Damage mechanism

ABSTRACT

This study investigated the effects of multiaxial cyclic loading on the initiation and propagation of fatigue cracks in an industrial-grade aluminum alloy. Four different loading cases, including 90° out-of-phase and asynchronous loading, were used under the control of strain. The study used cellulose acetate film replication and SEM fractography techniques to increase the understanding of the evolution of fatigue damage on specimen surfaces. The material exhibited a shear damage mechanism with a significant amount of small cracks coalescence. It was explained why, despite a high agreement with the assumptions of the critical plane approach, the predicted fatigue life was overestimated at high loading levels. A correlation between the crack initiation period and overall fatigue life, regardless of loading case, was presented, which has a potential for practical applications.

1. Introduction

Predicting multiaxial fatigue life is a broad field that involves the formulation of many Fatigue Damage Parameters (FDPs), which are used to predict fatigue life [1–5]. FDPs found in the literature can be grouped based on the physical quantities they are derived from. These quantities typically include ranges of shear and normal strains, stresses and energies. Depending on the material under investigation [6,7] and the characteristics of the loading, these parameters can estimate fatigue life with varying degrees of accuracy [8]. FDPs based on the critical plane approach have become particularly popular [9–13]. The critical plane is defined as a plane where the value of a certain parameter reaches its maximum.

The response of any metal to loading depends on its microstructure [14], from the structure of the crystallographic lattice to the grain sizes and the structure of the precipitates and dislocations [15,16]. Characterization of fatigue process, without going into the atomic scale and the interactions of individual grains, phases, dislocations, oxidation of grain boundaries or the tips of cracks [17], can be realized by analyzing the process of initiation and growth of small cracks occurring in the material during cyclic loading in order to develop predictive models [18]. In the paper by Kanazawa et al. [19], the influence of the phase shift between components of multiaxial loading on the direction of small crack growth and its correlation with the plane of maximum shear strain was analyzed. In the paper by Zhang and Miller [20], it was shown that a longer fatigue life was observed in specimens preloaded axially and then torsionally than in pure torsionally loaded specimens. The reasons for this phenomenon are the features of the crack growth mechanism, especially related to the direction of initiation of small cracks depending on the loading case. Based on the results of such analyses, a whole range of FDPs was created that significantly improved the accuracy of fatigue life prediction [21].

The process of fatigue damage can be divided into three stages, known as crack nucleation, crack growth, and final failure. During crack nucleation, microscale phenomena occur within individual grains through the formation of slip bands. In the propagation stage, initiated cracks propagate and increase in size with each loading cycle. At small crack sizes, propagation is influenced by the local strain state (stage I), and such cracks are referred to as small cracks. Once cracks exceed a certain size, typically around a few hundred micrometers, their transition to long cracks occurs, as they begin to create their own plastic zone at the crack tip [22], and the crack growth shifts to stage II. Stage II involves the formation of fatigue striations, which can be observed on the fracture surface of damaged specimens. The third stage is the final failure of the specimen or unstable crack growth (stage III), accompanied by a noticeable decrease in material stiffness, and the fatigue striations on the fracture surface transform into an irregular fracture surface [23]. The analysis of the mechanism of initiation and propagation of

* Corresponding author.
E-mail address: lukasz.pejkowski@pbs.edu.pl (Ł. Pejkowski).

https://doi.org/10.1016/j.ijfatigue.2024.108282
Received 5 January 2024; Received in revised form 23 February 2024; Accepted 13 March 2024
Available online 22 March 2024
0142-1123/

small cracks is crucial for identifying the loading parameters on which the fatigue damage accumulation process depends [24,25].

The aim of the present paper was to study the effect of multiaxial cyclic loading on the process of fatigue crack initiation and propagation in a frequently used industrial aluminum alloy. The paper presents the results of fatigue tests for four selected loading cases, including non-proportional and asynchronous combinations, in the elastic–plastic deformation range. It is a continuation of research performed earlier, concerning the analysis of cracks observed on the surface of specimens after fatigue tests [8] and the analysis of the effect of out-of-phase and asynchronous loadings on the stress–strain response [26]. Emphasis in this paper is placed on the analysis of fatigue damage development on the surface of specimens during fatigue tests and fractographic analysis of specimen fractures. A combination of observation techniques using cellulose acetate film replication and SEM fractography provided a deeper understanding of the importance of loading complexity on fatigue damage development. An analysis was conducted to study the effect of loading case characteristics on the stages of crack initiation and propagation, growth rate, and small crack initiation directions. The relationship between the crack initiation stage and the fatigue life of specimens, regardless of the loading case, was recognized. The observed phenomena have been related to the waveforms of shear and normal strains on the plane of initiation of small cracks.

2. Materials and methods

Thin-walled specimens manufactured from PA38-T6 aluminum alloy (AW-6060) were used in the study. The chemical composition of the alloy according to PN-EN 573–3 standard is shown in Table 1. The basic mechanical properties, Young's modulus E, 0.2 % offset yield stress σ_{y02}, ultimate tensile strength σ_u and corresponding strain ε_{σ_u}, elastic Poisson's ratio ν_e, cyclic strength coefficient K' and cyclic strain hardening exponent n', which were determined in an earlier paper [26] are shown in Table 2. The geometry of the specimens is shown in Fig. 1. The surfaces of the specimens' gage sections were carefully polished with diamond pastes of a gradation up to 8 μm before loading to remove any scratches and reduce roughness. The polishing resulted in a mirror-like surface with no scratches observable under an optical microscope. The roughness parameter Ra determined with the Mitutoyo Surftest SJ-210 was $Ra = 0.040$ μm. The gauge diameter of the specimens was measured using an optical measuring microscope.

Some of the experimental results were generated in the earlier research [26,27]. The data set is quite extensive and unique, and therefore eagerly used by other authors [5,28–31]. In order to apply the cellulose acetate film replication technique, the present research replicated the selected cases and loading levels. It is to be emphasized that the specimens used in the previous and present experiments were made from exactly the same batch of material and in the same manufacturing process. The specimens were subjected to cyclic tension–compression (TC), torsion (TOR), 90° out-of-phase loading (OP), and asynchronous loading (ASN1). The parameters of the strain waveforms for these cases are presented in Table 3, where ε_a, γ_a, f_ε, f_γ are amplitudes and frequencies of normal and shear strains, respectively, φ is a phase shift angle, and λ is the shear to normal strain ratio. Strain paths, waveforms and signal parameters are shown in Fig. 2.

The fatigue tests were conducted on an Instron 8874 servo-hydraulic axial–torsional testing machine aligned according to ASTM E1012–14 procedure. An Epsilon 3550 axial–torsional extensometer was used to strain-control the tests. Control, programming, and signal recording were performed using the WaveMatrix software. The recorded signals were processed and analyzed using MATLAB R2023a and Microsoft® Excel® for Microsoft 365 software. The specimen failure criterion (N_f) was a 5 % decrease in the axial force. A similar definition was applied for pure torsional loading in the torsional channel. The beginning of loading drop is usually considered as a moment of crack initiation [32]. Based on the hysteresis loops from the middle of the fatigue life, the strain and stress ranges were determined. The shear stress values were calculated using the midsection method, following the recommendations of the ASTM E2207-02 standard, for the elastic–plastic strain range [33]:

$$\tau = \frac{16T}{\left(\pi\left(d_o^2 - d_i^2\right)\left(d_o + d_i\right)\right)} \tag{1}$$

The equivalent stress values were determined as the maximum over time:

$$\sigma_{eq} = \max_t\left(\sqrt{\sigma(t)^2 + 3\tau(t)^2}\right) \tag{2}$$

where $\sigma(t)$ and $\tau(t)$ are instantaneous values of normal and shear stresses, respectively. The equivalent total strain was calculated alike, considering additionally the elastic–plastic deformation regime:

$$\varepsilon_{eq} = \max_t\left(\frac{1}{\sqrt{2}\left(1+\nu_{eq}\right)}\sqrt{2\varepsilon(t)^2\left(1+\nu_{eq}\right)^2 + \frac{3}{2}\gamma(t)^2}\right) \tag{3}$$

where $\varepsilon(t)$ and $\gamma(t)$ are instantaneous values of normal and shear total strains, and equivalent Poisson's ratio is given by:

$$\nu_{eq} = \frac{\nu_e\varepsilon_{eq}^e + \nu_p\varepsilon_{eq}^p}{\varepsilon_{eq}} \tag{4}$$

where ν_e is the elastic Poisson's ratio, ν_p is the plastic Poisson's ratio, $\varepsilon_{eq}^e = \sigma_{eq}/E$ is the equivalent elastic strain and $\varepsilon_{eq}^p = \varepsilon_{eq} - \varepsilon_{eq}^e$ is the equivalent plastic strain. Plastic Poisson's ratio was set to be $\nu_p = 0.5$, due to the plastic incompressibility assumption. The Basquin curve (5), and the Basquin-Manson-Coffin curve (6) were determined, based on the uniaxial fatigue data, using the least square curve fitting. Linear functions were fitted in a double logarithmic coordinates. The independent variable was the logarithm of elastic strain amplitude, $\log(\varepsilon_a^e)$, plastic strain amplitude, $\log(\varepsilon_a^p)$, or stress amplitude, $\log(\sigma_a)$. The dependent variable was the logarithm of the number of reversals to failure, $\log(2N_f)$. The Basquin and Basquin-Manson-Coffin equations are given below:

$$\sigma_a = \sigma_f'\left(2N_f\right)^b \tag{5}$$

$$\varepsilon_a = \varepsilon_a^e + \varepsilon_a^p = \frac{\sigma_f'}{E}\left(2N_f\right)^b + \varepsilon_f'\left(2N_f\right)^c \tag{6}$$

where σ_a is the stress amplitude, σ_f' is the fatigue strength coefficient, b is the fatigue strength exponent, $2N_f$ is the fatigue life in reversals to failure, ε_a is the total strain amplitude, ε_a^e is the elastic strain amplitude,

Table 2
Basic mechanical properties of PA38-T6 aluminum alloy determined experimentally [26].

E, GPa	σ_{y02}, MPa	σ_u, MPa	ε_{σ_u}, mm/mm	ν_e, –	K', MPa	n', –
68.3	191.5	229.1	0.094	0.35	288.1	0.051

Table 1
Chemical composition of PA38 aluminum alloy according to PN-EN 573–3 standard.

Element	Si	Fe	Cu	Mn	Mg	Cr	Zn	Ti	Other	Al
Percentage	0.3–0.6	0.1–0.3	<0.1	<0.1	0.35–0.6	<0.05	<0.15	<0.1	<0.15	Balance

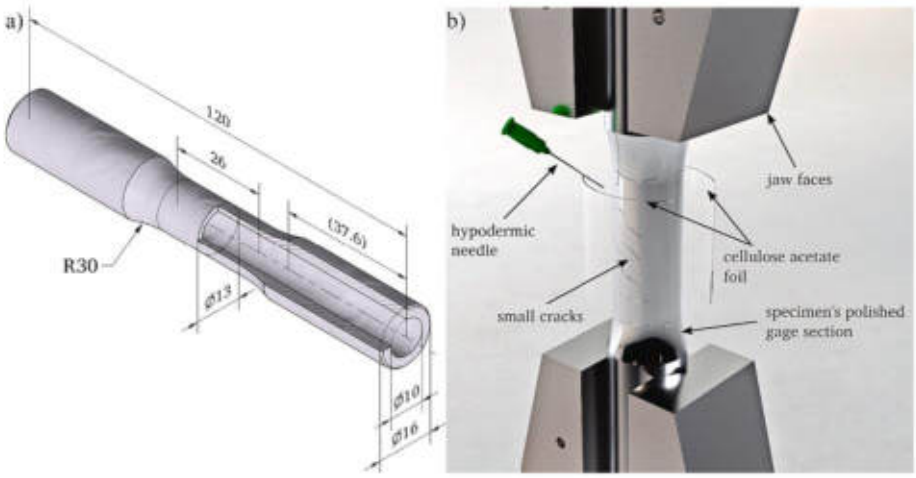

Fig. 1. (a) geometry of thin-walled pa38-t6 aluminum alloy specimens (dimensions in millimeters), (b) replication procedure.

Table 3
Waveform parameters for selected loading cases.

Channel	Waveforms			
Axial	$\varepsilon(t) = \varepsilon_a \sin(2\pi f_\varepsilon t)$			
Torsional	$\gamma(t) = \gamma_a \sin(2\pi f_\varepsilon t + \varphi)$			
	Loading case			
Signal parameters	TC	TOR	OP	ASN1
$\lambda = \gamma_a/\varepsilon_a$	0	∞	$\sqrt{3}$	$\sqrt{3}$
φ	0	0	$\pi/2$	0
f_γ/f_ε	1	1	1	1/2

ε_a^p is the plastic strain amplitude, $\varepsilon_f^{'}$ is the fatigue ductility coefficient, and c is the fatigue ductility exponent. The Basquin-Manson-Coffin parameters fitted for the aluminum alloy under study are shown in Table 4.

The 125 μm thick cellulose acetate film along with auxiliary tools were used for replica fabrication (Fig. 1(b)). To capture the entire surface of the specimens, the fatigue tests were conducted in two stages. In the first stage, the tests were strain-controlled to record the displacement history of the testing machine heads and fatigue life. In the second stage, the first step was repeated without the extensometer attached. Based on the recorded history, the machine heads displacement was controlled and the tests were paused every 10 % of the expected fatigue life to produce surface replicas of the specimen. The replication procedure, developed based on a description in Shamsaei's thesis [34], was adapted to the conditions of the current study and described more in [35]. A Delta Optical MET-1000-TRF metallographic microscope equipped with a DLT-Cam PRO 12MP digital camera and dedicated DLTCamViewer software was used to take pictures of the replicas. Direct photographs of the specimens were registered using the Olympus Lext OLS 4000 laser confocal microscope. An objective magnification × 50 was used to obtain a 2D and 3D images. The scan size was 258 μm × 258 μm. SEM images of the specimen fractures and EDS chemical composition analysis were performed on a JEOL JSM-6480LV scanning electron microscope using a dedicated tilting cylindrical specimen mounting table. The surfaces of the metallographic specimens were ground and polished with a diamond suspension with a gradation of up to 1 μm on a FORCIPOL 202 metallographic grinder-polisher. Keller's reagent, which contained 0.5 ml HF (40 %), 1 ml HCl (31 %), 1.5 ml HNO3 (80 %), and 47 ml H2O, was used to etch the polished surfaces of the specimens for 300 s at room temperature. The images of the metallographic specimens were recorded on an optical metallographic microscope. Grain size was determined under the ASTM E112 standard.

3. Results

Fig. 3 shows the metallographic cross-sectional views of the axial and transverse sections of the tested specimens to give a basic view of the material's microstructure. Clear grain boundaries and distribution of precipitates are visible. The size of the grains and their distribution are homogeneous. The grain sizes for the axial and transverse sections are $n_a = 5.5$ and $n_t = 5.7$, corresponding to averages of 59 μm and 57 μm, respectively. The axial section (Fig. 3(a)) shows bands of clusters of AlFeSi precipitates. This is a remnant of chemical inhomogeneity after the tube drawing treatment.

The fatigue life testing results of the tests performed under the strain and displacement control were compiled together with the results of earlier tests in a strain-fatigue life plot in Fig. 4, where fatigue life is given as a number of cycles to failure, N_f. Since in the case of

Table 4
Parameters of the Basquin-Manson-Coffin curve for PA38-T6 aluminum alloy.

$\sigma_f^{'}$, MPa	b, –	$\varepsilon_f^{'}$, mm/mm	c, –
392.65	−0.08788	0.6368	−0.8336

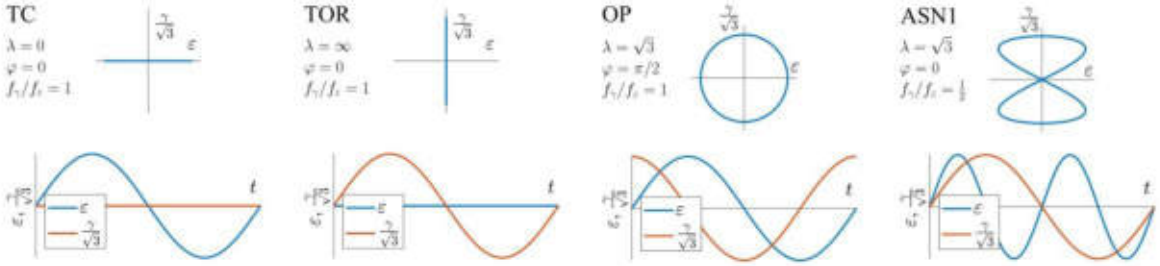

Fig. 2. Strain paths, waveforms and parameters of applied loadings.

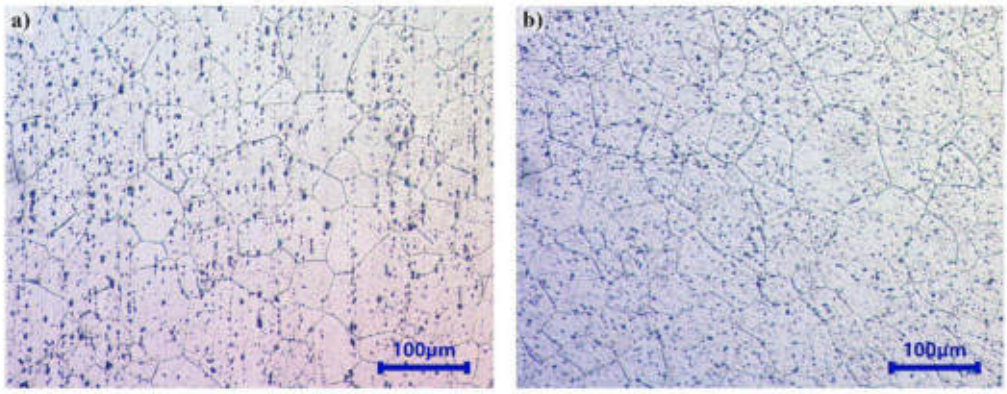

Fig. 3. PA38-T6 microstructure in (a) axial and (b) transverse sections of the metallographic specimens.

asynchronous loading, N_f cannot be determined unequivocally, it is presented on two separate plots, counting cycles from the axial channel (Fig. 4(a)) and the torsional channel (Fig. 4(b)). Colors represents various loading scenarios. The symbols used indicate: empty circles – results from previous tests (non-polished specimens, strain control); full circles – polished specimens, strain control; triangle – polished specimens, displacement control (no extensometer, surface replication). The Basquin-Manson-Coffin (BMC) curve, fitted to the axial tests data, is also shown in Fig. 4.

Longer fatigue life is observed in the proportional loading cases (TC and TOR) compared to the non-proportional cases (OP and ASN1). Depending on how the cycles are counted, the ASN1 case resulted in a fatigue life similar to or shorter than the OP case. Such correlations can be observed by comparing the tests using the Huber-Mises equivalent strain ε_{eq}. When comparing the fatigue life as a function of Huber-Mises equivalent stress, σ_{eq} (Fig. 5), no such relationship is observed. These differences result from additional cyclic hardening visible in Fig. 6, where the non-proportional cases can be distinguished. On this graph, the loading cases and test methods are labeled the same as in Fig. 4. Fig. 6 also presents the monotonic tensile curve (*Mon.*) and the ultimate tensile strength (R_m) for reference. The TC and TOR loading cases present less cyclic hardening. In contrast, at higher OP and ASN1 loading levels, the stress amplitudes exceed the R_m values. A more detailed analysis of this issue is presented in the paper by Pejkowski and Skibicki [26].

The moment of appearance of the first cracks, the direction and density of the cracks and their development during the fatigue tests were investigated using replicas of the specimens' surfaces. Selected replicas made at fatigue life close to N_f are shown in Fig. 7. All shots were taken so that the axis of the specimens is in the vertical position. At the top of each shot, the loading case, loading level, the percent of the fatigue life, and the number of cycles at which the replica was made were given. The size marker on the bottom-right shot applies to all the shots shown. Some shots show air bubbles, which are an imperfection of the replicas as a secondary effect of significant surface deformation just before the specimens failed, as can also be seen in other papers [36,37].

Regardless of the loading case and level, the coalescence of small cracks was recognized as the dominant mechanism of macro cracks formation in the studied loading range. Small cracks initiated and propagated independently of each other until the tips of adjacent cracks approached each other. Then, they linked into one larger crack, which grew faster than the previous ones. The coalesced cracks linked into an increasing number of successive small cracks until the specimen fracture. Despite the loading case, the density of the cracks increased with the strain level. The cracks initiated faster and closer to each other, and therefore linked at shorter lengths.

For the TC case, small cracks usually initiated at angles of 45° to 90° relative to the specimen axis. This is explained more extensively in the Discussion section. Small cracks are visible on the replicas only when at least three small cracks are connected, recognized as connected three straight sections that slightly differ in direction. This means that these cracks formed early on, but remained undetectable by the replication technique because the cellulose acetate dissolved in acetone did not penetrate the crack fissure. In the later stages of crack growth, the linking of successive individual small cracks into the tip of a larger crack was observed. When the small cracks linked, they did not propagate further in the original direction. Rather, only the tips of the large cracks

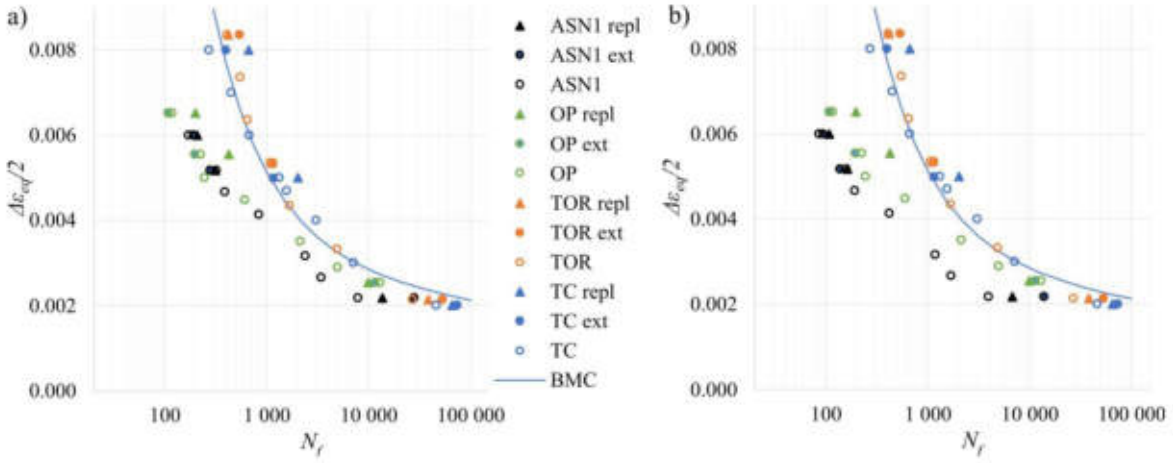

Fig. 4. Strain-fatigue life graphs along with Basquin-Manson-Coffin (BMC) curve for axial loading. For the ASN1 case, the number of cycles in the graph (a) based on the axial channel, (b) based on the torsional channel.

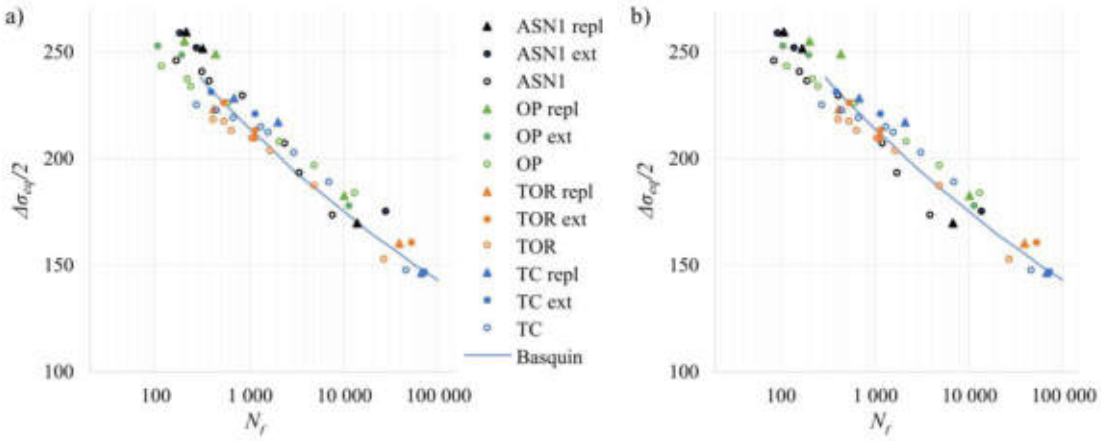

Fig. 5. Stress-fatigue life graphs along with Basquin curve for axial loading. For the ASN1 case, the number of cycles in the graph (a) based on the axial channel, (b) based on the torsional channel.

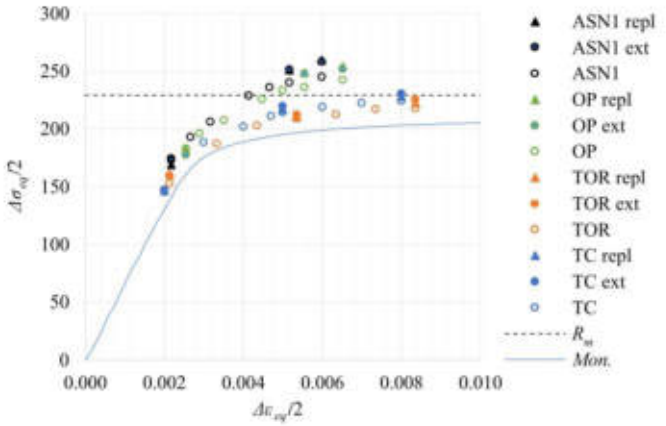

Fig. 6. Cyclic hardening – midlife peak stresses compared with a fragment of the stress–strain response from the monotonic tensile test (Mon.), and the ultimate tensile strength (R_m).

propagated further randomly to the next, closest crack. Cracks that have been "covered" by a larger crack nearby have stopped propagating. This phenomenon has been described previously in [23].

For the TOR case, the direction of initiation and propagation of small cracks was 0° and 90° relative to the specimen axis. The small cracks coalesced to form a network of cracks, but unlike under TC, when they encountered a second crack, they continue to propagate in the same direction. Propagating in a single straight line, cracks often become much longer than the average grain size. In all TOR specimens, the main crack formed in the 0° direction relative to the specimen axis.

For the OP case, small cracks were observed in all directions, but cracks propagating at 90° regarding the specimen axis were noticeably larger. Fragments of the main crack at different angles are often links connecting parallel cracks, formed because of the interaction between two crack tips [25]. On the specimen's surface at a high level of loading, significant surface wrinkling can be observed, which distinguishes it from TC and TOR tests. The density, propagation rate, and coalescence of cracks were also higher compared to the previously presented loading cases.

For the ASN1 case, small cracks initiated and propagated in all directions, similar to the OP case. However, two directions stand out, at angles close to 72° and 108°. During the duration of tests, it was observed that cracks propagated in these directions in separate half cycles. Similar to the OP case, significant surface wrinkling was observed.

To illustrate the observed coalescence phenomenon, Fig. 8 shows fragments of a specimen's surface before reaching the failure criterion, as well as one fragment after the failure, where the final main crack is visible. The red arrows show the cracks that participated in the formation of the main crack. It is evident that the coalescence process occurred simultaneously in multiple cracks. The same phenomenon was observed in all the tested specimens, regardless of the loading case. The fatigue damage process occurred throughout the entire surface of the specimens. It is not possible to identify a single crack responsible for the formation of the main crack. In the supplementary materials, animations of the development of cracks during the fatigue tests of all studied cases and loading levels, as well as high-resolution images, are provided.

In specimen loaded with the ASN1 case, the zigzag growth phenomenon became evident with the transition to Stage II. The series of slip bands formed during crack tip propagation exhibit notable regularity and symmetry. Fig. 9 presents images of replicas where independently initiated small cracks are indicated by blue arrows. Red arcs mark crack sections with visible zigzag growth that connect previously formed small cracks. The length of slip bands increases proportionally with the crack's length. Some small cracks that are visible in Fig. 9(b) were not discernible in Fig. 9(a), despite their certain existence during the earlier stage. Their pre-existence is evidenced by the lack of slip bands in the case of fragments indicated with blue arrows, which is typical for stage I. Because of their small size, these small cracks did not leave noticeable imprints on the applied replication film. The small cracks have a sharp edge because they formed by the stage I mechanism, while the propagating crack of larger size generates its own plastic zone, which can be recognized by the surface distortion around the crack tip. The direction of regular slip bands in the magnified section of Fig. 9(b) is marked with green lines.

To verify these observations, additional images were taken directly on the specimen's surface, and a 3D image was created using the laser confocal microscope. The surface of the specimen loaded with the ASN1 case at $e_{eq} = 0.002$ is shown in Fig. 10. The same section of the specimen surface is shown from above (Fig. 10(a)) and rotated in space for relief visibility (Fig. 10(b)). Visible crack with a series of slip bands can be seen. Small cracks with no plastic deformation of the surface are visible, as well as deformed fragments with slip bands. During direct observation of crack growth in the final test cycles, it was noted that each of the two directions indicated by the green lines in Fig. 9(a) activated separately in successive loading half-cycles.

The length of the longest crack at the end of the fatigue life L, depending on the loading level, is shown in Fig. 11. As the loading level increased, the length of the longest crack at specimens failure (a 5 % drop of axial force) decreased. The labels next to the points indicate the percentage of the number of cycles relative to the N_f value. The result for the lowest TOR case level should not be compared to the others, because

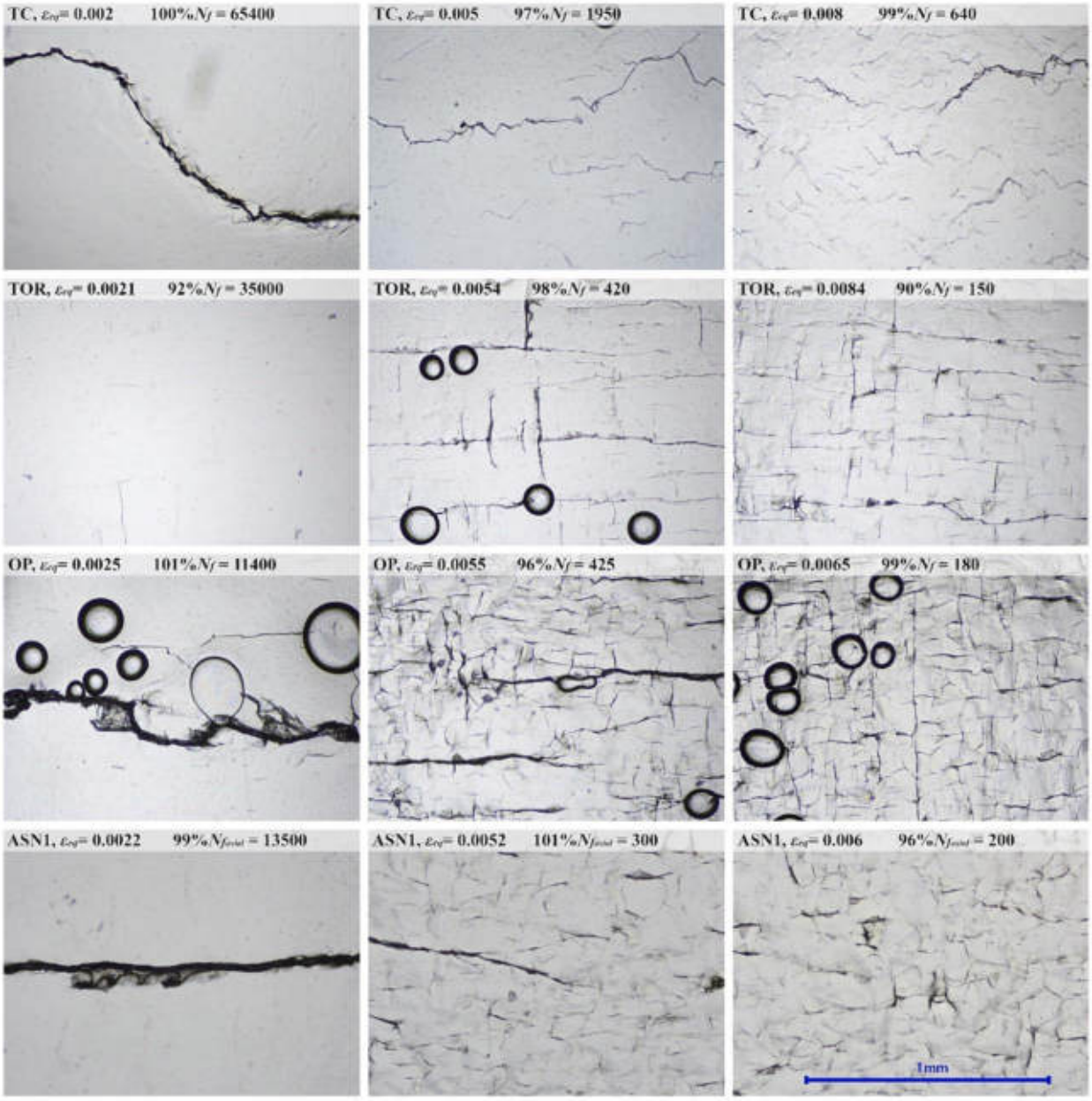

Fig. 7. The specimens' surfaces topography near the end of the life for three loading levels and four loading cases. For each image, the loading case, loading level, percentage of the number of cycles relative to N_f, and the absolute value of the number of cycles are given.

at lower strain levels, the crack initiation stage took a relatively long time. It can be seen how, as the loading level increases, the length of the largest cracks at N_f decreases, while the crack density increases, as seen in Fig. 7.

As discussed in the introduction, the fatigue damage process can be divided into three stages, called crack nucleation, crack growth and final fracture. The moment at which the change in crack initiation to propagation occurred was approximated as the number of cycles at making the first replica with visible cracks. The final failure or unstable crack growth typically began after meeting the criterion of a 5 % drop in the applied force, which defines the value of N_f. Fig. 12 presents the ratio of the number of cycles at the time of first crack detection to the fatigue life, N_i/N_f, depending on the loading case and the applied stress level. The X marks indicate tests in which small cracks definitely formed much earlier than before the first replica was made. This conclusion can be drawn from the high density and clearly initiated process of crack coalescence. This suggests that cracks must have formed in the initial cycles of loading. It should be noted that new small cracks continued to form until the end of the fatigue life of the specimens, regardless of the applied stress level and loading case. Analyzing the results, differences can be observed based on $\Delta\varepsilon_{eq}/2$ or $\Delta\sigma_{eq}/2$ to which the ratio N_i/N_f is compared. In Fig. 12(a), it can be seen that, regardless of the loading level, the N_i/N_f ratio decreases in the following order for the loading cases: TC, TOR, ASN1, and OP, with the non-proportional cases (OP and ASN1) being very close to each other. In Fig. 12(b), where the data is plotted against the equivalent stress level, two groups of cases can be distinguished: the proportional loading cases (TC and TOR), and the non-proportional cases (OP and ASN1) differing in the slope of the curves.

In order to exclude the influence of the loading parameter on interpreting the results, a graph was made showing the relationship between the time when the first cracks were recognized,N_i, and the fatigue life, N_f, (Fig. 13(a)) and between N_i and N_i/N_f ratio (Fig. 13(b)). In these graphs, the tests where small cracks must have formed before the first

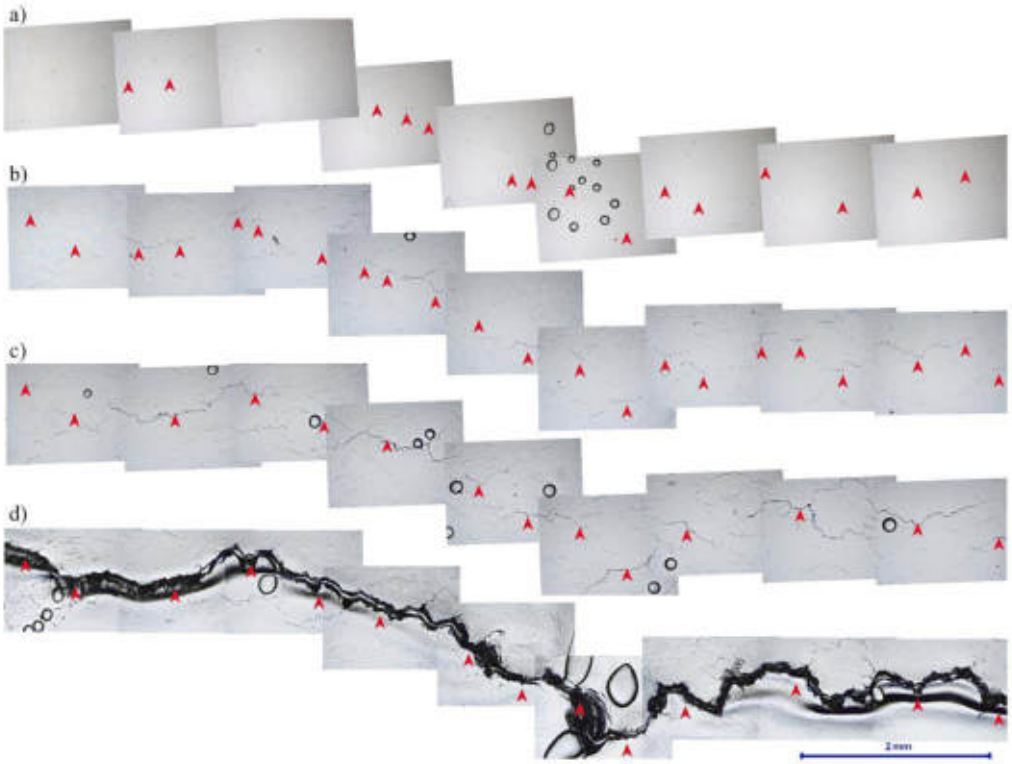

Fig. 8. Formation of the main crack through coalescence, registered using the replication technique; TC $\varepsilon_{eq} = 0.005$, (a) 45%N_f, (b) 75%N_f, (c) 97%N_f, (d) 102%N_f.

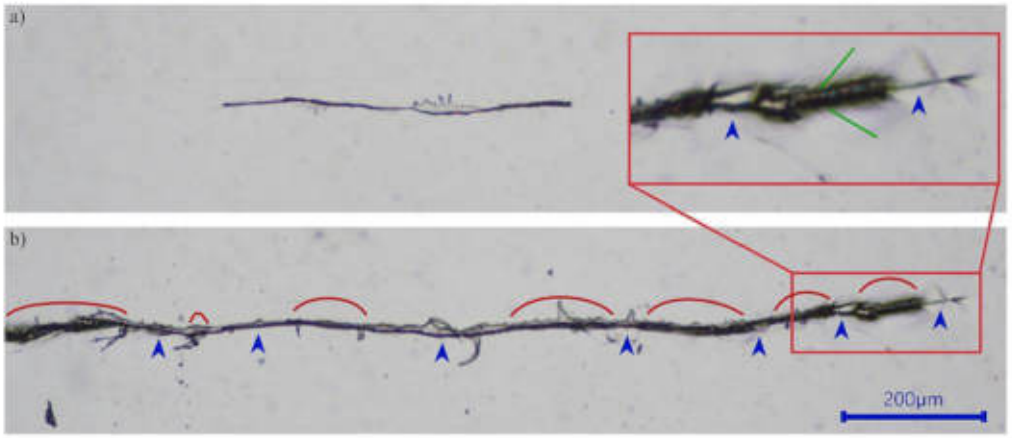

Fig. 9. Crack propagation on the surface of the specimen loaded with the ASN1 case at $\varepsilon_{eq} = 0.002$ (a) 66%N_f and (b) 88%N_f.

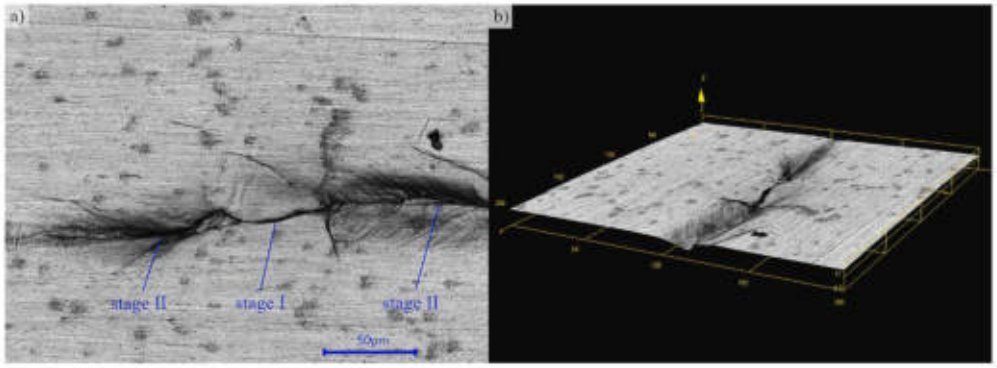

Fig. 10. Crack tip on the surface of the specimen loaded with the ASN1 case at $\varepsilon_{eq} = 0.002$ with visible zigzag crack growth. Images were obtained using the confocal laser microscope.

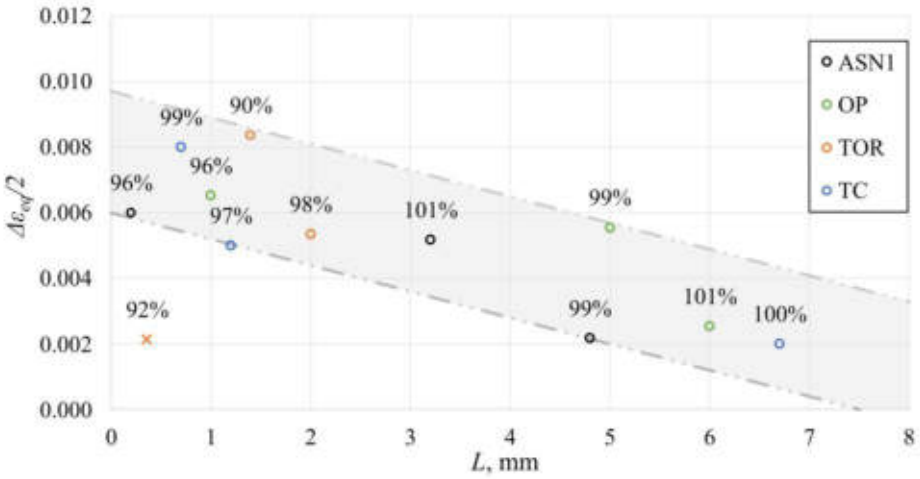

Fig. 11. Length of the largest crack at a time close to N_f. Labels next to the points indicate the percentage of the number of cycles relative to the N_f value.

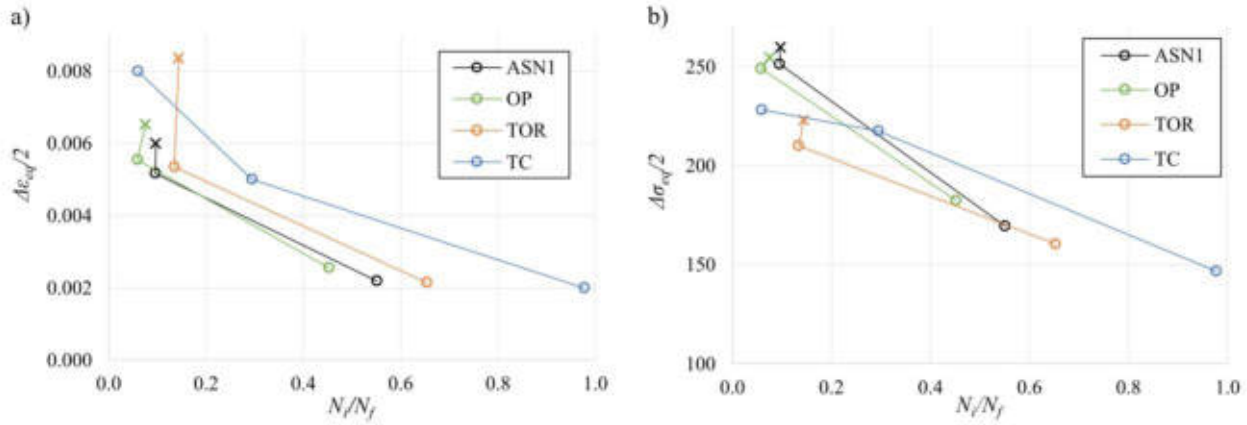

Fig. 12. Comparison of the moment of registration of the first cracks on the external surface of the specimens in relation to the fatigue life of individual specimens depending on the case and the level of (a) equivalent strain, and (b) equivalent stress. The X mark indicates specimens for which the first cracks formed significantly faster than the first replica made.

surface replica was made are marked with X. A power curve is plotted to approximate the results of all tests marked with small circles. It can be observed that all results form a consistent trend. The ratio of N_i/N_f, where the first small cracks can be observed relative to the fatigue life, correlates with the fatigue life itself.

Using the SEM fractography, small cracks origins, crack initiation zones (stage I), and fatigue striations formed during the stage II were identified. Selected fracture images are presented in Fig. 14. Origins of small cracks, indicated by the blue arrows, were formed on the surface of the specimens regardless of the case and loading level. The crack initiation zones are marked with a yellow dashed line. They have a relatively smooth surface and it can be seen that visible fatigue striations propagated from them, increasing in size with distance from the crack origin. Where there was a torsion channel involved (TOR, OP and ASN1), the surfaces of the fractures were almost completely obliterated by surfaces friction in the last phase of failure of the specimens. Despite this, it was possible to find preserved fragments in the fracture depressions providing information about the damage mechanism. As with the use of the replication technique, many crack origins were observed. For individual loading cases, the shape of crack initiation zones and

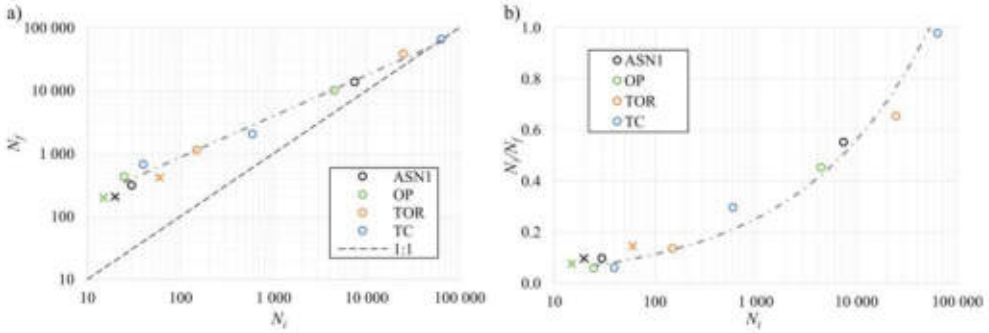

Fig. 13. Comparison of the moment of first crack registration on the Surface N_i (a) with the total fatigue life N_f and (b) with the N_i/N_f ratio and the power curve approximating the results.

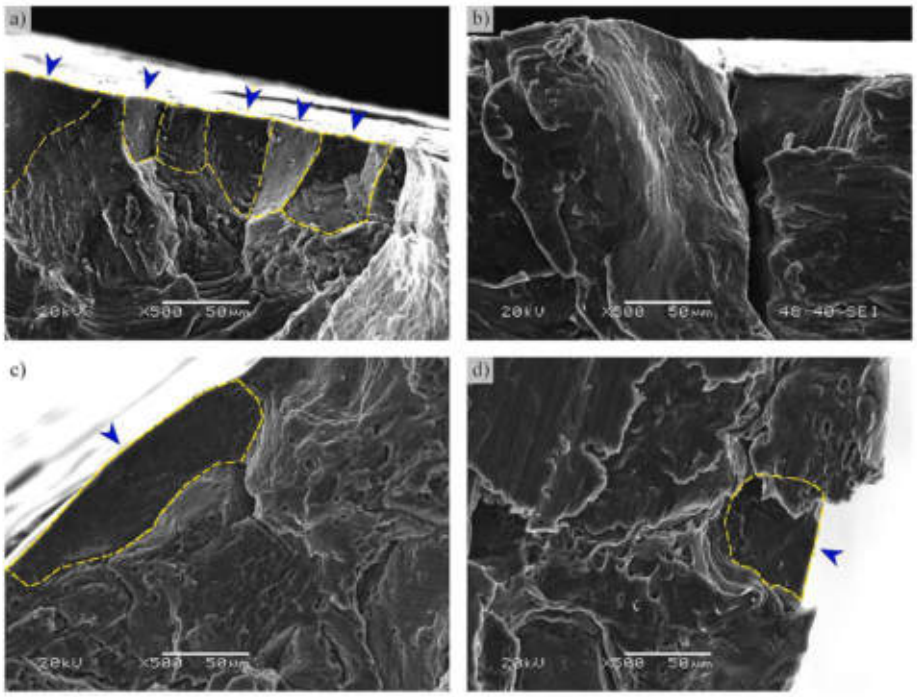

Fig. 14. Small crack initiation zones for selected loading cases. (a) TC $\varepsilon_{eq} = 0.005$, (b) TOR $\varepsilon_{eq} = 0.005$, (c) OP $\varepsilon_{eq} = 0.005$, (d) ASN1 $\varepsilon_{eq} = 0.005$. Blue arrows indicate crack nuclei, and the yellow dashed line indicates the crack initiation zones.

fatigue striations have their own characteristics, but within a single loading case, they differ only in size. As the loading level increased, the crack initiation zone, that is the smooth part of the fracture in which fatigue striations do not appear, decreased.

Crack propagation (stage II) was also observed, forming characteristic fatigue striations (Fig. 15). Small cracks linked neighboring cracks to form a single front that propagated deep into the material. As the crack size increased, the propagation rate also increased. In Fig. 15, multiple origins of small cracks can be observed, pointed by blue arrows, which have linked to form a single crack that propagated toward the center of the specimen cross-section. The zone of initiation (stage I) is marked with a yellow dashed line. Visible fatigue striations showed the direction of propagation, as marked by the red arrows. A red dashed line was used to show the transition from stable propagation (stage II) to uncontrolled propagation (stage III). As the loading level increased, the rate of increase in the distance between the striations increased. The AlFeSi precipitates present in the alloy structure had no noticeable impact on the surface structure of the fractures in stage I. However, in stage II, these precipitates caused distortion of the fatigue striations. A more detailed analysis of the fatigue fracture surface has been presented

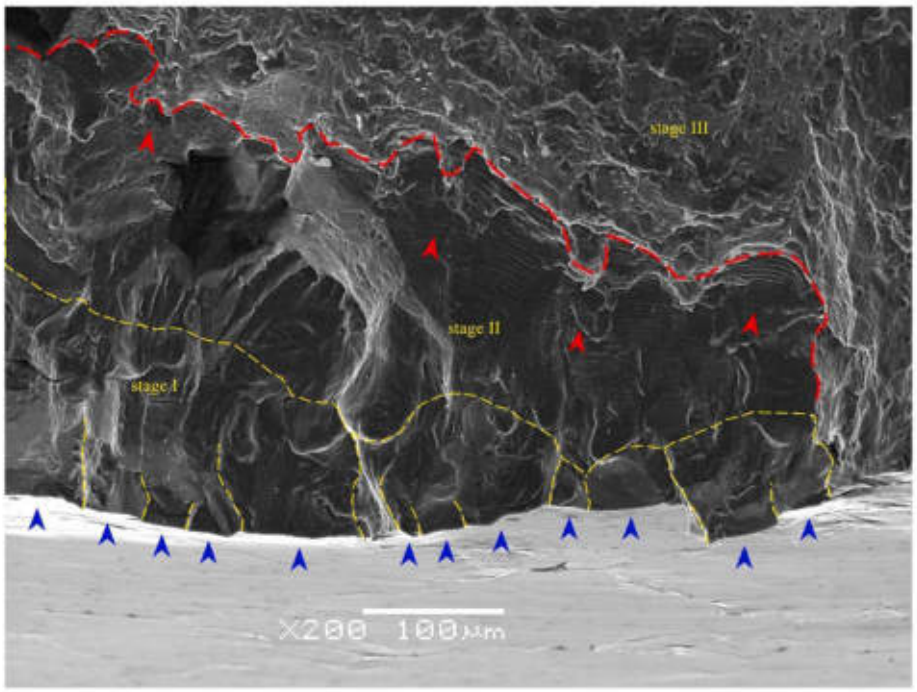

Fig. 15. Propagation of coalesced small cracks deep into the material. TC specimen at $\varepsilon_{eq} = 0.005$.

in [38]. In summary, at higher loading levels, the crack initiation zones were smaller, and the distances between consecutive striations increased faster with each loading cycle for each loading case studied.

Under ASN1 loading, the crack initiation zones exhibited features not observed in other loading cases. It is the only one among the cases tested where small plastic voids, similar to voids formed during monotonic tension, were observed on the crack surfaces. Fig. 16 shows enlarged sections of the specimens' fractures. Blue arrows point to crack origins, yellow dashed lines show crack initiation zones, yellow arrows point to voids and red arrows indicate the direction of crack propagation in fragments with visible fatigue striations. The yellow circle shows visible AlFeSi precipitation. It can be seen how larger voids have formed around such precipitations, but are still much smaller than those formed in the monotonic tensile test.

Fig. 17 shows selected fragments of specimen fractures in which clear fatigue striations are visible. Blue arrows indicate the crack origins, while red arrows show the direction of crack propagation. Comparing the images of replicas and fractures, it can be concluded that in the TC specimens, the propagation process was so slow that stage II was not observed on the surface of the specimens by replication (Fig. 17(a) and (b) vs. Fig. 8). The specimens' fractures near the surface consisted only of linked small cracks, with no stage II involvement near the surface of the specimens. Fatigue striations were formed only after the coalescence of several small cracks and the direction of propagation in each analyzed specimen was from the inner and outer surfaces to the center of the specimen mid-section. In cases of non-proportional loadings (OP and ASN1), faster crack propagation was observed, which could also be seen near the surface of the specimens through many crack bifurcations, indicating the stage II. At the final fractures, fatigue striations occurred much closer to the crack origin (Fig. 17(c), (d)). This phenomenon was most pronounced at the lowest loading levels, where the density of small cracks was the lowest. On the surface of the specimens, crack bifurcation was observed when the length of individual cracks exceeded about 0.4 mm.

4. Discussion

The polishing of the specimen surfaces and the method of control did not noticeably affect the fatigue life results of the tested loading cases in the elastic–plastic strain range. The fatigue life results of the tests performed do not deviate beyond the typical fatigue life scatter of the results of previous tests, as presented in Fig. 18 (see also Figs. 4 and 5). The combination of two microscopic methods for analyzing the fatigue damage mechanism provided a complementary approach, enhancing the understanding of the phenomena occurring in the material. Cellulose acetate foils were employed for replication, enabling precise monitoring of surface crack lengths during the fatigue tests. In turn, SEM fractographic analysis enabled the recognition of crack origins and characterization of the fatigue crack growth process. Fractography provided information about the origins of cracks on the inner surface of the specimens, that was unavailable for replication. Also, the depth and mechanisms of crack growth were identified. By using both techniques, it becomes possible to determine which fragments of the fracture were formed during the tests, and which were formed just before the specimen's failure or after the N_f value was exceeded. Consequently, it offers a more precise interpretation of the test results and a better understanding of the mechanisms of fatigue damage in the tested material.

In the studied aluminum alloy, for the tested loading range, the shear mechanism [39] was recognized as the main damage mechanism. Most of the testing time was taken up by the initiation and propagation of small cracks to small sizes. Fig. 19 shows the distributions of maximum shear and normal strains in the polar system for each loading case and indicates the directions of the maxima (dashed line). The observed directions of initiation and propagation of small cracks correlate with the directions of the planes in which the maximum values of shear strain occur. However, in later stages of crack growth, it is evident that the magnitude of normal strain on the crack plane had a noticeable influence on the crack propagation rate.

Fig. 20 presents the waveforms of shear and normal strains during a single loading cycle, observed on planes with maximum shear strains and the most pronounced cracks development. The agreement between the maximum shear strain plane with the planes where small cracks most frequently initiated was observed. The plane of maximum shear strain at TC is inclined at a 45° relative to the applied axial force. Yet, the intersection of this plane with the specimen's surfaces can generate crack lines positioned at angles ranging from 45° to 135° relative to the

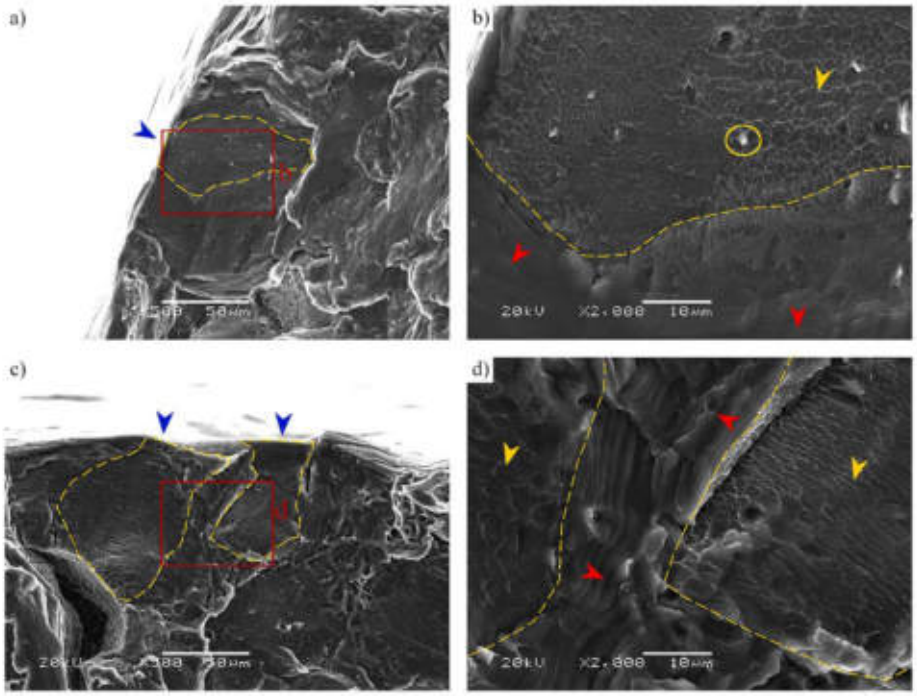

Fig. 16. Micro voids in origins of small cracks in ASN1 case-loaded specimens for levels $\varepsilon_{eq} = 0.005$ (a, b) and $\varepsilon_{eq} = 0.006$ (c, d).

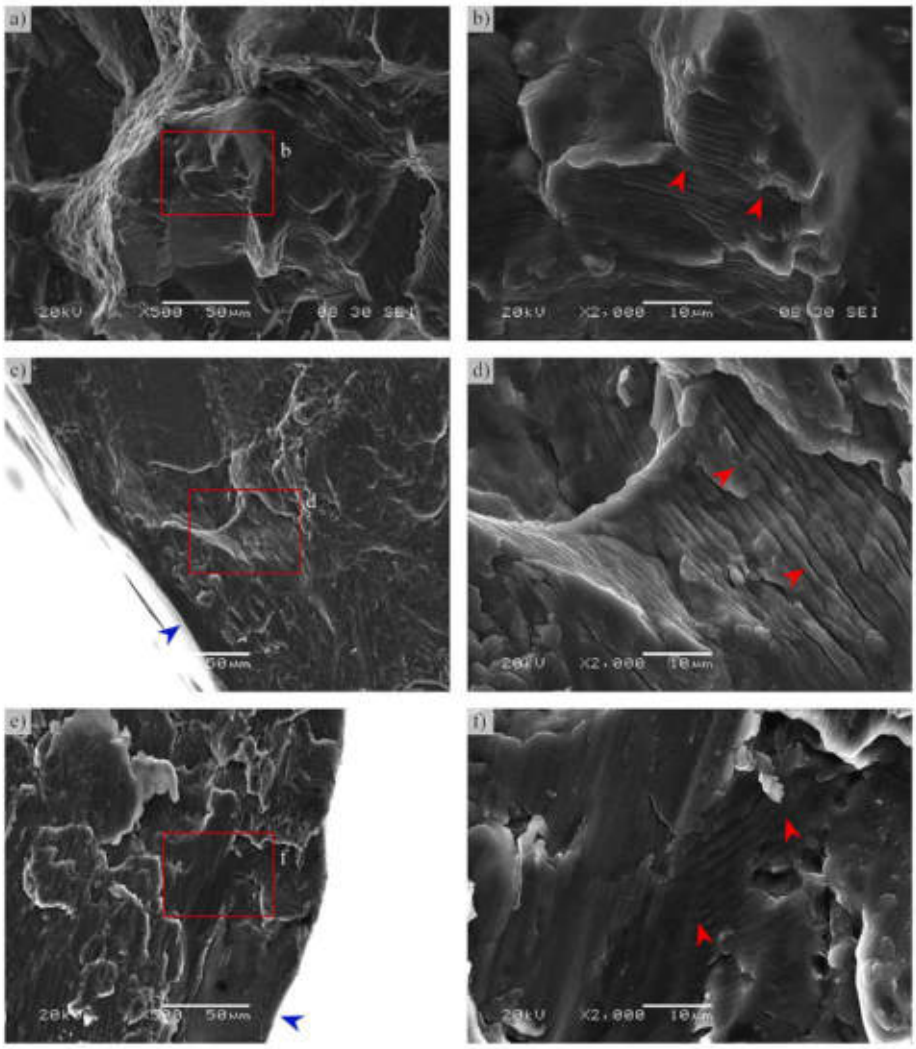

Fig. 17. Crack propagation into the depth of specimens with the presence of fatigue striations for specimens under TC (a and b), OP (c and d), and ASN1 (e and f) loadings. Blue arrows show the origin of the cracks. Red arrows indicate the direction of crack propagation with visible fatigue striations.

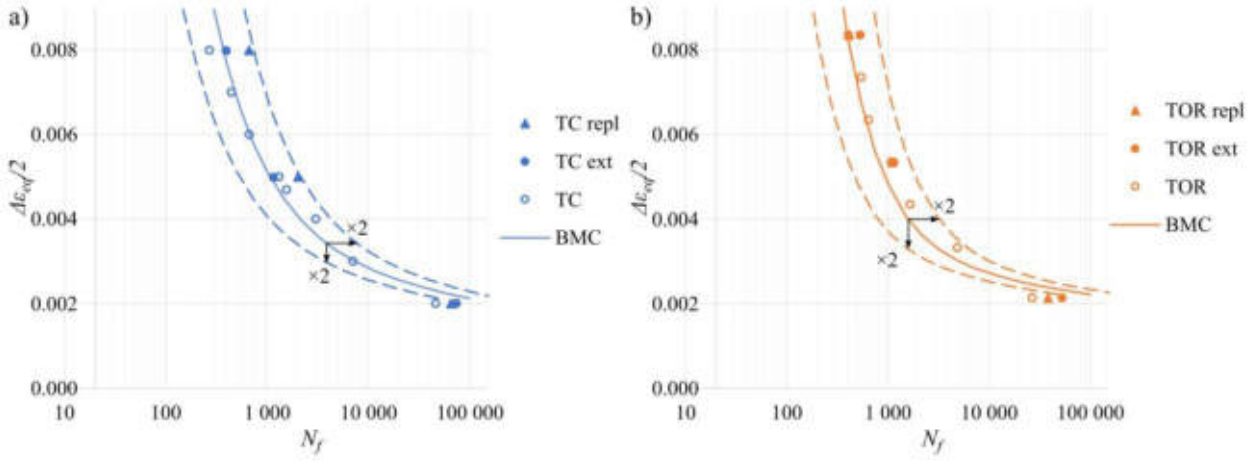

Fig. 18. A comparison of fatigue life for strain-controlled polished, unpolished, and displacement-controlled tests for axial (TC) and torsional (TOR) loadings.

specimen axis, as documented in the replicas (Figs. 7 and 8). The TOR case exhibited a unique crack growth pattern, with cracks propagating in the original directions even after coalescing. This may be due to the absence of normal strains on the plane of maximum shear strains, representing pure shear loading (Fig. 20(c)). The cracks did not change their propagation direction until the failure of the specimen, and no fatigue striations were observed. In other cases of loading, positive values of normal strain are also imposed on the plane of maximum shear strain, opening cracks and accelerating their growth.

It was observed that small cracks appeared much earlier for TOR

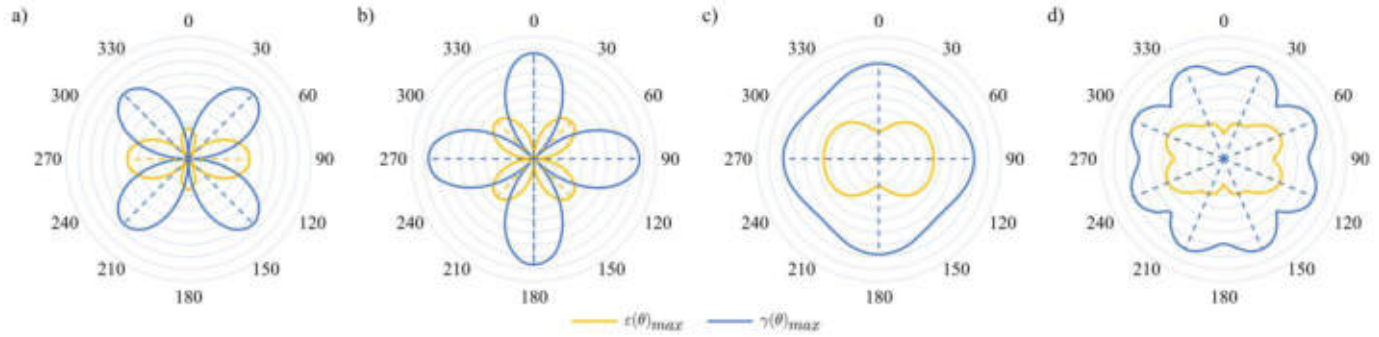

Fig. 19. Distribution of maximum normal strains $\varepsilon(\theta)$ and shear strains $\gamma(\theta)$ depending on the sectional plane location with respect to the axis of the specimen for: (a) TC, (b) TOR, (c) OP and (d) ASN1.

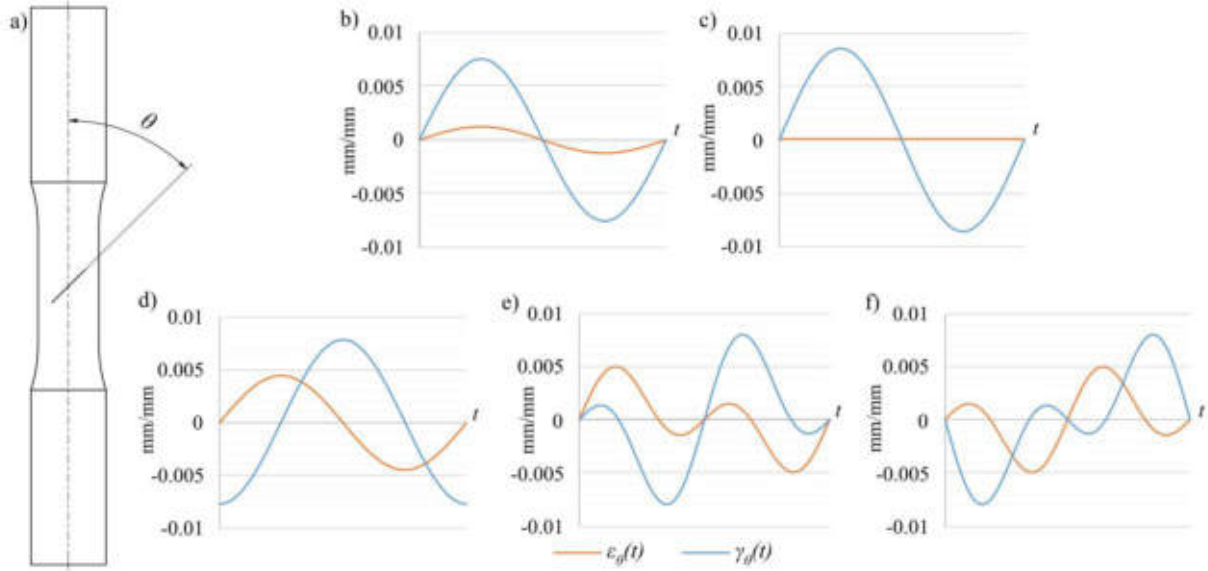

Fig. 20. History of shear and normal strains on the plane of maximum shear strain at $\varepsilon_{eq} = 0.005$: (a) the definition of θ angle, (b) TC for $\theta = 45^{\circ}$, (c) TOR for $\theta = 0^{\circ}$, (d) OP for $\theta = 90^{\circ}$, (e) ASN1 for $\theta = 68^{\circ}$, f) ASN1 for $\theta = 112^{\circ}$

compared to TC loading. In terms of fatigue life, these loading cases practically do not differ (Fig. 4). It can be inferred that the small cracks formed in the torsionally loaded specimens propagated at slower rates. The reason for this phenomenon may be the absence of normal strain on the plane of small cracks. Small cracks, given their size, generate a plastic zone at the crack tip that is sufficiently small to be influenced by the local strain state. In Fig. 20(b) and (c), the two loading cases can be compared for equal levels of equivalent strain. The range of shear strains on the analyzed plane is larger for TOR compared to TC, which explains the faster crack initiation. However, in the case of TC, there are additionally positive values of normal strains to further speed up propagation at a later stage of crack growth. Shamsaei and Fatemi [22] showed that tensile normal stress acting on the plane of small cracks contributes to faster crack propagation.

The differences in fatigue life between the tested cases of proportional and non-proportional loading are mainly related to the mutual position of the planes of maximum shear normal strains (Fig. 19(c) and (d)), as well as additional cyclic hardening for non-proportional loadings. Zhang and Miller showed that the combination of TOR and TC loading in a single test can be more or less damaging compared to the assumptions of damage cumulation hypotheses [20]. The reduction in fatigue life was attributed to the effect of initiated small shear cracks under TOR loading, which later propagated in the same direction through opening mechanism under TC loading. The non-proportional loading cases investigated in this paper comprise a transition from a state favorable for crack initiation (maximum shearing) to a state favorable for crack propagation (maximum normal stress) during each loading cycle. Even though the planes of maximum shear and normal strain coincide, these maxima do not occur simultaneously (Fig. 20 (d–f)). The additional non-proportional hardening results from the rotation of the plane of maximum shearing. This effect results in the activation of more slip systems in different directions, which significantly increases the dislocation density and the occurrence of dislocation cross-slip of different slip systems [40]. The intersecting slip systems form a structure that further increases the material's resistance to plastic deformation [40]. The effect of increased resistance to plastic strain is an increase in stress values during strain-controlled fatigue tests. Higher tensile stress values at the plane of small cracks accelerate the propagation process, reducing the fatigue life.

The fatigue life of the studied aluminum alloy was influenced by the density of the initiated cracks and the rate at which they propagate on a microscopic scale. Comparing the surface morphology of small cracks for each loading case (Fig. 14) and their shape shows that the processes at the microscopic scale differ depending on the loading case. Taking the small cracks formed at TC as a reference, the small cracks formed at OP were longer and shallower. Propagation in the direction tangential to the surface of the specimens occurred faster than in the material's depth, which suggests a greater stress concentration at the crack tip in the direction tangential to the specimen surface. The phenomena occurring in the crack tip line are not homogeneous and may be because of the non-

uniform distribution of shear stress [41]. This effect is amplified for larger cracks. The shape of the propagating cracks at ASN1 loading also showed this inhomogeneity, but the mechanism of small crack formation was clearly different from that occurring in the other cases, as the cracks were initially relatively deeper than those observed at TC, and their surface resembles a plastic fracture with small voids. It is likely that the small cracks at ASN1 loading were formed during a single loading cycle. This is certainly an interesting phenomenon, the extended study of which will enable a better understanding of the phenomena occurring in the material under asynchronous loading.

The initiated small cracks propagated at different rates depending on the loading case and level, but also on the size of the crack. A much faster increase in the distance between fatigue striations was observed for non-proportional loading cases. Fatigue striations form when cracks have a larger plastic zone at the crack tip. The increased propagation rate results in a reduced number of initiated small cracks before the first stage II cracks. As a result, the crack development process under low loading conditions more closely resembles the propagation of a single crack. As the primary crack propagates, it merges with smaller cracks, with minimal disruption to its propagation. A particularly interesting case is the propagation of cracks under ASN1 loading, as shown in Figs. 9 and 10. Cracks going to stage II formed numerous regular slip bands. The observed zigzag crack growth is a combination of two directions of crack propagation that activate alternately in each loading half-cycles. Analyzing the two planes for ASN1 shown in Fig. 20(e) and (f), it can be observed how peaks of maximum normal strain also occur in separate loading half-cycles. This sequence of strain states favors both the initiation of small cracks and faster propagation. Consequently, a shorter fatigue life is observed compared to proportional loading cases.

The observed mechanism of fatigue crack initiation and growth shows a strong correlation with the assumptions and structure of the Fatemi-Socie (FS) parameter [21]. The driving force behind fatigue damage, according to the FS parameter, is the shear strain, intensified by the normal stress occurring in the γ_{max} plane. Nevertheless, in the work of Pejkowski and Seyda [1], significantly higher predicted fatigue life $N_{f,cal}$ was obtained using the Fatemi-Socie parameter, compared to experimental fatigue life for the high-strain range. The explanation for the overestimated fatigue life, which also applies to the TC loading case, lies in the occurrence of crack coalescence, which significantly accelerated the damage process. The Fatemi-Socie FDP considers the growth of a single crack, similar to that observed at the lowest loading levels tested (Fig. 7, left column), where cracks admittedly coalesced, but developed in a manner similar to a single crack propagation (Fig. 9). However, at higher loading levels (Fig. 7, right column), crack coalescence became the predominant mechanism of material failure. In this situation, specimens were damaged at much shorter crack lengths (Fig. 11). The differences in fatigue life prediction using the Fatemi-Socie parameter and the actual experimental results highlight the importance of awareness of crack coalescence as a critical factor influencing fatigue life in certain loading conditions. As discussed by other researchers [42–44], the interactions between closely spaced cracks are difficult to model [43], but strongly affects the fatigue life and structural integrity [45]. Furthermore, in [46,47], it was concluded that the existing methods for predicting the coalescence often regard long and coplanar cracks. Other research focuses on details of the interaction of two cracks [48]. The more advanced methods of fatigue crack growth and coalescence were developed and verified for scenarios that are far from those occurred in the present research [49–52], and their application would be unpractical with such a high density of small cracks. The above considerations lead to a conclusion that the choice of the most adequate multiaxial fatigue damage parameter for fatigue life prediction should be based on the identification of the physical damage mechanism. The occurrence of crack coalescence becomes the limit of applicability of such fatigue damage accumulation models, which are based on the development of a single crack.

Turning to the analysis of the moment of registration of the first small cracks, significant differences can be seen depending on the case and loading level both comparing the level of equivalent strain (Fig. 12(a)) and equivalent stress (Fig. 12(b)). The faster capture of small cracks for higher levels has to do with the activation of more slip systems, as discussed earlier. For equal levels of equivalent strain for different non-proportional loading cases, cracks initiate faster compared to proportional loading cases. In Fig. 13, a purely phenomenological analysis was shown. It is free from any computational assumptions, even those related to the definition of equivalent strains or stresses, and avoids the inaccuracies associated with determining shear stresses during torsion in the elastic–plastic strain range [41]. Fig. 13(b) shows the predictive potential of surface state analysis regardless of the loading case for the low-cycle loading range. By monitoring the surface condition, the final fatigue life can be estimated. Going further by quantitatively analyzing the density, length and direction cracks captured by the replicas, one can attempt to create a measure of cumulative fatigue damage. A similar approach was presented in papers [53,54] in which analysis of microscopic images of specimen surfaces was used to create a fatigue damage parameter. The method for estimating cumulative fatigue damage based on the analysis of cellulose acetate replicas has great potential for engineering practice to evaluate real machine components without having to move the structures to the laboratory.

5. Summary

The following conclusions were made based on the results of the performed experiments and analyses:

1. The combination of SEM fractographic analysis with the replication technique of surfaces during fatigue increases the quality of the results obtained and leads to an understanding of the mechanisms of fatigue damage initiation and propagation.
2. Both the processes of initiation and propagation depend strongly on the specifics of the loading case. A non-proportional loading accelerates crack propagation because of the alternation of maximum shear strains and normal strains on the plane of small cracks, as well as additional hardening of the material that increases crack opening stresses.
3. In the case of ASN1-loaded specimens, the asynchronicity of the loading resulted in two directions of crack propagation in individual half-cycles, explaining the observed rapid crack propagation through a zigzag growth pattern.
4. The cracks under the TOR case initiated and propagated in two directions for the whole fatigue life even after linking with neighboring cracks, which can be explained by the absence of normal strain in the crack plane.
5. The shape of crack initiation zones differs depending on the loading condition. Micro-void formation in the crack initiation zones was observed under asynchronous loading, which did not occur in other investigated loading conditions.
6. The fatigue life of the alloy was related to the density and propagation rate of small cracks on a microscopic scale. Crack coalescence at higher loading levels significantly accelerated the damage process, shortening the fatigue life.
7. Although there is a clear correlation between the fatigue mechanism of the tested alloy and the Fatemi-Socie parameter assumptions and structure, this parameter tends to overestimate fatigue lives in all loading cases at higher loading levels. This is attributed to the significant impact of crack coalescence, which greatly accelerates the damage process.
8. There is a correlation between the moment when the first cracks are registered and the fatigue life in the studied loading range. Presumably, it is possible to develop a method of fatigue life prediction based on the register of the first small cracks visible regardless of the loading case for the range of low-cycle multiaxial fatigue.

CRediT authorship contribution statement

Jan Seyda: Conceptualization, Methodology, Software, Validation, Formal analysis, Investigation, Data Curation, Writing - Original Draft, Writing - Review & Editing, Visualization, Project administration. **Łukasz Pejkowski:** Writing – review & editing, Visualization, Supervision, Software, Methodology, Funding acquisition, Formal analysis, Conceptualization. **Mateusz Chorobiński:** Investigation.

Declaration of competing interest

The authors declare that they have no known competing financial interests or personal relationships that could have appeared to influence the work reported in this paper.

Data availability

Data will be made available on request.

Acknowledgements

The authors wish to express their gratitude to Dr. Ali Fatemi, the Ring Companies Endowed Professor at the University of Memphis, and Dr. Sebastian Henkel from Technische Universität Bergakademie Freiberg for their valuable suggestions for using the replication technique.

Appendix A. Supplementary material

Supplementary data to this article can be found online at https://doi.org/10.1016/j.ijfatigue.2024.108282.

References

[1] Karolczuk A, Liu Y, Kluger K, Derda S, Skibicki D, Pejkowski Ł. Physics-constrained Gaussian process for life prediction under in-phase multiaxial cyclic loading with superposed static components. Int J Fatigue 2023;175:107776. https://doi.org/10.1016/j.ijfatigue.2023.107776.
[2] Karolczuk A, Kluger K, Palin-Luc T. Fatigue failure probability estimation of the 7075–T651 aluminum alloy under multiaxial loading based on the life-dependent material parameters concept. Int J Fatigue 2021;147:106174. https://doi.org/10.1016/j.ijfatigue.2021.106174.
[3] Karolczuk A, Kurek M. Fatigue life uncertainty prediction using the Monte Carlo and Latin hypercube sampling techniques under uniaxial and multiaxial cyclic loading. Int J Fatigue 2022;160:106867. https://doi.org/10.1016/J.IJFATIGUE.2022.106867.
[4] Papuga J, Margetin M, Chmelko V. Various parameters of the multiaxial variable amplitude loading and their effect on fatigue life and fatigue life computation. Fatigue Fract Eng Mater Struct 2021;44:2890–912. https://doi.org/10.1111/ffe.13560.
[5] Wei Z, Dong P, Mei J, Pei X, Ravi SK. A moment of load path-based parameter for modeling multiaxial fatigue damage of welded structures. Int J Fatigue 2023;171. https://doi.org/10.1016/j.ijfatigue.2023.107575.
[6] Papuga J, Kaľavský A, Lutovinov M, Vízková I, Parma S, Nesládek M. Evaluation of data sets usable for validating multiaxial fatigue strength criteria. Int J Fatigue 2021;145:106093. https://doi.org/10.1016/J.IJFATIGUE.2020.106093.
[7] Papuga J, Vízková I, Nesládek M, Trubelová. Validation data set for testing the criteria for multiaxial fatigue strength estimation. Fatigue Fract Eng Mater Struct 2018;41:2259–71. https://doi.org/10.1111/ffe.12822.
[8] Pejkowski Ł, Seyda J. Fatigue of four metallic materials under asynchronous loadings : Small cracks observation and fatigue life prediction. Int J Fatigue 2021;142:105904. https://doi.org/10.1016/j.ijfatigue.2020.105904.
[9] Markham MJ, Fatemi A. Multiaxial fatigue life predictions of additively manufactured metals using a hybrid of linear elastic fracture mechanics and a critical plane approach. Int J Fatigue 2024;178. https://doi.org/10.1016/j.ijfatigue.2023.107979.
[10] Cruces AS, Branco R, Borrego LP, Lopez-Crespo P. Energy-based critical plane fatigue methods applied to additively manufactured 18Ni300 steel. Int J Fatigue 2023;170. https://doi.org/10.1016/j.ijfatigue.2023.107548.
[11] Poczklán L, Polák J, Kruml T. Comparison of critical plane models based on multiaxial low-cycle fatigue tests of 316L steel. Int J Fatigue 2023;171:107569. https://doi.org/10.1016/j.ijfatigue.2023.107569.
[12] Ferreira JLA, Dias JN, Cardoso EU, Araújo JA, da Silva CRM. A contribution to the identification of the critical plane using the maximum variance method. Int J Fatigue 2022;165:107228. https://doi.org/10.1016/j.ijfatigue.2022.107228.
[13] Bibbo ND, Baumgartner J, Arora V. Comparative study of critical plane fatigue criteria on multiaxial variable amplitude loaded welded test specimens. Int J Fatigue 2022;158:106670. https://doi.org/10.1016/J.IJFATIGUE.2021.106670.
[14] Zheng Z, Zhan M, Fu MW. Microstructural and geometrical size effects on the fatigue of metallic materials. Int J Mech Sci 2022;218. https://doi.org/10.1016/j.ijmecsci.2021.107058.
[15] Lu D, Lin B, Liu T, Deng S, Guo Y, Li J, et al. Effect of grain structure on fatigue crack propagation behavior of Al-Cu-Li alloys. J Mater Sci Technol 2023. https://doi.org/10.1016/J.JMST.2022.10.085.
[16] Tang K, Chen K, Ferro P, Berto F. Quantifying lamellar microstructural effect on the fatigue performance of bimodal Ti-6Al-4V with microdefect. Int J Fatigue 2022;163. https://doi.org/10.1016/J.IJFATIGUE.2022.107045.
[17] Stopka KS, McDowell DL. Microstructure-sensitive computational multiaxial fatigue of Al 7075–T6 and duplex Ti-6Al-4V. Int J Fatigue 2020;133. https://doi.org/10.1016/j.ijfatigue.2019.105460.
[18] Kurath P, Socie DF. The relationship between observed fatigue damage and life estimation models. Urbana 1988.
[19] Kanazawa K, Miller KJ, Brown MW. Low-Cycle Fatigue Under Out-of-Phase Loading Conditions. J Eng Mater Technol 1977;99:222–8.
[20] Zhang W, Miller KJ. A study of cumulative fatigue damage under variable loading-mode conditions. Fatigue Fract Eng Mater Struct 1996;19:229–39. https://doi.org/10.1111/j.1460-2695.1996.tb00962.x.
[21] Fatemi A, Socie DF. A critical plane approach to multiaxial fatigue damage including out-of-phase loading. Fatigue Fract Eng Mater Struct 1988;11:149–65. https://doi.org/10.1111/j.1460-2695.1988.tb01169.x.
[22] Shamsaei N, Fatemi A. Small fatigue crack growth under multiaxial stresses. Int J Fatigue 2014;58:126–35. https://doi.org/10.1016/j.ijfatigue.2013.02.002.
[23] Milella PP. Fatigue and corrosion in metals. Milano: Springer Milan; 2013. doi: 10.1007/978-88-470-2336-9.
[24] Gates N, Fatemi A. Notched fatigue behavior and stress analysis under multiaxial states of stress. Int J Fatigue 2014;67:2–14. https://doi.org/10.1016/j.ijfatigue.2014.01.014.
[25] Fatemi A, Gates N, Socie DF, Phan N. Fatigue crack growth behaviour of tubular aluminium specimens with a circular hole under axial and torsion loadings. Eng Fract Mech 2014;123:137–47. https://doi.org/10.1016/j.engfracmech.2014.04.010.
[26] Pejkowski Ł., Skibicki D. Stress-strain response and fatigue life of four metallic materials under asynchronous loadings: experimental observations. Int J Fatigue 2019;128:105202. https://doi.org/10.1016/j.ijfatigue.2019.105202.
[27] Skibicki D, Pejkowski Ł. The relationship between additional non-proportional hardening coefficient and fatigue life. Int J Fatigue 2019;123:66–78. https://doi.org/10.1016/j.ijfatigue.2019.02.011.
[28] Pandey V, Arora P, Gupta SK, Khutia N, Pratim DP. Validating cyclic plasticity material model for three materials subjected to asynchronous axial-torsion conditions. Int J Fatigue 2023. https://doi.org/10.1016/j.ijfatigue.2023.108124.
[29] Scorza D. Fatigue Life Assessment of Metals under Multiaxial Asynchronous Loading by Means of the Refined Equivalent Deformation Criterion. Metals (Basel) 2023;13. doi:10.3390/met13030636.
[30] Arora P, Gupta SK, Samal MK, Chattopadhyay J. Validating generality of recently developed critical plane model for fatigue life assessments using multiaxial test database on seventeen different materials. Fatigue Fract Eng Mater Struct 2020;43:1327–52. https://doi.org/10.1111/ffe.13169.
[31] Arora P, Gupta SK, Samal MK, Chattopadhyay J. Comparing fatigue life prediction capability of critical plane models using multiaxial test database on 17 materials. Fatigue Fract Eng Mater Struct 2023;46:1330–56. https://doi.org/10.1111/ffe.13928.
[32] Das P, Khutia N, Dey PP, Arora P, Gupta SK. Multi-objective cyclic plastic modelling of cyclic hardening and softening characteristics of nuclear piping SA333 gr. 6 carbon steel. Int J Fatigue 2024:180. https://doi.org/10.1016/j.ijfatigue.2023.108082.
[33] E2207-02 (ASTM International). Standard Practice for Strain-Controlled Axial-Torsional Fatigue Testing with Thin-Walled Tubular Specimens n.d.;03.
[34] Shamsaei N. Multiaxial fatigue and deformation including non-proportional hardening and variable amplitude loading effects; 2010.
[35] Seyda J, Pejkowski Ł., Skibicki D. Identification of fatigue damage mechanism in PA38-T6 aluminum alloy under multiaxial loadings – initial research. Proc Struct Integr 2020;28:1458–66. https://doi.org/10.1016/j.prostr.2020.10.119.
[36] Zhou X-P, Shang D-G, Li D-H, Wang J-J, Zhao Y-R, Li W. Life prediction method based on short crack propagation considering additional damage under axial-torsional non-proportional loading. Int J Fatigue 2022;161:106888. https://doi.org/10.1016/J.IJFATIGUE.2022.106888.
[37] Rabbolini S, Beretta S, Foletti S, Riva A. Short crack propagation in LCF regime at room and high temperature in Q & T rotor steels. Int J Fatigue 2015;75:10–8. https://doi.org/10.1016/j.ijfatigue.2015.01.009.
[38] Seyda J, Pejkowski Ł. SEM analysis of PA38-T6 aluminum alloy thin-walled tubular specimen fatigue fracture, and comparison to surface replication results. MATEC Web Conf 2021:338.
[39] Socie D, Marquis G. Multiaxial fatigue. Society of Automotive Engineers; 2000.
[40] Zhou Z, Liu X, He G, Liao Y, Huang Z, Pan J, et al. A comparison of uniaxial and multiaxial non-proportional fatigue properties in cast Al-Si-Cu-T6 alloys solidified at two cooling rates: fatigue behavior, fracture characteristics and dislocation evolution. Mater Charact 2022;189:111957. https://doi.org/10.1016/j.matchar.2022.111957.
[41] Seyda J, Pejkowski Ł., Skibicki D. The shear stress determination in tubular specimens under torsion in the elastic-plastic strain range from the perspective of

fatigue analysis. Materials (Basel) 2020;13:1–16. https://doi.org/10.3390/ma13235583.
[42] Shen Z, Chen C, Xuan H, Quan C, Chen H, Zheng Y. Study on multiple fatigue cracks growth in the web of a hollow compressor impeller. Eng Fract Mech 2023;292:109582. https://doi.org/10.1016/j.engfracmech.2023.109582.
[43] Jeong DY, Brewer JC. On the linkup of multiple cracks 1995;51. https://doi.org/10.1016/0013-7944(94)00267-L.
[44] Ma L, Wang X, Feng XQ, Yu SW. Numerical analysis of interaction and coalescence of numerous microcracks. Eng Fract Mech 2005;72:1841–65. https://doi.org/10.1016/j.engfracmech.2004.08.009.
[45] Branco R, Costa JD, Antunes FV. Fatigue behaviour and life prediction of lateral notched round bars under bending-torsion loading. Eng Fract Mech 2014;119:66–84. https://doi.org/10.1016/j.engfracmech.2014.02.009.
[46] Tan JT, Chen BK. Coalescence and growth of two coplanar short cracks in AA7050-T7451 aluminium alloys. Eng Fract Mech 2013;102:324–33. https://doi.org/10.1016/j.engfracmech.2013.03.002.
[47] Branco R, Antunes FV, Costa JD. A review on 3D-FE adaptive remeshing techniques for crack growth modelling. Eng Fract Mech 2015;141:170–95. https://doi.org/10.1016/j.engfracmech.2015.05.023.
[48] Legrand L, Lazarus V. Front shape and loading evolution during cracks coalescence using an incremental perturbation method. Eng Fract Mech 2015;133:40–51. https://doi.org/10.1016/j.engfracmech.2014.10.026.
[49] Ruiz-Muñoz GA. Method to analyse multiple site damage fatigue before and after crack coalescence. Eng Fract Mech 2018;188:416–30. https://doi.org/10.1016/j.engfracmech.2017.09.011.
[50] O'Hara P, Duarte CA, Eason T. A two-scale generalized finite element method for interaction and coalescence of multiple crack surfaces. Eng Fract Mech 2016;163:274–302. https://doi.org/10.1016/j.engfracmech.2016.06.009.
[51] Xu M, Yuan H. Characterization of crack-tip fields for elastoplastic fatigue crack growth Part II: Effects of crack closure and in-plane constraint. Eng Fract Mech 2023;291:109543. https://doi.org/10.1016/j.engfracmech.2023.109543.
[52] Escalero M, Muniz-Calvente M, Zabala H, Urresti I, Branco R, Antunes FV. A methodology for simulating plasticity induced crack closure and crack shape evolution based on elastic–plastic fracture parameters. Eng Fract Mech 2021;241:107412. https://doi.org/10.1016/j.engfracmech.2020.107412.
[53] Karuskevich M, Karuskevich O, Maslak T, Schepak S. Extrusion/intrusion structures as quantitative indicators of accumulated fatigue damage. Int J Fatigue 2012;39:116–21. https://doi.org/10.1016/J.IJFATIGUE.2011.02.007.
[54] Pejkowski Ł., Karuskevich M, Maslak T. Extrusion/intrusion structure as a fatigue indicator for uniaxial and multiaxial loading. Fatigue Fract Eng Mater Struct 2019;42:2315–24. https://doi.org/10.1111/ffe.13066.

Materials Science & Engineering A 817 (2021) 141343

Contents lists available at ScienceDirect

Materials Science & Engineering A

journal homepage: www.elsevier.com/locate/msea

Mechanical properties and microscopic analysis of sintered rhenium subjected to monotonic tension and uniaxial fatigue

Jan Seyda, Dariusz Skibicki, Łukasz Pejkowski *, Andrzej Skibicki, Piotr Domanowski, Paweł Maćkowiak

UTP University of Science and Technology, Faculty of Mechanical Engineering, Kaliskiego 7, 85-796, Bydgoszcz, Poland

ARTICLE INFO

Keywords:
Sintered rhenium
HCP metals
S–N curve
Estimation methods
Cracking

ABSTRACT

Some reports on the mechanical testing of pure rhenium can be found in the literature. However, very few studies have been published regarding the fatigue properties of rhenium. To gain new knowledge on this subject, the present research aimed to determine mechanical properties in monotonic tension, hardness, and stress-controlled fatigue tests of sintered rhenium. The results of the basic mechanical tests are in agreement with data in the literature. The determined exploratory S–N fatigue curve for pure, sintered rhenium is a unique result, and it cannot be compared with others. Based on the monotonic tests data, estimated S–N curves were also determined. The comparison of the experimental curve and the estimated curves showed the usefulness of approximation methods to estimate the fatigue properties of rhenium. Considering the high cost of conducting research on rhenium, this is especially important for engineering design. Subsequently, microscopic fracture analysis and microstructure evolution observation were performed. Microscopic observations were made using a light optical microscope and a scanning electron microscope. Based on the performed metallographic analyses, it was found that under fatigue and monotonic loadings, cracks propagated along the grain boundaries, and the pores present in the material did not affect this process. It was confirmed that the basic deformation mechanism in sintered rhenium is twinning. To sum up, the present work provides new data on the strength properties of rhenium and helps to better understand the deformation and damage processes of this metal.

1. Introduction

Rhenium (Re) is a refractory metal which is recognized as a high-performance engineering material [1]. It has a high melting temperature, strain hardening exponent, tensile strength, and hardness, and a low coefficient of friction [2]. It is also characterized by high erosion resistance and creep rupture strength over a wide temperature range [3]. One major application area for pure rhenium is in the aerospace industry [4]. However, its properties make it also attractive for aircraft, nuclear, petrochemical, energy, electrical, and biomedical applications [3,5]. Rhenium is also used as an alloying component [6–8] or as a representative of the hexagonal close-packed crystal lattice [9,10].

Rhenium rarely occurs as a pure element; it most commonly is produced as a byproduct of copper mining [11]. The two principal manufacturing processes of rhenium are through powder metallurgy and chemical vapor deposition, but recently it has also been produced through electroplating and electrodeposition [5,12–14]. The physical and basic mechanical properties of rhenium, the types of manufacturing processes, and the applications of rhenium and its alloys have been discussed in previous research [4,13,15].

There are very few studies regarding the relationship between the microstructure and the exceptionally high work-hardening behavior of rhenium, though those that do exist are quite detailed. The first such research was reported by Kacher and Minor [16], who explain that rhenium's plasticity is characterized by a large amount of twin formation and propagation, including twin transmission across grain boundaries. Sabisch and Minor [17,18] compared the deformation mechanisms under tension and compression in detail. The authors noticed a tension-compression asymmetry and explained that the reason is that the twin favorability of the microstructure forces the creation of many more twins during compression than does tension. Kacher et al. [19] investigated over 1000 grain boundary/twin interactions in pure rhenium after uniaxial compression. Based on the statistical analysis of crystallographic factors such as the grain boundary disorientation angle,

* Corresponding author.
E-mail address: lukasz.pejkowski@utp.edu.pl (Ł. Pejkowski).

https://doi.org/10.1016/j.msea.2021.141343
Received 23 February 2021; Received in revised form 20 April 2021; Accepted 22 April 2021
Available online 3 May 2021

displacement gradient tensor accommodation, twin plane, and shear vector alignment, different types of interactions were determined. In recent work, Jiang et al. [20] explained the high strength and ductility of rhenium based on the understanding of the origin of its unique predominance of $\{11\bar{2}1\}$ twinning.

Despite the growing use of rhenium in various engineering industries, very few studies exist in the literature regarding its fatigue properties and behavior [21]. The reasons are excessive costs, limited availability of material, and difficult manufacturability of specimens. Fatigue tests are mainly conducted for the space industry, and their range is very limited. Usually, these are tension-compression tests conducted on single specimens. Their objective is to check if the material has a fatigue life longer than 100 cycles for the correspondence between the loading amplitude and the yield stress [22–25]. The results of fatigue tests carried out until the failure of specimens can be found in work by Adams [21]. However, due to the small number of fatigue tests and the large scattering of the results, the results cannot be presented in the form of a fatigue curve. In the opinion of researchers, the available fatigue tests are not a sufficient source of data for design purposes [25,26].

The goal of the present work was to conduct high-cycle, stress-controlled fatigue tests of pure, sintered rhenium. The research also included the microscopic analysis of the initial microstructure, changes of the specimens' gauge sections' topology introduced by tests, and fracture surfaces. The fatigue tests were preceded by the determination of basic mechanical properties by monotonic tension and hardness tests. The experimental fatigue curve was compared with the estimated curves which were developed using the ultimate tensile strength value. Based on microscopic analyses, the fatigue damage mechanism and deformation mechanism were determined.

2. Materials and methods

2.1. Material and specimen preparation

The specimens were manufactured from 99.99% pure rhenium sheets purchased from Rhenium Alloys, Inc. Plates were manufactured using powder metallurgy. As specified by the manufacturer, powder with a mean size of 26 μm was mechanically pressed and then sintered to 98% density at 2350 °C. Then, sheets were rolled to size with densities greater than 99%. The dimensions of the plate and fatigue specimens, the orientation of the specimens relative to the pressing and loading directions, and the numeration of surfaces are shown in Fig. 1. The dimensions of the specimens used in monotonic tension tests were slightly different. They are given in brackets and highlighted in red color in Fig. 1. Especially, the gauge section was longer than in case of fatigue specimens, and was equal to 14 mm. Higher length was used to precisely measure the strain using the contact extensometer. The specimens were cut out using the wire electrical discharge machining method. For this purpose, 0.25 mm CuZn37 brass wire was used. The cutting process was carried out by applying a special high-voltage (300 V) program dedicated to sintered materials. Due to the high melting temperature of rhenium, the maximum available impulse current was used, i.e., 5 A.

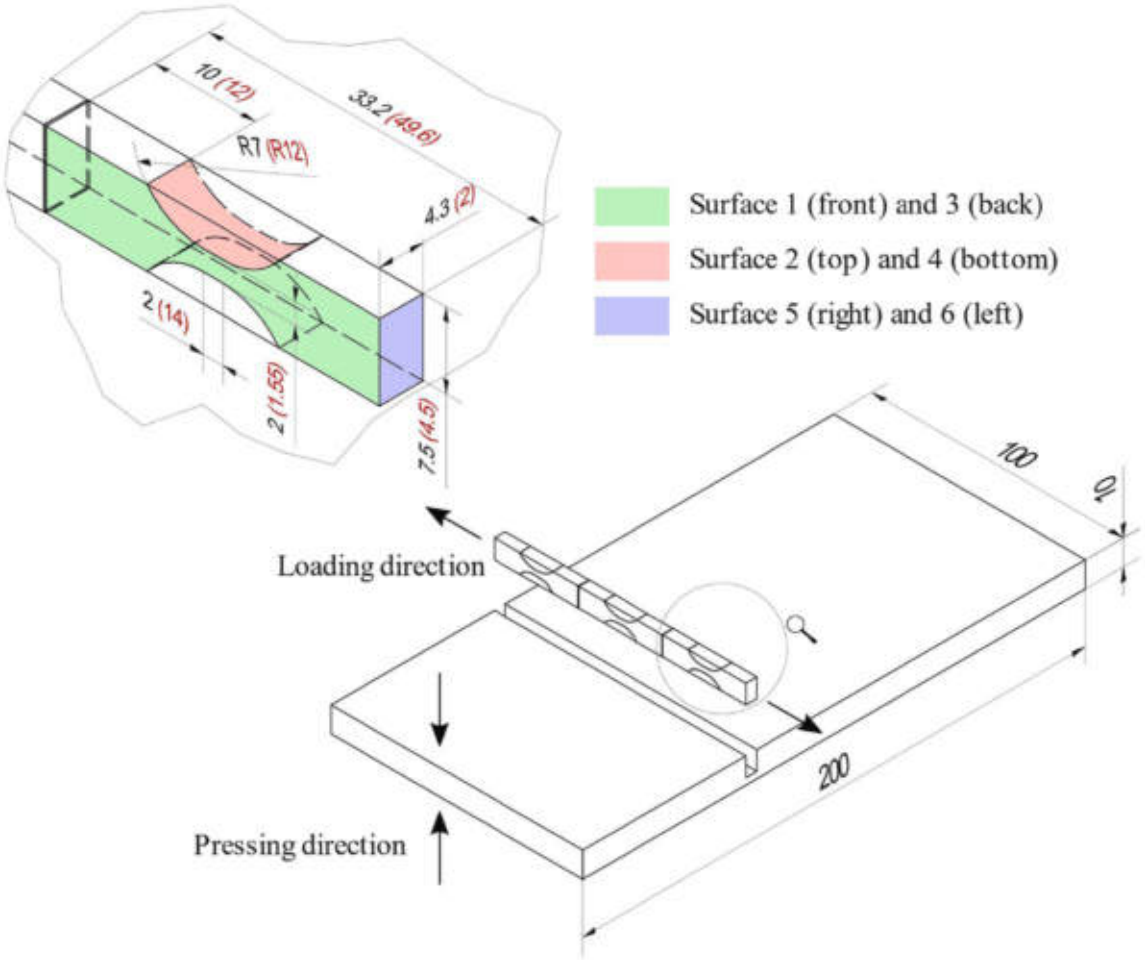

Fig. 1. The dimensions of the plate and fatigue specimens (in millimeters), pressing and loading directions, and surface numeration and designation; values in brackets and highlighted in red color are given for the specimens used in monotonic tension tests. (For interpretation of the references to color in this figure legend, the reader is referred to the Web version of this article.)

The remaining cutting parameters were determined based on the parameters usually used for sintered carbides, but they were modified by extending the pause time between current impulses and reducing the cutting speed. The cutting speed was optimized to be as high as possible while eliminating sticking of the wire to the processed material.

After being cut off from the plate, the specimens were polished to have mirror-like surfaces using diamond pastes of different grades. Rhenium strongly hardens due to deformation, thus the polishing of specimens using the abrasive method turned out to be very laborious. It required gradual polishing with diamond pastes of 80 μm–1 μm gradation. The final stages of polishing were carried out with cotton wipes moistened with distilled water. Polishing removed a zone of material that had changed during the wire electrical discharge cutting. This zone was 5–25 μm deep. A picture of a specimen mounted in the testing machine grips is presented in Fig. 2.

2.2. Specimen measurements and hardness tests

Measurements of the cross-section dimensions of the specimen gauge sections were made using a properly calibrated digital microscope. These measurements were necessary to precisely determine the axial stress. The specimens were also weighed on a RADWAG analytical balance with an accuracy of 0.1 mg. Based on the dimensions and weight measurements, the density was determined. It turned out to be 98%, comparing to the solid material, and was very close to the density stated by the manufacturer. Hardness tests were carried out, according to recommendations of the ISO 6507-1 standard, using a Vickers microhardness tester, Shimadzu HMV-G20DT. Five repeated HV1 measurements were performed on each of the tested surfaces. The loading was 1 kg, and it was applied in a time of 10 s–15 s. The minimum distance from the specimen's edge was 2.5 d, where d is a linear dimension of the penetrator mark. The minimum distance between marks was 3 d.

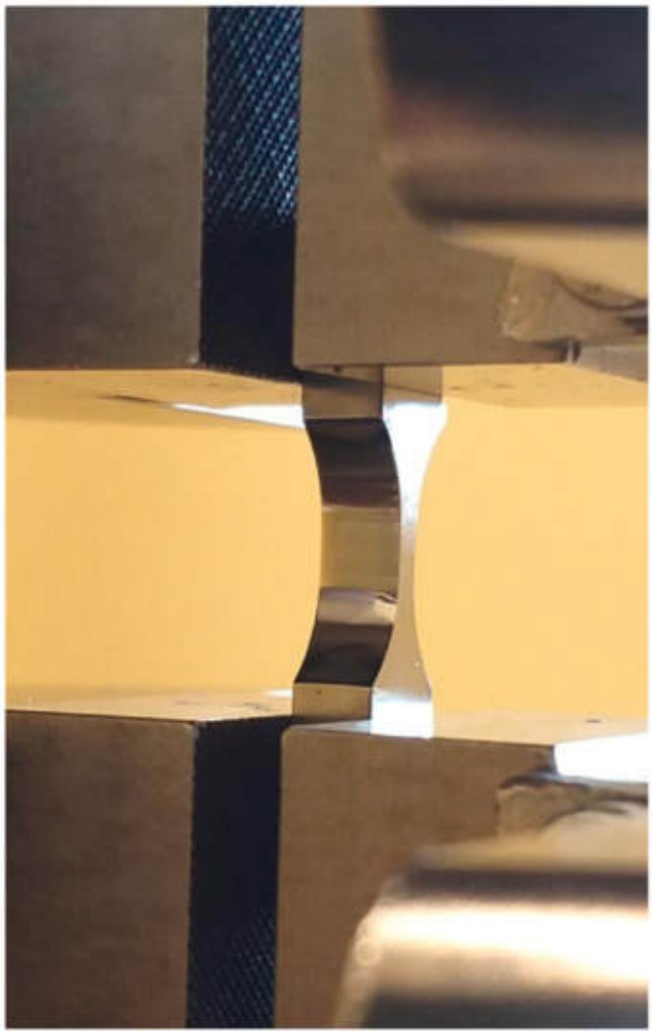

Fig. 2. Polished specimen mounted in the grips of the testing machine.

2.3. Strength tests

Monotonic uniaxial tension tests and fatigue tests were carried out using the biaxial Instron 8874 testing system, with the range of axial force $\Delta F = \pm 25$ kN. For the monotonic tension tests, the uniaxial Instron 2620–601 extensometer was used. Due to the high-cycle regime of fatigue tests, they were conducted in stress-control mode and with accordance to the recommendations of the ISO 6892-1 standard [27]. The S–N fatigue curve was determined using exploratory research methodology according to the recommendations of the ASTM-E739-91 standard [28].

2.4. Light optical microscopy and scanning electron microscopy

The surfaces of the fatigued specimens were observed with a scanning electron microscope (SEM), JEOL JSM-5600, as well as under a light microscope, Delta Optical MET-1000-TRF, equipped with a 12 Mpx digital camera and DLTCamViewer software. The pictures of the metallographic specimens were taken in polarized light. The vertical axes of all specimen surface pictures coincided with the vertical axes of the specimens, i.e., the loading direction.

2.5. Preparation of the metallographic specimens

The surfaces of the metallographic specimens were polished with diamond paste and suspensions, both with 80 μm–1 μm gradation using a FORCIPOL 202 metallographic grinding and polishing machine. The polished surfaces were etched with a reagent specified in the ASTM E407-07 standard [29], consisting of 5 ml of HF (40%), 10 ml of HNO_3 (80%), and 50 ml of $C_2H_6O_3$ (80%), for 300 s at room temperature.

3. Results and discussion

3.1. Metallographic analyses of undeformed material

In the process of powder sintering, the crystallographic structure shown in Fig. 3 was formed. The colors of the grains were different due

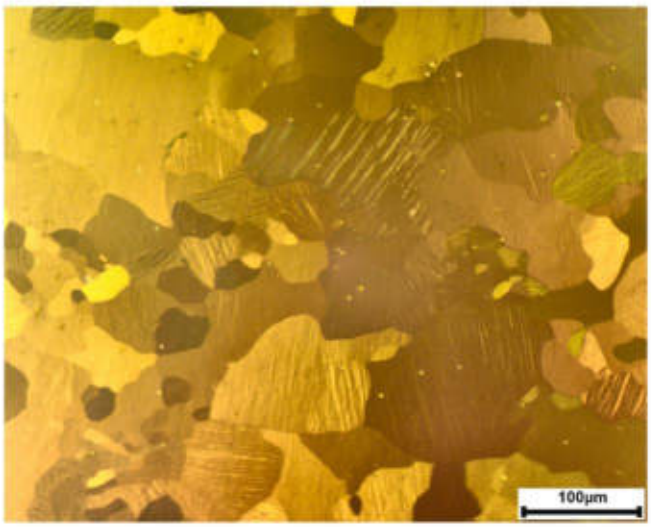

Fig. 3. Metallographic specimen of rhenium, before loading.

to their different orientations, which were revealed under polarized light. The grain size varied greatly and was in the range from 10 μm to 200 μm. The distribution of grain size is presented in Fig. 4. The standard grain size, $n = 6.4$, was determined according to ASTM E112-13 [30]. The measured area fraction of twins was approximately 12,7%. It was determined using combined manual and computer processing of the polarized light images. The area occupied by twins was automatically detected in the images, which were initially adjusted, using various filters in a GIMP software. Then, it was manually corrected, and the area fraction of twins was measured using the ImageJ software.

Variations in the microstructure produce local stress-strain irregularities. This contributes to the formation of cleavage cracks. This mechanism is described in detail by Armstrong [31]. The effect of grain size variation, which causes brittle fracture, impacts the monotonic and fatigue properties of sintered rhenium and will often be referred to later in this paper. Fig. 4 also presents the size of the unsintered powder particles provided by the producer. The comparison of both histograms shows that the grain sizes were statistically larger than the powder particle size. Most of the grains were characterized by clearly arched boundaries. The diversified size and shape of the grain boundaries prove the occurrence of secondary recrystallization, during which the grains with a more favorable orientation grew at the expense of the neighboring grains. Deformation twins were observed in almost every grain, and they often involved whole grains (Fig. 3). The existence of multiple twins was most likely the result of the last stage of the production process, i.e., rolling and specimen polishing. When examining specimens of the single-phase AM30 magnesium alloy, a material with a hexagonal crystal lattice similar to that of rhenium, Roostaei and Jahed observed a similar structure of extensive twinning [32]. In Ref. [33], Vlcak et al. also showed that mechanical polishing resulted in surface hardening of pure titanium.

The presence of pores is characteristic for sintered powder materials. In Fig. 3, the pores can be observed as the light points, and in the SEM picture (Fig. 5), examples of pores are marked with black arrows. Due to the high sinter density, there were few pores, and they reached a maximum size of 10 μm. In the SEM images at higher magnification, the hexagonal structure of the pore cross-sections in the cleavage planes can be seen (Fig. 6a). Furthermore, in Fig. 6b and c, larger parts of the pores' insides can be seen. Shapes of the pores were very regular and had no sharp edges. Interestingly, pores in the diffusion process of atom accommodation during recrystallization annealing took a form similar to that of apatite crystal (Fig. 6 e), which, like rhenium, has a hexagonal crystal lattice.

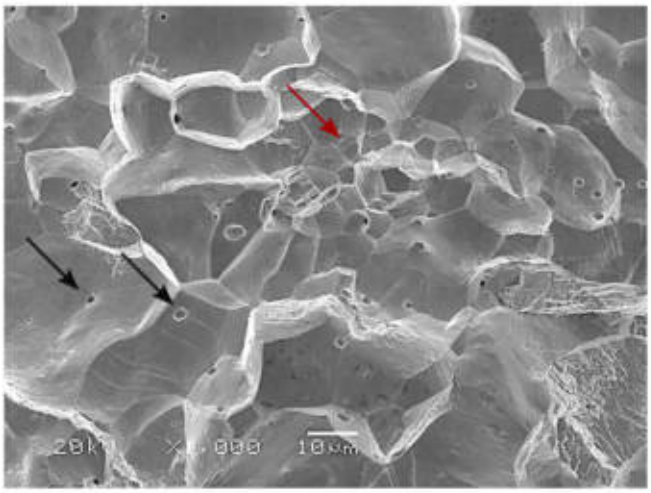

Fig. 5. Pores on the fracture surface (black arrows) of Specimen 8; a cluster of small grains is also marked (red arrow). (For interpretation of the references to color in this figure legend, the reader is referred to the Web version of this article.)

3.2. Basic mechanical properties

The monotonic tension tests were performed using two specimens, with strain rates $\dot{\varepsilon} = 1{\cdot}10^{-4}$ and $\dot{\varepsilon} = 5{\cdot}10^{-5}$, respectively. The resultant stress-strain curves are presented in Fig. 7. Based on the graphs, the following strength properties were determined: Young modulus E, offset yield stress $\sigma_{0.2}$, ultimate tensile strength σ_u, and strain at failure ε_f (Table 1). The determined material parameter values were similar to those obtained by Biaglow [22,23]. The scatter of the results is noticeable, which is usually atypical for a monotonic tension test. Sabisch and Minor explained that this type of discrepancy is attributed to the difference in the grain size distribution within and between specimens [18]. Low fracture strain (smaller than 15%) in the tension testing can be explained by the brittleness of grain boundaries of sintered metal [35].

Hardness measurements were made on the specimen surfaces marked in Fig. 1. The results are given in Table 2. Differences in hardness resulted from the location of the tested surfaces in relation to the directions of loadings exerted during pressing of the powder being sintered. Surfaces 2–4, which were normal to the pressing direction, had a higher hardness than tangent surfaces 1–3 and 5–6. Based on the hardness measurements, the ultimate tensile strength was estimated using the Bäumel-Seeger's equation ([36,37] after [38]). The

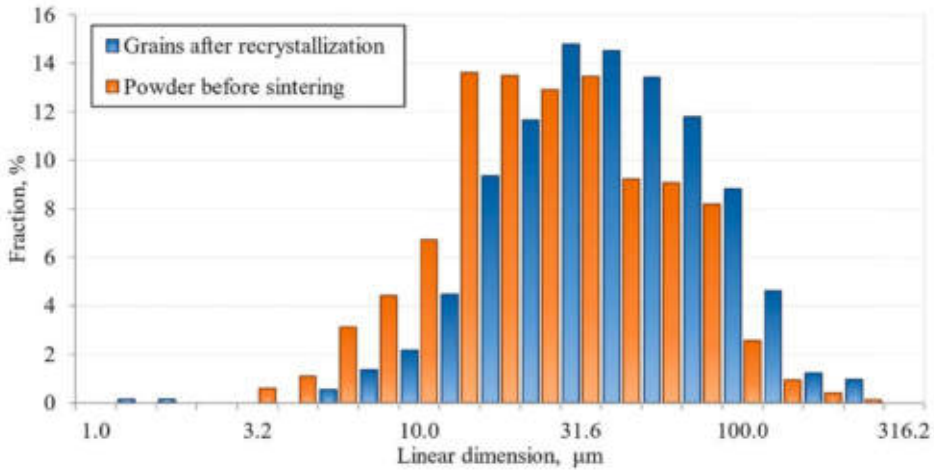

Fig. 4. Histogram of the sintered material grain size and powder particle size before sintering.

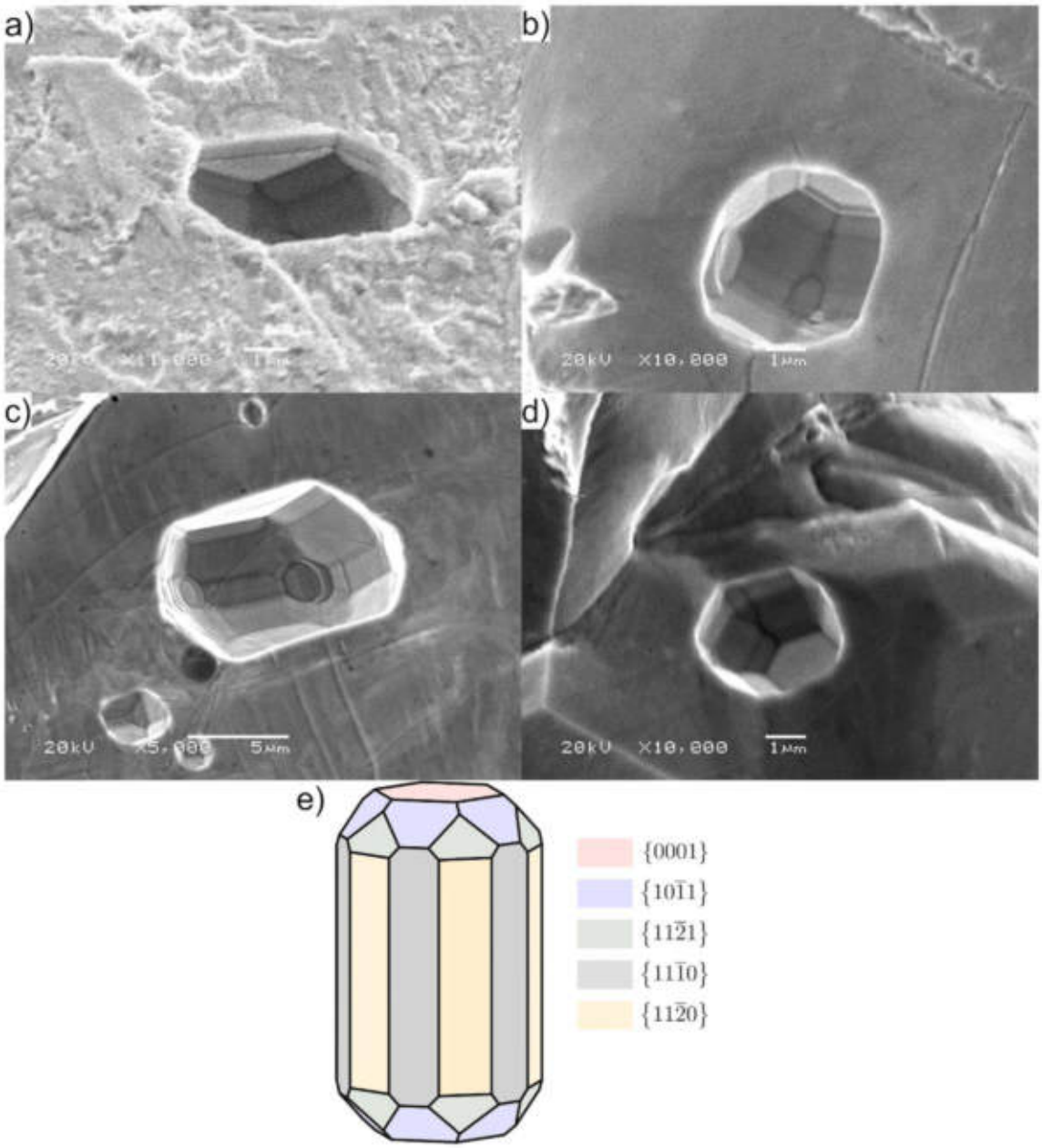

Fig. 6. a–d) pores in the sintered rhenium (Specimen 8), and e) one form of apatite crystal (reproduced after [34]).

experimentally obtained values of ultimate tensile strength were comparable with those obtained from the estimation based on hardness. According to the manufacturer's data (Rhenium Alloys, Inc.), hardness for annealed rhenium is 170 HV. The experimental results obtained in this study were higher as a result of hardening, which was caused by rolling and polishing with diamond paste. This is confirmed by the deformation twins shown in Fig. 3.

The period of nucleation and the growth of small cracks have the greatest influence on fatigue life scatter [39,40]. Scatter of this life period can be large because it is sensitive to various influences, such as material surfaces. The longer this stage is, e.g., for low stress values, the greater the fatigue life scatter; the shorter this stage, the smaller the scatter [40]. Due to the lack of geometric notches and the mirror-polished surface of the specimens in the present study, the small scatter of fatigue life and thus the short period of nucleation of small microcracks should be attributed to a large variation in grain size, which caused local stress-strain irregularities.

3.3. Fatigue properties

Table 3 presents six results of the fatigue tests. Fig. 8 shows five of these results, omitting the specimen that did not fail (no. 3). The results were fitted with the Basquin equation of parameters where $\sigma_f^{'} = 627.8$ MPa and $b = -0.04$:

$$\sigma_{Nf} = 627.8(N_f)^{-0.04} \quad (1)$$

The coefficient of determination for the fitted curve was $R^2 = 0.988$, which indicates a very good fit of the equation to the experimental data points. The smaller scatter of results than in case of the monotonic tension tests was observed. It can be explained by the higher cross section area. Although the grain size was very varied, the number of grains was a few times higher than in case of specimens used in the monotonic tension tests. This resulted in decreased influence of the grain size.

Notably, the fatigue strength exponent of rhenium, $b = -0.04$, is significantly higher than that of other metals. For example, the slopes of

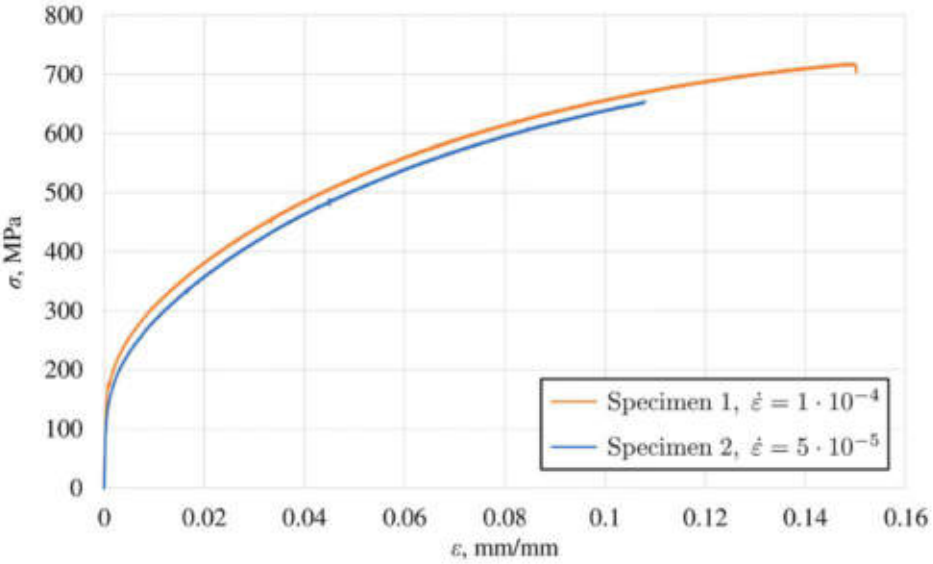

Fig. 7. Monotonic engineering stress-strain curves.

Table 1
Basic mechanical properties of sintered rhenium.

	Young modulus E, GPa	0.2 Yield stress $\sigma_{0.2}$, MPa	Ultimate Tensile Strength σ_u, MPa	Strain at failure ε_f, %
Specimen 1	356.1	179.0	718.3	15.0
Specimen 2	339.0	189.5	654.5	10.8
Pressed and	430.9	227.5	677.8	9.8
Sintered	411.6	206.8	757.8	13.2
	405.4	213.7	713.6	11.2
	392.3	234.4	841.2	16.2
Rolled Sheet	420.6	568.1	921.9	16.4
	434.4	500.9	943.2	17.2

Table 2
Vickers hardness data.

Surfaces	1–3	2–4	5–6
HV1	198	269	248
σ_u in MPa, estimated on HV1 according to Bäumel-Seeger's equation ([36,37] after [38])	604	838	768

Table 3
Fatigue life of sintered rhenium.

Specimen no.	Stress amplitude σ_a, MPa	Fatigue life N_f, cycles	Comments
3	135.30	84 562 484	not failed
7	347.57	3 316 398	
5	351.75	1 496 423	
8	372.34	521 231	
6	376.22	364 018	
4	410.63	40 747	

the Basquin curves for carbon steels, austenitic steels, aluminum alloys, and titanium alloys are much greater, so the fatigue strength exponents for these materials are much smaller and amount approximately from −0.06 to −0.15 ([40–42]). The small slope of the S–N curve is due to the very good surface quality and small specimen size, and it is typical for brittle materials [43].

It is also worth noting that the stress value for a half cycle, according to the determined Basquin equation, is 641 MPa, which is close to the experimental values of ultimate tensile strength σ_u (see Table 1).

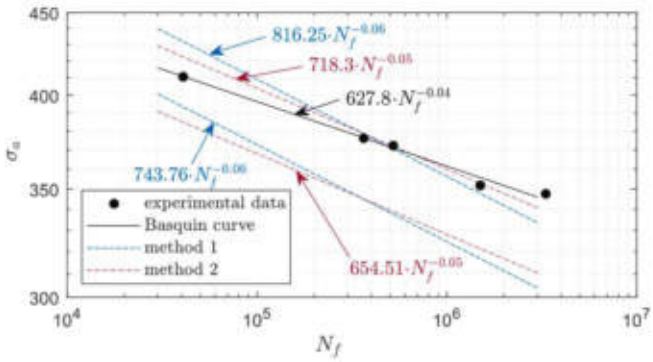

Fig. 8. Experimental and estimated S–N curves; black line – Basquin curve fitted to the experimental data; blue dashed lines – S–N curves estimated using the first method, based on the data for Specimen 1 (upper line) and Specimen 2 (bottom line); red dash-dot lines – S–N curves estimated using the second method, based on the data for Specimen 1 (upper line) and Specimen 2 (bottom line). (For interpretation of the references to color in this figure legend, the reader is referred to the Web version of this article.)

Taking into account the high costs of research on rhenium, the approximate methods of obtaining S–N curves were verified for the needs of engineering practice. For this purpose, two methods were used to interpolate the S–N curve between two points. According to the first method, the coordinates of these two points were (σ_{1000}, $N_f = 10^3$) and (σ_f, $N_f = 10^6$), which were the stress amplitude corresponding to 10^3 cycles of loading and the assumed fatigue limit, respectively [44]. The σ_{1000} and σ_f values were estimated based on the ultimate tensile strength, having values of $\sigma_{1000} = 0.75 \cdot \sigma_u$ and $\sigma_f = 0.5 \cdot \sigma_u C_L C_D C_S C_R$, where load factor $C_L = 0.9$, size factor $C_D = 1.1$, surface finish factor $C_S = 1$, and reliability factor $C_R = 1$ [44]. According to the second method, the S–N curve was interpolated between points (σ_u, $N_f = 1$) and (σ_f, $N_f = 10^6$), representing the ultimate tensile stress and assumed fatigue limit, respectively [40]. In the case of materials having $\sigma_u \leq 1400$ MPa, $\sigma_f = 0.5 \cdot \sigma_u C_L C_D C_S C_R$, like in the first method. S–N curves determined in this way have slightly higher slopes than those determined experimentally. For the first method, $b = -0.06$, and for the second one, $b = -0.05$. However, the estimated S–N curves are quite good approximations of the experimental results. However, it should be noticed that the methods applied above are based on the values of σ_u, which are

characterized by a noticeable scatter for the analyzed sintered material. This scatter creates additional uncertainty when estimating the S–N curve with approximate methods.

Specimen 3 did not fail under 135 MPa of stress amplitude. This is understandable because the fatigue limit estimated on the basis of the ultimate strength was more than twice as large as those of Specimens 1 and 2, which were $\sigma_f = 355$ MPa and $\sigma_f = 323$ MPa, respectively.

3.4. Fracture analysis after monotonic tension

In Fig. 9, the fracture surface of a specimen subjected to the monotonic tension test is presented. Subsequent magnifications of the picture from Fig. 9a can be seen in parts b–e. The vast majority of the fracture surface shows cracks propagating along the grain boundaries. Intergranular decohesion is one of the basic ways for sintered materials to crack [45]. However, areas of plastic deformation are also visible (Fig. 9c and d). These areas are in the form of voids extending significantly along the crystallographic structure of a single grain (green arrows). In Fig. 9d, secondary intergranular fracture (red arrow) and transgranular fracture (yellow arrow) can also be observed. These cracks are accompanied by slip bands which indicate the ductility of intergranular fracture [46].

Fig. 10 shows a grain with a crystallographic structure orientation more favorable to plastic deformation than adjacent grains. The grain was deformed by the formation of slip bands and twins, resulting in a stepped side surface (red arrow). With the elongation of the grain, its cross-section decreased (in relation to the loading direction), causing intergranular decohesion (yellow arrow).

The monotonic fracture of the sintered rhenium is usually intergranular fracture or, to a lesser extent, plastic transgranular fracture. Occasionally, fragments of cleavage fractures can be found.

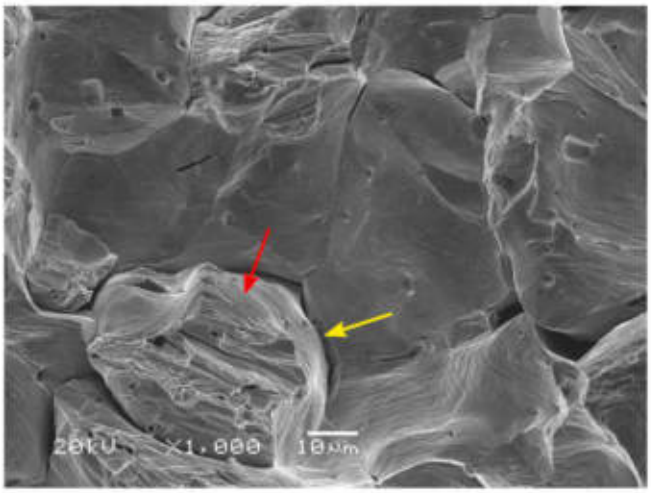

Fig. 10. SEM picture of the fracture surface of Specimen 2; one of the grains, significantly plastically deformed by twinning and slip bands, caused an intergranular fracture.

Intergranular decohesion constitutes a large share of plastic deformation. Similarly, fracture surfaces of rhenium that were obtained by shearing were characterized by Panfilov et al. [47].

3.5. Fracture analysis after fatigue tests

Fig. 11 shows consecutive magnifications of the fatigue fracture of Specimen 8. The presented fracture is not a typical fatigue fracture, which usually is obtained for counterparts manufactured using classical

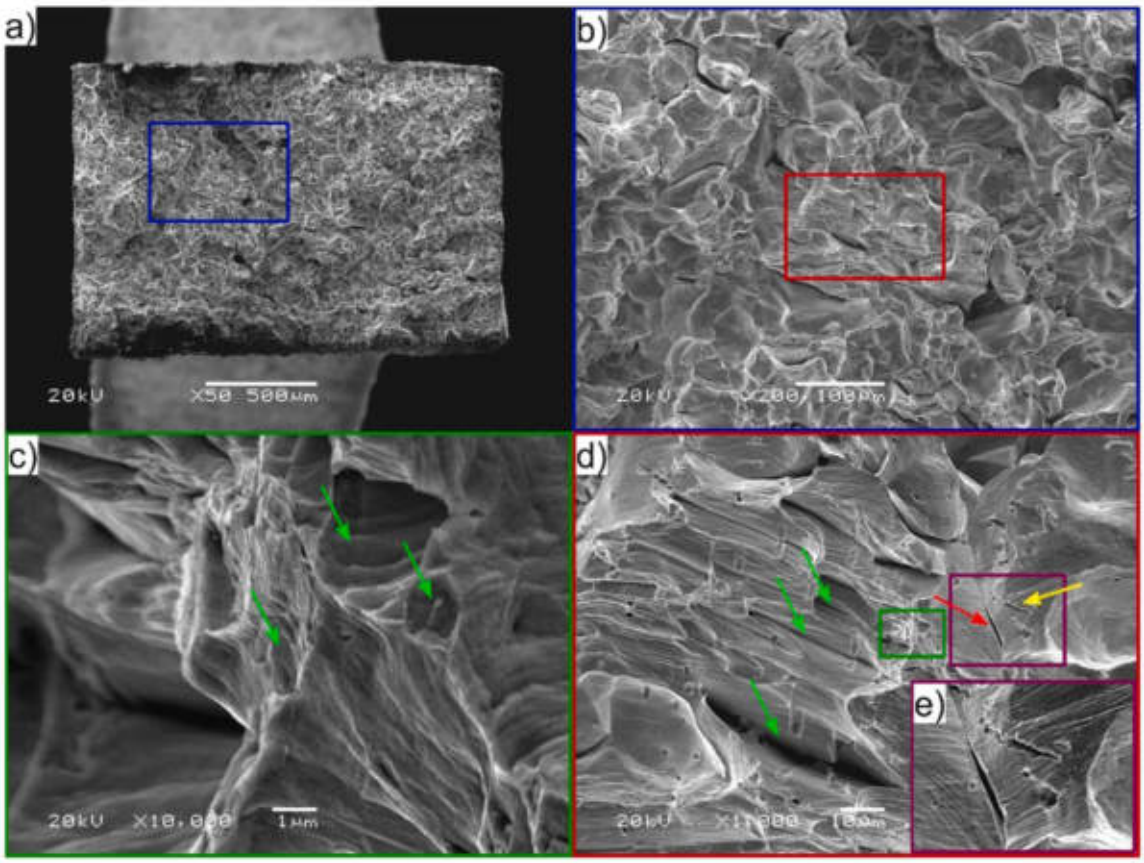

Fig. 9. SEM pictures of the fracture surface of Specimen 2; a) and b) show intergranular decohesion; c) and d) show transgranular ductile dimple fracture; e) secondary transgranular and intergranular cracks and accompanying slip bands.

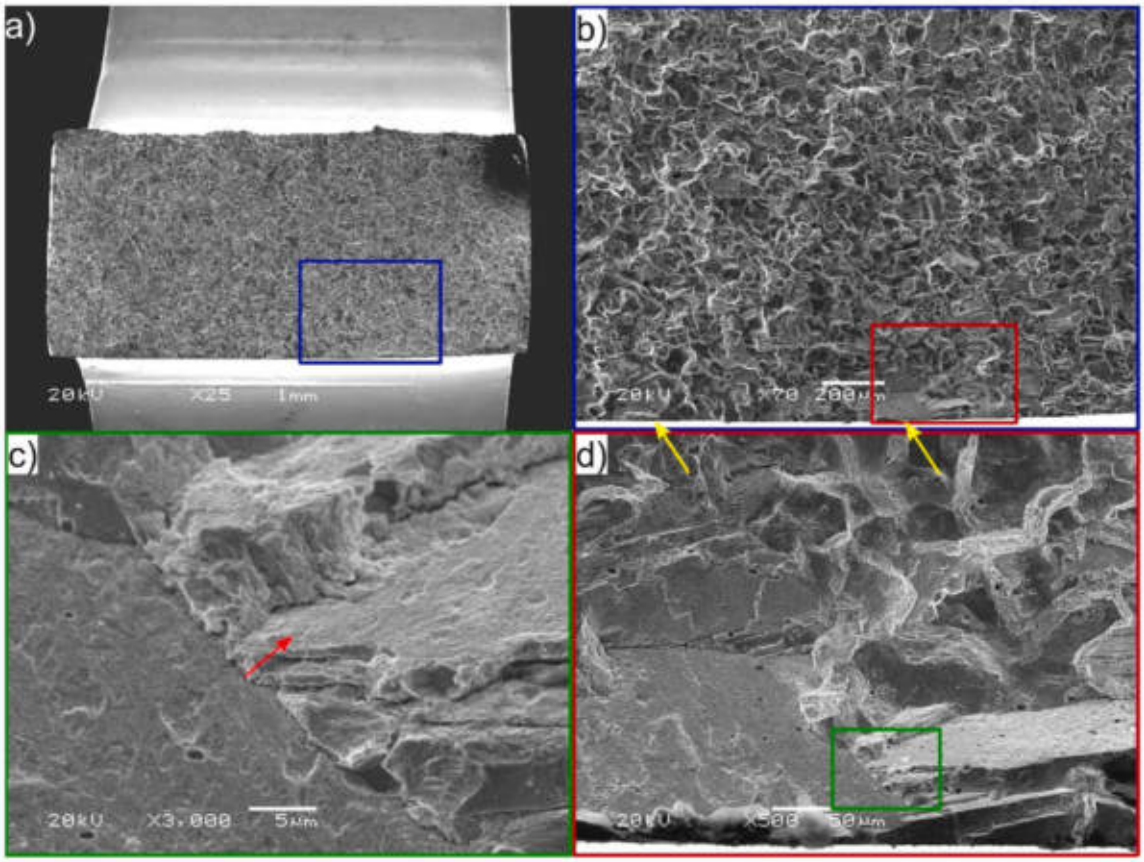

Fig. 11. SEM picture of the fatigue fracture surface of Specimen 8.

technologies like casting or forging. A fatigue zone with typical features like progression marks, ratchet marks, or fatigue striations [48] cannot be distinguished. The fatigue fracture surface shows some similarity to fractures after monotonic tension because cracks propagated along the grain boundaries, as they do in post-monotonic tension fractures. Cracks initiated at many origins (Fig. 11c and d). A cleavage (transgranular) crack included one to a maximum of three adjacent grains, which then propagated intergranular cracks. The vast majority of such origins were located near the specimens' surfaces. In Fig. 11b, two origins are indicated by arrows. In Fig. 11c, one can observe cleavage fractures which propagated from one grain to the adjacent ones (red arrow), characterized by a large difference in the angles of the cleavage planes between the grains. The large angle is due to the small number of cleavage planes in materials with a hexagonal lattice.

In Fig. 12, many different features of the fatigue fracture surface can be seen. Number 1 is the intergranular fracture, and Number 2 is the transgranular fracture. In areas 3 and 4 there is a plastic fracture. On Surface 5 of the transgranular fracture, a three-direction system at a 60° angle is visible, and it was formed by intersecting deformation twins. Numerous pores can be seen on Surface 6. Since their spatial orientation is the same, it can be assumed that they were formed in one grain. Fig. 12 is an example of how fatigue fracture of sintered materials can frequently be combinations of dimple rupture, cleavage, and intergranular failure micromechanisms [45].

In a review paper by Pineau et al. [49], it was stated that for metals with a hexagonal lattice, the basic cleavage plane is the basal plane {0001}. Three cleavage planes were identified using the geometry of pores intersecting in the cleavage planes in Fig. 13a–d as an indicator of the arrangement of the crystallographic lattice of a single grain (Fig. 6e) and by using the experimentally observed primary slip and twin systems in magnesium (Fig. 13e) [50]. Using the results obtained by Sabisch and Minor [17,18], it can be concluded that the cleavage planes coincide

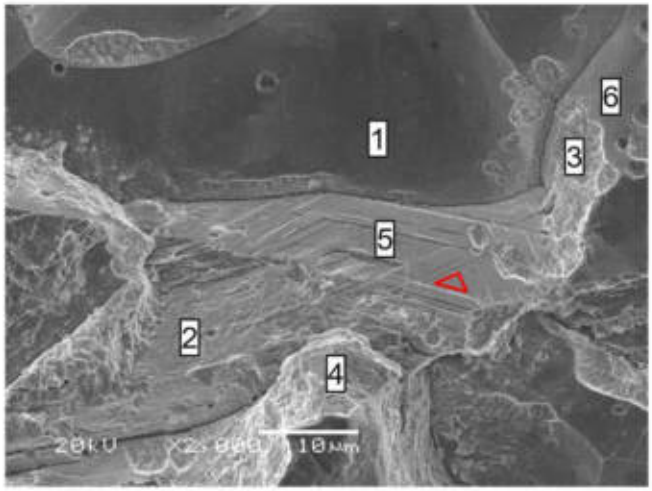

Fig. 12. SEM picture of the fatigue fracture surface of Specimen 8.

with the slip planes, which are the basal slip plane {0001}, prismatic slip plane $\{11\bar{2}0\}$, and pyramidal slip plane $\{10\bar{1}1\}$. So, in the pictures of the cleavage fracture in Fig. 13, the following cleavage directions can be found: basal plane {0001} and pyramidal plane $\{10\bar{1}1\}$ (Fig. 13a), and prismatic plane $\{11\bar{2}0\}$ (Fig. 13b), basal plane {0001}, and prismatic plane $\{11\bar{2}0\}$ (Fig. 13c and d). The most frequently appearing cleavage planes were basal planes {0001} and prismatic planes $\{11\bar{2}0\}$. The basal planes' fracture surfaces were smooth (Fig. 13d, blue arrow). These are the planes with the highest tendency to cleave or split [50]. A number of surface irregularities were observed on the remaining planes. In

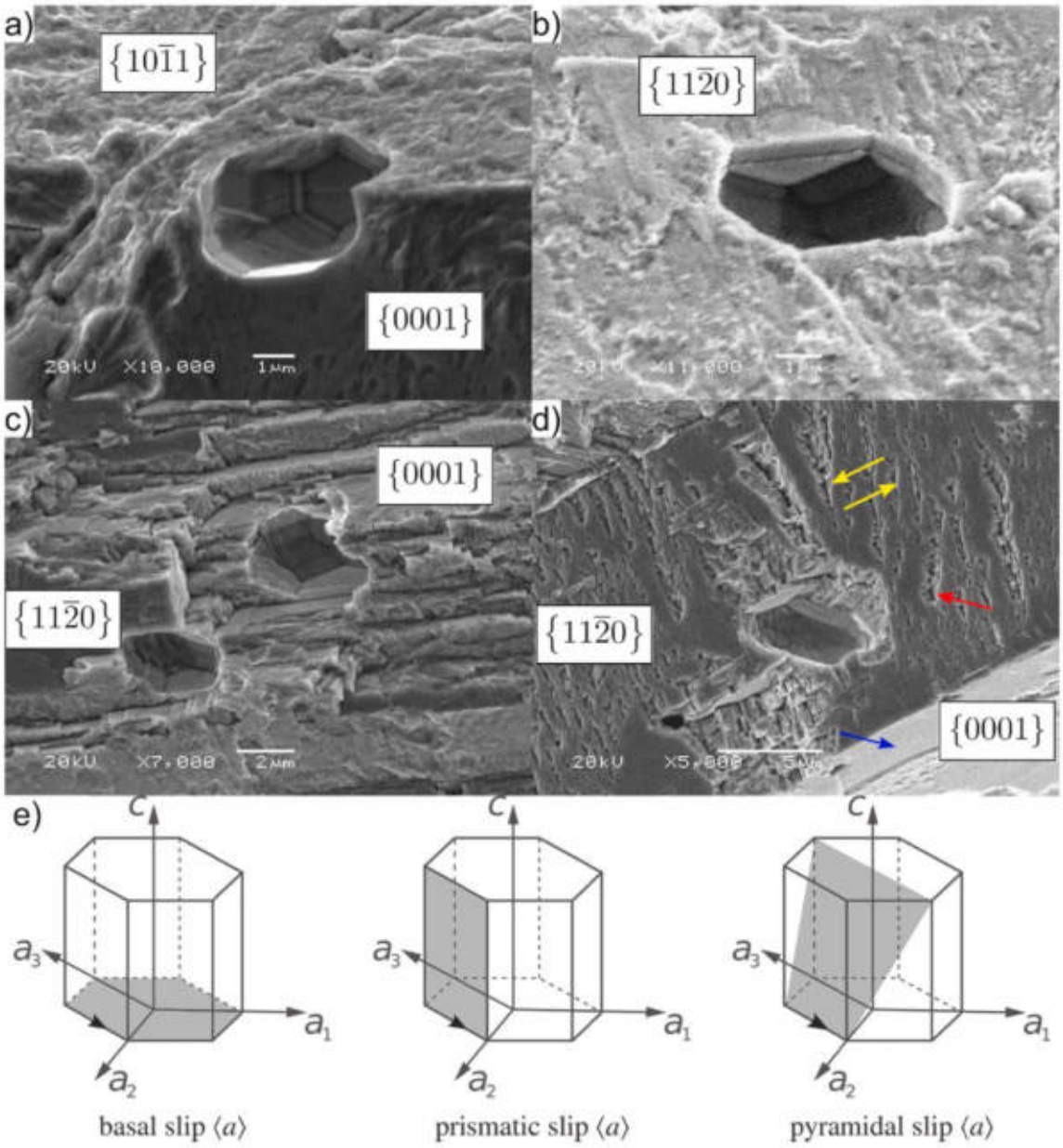

Fig. 13. a–d) SEM pictures of the cleavage fragments of the fracture with visible pores of Specimen 8, on the basis of which the cleavage planes were determined; e) primary slip and twin systems in hexagonal lattice for magnesium (source – Chang and Kochmann [50]).

Fig. 13d, there is a pore which was deformed by numerous slip bands. The yellow arrows indicate the slip direction. The red arrow points to one of the many "tongues" which formed at the intersection of the main fracture plane and the mechanical twins [49]. "Tongues" form when a developing cleavage fracture meets deformation twins [51].

Based on the analysis of fatigue fractures which accounted for pores, no influence of geometrical or microstructural discontinuities on crack development were found, including discontinuities such as pores, their agglomerates, prior particle surfaces, interfaces, or interphase boundaries. This behavior is characteristic of sintered materials with high densities, i.e., materials with a small number of pores of regular shapes and small sizes [52].

Usually, both monotonic and fatigue fractures are intergranular. However, the fatigue fracture had its own specificity. Unlike monotonic fracture, fatigue fracture was brittle—it was not accompanied by plastic deformation. On the surface of the fatigue fracture (Figs. 5 and 12), no intergranular or transgranular secondary cracks associated with the slip bands or the deformation twins could be seen (Figs. 9d and 10). Furthermore, another feature that did not occur in the fatigue fracture was plastic areas which may have involved several grains. The plasticity could be observed in small, local areas (Fig. 12). The second difference between the monotonic and fatigue fractures was that certain fracture features practically did not occur under monotonic tension, namely cleavage areas that play a key role at the stage of fatigue crack initiation.

3.6. Specimen surface analysis after fatigue tests

After conducting the fatigue tests, the specimens' surfaces were investigated using an optical, metallographic microscope. On Surfaces 1–3, numerous intergranular cracks that had developed evenly over the entire surface were visible (Fig. 14). The grains revealed by the cracks corresponded to the grain sizes of the metallographic specimen (Fig. 3). Although cracks developed randomly along the grain boundaries, they mostly developed in the direction normal to the loading. In Fig. 14, a small crack (blue arrow) spanning several grains perpendicular to the loading direction is clearly visible. On the other hand, deformation twins

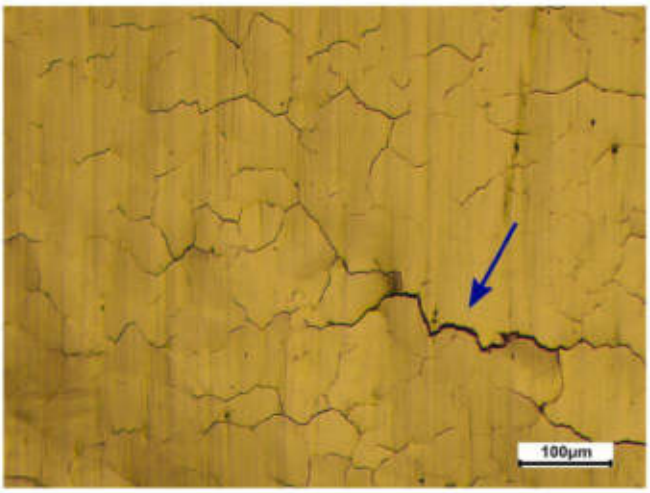

Fig. 14. Picture of Surface 1 of Specimen 5, after the fatigue test.

appeared on surfaces 2–4 (Fig. 15). This observation is consistent with the results of the studies of Sabisch and Minor [17,18], who stated that twinning becomes the dominant strain accommodation in rhenium. Additionally, as stated in the quoted papers, twins typically form in one direction. Rarely, twins can be seen in two directions due to them blocking each other.

Often, the boundaries of deformation twins were the sources of crack initiation (Fig. 16). These cracks were perpendicular to the loading direction. Twin lamellae are often sources of fatigue cracks in hexagonal metals, such as magnesium [32]. The disappearance of deformation twins can be observed in the vicinity of microcracks due to the concentration of plastic deformation.

The analysis revealed an anisotropy of the morphology of Surfaces 1–3 and 2–4. Both surfaces had the same orientation with respect to the loading of the specimens. However, cracks appeared on Surfaces 1–3 which were normal to the sintering pressure direction and characterized by lower hardness. Conversely, deformation twins were visible on Surfaces 2–4 which were tangent to the direction of the sintering pressure and were characterized by greater hardness.

3.7. Metallographic analyses after monotonic tension tests

On Surfaces 1–3 and 2–4, pictures of metallographic specimens were taken after carrying out tension tests. Numerous cracks could be observed on Surfaces 1–3 (Fig. 17). All cracks were intergranular. The direction of growth of all cracks was approximately perpendicular to the

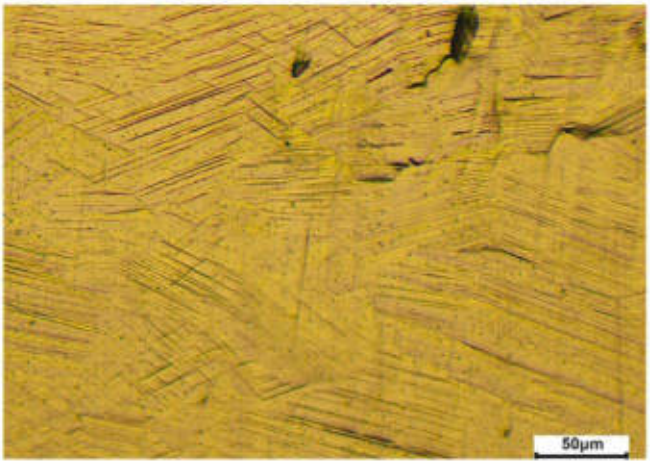

Fig. 15. Picture of Surface 4 of Specimen 8, after the fatigue test.

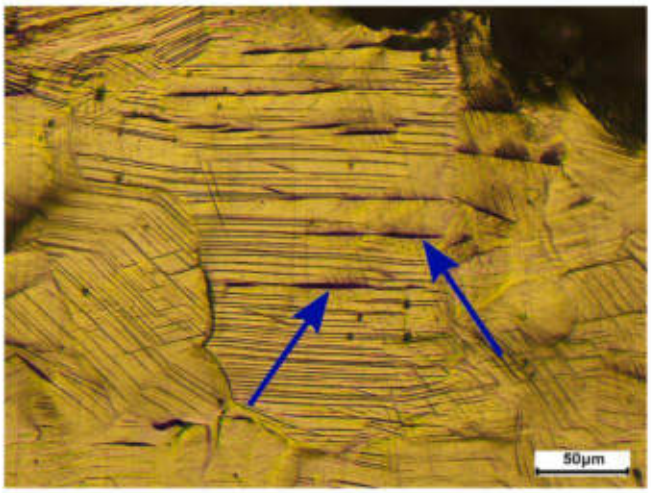

Fig. 16. Picture of Surface 4 of Specimen 8, after the fatigue test.

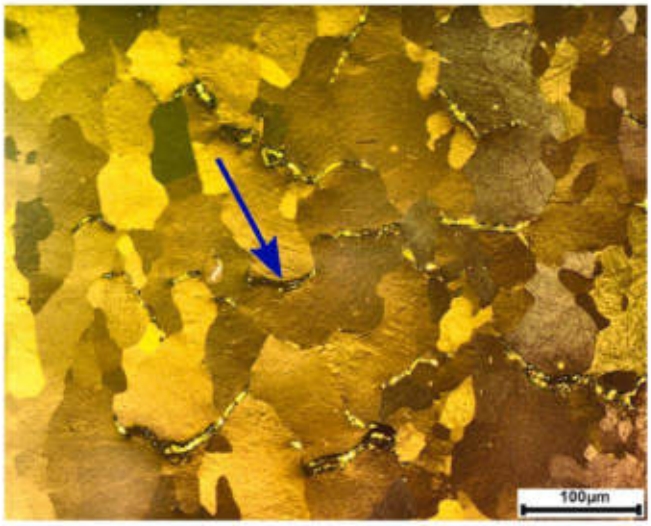

Fig. 17. Picture of Surface 1 of Specimen 2, after the monotonic tension test; the surface was polished and etched prior to taking pictures.

direction of the maximum normal stress. On Surfaces 2–4, there were grains with a large number of deformation twins, as well as systems of twins that intersected with each other (Fig. 18a, blue arrow). Inside the individual grains, especially around the twins, changing colors of polarized light were observed (Fig. 18b, blue arrow). Based on the conclusions of Sabisch and Minor [18], it can be presumed that the present results indicate the accumulation of dislocations around the twins. According to these authors, the twinning mechanism coexists with dislocation plasticity for high levels of deformation.

3.8. Metallographic analyses after fatigue tests

On Surfaces 1–3, single intergranular cracks were seen in the direction normal to the loading after fatigue tests (Fig. 19). However, there were numerous twins on Surfaces 2–4 (Fig. 20). This is consistent with the observation of the free surface after fatigue (Fig. 14). Systems of parallel cracks inside the grains were also visible. These cracks developed along the twinning plane, similar to how they would under monotonic loading (Fig. 16). Similarly, Roostaei and Jahed also observed fatigue cracks along the twinning planes for magnesium alloy [32]. In rhenium, some grains had intersecting cracks (Fig. 20). The directions of the cracks were at an angle of 45° to the loading (blue

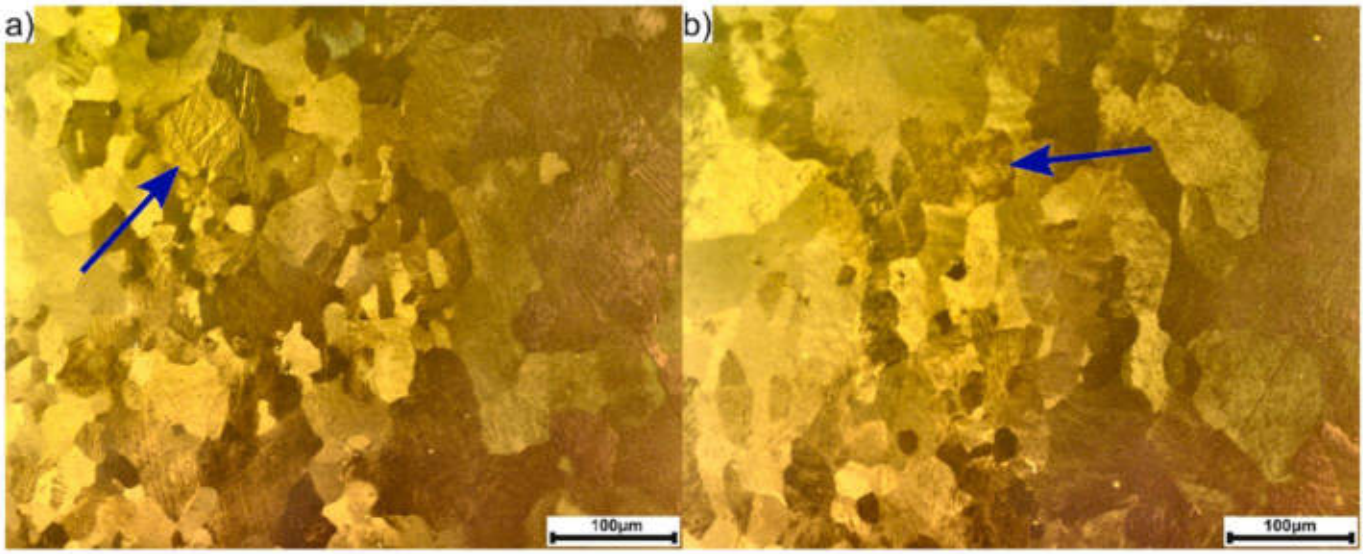

Fig. 18. Picture of Surface 2 of Specimen 2, after the monotonic tension test; the surface was polished and etched prior to taking pictures.

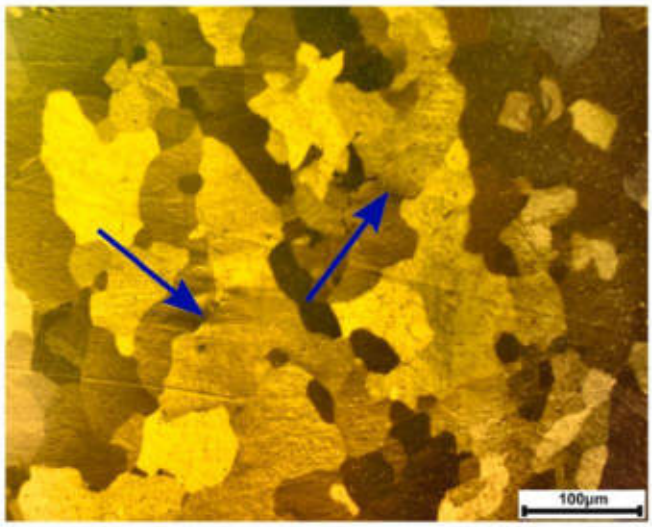

Fig. 19. Picture of Surface 1 of Specimen 7, after the fatigue test; the surface was polished and etched prior to taking pictures.

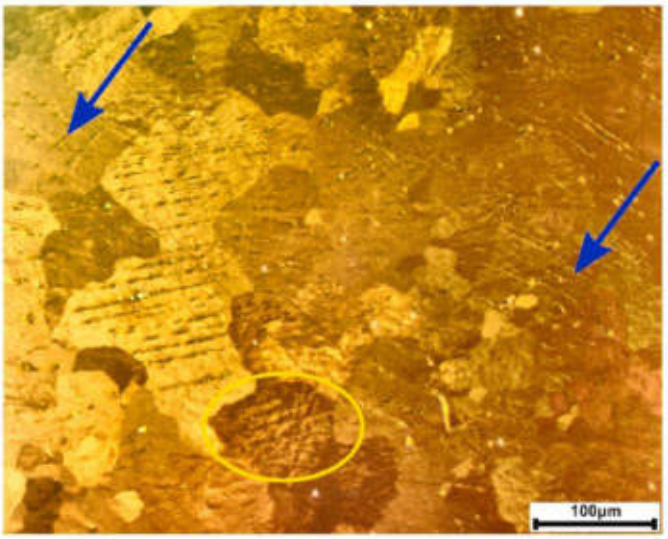

Fig. 20. Picture of Surface 2 of Specimen 6, after the fatigue test; the surface was polished and etched prior to taking pictures.

arrows), in the plane of the maximum shear strain. As above, the change in color of polarized light indicated a pile of dislocations around twins and cracks. An example of such an area is marked in yellow in Fig. 20.

4. Conclusions

1) Tensile properties such as the yield stress, ultimate tensile strength, and strain at breaking are characterized by some scatter. The reason for this may be the crystallographic structure of the sinter, which is distinguished by a large variation in grain size.
2) The S–N curve was fitted with a very high coefficient of determination $R^2 = 0.988$. On one hand, this may have been due to the geometry of the samples, such as their small size and very high surface smoothness. On the other hand, the high R^2 may have resulted from the material features of rhenium, namely the brittleness of the grain boundaries.
3) The determined fatigue curve has a very low slope. Basquin's exponent is just $c = -0.04$. This is the result of the polishing of the specimens' surfaces, the existence of small and few regular-shaped pores in the sinter, and the brittleness of the grain boundaries.
4) Since the tested sinter has a high density, the pores do not affect the development of the fatigue cracks. The pores are sparse, regularly shaped, and small in size.
5) Approximation methods allowed for safe estimation of the fatigue life of rhenium in the high-cycle range. Nevertheless, it should be remembered that all methods based on monotonic data are subject to great uncertainty, such as in the case of sintered rhenium with scatter of properties.
6) Fatigue cracks propagated along the grain boundaries which were formed by sintering. The grain boundary fracture was the dominant mechanism of monotonic and fatigue crack propagation in rhenium.
7) Under monotonic tension and fatigue loading, cracks developed in the direction normal to the loading.
8) The fractures of specimens subjected to monotonic tension are characterized by high plasticity, which is apparent based on the presence of numerous twins and slip bands. A significant part of

the fracture consisted of intergranular decohesion, and a smaller part consisted of plastic areas.

9) The fatigue fracture was much less plastic than the monotonic fracture. Cracks initiated in the cleavage planes and propagated in these planes through a minimum of one and a maximum of three grains. Then, they propagated in a brittle, intergranular manner.
10) There was no significant difference in fractures or in the topography of the side surfaces of fatigue specimens with different stress levels. The mechanism of fatigue crack initiation and development was identical for each specimen in the entire tested loading amplitude range.
11) Three cleavage planes were identified in the fatigue fracture surfaces: the most common was the basal plane $\{0001\}$, then the prismatic plane $\{11\bar{2}0\}$, and lastly the pyramidal plane $\{10\bar{1}1\}$.
12) The sintered rhenium had an anisotropy of mechanical properties. In the direction normal to pressing in the technological process, rhenium had a much greater hardness and strength than it did in the tangential directions.
13) The deformation of rhenium takes place mainly through the twinning mechanism with some dislocations in planes, which is a process that is analogous to the active systems in magnesium and its alloys.

Data availability

The data supporting the findings of this study are available from the corresponding authors upon request.

CRediT authorship contribution statement

Jan Seyda: Conceptualization, Methodology, Validation, Investigation, Resources. **Dariusz Skibicki:** Conceptualization, Validation, Formal analysis, Investigation, Writing – original draft. **Łukasz Pejkowski:** Conceptualization, Methodology, Investigation, Writing – review & editing, Visualization. **Andrzej Skibicki:** Investigation. **Piotr Domanowski:** Conceptualization, Resources, Funding acquisition. **Paweł Maćkowiak:** Resources.

Declaration of competing interest

The authors declare that they have no known competing financial interests or personal relationships that could have appeared to influence the work reported in this paper.

References

[1] E. Scerri, Recognizing rhenium, Nat. Chem. 2 (2010) 598, https://doi.org/10.1038/nchem.717.
[2] J. Wang, S. Bai, Y. Ye, H. Zhang, L. Zhu, Microstructure and mechanical properties of rhenium prepared by electroforming in NaCl-KCl-CsCl-K2ReCl6 molten salts, Int. J. Refract. Metals Hard Mater. 72 (2018) 263–269, https://doi.org/10.1016/j.ijrmhm.2018.01.001.
[3] W. Wu, N. Eliaz, E. Gileadi, Electrodeposition of Re-Ni alloys from aqueous solutions with organic additives, Thin Solid Films 616 (2016) 828–837, https://doi.org/10.1016/j.tsf.2016.10.012.
[4] B.D. Bryskin, Evaluation of properties and special features for high-temperature applications of rhenium, AIP Conf. Proc. 246 (1992) 278–291, https://doi.org/10.1063/1.41837.
[5] A. V Naumov, Rhythms of rhenium, Russ. J. Non-Ferrous Metals 48 (2007) 418–423, https://doi.org/10.3103/S1067821207060089.
[6] K. Bochenek, W. Węglewski, J. Morgiel, M. Maj, M. Basista, Enhancement of fracture toughness of hot-pressed NiAl-Re material by aluminum oxide addition, Mater. Sci. Eng. 790 (2020) 6–11, https://doi.org/10.1016/j.msea.2020.139670.
[7] Z.H. Tan, X.G. Wang, L.H. Ye, G.C. Hou, R. Li, Y.H. Yang, J.L. Liu, J.D. Liu, L. Yang, B. Wang, P. Dong, J.G. Li, Y.Z. Zhou, X.F. Sun, Effects of rhenium on the microstructure and creep properties of novel nickle-based single crystal superalloys, Mater. Sci. Eng. 761 (2019), https://doi.org/10.1016/j.msea.2019.138042.
[8] K. Majchrowicz, Z. Pakieła, T. Brynk, B. Romelczyk-Baishya, M. Płociński, T. Kurzynowski, E. Chlebus, Microstructure and mechanical properties of Ti–Re alloys manufactured by selective laser melting, Mater. Sci. Eng. 765 (2019), https://doi.org/10.1016/j.msea.2019.138290.
[9] S. Kajita, T. Nojima, T. Okuyama, Y. Yamamoto, N. Yoshida, N. Ohno, Helium-plasma–induced straight nanofiber growth on HCP metals, Acta Mater. 181 (2019) 342–351, https://doi.org/10.1016/j.actamat.2019.09.053.
[10] Y. He, B. Li, C. Wang, S.X. Mao, Direct observation of dual-step twinning nucleation in hexagonal close-packed crystals, Nat. Commun. 11 (2020) 1–8, https://doi.org/10.1038/s41467-020-16351-0.
[11] D.A. John, R.R. Seal, D.E. Polyak, Rhenium, vol. 1802, USGS Numbered Ser, 2017, p. 62, https://doi.org/10.3133/pp1802P.
[12] A. Naor, N. Eliaz, E. Gileadi, Electrodeposition of rhenium-nickel alloys from aqueous solutions, Electrochim. Acta 54 (2009) 6028–6035, https://doi.org/10.1016/j.electacta.2009.03.003.
[13] A. Naor, N. Eliaz, E. Gileadi, S.R. Taylor, Properties and applications of rhenium and its alloys, AMMTIAC Q 5 (2010) 11–15, https://doi.org/10.1016/j.brainres.2006.04.097.
[14] O.D. Neikov, S.S. Naboychenko, I.B. Murashova, N.A. Yefimov, Production of refractory metal powders, in: Handb. Non-ferrous Met. Powders, second ed., Elsevier Ltd., 2019, pp. 685–755, https://doi.org/10.1016/b978-0-08-100543-9.00023-3.
[15] A.J. Sherman, R.H. Tuffias, R.B. Kaplan, The properties and applications of rhenium produced by CVD, JOM (J. Occup. Med.) 43 (1991) 20–23, https://doi.org/10.1007/BF03220615.
[16] J. Kacher, A.M. Minor, Twin boundary interactions with grain boundaries investigated in pure rhenium, Acta Mater. 81 (2014) 1–8, https://doi.org/10.1016/j.actamat.2014.08.013.
[17] J.E.C. Sabisch, A.M. Minor, Microstructural evolution of rhenium Part I: Compression, Mater. Sci. Eng. 732 (2018) 251–258, https://doi.org/10.1016/j.msea.2018.06.057.
[18] J.E.C. Sabisch, A.M. Minor, Microstructural evolution of rhenium Part II: Tension, Mater. Sci. Eng. 732 (2018) 259–272, https://doi.org/10.1016/j.msea.2018.06.059.
[19] J. Kacher, J.E. Sabisch, A.M. Minor, Statistical analysis of twin/grain boundary interactions in pure rhenium, Acta Mater. 173 (2019) 44–51, https://doi.org/10.1016/j.actamat.2019.04.051.
[20] L. Jiang, V.R. Radmilović, J.E.C. Sabisch, L. Qi, A.M. Minor, D.C. Chrzan, M. Asta, Twin nucleation from a single <c+a> dislocation in hexagonal close-packed crystals, Acta Mater. 202 (2021) 35–41, https://doi.org/10.1016/j.actamat.2020.10.038.
[21] R. Adams, Microstructural and Mechanical Property Characterization of Laser Additive Manufactured (LAM) Rhenium, Arizona State Univesity, 2012, https://doi.org/10.1017/CBO9781107415324.004.
[22] J.A. Biaglow, Rhenium material properties, NASA Tech. Memo. 107043 (1995), https://doi.org/10.2514/6.1995-2398.
[23] J.A. Biaglow, Rhenium material properties, in: 31st Jt. Propuls, Conf. Exhib., San Diego, CA, 1995, https://doi.org/10.2514/6.1995-2398.
[24] M.L. Chazen, Materials property test results of rhenium, in: 31st AIAA/ASME/SAE/ASEE Jt. Propuls, Conf. Exhib., San Diego, CA, 1995, https://doi.org/10.2514/6.1995-2938.
[25] B.D. Reed, J.A. Biaglow, S.J. Schneider, Iridium-coated rhenium radiation-cooled rockets, NASA Tech. Memo. (1997), 107453.
[26] J.R. Wooten, P.T. Lansaw, High temperature oxidation-resistant thruster research, NASA contract, For. Rep. 185233 (1990).
[27] ISO 6892-1, Metallic Materials - Tensile Testing - Part 1: Method of Test at Room Temperature, 2019.
[28] ASTM E739-10, Standard Practice for Statistical Analysis of Linear or Linearized Stress-Life (S-N) and Strain-Life (ε-N) Fatigue Data, 2015.
[29] ASTM E407-07, Standard Practice for Microetching Metals and Alloys, 2015.
[30] ASTM E112-13, Standard Test Methods for Determining Average Grain Size, 2013.
[31] R.W. Armstrong, Material grain size and crack size influences on cleavage fracturing, Philos. Trans. R. Soc. A Math. Phys. Eng. Sci. 373 (2015), https://doi.org/10.1098/rsta.2014.0124.
[32] A.A. Roostaei, H. Jahed, Role of loading direction on cyclic behaviour characteristics of AM30 extrusion and its fatigue damage modelling, Mater. Sci. Eng. 670 (2016) 26–40, https://doi.org/10.1016/j.msea.2016.05.116.
[33] P. Vlcak, J. Fojt, J. Drahokoupil, V. Brezina, J. Sepitka, T. Horazdovsky, J. Miksovsky, F. Cerny, M. Lebeda, M. Haubner, Influence of surface pre-treatment with mechanical polishing, chemical, electrochemical and ion sputter etching on the surface properties, corrosion resistance and MG-63 cell colonization of commercially pure titanium, Mater. Sci. Eng. C 115 (2020) 111065, https://doi.org/10.1016/j.msec.2020.111065.
[34] P. Ptáček, Apatites and Their Synthetic Analogues - Synthesis, Structure, Properties and Applications, IntechOpen, 2016.
[35] R. Kimura, Y. Kariya, N. Mizumura, K. Sasaki, Effect of sintering temperature on fatigue crack propagation rate of sintered Ag nanoparticles, Mater. Trans. 59 (2018) 612–619, https://doi.org/10.2320/matertrans.M2017392.
[36] C. Boller, T. Seeger, Materials Data for Cyclic Loading, Elsevier, Amsterdam ; New York, 1987.
[37] A. Bäumel, T. Seeger, C. Boller, Materials Data for Cyclic Loading, Supplement 1, Elsevier, Amsterdam ; New York, 1990.
[38] K.S. Lee, J.H. Song, Estimation methods for strain-life fatigue properties from hardness, Int. J. Fatig. 28 (2006) 386–400, https://doi.org/10.1016/j.ijfatigue.2005.07.037.
[39] J. Schijve, Fatigue of structures and materials, Int. J. Fatig. 25 (2009) 1–622, https://doi.org/10.1007/978-1-4020-6808-9.

[40] R.I. Stephens, A. Fatemi, R.R. Stephens, H.O. Fuchs, Metal Fatigue in Engineering, Wiley, 2000.
[41] F.C. Campbell, Fatigue and Fracture: Understanding the Basics, ASM International, Materials Park, Ohio, 2012, https://doi.org/10.31399/asm.tb.ffub.9781627083034.
[42] S.S. Manson, G.R. Halford, Fatigue and Durability of Structural Materials, ASM International, 2006.
[43] B.A. Lerch, R.D. Noebe, Low-cycle fatigue behavior of polycrystalline NiAl at 1000 K, Metall. Mater. Trans. 25 (1994) 309–319, https://doi.org/10.1007/BF02647976.
[44] Y.-L. Lee, J. Pan, R.B. Hathaway, M.E. Barkey, Fatigue Testing and Analysis (Theory and Practice), Elsevier Butterworth-Heinemann, 2005.
[45] E. Dudrova, M. Kabátova, A review of failure of sintered steels: fractography of static and dynamic crack nucleation, coalescence, growth and propagation, Powder Metall. 59 (2016) 148–167, https://doi.org/10.1080/00325899.2016.1145786.
[46] Y. Cheng, Z.H. Jin, Y.W. Zhang, H. Gao, On intrinsic brittleness and ductility of intergranular fracture along symmetrical tilt grain boundaries in copper, Acta Mater. 58 (2010) 2293–2299, https://doi.org/10.1016/j.actamat.2009.11.033.
[47] P. Panfilov, G.P. Panfilov, D. Zaytsev, Deformation behavior of polycrystalline rhenium under shear testing at room temperature, Mater. Lett. 277 (2020) 128379, https://doi.org/10.1016/j.matlet.2020.128379.
[48] Ł. Pejkowski, D. Skibicki, J. Sempruch, High cycle fatigue behavior of austenitic steel and pure copper under uniaxial , proportional and non-proportional loading, in: Stroj. Vestn. - J. Mech. Eng. (2014) 549–560, https://doi.org/10.5545/sv-jme.2013.1600.
[49] A. Pineau, A.A. Benzerga, T. Pardoen, Failure of metals I: brittle and ductile fracture, Acta Mater. 107 (2016) 424–483, https://doi.org/10.1016/j.actamat.2015.12.034.
[50] Y. Chang, D.M. Kochmann, A variational constitutive model for slip-twinning interactions in hcp metals: application to single- and polycrystalline magnesium, Int. J. Plast. 73 (2015) 39–61, https://doi.org/10.1016/j.ijplas.2015.03.008.
[51] F. Sorbello, P.E.J. Flewitt, G. Smith, A.G. Crocker, The role of deformation twins in brittle crack propagation in iron-silicon steel, Acta Mater. 57 (2009) 2646–2656, https://doi.org/10.1016/j.actamat.2009.02.011.
[52] B. Weiss, H. Danninger, Fatigue of powder metallurgy materials, Encycl. Mater. Sci. Technol. (2001) 2978–2981, https://doi.org/10.1016/b0-08-043152-6/00529-5.

6.2 Oświadczenie Autora rozprawy doktorskiej

Załącznik nr 3 do
Instrukcji drukowania, gromadzenia, rejestrowania i udostępniania rozpraw doktorskich przez rady naukowe dyscyplin (dyscyplin artystycznych) prowadzących postępowanie w sprawie nadania stopnia naukowego doktora

Oświadczenie Autora rozprawy doktorskiej

mgr inż. Jan Seyda
(tytuł zawodowy, imiona i nazwisko autora rozprawy doktorskiej)

Szkoła Doktorska Politechniki Bydgoskiej im. Jana i Jędrzeja Śniadeckich
(miejsce pracy/afiliacja)

OŚWIADCZENIE

Oświadczam, iż mój wkład autorski w niżej wymienionych artykułach naukowych stanowiących cykl publikacji rozprawy doktorskiej był następujący*:

1. Pejkowski Ł, Seyda J. Fatigue of four metallic materials under asynchronous loadings: Small cracks observation and fatigue life prediction, International Journal of Fatigue (Elsevier), 2021, 142, 105904, 1-18, DOI: 10.1016/j.ijfatigue.2020.105904, 140 pkt. MNiSW, IF 5.489.
   Wykonane zadania przez Doktoranta w ramach artykułu:
   a) metodologia
   b) badania mikroskopowe
   c) walidacja
   d) przygotowanie pierwotnego szkicu
   e) wizualizacja

2. Pejkowski Ł, Seyda J, Skibicki D. Short cracks observations on surfaces of specimens made of three materials, subjected to synchronous and asynchronous multiaxial loadings, Matec Web of Conferences (EDP Sciences), 2019, 300, 1-8, DOI: 10.1051/matecconf/201930015002, 5 pkt. MNiSW.
   Wykonane zadania przez Doktoranta w ramach artykułu:
   a) metodologia
   b) badania mikroskopowe
   c) walidacja
   d) wizualizacja

3. Seyda J, Pejkowski Ł, Skibicki D. The shear stress determination in tubular specimens under torsion in the elastic–plastic strain range from the perspective of fatigue analysis. Materials (MDPI), 2020, 13, 23, 1-16, DOI: 10.3390/ma13235583, 140 pkt. MNiSW, IF 3.623.
   Wykonane zadania przez Doktoranta w ramach artykułu:
   a) metodologia
   b) oprogramowanie
   c) walidacja
   d) zasoby
   e) analiza formalna
   f) przygotowanie pierwotnego szkicu
   g) wizualizacja

---

* *W przypadku prac dwu- lub wieloautorskich wymagane są oświadczenia kandydata do stopnia doktora oraz współautorów, wskazujące na ich merytoryczny wkład w powstanie każdej pracy (np. twórca hipotezy badawczej, pomysłodawca badań, wykonanie specyficznych badań – np. przeprowadzenie konkretnych doświadczeń, opracowanie i zebranie ankiet itp., wykonanie analizy wyników, przygotowanie manuskryptu artykułu i inne). Określenie wkładu danego autora, w tym kandydata do stopnia doktora, powinno być na tyle precyzyjne, aby umożliwić dokładną ocenę jego udziału i roli w powstaniu każdej pracy.*

4. Seyda J, Pejkowski Ł, Skibicki D. Identification of fatigue damage mechanism in PA38-T6 aluminum alloy under multiaxial loadings – Initial research. Procedia Structural Integrity (Elsevier), 2020, 28, - , 1458-1466, DOI: 10.1016/j.prostr.2020.10.119, 5 pkt. MNiSW. Wykonane zadania przez Doktoranta w ramach artykułu:
   a) konceptualizacja
   b) metodologia
   c) przygotowanie próbek
   d) badania wytrzymałościowe
   e) badania techniką replikacji
   f) badania mikroskopowe
   g) oprogramowanie
   h) walidacja
   i) analiza formalna
   j) zasoby
   k) gromadzenie danych
   l) przygotowanie pierwotnego szkicu
   m) wizualizacja

5. Seyda J, Pejkowski Ł. SEM analysis of PA38-T6 aluminum alloy thin-walled tubular specimen fatigue fracture, and comparison to surface replication results, Matec Web of Conferences (EDP Sciences), 2019, 300, 1-8, DOI: 10.1051/matecconf/201930015002, 5 pkt. MNiSW. Wykonane zadania przez Doktoranta w ramach artykułu:
   a) konceptualizacja
   b) metodologia
   c) przygotowanie próbek
   d) badania wytrzymałościowe
   e) badania fraktograficzne
   f) oprogramowanie
   g) walidacja
   h) analiza formalna
   i) zasoby
   j) gromadzenie danych
   k) przygotowanie pierwotnego szkicu
   l) wizualizacja

6. Seyda J, Pejkowski Ł, Chorobiński M. Study on the behavior of small cracks in PA38-T6 (6060-T6) aluminum alloy under multiaxial fatigue loadings. International Journal of Fatigue (Elsevier), 2024, 184, 108282, DOI: 10.1016/S1003-6326(23)66333-2, 140 pkt. MNiSW, IF 6.000.
   Wykonane zadania przez Doktoranta w ramach artykułu:
   a) konceptualizacja
   b) metodologia
   c) przygotowanie próbek
   d) badania wytrzymałościowe
   e) badania techniką replikacji
   f) badania mikroskopowe
   g) badania fraktograficzne
   h) oprogramowanie
   i) walidacja
   j) analiza formalna
   k) zasoby
   l) gromadzenie danych
   m) przygotowanie pierwotnego szkicu
   n) pisanie - recenzowanie i edycja
   o) wizualizacja

7. Seyda J, Skibicki D, Pejkowski Ł, Skibicki A, Domanowski P, Maćkowiak P. Mechanical properties and microscopic analysis of sintered rhenium subjected to monotonic tension and uniaxial fatigue. Materials Science and Engineering A (Elsevier), 2021, 817, 141343, 1-13, DOI: 10.1016/j.msea.2021.141343, 140 pkt. MNiSW, IF 6.044.
   Wykonane zadania przez Doktoranta w ramach artykułu:
   a) konceptualizacja
   b) metodologia
   c) przygotowanie próbek
   d) badania wytrzymałościowe
   e) badania fraktograficzne
   f) badania metalograficzne
   g) oprogramowanie
   h) walidacja
   i) zasoby
   j) gromadzenie danych
   k) wizualizacja

Bydgoszcz 08.04.2024
miejscowość, data

Jan Seyda
Podpis Autora rozprawy doktorskiej

Ł. Pejkowski
Podpis promotora

6.3 Oświadczenia Współautorów artykułów naukowych

Załącznik nr 3 do
Instrukcji drukowania, gromadzenia, rejestrowania i udostępniania rozpraw doktorskich przez rady naukowe dyscyplin (dyscyplin artystycznych) prowadzących postępowanie w sprawie nadania stopnia naukowego doktora

Oświadczenie Współautora

Dr hab. inż. Łukasz Pejkowski
(tytuł zawodowy, imiona i nazwisko współautora)

Politechnika Bydgoska im. Jana i Jędrzeja Śniadeckich, Wydział Inżynierii Mechanicznej, Katedra Mechaniki i Metod Komputerowych
(miejsce pracy/afiliacja)

OŚWIADCZENIE

Oświadczam, iż mój wkład autorski w niżej wymienionym/wymienionych artykule/artykułach naukowym/naukowych był następujący*:

1. Pejkowski Ł, Seyda J. Fatigue of four metallic materials under asynchronous loadings: Small cracks observation and fatigue life prediction, International Journal of Fatigue (Elsevier), 2021, 142, 105904, 1-18, DOI: 10.1016/j.ijfatigue.2020.105904, 140 pkt. MNiSW, IF 5.489. Wykonane zadania w ramach artykułu:
    a) konceptualizacja
    b) metodologia
    c) badania wytrzymałościowe
    d) walidacja
    e) analiza formalna
    f) gromadzenie danych
    g) przygotowanie pierwotnego szkicu
    h) pisanie - recenzowanie i edycja
    i) wizualizacja
    j) nadzór
    k) administracja projektu
    l) zdobycie finansowania

* *W przypadku prac dwu- lub wieloautorskich wymagane są oświadczenia kandydata do stopnia doktora oraz współautorów, wskazujące na ich merytoryczny wkład w powstanie każdej pracy (np. twórca hipotezy badawczej, pomysłodawca badań, wykonanie specyficznych badań – np. przeprowadzenie konkretnych doświadczeń, opracowanie i zebranie ankiet itp., wykonanie analizy wyników, przygotowanie manuskryptu artykułu i inne). Określenie wkładu danego autora, w tym kandydata do stopnia doktora, powinno być na tyle precyzyjne, aby umożliwić dokładną ocenę jego udziału i roli w powstaniu każdej pracy.*

2. Pejkowski Ł, Seyda J, Skibicki D. Short cracks observations on surfaces of specimens made of three materials, subjected to synchronous and asynchronous multiaxial loadings, Matec Web of Conferences (EDP Sciences), 2019, 300, 1-8, DOI: 10.1051/matecconf/201930015002, 5 pkt. MNiSW.
   Wykonane zadania w ramach artykułu:
   a) konceptualizacja
   b) metodologia
   c) badania wytrzymałościowe
   d) walidacja
   e) analiza formalna
   f) gromadzenie danych
   g) przygotowanie pierwotnego szkicu
   h) pisanie - recenzowanie i edycja
   i) wizualizacja
   j) nadzór
   k) administracja projektu
   l) zdobycie finansowania

3. Seyda J, Pejkowski Ł, Skibicki D. The shear stress determination in tubular specimens under torsion in the elastic–plastic strain range from the perspective of fatigue analysis. Materials (MDPI), 2020, 13, 23, 1-16, DOI: 10.3390/ma13235583, 140 pkt. MNiSW, IF 3.623.
   Wykonane zadania w ramach artykułu:
   a) konceptualizacja
   b) metodologia
   c) oprogramowanie
   d) walidacja
   e) gromadzenie danych
   f) przygotowanie pierwotnego szkicu
   g) pisanie - recenzowanie i edycja
   h) wizualizacja
   i) administracja projektu
   j) zdobycie finansowania

4. Seyda J, Pejkowski Ł, Skibicki D. Identification of fatigue damage mechanism in PA38-T6 aluminum alloy under multiaxial loadings – Initial research. Procedia Structural Integrity (Elsevier), 2020, 28, - , 1458-1466, DOI: 10.1016/j.prostr.2020.10.119, 5 pkt. MNiSW.
   Wykonane zadania w ramach artykułu:
   a) analiza formalna
   b) zasoby
   c) przygotowanie pierwotnego szkicu
   d) pisanie - recenzowanie i edycja
   e) nadzór

5. Seyda J, Pejkowski Ł. SEM analysis of PA38-T6 aluminum alloy thin-walled tubular specimen fatigue fracture, and comparison to surface replication results, Matec Web of Conferences (EDP Sciences), 2019, 300, 1-8, DOI: 10.1051/matecconf/201930015002, 5 pkt. MNiSW.
   Wykonane zadania w ramach artykułu:
   a) analiza formalna
   b) zasoby
   c) przygotowanie pierwotnego szkicu
   d) pisanie - recenzowanie i edycja
   e) nadzór

6. Seyda J, Pejkowski Ł, Chorobiński M. Study on the behavior of small cracks in PA38-T6 (6060-T6) aluminum alloy under multiaxial fatigue loadings. International Journal of Fatigue (Elsevier), 2024, 184, 108282, DOI: 10.1016/S1003-6326(23)66333-2, 140 pkt. MNiSW, IF 6.000.
   Wykonane zadania w ramach artykułu:
   a) konceptualizacja
   b) analiza formalna
   c) oprogramowanie
   d) zasoby
   e) pisanie - recenzowanie i edycja
   f) nadzór

7. Seyda J, Skibicki D, Pejkowski Ł, Skibicki A, Domanowski P, Maćkowiak P. Mechanical properties and microscopic analysis of sintered rhenium subjected to monotonic tension and uniaxial fatigue. Materials Science and Engineering A (Elsevier), 2021, 817, 141343, 1-13, DOI: 10.1016/j.msea.2021.141343, 140 pkt. MNiSW, IF 6.044.
   Wykonane zadania w ramach artykułu:
   a) konceptualizacja
   b) metodologia
   c) badania wytrzymałościowe
   d) analiza formalna
   e) zasoby
   f) przygotowanie pierwotnego szkicu
   g) pisanie - recenzowanie i edycja

Jednocześnie wyrażam zgodę na przedłożenie wyżej wymienionej/wymienionych pracy/prac przez …….. mgr inż. Jan Seyda……. (podać tytuł zawodowy imię i nazwisko kandydata do stopnia doktora) jako część rozprawy doktorskiej opartej na zbiorze opublikowanych i powiązanych tematycznie artykułów naukowych.

Bydgoszcz, 08.04.2024
.....
miejscowość, data

Ł. Pejkowski
.....
podpis Współautora

Załącznik nr 3 do
Instrukcji drukowania, gromadzenia, rejestrowania i udostępniania rozpraw doktorskich przez rady naukowe dyscyplin (dyscyplin artystycznych) prowadzących postępowanie w sprawie nadania stopnia naukowego doktora

Oświadczenie Współautora

Prof. dr hab. inż. Dariusz Skibicki
(tytuł zawodowy, imiona i nazwisko współautora)

Politechnika Bydgoska im. Jana i Jędrzeja Śniadeckich, Wydział Inżynierii Mechanicznej, Katedra Mechaniki i Metod Komputerowych
(miejsce pracy/afiliacja)

OŚWIADCZENIE

Oświadczam, iż mój wkład autorski w niżej wymienionym/wymienionych artykule/artykułach naukowym/naukowych był następujący*:

1. Pejkowski Ł, Seyda J, Skibicki D. Short cracks observations on surfaces of specimens made of three materials, subjected to synchronous and asynchronous multiaxial loadings, Matec Web of Conferences (EDP Sciences), 2019, 300, 1-8, DOI: 10.1051/matecconf/201930015002, 5 pkt. MNiSW.
   Wykonane zadania w ramach artykułu:
   a) analiza formalna
   b) pisanie - recenzowanie i edycja

2. Seyda J, Pejkowski Ł, Skibicki D. The shear stress determination in tubular specimens under torsion in the elastic–plastic strain range from the perspective of fatigue analysis. Materials (MDPI), 2020, 13, 23, 1-16, DOI: 10.3390/ma13235583, 140 pkt. MNiSW, IF 3.623.
   Wykonane zadania w ramach artykułu:
   a) analiza formalna
   b) pisanie - recenzowanie i edycja
   c) nadzór

3. Seyda J, Pejkowski Ł, Skibicki D. Identification of fatigue damage mechanism in PA38-T6 aluminum alloy under multiaxial loadings – Initial research. Procedia Structural Integrity (Elsevier), 2020, 28, - , 1458-1466, DOI: 10.1016/j.prostr.2020.10.119, 5 pkt. MNiSW.
   Wykonane zadania w ramach artykułu:
   a) zasoby
   b) pisanie - recenzowanie i edycja

---

* *W przypadku prac dwu- lub wieloautorskich wymagane są oświadczenia kandydata do stopnia doktora oraz współautorów, wskazujące na ich merytoryczny wkład w powstanie każdej pracy (np. twórca hipotezy badawczej, pomysłodawca badań, wykonanie specyficznych badań – np. przeprowadzenie konkretnych doświadczeń, opracowanie i zebranie ankiet itp., wykonanie analizy wyników, przygotowanie manuskryptu artykułu i inne). Określenie wkładu danego autora, w tym kandydata do stopnia doktora, powinno być na tyle precyzyjne, aby umożliwić dokładną ocenę jego udziału i roli w powstaniu każdej pracy.*

4. Seyda J, Skibicki D, Pejkowski Ł, Skibicki A, Domanowski P, Maćkowiak P. Mechanical properties and microscopic analysis of sintered rhenium subjected to monotonic tension and uniaxial fatigue. Materials Science and Engineering A (Elsevier), 2021, 817, 141343, 1-13, DOI: 10.1016/j.msea.2021.141343, 140 pkt. MNiSW, IF 6.044.
   Wykonane zadania w ramach artykułu:
   a) konceptualizacja
   b) analiza formalna
   c) zasoby
   d) gromadzenie danych
   e) przygotowanie pierwotnego szkicu
   f) nadzór

Jednocześnie wyrażam zgodę na przedłożenie wyżej wymienionej/wymienionych pracy/prac przez ..... mgr inż. Jan Seyda..... (podać tytuł zawodowy imię i nazwisko kandydata do stopnia doktora) jako część rozprawy doktorskiej opartej na zbiorze opublikowanych i powiązanych tematycznie artykułów naukowych.

Bydgoszcz, 26.01.2024
.....
miejscowość, data

D. Skibicki
.....
podpis Współautora

Załącznik nr 3 do
Instrukcji drukowania, gromadzenia, rejestrowania i udostępniania rozpraw doktorskich przez rady naukowe dyscyplin (dyscyplin artystycznych) prowadzących postępowanie w sprawie nadania stopnia naukowego doktora

Oświadczenie Współautora

mgr inż. Mateusz Chorobiński
(tytuł zawodowy, imiona i nazwisko współautora)

Politechnika Bydgoska im. Jana i Jędrzeja Śniadeckich, Wydział Technologii i Inżynierii Chemicznej, Zakład Fizykochemii Powierzchni
(miejsce pracy/afiliacja)

OŚWIADCZENIE

Oświadczam, iż mój wkład autorski w niżej wymienionym/wymienionych artykule/artykułach naukowym/naukowych był następujący*:

1. Seyda J, Pejkowski Ł, Chorobiński M. Study on the behavior of small cracks in PA38-T6 (6060-T6) aluminum alloy under multiaxial fatigue loadings. International Journal of Fatigue (Elsevier), 2024, 184, 108282, DOI: 10.1016/S1003-6326(23)66333-2, 140 pkt. MNiSW, IF 6.000.
   Wykonane zadania w ramach artykułu:
   a) badania mikroskopowe powierzchni próbek

Jednocześnie wyrażam zgodę na przedłożenie wyżej wymienionej/wymienionych pracy/prac przez …….. mgr inż. Jan Seyda…… (podać tytuł zawodowy imię i nazwisko kandydata do stopnia doktora) jako część rozprawy doktorskiej opartej na zbiorze opublikowanych i powiązanych tematycznie artykułów naukowych.

Bydgoszcz, 09.04.2024 r.
miejscowość, data

Mateusz Chorobiński
podpis Współautora

* *W przypadku prac dwu- lub wieloautorskich wymagane są oświadczenia kandydata do stopnia doktora oraz współautorów, wskazujące na ich merytoryczny wkład w powstanie każdej pracy (np. twórca hipotezy badawczej, pomysłodawca badań, wykonanie specyficznych badań – np. przeprowadzenie konkretnych doświadczeń, opracowanie i zebranie ankiet itp., wykonanie analizy wyników, przygotowanie manuskryptu artykułu i inne). Określenie wkładu danego autora, w tym kandydata do stopnia doktora, powinno być na tyle precyzyjne, aby umożliwić dokładną ocenę jego udziału i roli w powstaniu każdej pracy.*

Załącznik nr 3 do
Instrukcji drukowania, gromadzenia, rejestrowania i udostępniania rozpraw doktorskich przez rady naukowe dyscyplin (dyscyplin artystycznych) prowadzących postępowanie w sprawie nadania stopnia naukowego doktora

Oświadczenie Współautora

Dr inż. Andrzej Skibicki
(tytuł zawodowy, imiona i nazwisko współautora)

Politechnika Bydgoska im. Jana i Jędrzeja Śniadeckich, Wydział Inżynierii Mechanicznej, Katedra Podstaw Konstrukcji Maszyn i Inżynierii Biomedycznej
(miejsce pracy/afiliacja)

OŚWIADCZENIE

Oświadczam, iż mój wkład autorski w niżej wymienionym/wymienionych artykule/artykułach naukowym/naukowych był następujący*:

1. Seyda J, Skibicki D, Pejkowski Ł, Skibicki A, Domanowski P, Maćkowiak P. Mechanical properties and microscopic analysis of sintered rhenium subjected to monotonic tension and uniaxial fatigue. Materials Science and Engineering A (Elsevier), 2021, 817, 141343, 1-13, DOI: 10.1016/j.msea.2021.141343, 140 pkt. MNiSW, IF 6.044. Wykonane zadania w ramach artykułu:
   a) badania metalograficzne,

Jednocześnie wyrażam zgodę na przedłożenie wyżej wymienionej/wymienionych pracy/prac przez ..... mgr inż. Jan Seyda..... (podać tytuł zawodowy imię i nazwisko kandydata do stopnia doktora) jako część rozprawy doktorskiej opartej na zbiorze opublikowanych i powiązanych tematycznie artykułów naukowych.

Bydgoszcz, 29.01.2024
miejscowość, data

ASkibicki
podpis Współautora

* *W przypadku prac dwu- lub wieloautorskich wymagane są oświadczenia kandydata do stopnia doktora oraz współautorów, wskazujące na ich merytoryczny wkład w powstanie każdej pracy (np. twórca hipotezy badawczej, pomysłodawca badań, wykonanie specyficznych badań – np. przeprowadzenie konkretnych doświadczeń, opracowanie i zebranie ankiet itp., wykonanie analizy wyników, przygotowanie manuskryptu artykułu i inne). Określenie wkładu danego autora, w tym kandydata do stopnia doktora, powinno być na tyle precyzyjne, aby umożliwić dokładną ocenę jego udziału i roli w powstaniu każdej pracy.*

Załącznik nr 3 do
Instrukcji drukowania, gromadzenia, rejestrowania i udostępniania rozpraw doktorskich przez rady naukowe dyscyplin (dyscyplin artystycznych) prowadzących postępowanie w sprawie nadania stopnia naukowego doktora

Oświadczenie Współautora

Dr hab. inż. Łukasz Pejkowski
(tytuł zawodowy, imiona i nazwisko współautora)

Politechnika Bydgoska im. Jana i Jędrzeja Śniadeckich, Wydział Inżynierii Mechanicznej, Katedra Mechaniki i Metod Komputerowych
(miejsce pracy/afiliacja)

OŚWIADCZENIE

Oświadczam, iż mój wkład autorski w niżej wymienionym/wymienionych artykule/artykułach naukowym/naukowych był następujący*:

1. Pejkowski Ł, Seyda J. Fatigue of four metallic materials under asynchronous loadings: Small cracks observation and fatigue life prediction, International Journal of Fatigue (Elsevier), 2021, 142, 105904, 1-18, DOI: 10.1016/j.ijfatigue.2020.105904, 140 pkt. MNiSW, IF 5.489. Wykonane zadania w ramach artykułu:
    a) konceptualizacja
    b) metodologia
    c) badania wytrzymałościowe
    d) walidacja
    e) analiza formalna
    f) gromadzenie danych
    g) przygotowanie pierwotnego szkicu
    h) pisanie - recenzowanie i edycja
    i) wizualizacja
    j) nadzór
    k) administracja projektu
    l) zdobycie finansowania

* *W przypadku prac dwu- lub wieloautorskich wymagane są oświadczenia kandydata do stopnia doktora oraz współautorów, wskazujące na ich merytoryczny wkład w powstanie każdej pracy (np. twórca hipotezy badawczej, pomysłodawca badań, wykonanie specyficznych badań – np. przeprowadzenie konkretnych doświadczeń, opracowanie i zebranie ankiet itp., wykonanie analizy wyników, przygotowanie manuskryptu artykułu i inne). Określenie wkładu danego autora, w tym kandydata do stopnia doktora, powinno być na tyle precyzyjne, aby umożliwić dokładną ocenę jego udziału i roli w powstaniu każdej pracy.*

Z.16.2021.2022

Załącznik nr 3 do
Instrukcji drukowania, gromadzenia, rejestrowania i udostępniania rozpraw doktorskich przez rady naukowe dyscyplin (dyscyplin artystycznych) prowadzących postępowanie w sprawie nadania stopnia naukowego doktora

Oświadczenie Współautora

Dr hab inż. Piotr Domanowski
(tytuł zawodowy, imiona i nazwisko współautora)

Politechnika Bydgoska im. Jana i Jędrzeja Śniadeckich, Wydział Inżynierii Mechanicznej, Katedra Technik Wytwarzania
(miejsce pracy/afiliacja)

OŚWIADCZENIE

Oświadczam, iż mój wkład autorski w niżej wymienionym/wymienionych artykule/artykułach naukowym/naukowych był następujący*:

1. Seyda J, Skibicki D, Pejkowski Ł, Skibicki A, Domanowski P, Maćkowiak P. Mechanical properties and microscopic analysis of sintered rhenium subjected to monotonic tension and uniaxial fatigue. Materials Science and Engineering A (Elsevier), 2021, 817, 141343, 1-13, DOI: 10.1016/j.msea.2021.141343, 140 pkt. MNiSW, IF 6.044. Wykonane zadania w ramach artykułu:
   a) konceptualizacja
   b) zasoby – dostarczenie materiału.

Jednocześnie wyrażam zgodę na przedłożenie wyżej wymienionej/wymienionych pracy/prac przez …….. mgr inż. Jan Seyda…… (podać tytuł zawodowy imię i nazwisko kandydata do stopnia doktora) jako część rozprawy doktorskiej opartej na zbiorze opublikowanych i powiązanych tematycznie artykułów naukowych.

Bydgoszcz 26.01.2024
miejscowość, data

podpis Współautora

* *W przypadku prac dwu- lub wieloautorskich wymagane są oświadczenia kandydata do stopnia doktora oraz współautorów, wskazujące na ich merytoryczny wkład w powstanie każdej pracy (np. twórca hipotezy badawczej, pomysłodawca badań, wykonanie specyficznych badań – np. przeprowadzenie konkretnych doświadczeń, opracowanie i zebranie ankiet itp., wykonanie analizy wyników, przygotowanie manuskryptu artykułu i inne). Określenie wkładu danego autora, w tym kandydata do stopnia doktora, powinno być na tyle precyzyjne, aby umożliwić dokładną ocenę jego udziału i roli w powstaniu każdej pracy.*

Załącznik nr 3 do
Instrukcji drukowania, gromadzenia, rejestrowania i udostępniania rozpraw doktorskich przez rady naukowe dyscyplin (dyscyplin artystycznych) prowadzących postępowanie w sprawie nadania stopnia naukowego doktora

Oświadczenie Współautora

Dr inż. Paweł Maćkowiak
(tytuł zawodowy, imiona i nazwisko współautora)

Politechnika Bydgoska im. Jana i Jędrzeja Śniadeckich, Wydział Inżynierii Mechanicznej, Katedra Podstaw Konstrukcji Maszyn i Inżynierii Biomedycznej
(miejsce pracy/afiliacja)

OŚWIADCZENIE

Oświadczam, iż mój wkład autorski w niżej wymienionym/wymienionych artykule/artykułach naukowym/naukowych był następujący*:

1. Seyda J, Skibicki D, Pejkowski Ł, Skibicki A, Domanowski P, Maćkowiak P. Mechanical properties and microscopic analysis of sintered rhenium subjected to monotonic tension and uniaxial fatigue. Materials Science and Engineering A (Elsevier), 2021, 817, 141343, 1-13, DOI: 10.1016/j.msea.2021.141343, 140 pkt. MNiSW, IF 6.044.
   Wykonane zadania w ramach artykułu:
   a) przygotowanie próbek – cięcie próbek.

Jednocześnie wyrażam zgodę na przedłożenie wyżej wymienionej/wymienionych pracy/prac przez …….. mgr inż. Jan Seyda…… (podać tytuł zawodowy imię i nazwisko kandydata do stopnia doktora) jako część rozprawy doktorskiej opartej na zbiorze opublikowanych i powiązanych tematycznie artykułów naukowych.

Bydgoszcz 26.01.2024
miejscowość, data

Maćkowiak Paweł
podpis Współautora

* *W przypadku prac dwu- lub wieloautorskich wymagane są oświadczenia kandydata do stopnia doktora oraz współautorów, wskazujące na ich merytoryczny wkład w powstanie każdej pracy (np. twórca hipotezy badawczej, pomysłodawca badań, wykonanie specyficznych badań – np. przeprowadzenie konkretnych doświadczeń, opracowanie i zebranie ankiet itp., wykonanie analizy wyników, przygotowanie manuskryptu artykułu i inne). Określenie wkładu danego autora, w tym kandydata do stopnia doktora, powinno być na tyle precyzyjne, aby umożliwić dokładną ocenę jego udziału i roli w powstaniu każdej pracy.*